Physics-Based Near-Earth Radiowave Propagation Modeling and Simulation

by
DaHan Liao

A dissertation submitted in partial fulfillment
of the requirements for the degree of
Doctor of Philosophy
(Electrical Engineering)
in The University of Michigan
2009

Doctoral Committee:

Professor Kamal Sarabandi, Chair
Professor Eric Michielssen
Professor Wayne E. Stark
Associate Professor Mahta Moghaddam

Leo Tolstoy once wrote that the only certain happiness in life is to live for others. I have been fortunate to be a beneficiary of this sentiment as followed by those close to me. So I gratefully dedicate this to those constant shepherds of my life—the ones in my family.

ACKNOWLEDGEMENTS

In retrospect, I would like to thank the faculty, staff, and students at The Radiation Laboratory at The University of Michigan for making my stay there a pleasant and productive experience as I carried out the research work for this dissertation. I am grateful to the members of my dissertation committee, Professor Eric Michielssen, Professor Mahta Moghaddam, and Professor Wayne Stark, for devoting their time and energy into this project; especially, I would like to express my appreciation to my research advisor, Professor Kamal Sarabandi, for so kindly providing his seemingly-infinite wisdom, attentive mentorship, and thoughtful understanding in support of my graduate studies. Finally, I am thankful to the U.S. Army Research Laboratory for funding this research through the Collaborative Technology Alliances (Communications and Networks) program.

D.H.L.

Ann Arbor

12 December 2008

TABLE OF CONTENTS

LIST OF FIGURES

Figure

LIST OF TABLES

Table

LIST OF APPENDICES

Appendix

CHAPTER I

Introduction

An understanding of the interaction of the radiowave with its environment is important for supporting the engineering of robust wireless communication systems. The electromagnetic propagation characteristics of an environment—itself is a physical domain which can consist of urban, suburban, and natural scenes, or various hybridizations thereof—directly influence the design of system components such as RF transceivers, antennas, transmission waveforms, modulation schemes, and channel coding techniques. Propagation simulation tools, when properly formulated and applied, therefore can become essential instruments in facilitating network planning, performance evaluation, and signal coverage optimization. Over the years, as it will be discussed in the section hereafter, a variety of specialized simulation tools have been developed, and the progress in propagation modeling is mostly driven by the evolution in wireless applications. A burgeoning application of interest is the near-earth wireless system, which is becoming an integral part of many environmental and military surveillance infrastructures. The two defining characteristics of this type of system are that they are low-power and low-profile; as the transceivers in the communication network operate in the near-ground region, there are a number of challenging propagation issues that need to be modeled, simulated, and understood.

Assessing from the electromagnetic standpoint, the near-earth environment is a very harsh environment for radiowave propagation. For instance, the signal spreads out asymptotically from the transmitter as $1/distance^4$—even in the presence of a line-of-sight path; this power divergence feature can in turn become the primary factor in determining the energy constraint for low-power transmission; the unique properties, or complications, of near-earth propagation such as surface wave propagation, non-plane wave propagation, and higher order reflection and diffraction phenomena pose additional constraints that often beset the validity of classical analytical ray-tracing and physical optics techniques—and their heuristic extensions; furthermore, ground proximity effects can drastically change and degrade the performance of conventional antennas that have been designed without considering the ramifications of these effects. All these issues pertaining to the near-ground radio channel have not been thoroughly investigated; as such, this is the impetus for this study, the objective of which is to develop a set of modeling tools that can be used by the radio engineer to simulate the behaviors of the electromagnetic wave propagating in the near-ground environment. The scope of the problem cannot be overstated, and this study, ultimately, could only serve as a partial fulfillment to the vast amount of analysis that is needed for a complete understanding of the problem itself; nevertheless, it is intended that this work would become a useful complement and extension to existing propagation routines and would bring forth additional insights that have not been reported previously.

In the following sections, a more detailed explanation of the task undertaken in this work is presented—first, relevant background information is introduced; then the motivation for this work is established; finally, the research methodology and outline, or overview, are discussed.

1.1 Background

Marconi experimentally demonstrated the feasibility of wireless telecommunication in 1897. Since then, the technology of wireless telecommunication, or the transmission of information via radiowaves, has flourished in progressively more sophisticated forms—appearing first as novelties and gradually becoming everyday conveniences—from the wireless telegraph, to radio, to television, to cellular phones, and—most recently—to WLAN and WiMax. The interaction of radiowaves with the environment became a subject of intense interest shortly after Marconi's experiment. Early pioneers such as Van der Pol, Sommerfeld, Bremmer, and Norton undertook observation-based investigations into the propagation and diffraction of low-frequency radiowaves around the earth's surface, while Millington and Eckersley examined the refraction effects of the atmosphere [6]. The studies carried out by these investigators led to the first tabulation of propagation loss curves for sky waves and ground waves at the LF and HF bands for large antenna heights. The widespread use of VHF television and mobile radio during the 1950s necessitated the need to account for the effects of moderate-scale terrain features and buildings and initiated the development of contemporary "ray-tracing" routines. Subsequently, extensions to ray propagation schemes were formulated in the form of geometrical theory of diffraction (GTD) and uniform theory of diffraction (UTD). The proliferation of commercial handheld cellular service in the 1980s prompted the use of empirically-derived statistical models such as the Okumura-Hata model and the Walfisch-Ikegami model for signal prediction in urban areas; while continued to be widely used today for cellular, WLAN, and WiMAX coverage planning, these models, however, cannot be applied to small and micro radio cells. As demand for accuracy increases, full-

wave numerical propagation models—viz., integral equation solvers, finite difference solvers, and parabolic equation methods—began to emerge near the latter part of the 20th century.

As briefly outlined above—and chronologically illustrated in Figure 1.1, the progress in radiowave propagation modeling is predominately dictated by the evolution in telecommunications technology. The rise in the number of deployment of unattended ground sensor networks for environmental and military surveillance applications has prompted the need for a more complete understanding of near-earth wireless communication channels. An unattended ground sensor (UGS) is a low-power and low-profile wireless transceiver that gathers a variety of data (acoustic, magnetic, seismic, meteorological, etc.) from its surrounding and then transmits this information to another node within the network or to a central processing station. The UGS has been identified and accepted as an important component of the Army's Future Combat System (FCS) with applications ranging from perimeter enforcement to battlefield condition monitoring. Since the heights of the transmitters and receivers in the network are low, ground conditions (i.e., soil composition, moisture content, roughness) and dielectric coverings (i.e., vegetation, snow) can have substantial effects on signal coverage and would have to be included for an accurate and realistic understanding of the propagation characteristics and for the prediction of node connectivity.

The key operational requirements of an UGS transceiver node are the following [7]:

Low visual signature: a small form factor is required to evade detection. A low-profile, miniaturized antenna design is consequently desired.

Low power consumption: as the UGS unit is battery powered, the RF circuitry, the transmission waveform and protocol, and the radio link must be properly chosen and designed to support missions as long as 60 days. The inherent low-power constraint of

Hardware Component	Production Cost
Antennas and radio	\$1000–\$3000
GPS	\$100
Electronic compass	\$400–\$700
Main processor, DSP, microphone array	\$500
Case	\$150
Connectors	\$50
Batteries	\$200
Geophone	\$75
Windscreen	<\$50

Table 1.1: Costs of UGS components [5].

the network places stringent requirements on the fabrication of the UGS module. As the transceiver is the most expensive part of the module (Table 1.1), the importance of a proper understanding of propagation issues for the establishment of an accurate link budget is evident. Simulation tools established for network technologies such as IEEE 802.11, Bluetooth, and cellular 3G/4G are focused on broadband systems with high power and high data rates and therefore are not appropriate for low-power applications.

Long range connectivity with ground level antennas: it is well-known that system power efficiency decreases dramatically with decreasing antenna height; for large nodal separation distances (up to several kilometers), optimizing network performance for the near-ground channel is especially challenging since the radiowave has to interact with the ground and terrain obstacles at grazing angles.

Secure RF link: for military-related applications, a secure link is needed to provide low probability of detection and intercept. A 20–30 dB jamming resistant link is often required. A judicious balance must be established between the tradeoffs of low-power emission and reliable connectivity. Issues such as operational frequency, bandwidth, data rate, transmission waveform, modulation, and routing and channel protocols are inter-related and all have to be assessed with respect to the propagation link budget.

1.2 Motivation

Wireless connectivity among sensors in an UGS system is critical, and due to the requirement of a low-power sensor grid, the ability to accurately predict the effects of the propagation channel on system performance is essential in designing for maximum efficiency. The initial phase of UGS network deployment is wireless planning, the goal of which is to develop a coverage map (a solution, or—in this case—a node constellation) constrained on a system quality factor such as average signal level, bit error rate, or interference occurrency. Wireless planning is divided into two stages: (1) evaluation and optimization of performance using propagation coverage and analysis tools; (2) confirmation of performance through field measurements. Accurate and efficient propagation models are crucial to the RF engineer in the development of a solution of the planning optimization algorithm, as the optimization process could be the most computationally demanding part of the planning phase. For low-power systems such as UGS networks, propagation losses become the dominant energy and efficiency constraint; an understanding of the causes of these losses is required in the construction and evaluation of mitigation schemes and signal coding techniques.

In assessing the various environmental effects, those of the ground are substantial and site specific. Vegetation, ground roughness and undulations, soil-moisture, and many other factors affect the radio signal. There are also issues with regard to the proper choice of antennas for UGS applications. The performance characteristics such as input impedance and radiation pattern of antennas designed for operation in free space can drastically change once these antennas are placed near the ground. As each terrain feature has its own inherent electromagnetic problem to solve, various numerical and analytical methods are required to evaluate the effects on the

propagation channel from each one.

As alluded to earlier, adequate propagation models do not exist for very low antenna heights—to support either coarse or detailed analysis and prediction of sensor network performance, for the validity of the models aforementioned in Section 1.1 is biased toward applications defined by placement of transmitters and receivers relatively far above the ground surface. As a result, the proper design and planning of near-ground networks require not only the re-examination and refinement of solutions established for "off-ground" systems but also the development of new propagation simulation paradigms. In supporting the deployment of this new generation of networks, there are only a limited number of detailed studies—either theoretical or empirical—available in literature discussing the effects of ground properties on communication channels located directly on the ground. Partial efforts have been made—for example, in [8] and [9]—to characterize near-ground channels through measurement campaigns. In [8], line-of-sight and forest-obstructed signal paths are studied at 300 MHz and 1900 MHz with the derivation of path-loss models as a function of transceiver height, range, and frequency by simply fitting the measurement data to generic path-loss equations. A similar heuristic curve-fitting approach is used in [9] to study the path-loss and shadowing variance behaviors of ground-lying antenna configurations in various indoor and outdoor environments at 800–1000 MHz. The shortcoming of these studies is that their empirical results are specific to the application parameters presented therein; in other words, when attempting to extend these results to more general propagation scenarios, their usefulness is likely to be compromised as they do not take into account many other parameters of interest such as ground or soil properties, vegetation density, antenna type, etc. Therefore, in order to fully and satisfyingly characterize the various types of propagation phe-

nomenology relevant to the near-ground channel, the physics behind the propagation must be understood, and hence "physics-based" modeling should be undertaken.

1.3 Research Approach and Overview

The physics-based propagation paradigm has been applied for general radiowave channel analysis by previous workers, including Casciato [10] and Koh [11]; akin to the presentation in those works, for the sake of improving practicality and accuracy, here, the derivation of the models is directly based on a contemplation and appreciation of the underpinning physical processes and electromagnetic mechanisms (Maxwellian modeling)—as opposed to based on heuristic techniques (e.g., measurement data curve-fitting). Although a near-ground wireless system such as the UGS network can be deployed in many types of environments, the focus of this study is on propagation domains defined by natural terrain features and obstacles; specifically, the solutions to an important chosen subset of fundamental canonical problems are formulated; by understanding the governing propagation peculiarities therein, these problems can become building blocks for the simulation of more complicated propagation scenes, including ones that may require the incorporation of the effects of man-made structures (e.g., buildings, roads) and atmospheric and meteorological phenomena.

As depicted in Figure 1.2, within this dissertation, physics-based near-ground RF propagation modeling is presented for the topics shown below.

1.3.1 Effects of Vegetation or Snow Layer on Near-Earth Wave Propagation

A classic problem that was first solved by Sommerfeld [12–14], radiowave propagation over a bare, finite-conducting, flat ground has deservedly garnered much attention over the decades due to its importance and the form of the integrals (so-called

Sommerfeld integrals) found in its solution. Following Sommerfeld, additional works for the same problem have been carried out by Norton [15,16] and Bãnos [17], resulting in efficient formulations for characterizing ground wave propagation. Although these formulations are sufficient for simple near-ground propagation scenarios, much work remains in evaluating the effects of dielectric coverings such as vegetation or snow layers.

The problem of near-earth wave propagation in the presence of a continuous dielectric layer such as a vegetation or snow covering is considered in Chapter II by modeling the propagation environment as a homogeneous two-layer medium (air/dielectric/ground). A number of studies have demonstrated the relevancy of the lateral wave for the case when both the transmitter and receiver are located within a simple half-space dielectric medium [18–24]. Unfortunately, for the generalized two-layer model, for configurations in which the transmitter or receiver (or both) is located above the dielectric layer, far field analytical expressions that include all propagation features do not exist. In this work, in order to arrive at a computational efficient solution for the two-layer model, a second order asymptotic evaluation for the electric fields of an arbitrarily-oriented, infinitesimal electric dipole—for source and observation points located in the vicinity of the air/dielectric interface—is carried out through the method of steepest descents. The formulations are valid in the far field, with the limitation that the exponentially-decaying pole and branch cut contributions have been ignored. It is observed that the Norton wave, though it is highly localized near the air/dielectric interface, is a significant contribution either when the dipole and observation points are both located above the dielectric layer or when one is above and the other is within the layer.

In investigating the effects of foliage in Chapter II, it is assumed that the vegeta-

tion layer is infinite in extent in the two dimensions parallel to the ground; another problem of interest can be reached by truncating the layer in one of the horizontal directions; the resultant influences of such an abrupt truncation on the radio signal need to be analyzed. In Chapter III, the far field radiation from an infinitesimal electric dipole embedded inside a truncated vegetation layer above a dielectric ground plane is calculated. Through an application of the equivalence or Huygens' principle, a semi-exact solution for the received field at locations exterior to the vegetation layer is obtained by a surface-field integration technique in which the spatial domain of integration is over a plane containing the truncated face of the vegetation canopy. The numerical results are computed using stationary phase approximations and show improvement over those determined through an existing ray-tracing approach. Simulation results are also compared against measured data from controlled experiments carried out within a laboratory environment using a well-characterized scaled-replica of the propagation medium at a proportionally higher frequency. It is shown that ray-tracing provides accurate results at distant points from the vegetation truncation plane when the receiver height is large in terms of the wavelength but slightly underestimates the path-loss when the receiver is close to the ground.

1.3.2 Effects of Undulating Terrain on Near-Earth Wave Propagation

Just as the effects of dielectric coverings need to be considered, those of the terrain irregularity encountered by an electromagnetic wave along its path of propagation should be taken into account as well in characterizing the near-ground radio channel. Commonly used analytical prediction models for dealing with irregular terrain profiles include knife-edge diffraction models—which are derived from Fresnel-Kirchhoff scalar theory for optics [25–27]; the Longley-Rice model [28]—which relies partly upon knife-edge diffraction as well as empirically-determined attenuation functions;

and wedge diffraction models [29, 30]—which use wedge diffraction coefficients in tracking the wavefront. By replacing the terrain features with simple geometries (i.e., knife-edges and wedges) and considering only first order interactions, these and other ray-tracing techniques, however, cannot provide sufficient accuracy in signal coverage prediction for near-ground networks, which often are placed in the deep terrain shadows, where the signal is characterized by higher order reflection and diffraction effects. Over a gently-varying terrain profile, for example, creeping surface wave modes play a significant role in propagating the electromagnetic wave along the surface; unfortunately, standard formulations for evaluating the diffraction around canonical shapes such as cylinders and parabolic curvatures do not fully capture all the propagation features; in addition, when heuristically extended to deal with generalized curvatures in long-distance propagation analysis, these formulations often lead to erroneous results for the regions located far beyond the shadow boundaries.

The popularity of the aforementioned GO/GTD/UTD-based ray-tracing techniques notwithstanding, research focus in recent years has shifted toward the practical implementation of finite difference and boundary integral equation (IE) simulators to fulfill the growing demand for signal coverage prediction models of realistic terrain scenes. The application of a computationally efficient, high-order accurate integral equation solver for predicting long-distance radiowave propagation over irregular terrain is described in Chapter IV. Although extensively chronicled in literature, classical IE solvers prove to be rather ill-suited for studying long-distance, over-terrain propagation because of the large computational cost and the inherent low-order accuracy. Two recent developments, however, have made IE solvers far more attractive for modeling terrain propagation phenomena. The first is the development of fast-multipole methods (FMM), which significantly improve the efficiency

of the solvers. The second is the emergence of high-order and error-controllable discretization schemes [31]. In view of these developments, an FMM-accelerated and high-order accurate Nyström solver is explored for analyzing wave propagation.

Specifically, a 2D surface integral equation-based Nyström solver in which a phase extraction technique is utilized to reduce the number of surface unknowns is implemented. As forward scattering is the dominant mechanism for the near-ground wave propagation scenario, the associated rapidly-varying phase components of the integral equation kernel and solution unknowns are deduced and isolated in advance and subsequently built into the solver. It is shown that by applying this method, when combining with an adaptive surface segmentation routine, as few as one to two average unknowns per wavelength is adequate in obtaining accurate solutions. This significantly reduces the memory storage and computational expense for the simulation of long-distance propagation effects. The efficiency of this method is further improved by incorporating it into the framework of the fast multipole scheme. The full details of the algorithm are discussed, along with performance comparisons of the new solver to a regular Nyström solver for terrain surfaces in terms of solution convergence.

The current numerical implementation can also be a valuable tool for validating existing asymptotic-based algorithms; in particular, it can be a convenient alternative for obtaining diffraction coefficient parameters, as shown in Chapter IV for a class of smooth dielectric surfaces. In addition, the developed full-wave simulator can facilitate the development of an efficient approximate model for analyzing propagation over small to moderate random terrain roughness—as described in Chapter V. For near-ground propagation configurations, as the rough terrain section located in between but in the far field of the transmitter and receiver points appears to be

electrically flat to the forward propagating wave, an approximate simplified model is derived with the replacement of this section with a physically flat section of an effective height, resulting in a problem with three physical sub-domains. This model implies that the mean received power and its fluctuation are primarily dictated by the statistics of the rough terrain local to the transmitter and receiver. Wave propagation over the three sub-domains is solved using a recursive, 2D Nyström-discretized-integral-equation-based forward marching scheme. Since the majority of the final terrain profile is flat and over which field interactions can be cast in terms of a block-Toeplitz matrix, large memory savings and computational speedup are achieved. The accuracy of the three-sub-domain model is demonstrated, and simulation results for the path-loss of LOS and NLOS (non-line-of-sight) links are presented for rough terrain with various random statistics.

For the treatment of random terrain surfaces, although the numerical models as outlined above and found in Chapters IV and V are shown to be highly efficient, it is also desirable to arrive at closed-form analytical expressions in encapsulating the stochastic scattering effects generated. These effects have been considered in previous works by simply introducing a correction factor into the flat-surface coherent reflection coefficient. Expressions for the correction factor derived from geometrical-optics and Kirchhoff models include the Ament approximation [32] and the Miller-Brown approximation [33, 34], which—respectively—are given by

$$\xi_A = e^{-\frac{1}{2}(2k_o\sigma\cos\theta)^2}, \tag{1.1}$$

$$\xi_{MB} = \xi_A I_o\left(\frac{1}{2}\left(2k_o\sigma\cos\theta\right)^2\right), \tag{1.2}$$

where I_o is the modified Bessel function of the first kind of order zero, σ is the terrain rms height, and θ is the grazing angle with respect to the normal as deter-

mined by the heights of the transmitter and receiver and surface mean. For near-ground or near-grazing propagation problems, however, simulation results indicate that applications of these roughness factors cannot generate accurate approximations for the mean field; the discrepancies observed can be explained by the fact that the geometrical-optics and Kirchhoff models ignore terrain shadowing. Furthermore, these factors are independent of the surface correlation function, which can be an important determinant of signal statistics. To formulate a modified—and more accurate—analytical expression for the rough surface reflection coefficient, an existing perturbation approach [35] is explored in Chapter VI for deriving the near-grazing scattering characteristics of the surface; consequently, the effective coherent reflection coefficient to the third order in the perturbation series is presented and validated for near-grazing propagation of 2D and 3D radiators.

1.3.3 Performance Analysis of Low-Profile, Electrically-Small, Near-Earth Antennas

Since environmental factors can directly influence the efficiency with which electromagnetic energy can be injected into an antenna as well as the manner in which the radiowave spreads out from the excited antenna, the issues of wave propagation and antenna design are inter-connected and must be evaluated simultaneously for a precise assessment of the wireless system performance; this observation is especially true for UGS networks as they function in extreme proximity to the ground environment, a circumstance which can give rise to effects critical for considerations related to antenna efficiency, input matching, radiation pattern, and the overall path-loss between the transmitter and receiver nodes. For simplicity, in accordance to standard antenna theory and practice, antennas are designed assuming a free space surrounding and subsequently—if needed—are tuned based on post-fabrication measurements in order to meet operational requirements; the behaviors of the antenna in a real-

istic environment can also be estimated by using pre-established correction factors. For instance, to account for ground effects, the antenna pattern is often calculated through the use of a two-ray model; this procedure, however, breaks down for near-ground applications due to the non-TEM aspect of the propagating signal and the manifestation of various modes of surface waves.

The enigmatic nature of an antenna's near-earth characteristics demands the development of a more rigorous modeling technique in analyzing its performance. In Chapter VII, an investigation into the simulation of low-profile, electrically-small antennas (located on a flat dielectric ground) for UGS networks is featured through the introduction of a terminal-to-terminal power tracking approach. While vertical wire antennas are shown to be less susceptible to propagation loss, a low-profile alternative is desired for UGS applications and is often required in the fabrication of low-cost, monolithic on-chip, miniaturized systems. In this study, the performances of different transceiver systems utilizing different types of near-ground antenna structures including the dipole, loop, ordinary circular slot, and cavity-backed circular slot are analyzed using a full-wave hybrid approach consisting of the moment method in conjunction with a near-ground asymptotic field propagation model. The figure of merit for comparison among the various configurations is identified as the efficiency factor calculated from the ratio of the input power at the transmitting antenna terminal to the received power at the receiving antenna terminal. The unique features of ground proximity effects as pertaining to near-ground operation are discussed and an optimal radiator is identified from the set of structures analyzed.

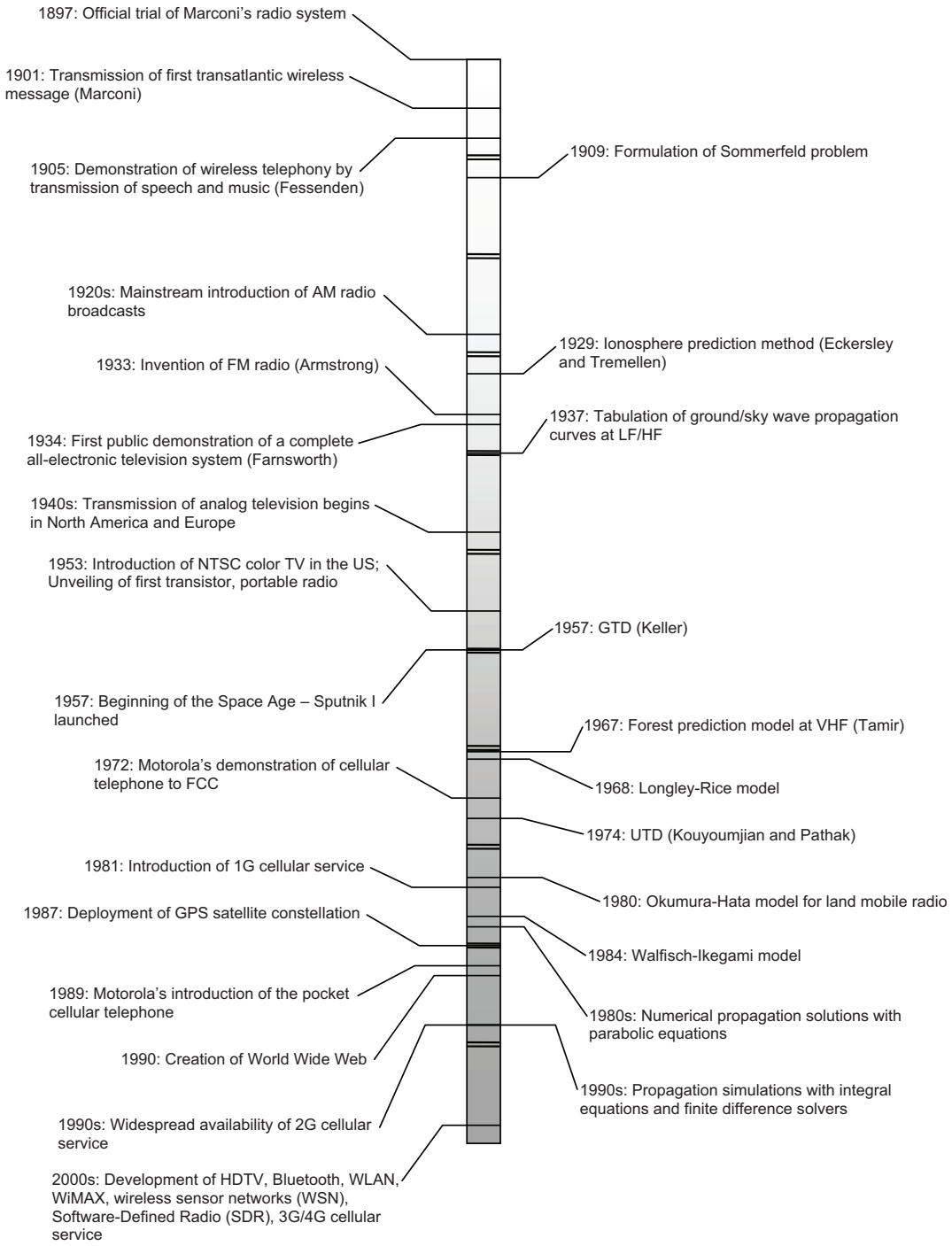

Figure 1.1: Developments in telecommunication technology and radiowave propagation modeling—a non-comprehensive overview, partially derived from the chronology outlined in [1].

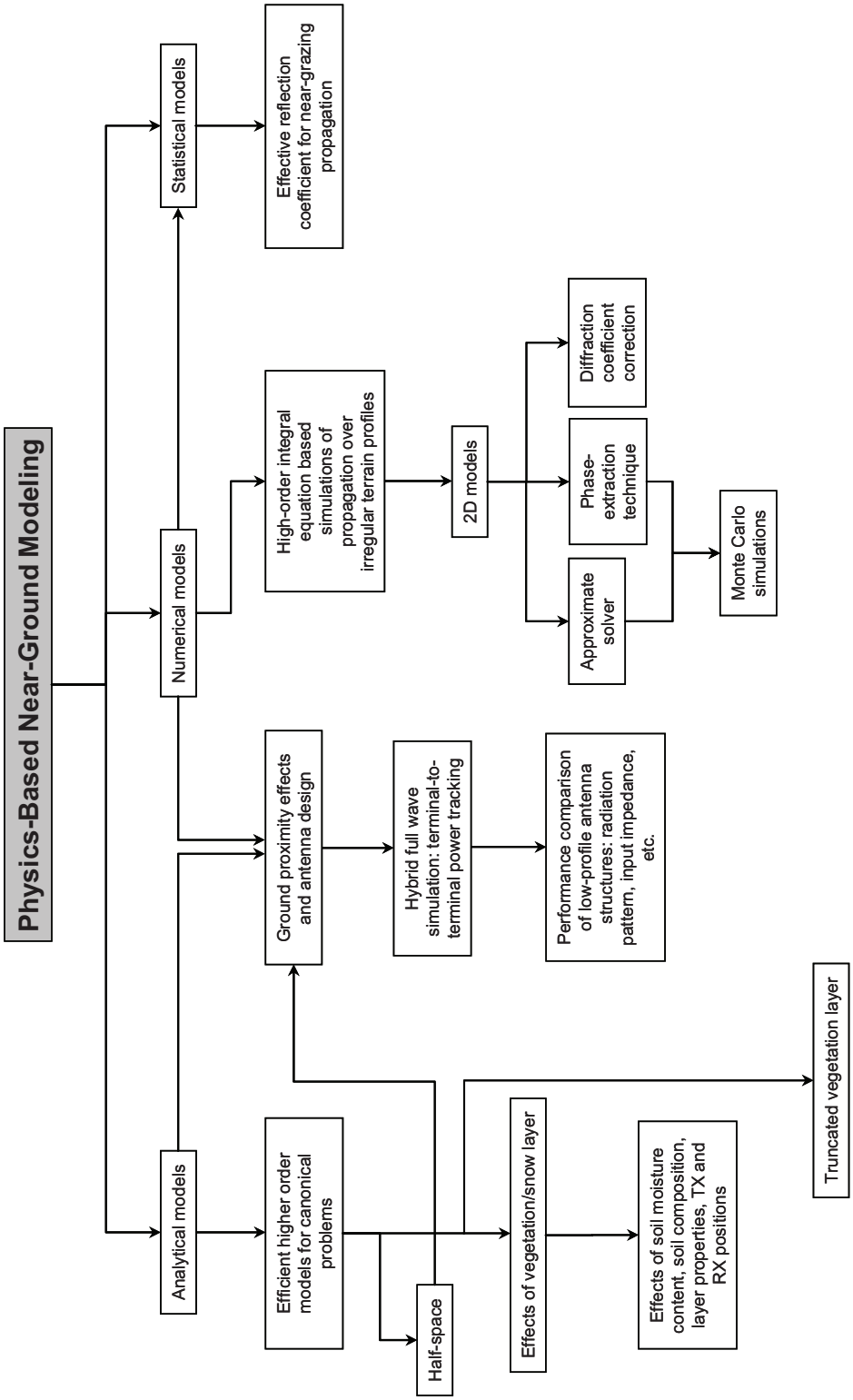

Figure 1.2: Research outline.

CHAPTER II

Near-Earth Wave Propagation Characteristics of Electric Dipole in Presence of Vegetation or Snow Layer

2.1 Introduction

The asymptotic solution to the problem of dipole radiation in the presence of a vegetated-terrain at VHF was studied first by Tamir [20, 21] and subsequently by others including Li *et al.* [22], Cavalcante and Giarola [23], and Sarabandi and Koh [24]. However, in all these studies, both the source and observation points are assumed to be embedded in the vegetation; for such a configuration, the far field radiation is dominated by the lateral wave and the Norton wave is of little importance; for the generalized configuration, in which the source and observation point locations can be arbitrary (with respect to the air/dielectric interface), a compact and comprehensive set of formulations for computing the total field cannot be found in existing literature. The more general problem of dipole radiation in the presence of a layered media has been thoroughly treated, but the associated equations are in integrals of the Sommerfeld form and are too complicated for computation when the source and observation points are far apart; the transformation of these integrals into asymptotic forms has been discussed, for instance, by Chew and Kong [36]—for a general two-layer medium but only for source and observation points directly *on* the air/dielectric interface—and by Marin and Pathak [37]—for applications pertaining

to grounded, lossless double-layer printed circuitry. While it is possible that the results generated by Marin and Pathak can be extended and specialized to the class of near-earth propagation problems treated in this work, no attempts have been made toward such an endeavor; in addition, although their closed-form expressions have been shown to be valid even in the near-field region of the source, the equations are rather involved and cannot be implemented easily as a consequence of the existence of poles and branch cuts as well as the proximity of these singularities to the saddle point. The objective of this chapter is to present field expressions assembled by retaining only a dominant asymptotic contribution; for application to propagation problems in the far field (or, as it is in the current case, when the transmitter and receiver are separated by hundreds or thousands of meters or even more), this simplification is justified and an accurate approximation to the far field radiation characteristics can be readily obtained in an efficient manner.

The present work is an extension of a previous study [24], which investigated the propagation characteristics for the case when both the source and observation points are embedded inside a vegetation layer. In this work, the analysis is broaden to the general case in which the locations of the source and observation points can be at any location above ground. Specifically, the following three configurations are analyzed in order: (1) source and observation points in air; (2) source in dielectric layer, observation point in air; (3) source and observation points in dielectric layer. The fields of other configurations can be easily deduced through the reciprocity principle. Since the third case has been thoroughly investigated by [24], only the results are presented here; for the complete derivation, the reader is referred to the original work.

The propagation of electromagnetic waves in the presence of vegetation or snow-

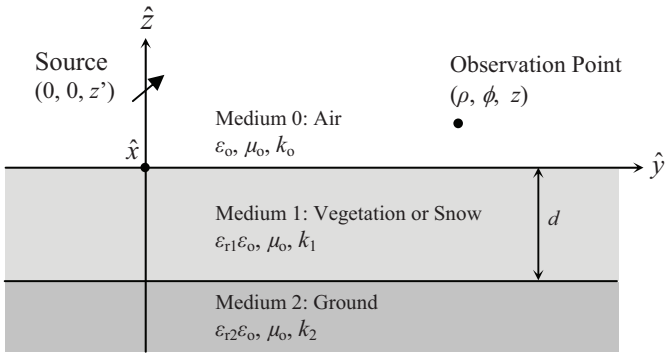

Figure 2.1: Two-layer medium model for calculating the fields of an arbitrarily-oriented electric dipole.

covered terrain can be understood by considering vegetation or snow as a homogeneous layer with an effective dielectric constant and analyzing the fields in the resulting two-layer medium (Figure 2.1). In order for this model to be accurate, especially in the case of a vegetation layer, the wavelength of propagation should be large compare to the dimensions of the features inside the layer (e.g., branches, leaves, spacing between individual plants). As suggested by [20–22], for a forest environment, the highest frequency at which the vegetation layer can be considered to be homogeneous is around 200 MHz; however, for short vegetation such as grass or crops, the effective medium theory is valid up to the frequency region of about 1 GHz before scattering from vegetation particles becomes significant. For a snow layer, the limit can be even extended to the millimeter-wave range due to low volume-scattering and the high degree of uniformity within the medium. The effective dielectric constants of the vegetation or snow layer and of the ground can be computed with the use of standard mixing models as described by [2–4, 38, 39].

From the spectral representation of the dyadic Green's function (as given by [40]), exact expressions for the fields of an infinitesimal electric dipole radiating in the presence of a two-layer medium can be derived. These expressions are listed in

Appendix A. In Section 2.2, asymptotic evaluations of these expressions in the most general form are carried out by applying the method of steepest descents. In Section 2.3, simulation results are presented, and the variation of each component of the electric field is analyzed in terms of the effective permittivity, thickness of the vegetation or snow layer, locations of the dipole and observation points, and frequency of operation.

2.2 Analytical Formulations

In this section, analytical formulations for the calculation of the electric fields radiating from a short dipole of arbitrary orientation situated above a dielectric ground plane in the presence of a layer of vegetation or snow are derived. The geometry of the problem is illustrated in Figure 2.1. As it has been noted, there are three primary configurations of interest, as a result of different combinations of the locations of the electric dipole and observation point. The dipole is assumed to be located on the z-axis with current moment vector $I_o\vec{l} = I_o(l_x\hat{x} + l_y\hat{y} + l_z\hat{z})$, and the observation point—identified with the usual cylindrical coordinates—is at (ρ, ϕ, z). In the type of propagation problems considered here, for analysis restricted to the far field, it can be assumed that the magnitudes of z', z, and d are much smaller than that of ρ—the radial distance between the dipole and the observation point. Also note that primed quantities are associated with the source, and the $exp(-i\omega t)$ convention is assumed and suppressed in all the formulations.

2.2.1 Case 1 ($z' > 0$ and $z > 0$)

Consider the simple case when the source and observation points are both located in the upper layer (air) of a one-layer medium (Figure 2.1, disregarding the last layer

for the moment), the total electric field for a vertical dipole can be written as

$$E_{x,y,z}^{total} = E_{x,y,z}^{direct} + E_{x,y,z}^{scattered}. \tag{2.1}$$

Specifically, at grazing angle ($z' \ll \rho$ and $z \ll \rho$), each component of the field can be expanded as follows:

$$E_z^{total} = \frac{i\omega u_o I_o l_z e^{ik_o\rho}}{4\pi}\left\{\frac{1}{\rho} + \frac{R_{TM}}{\rho} + \frac{C_{z,1}}{\rho^2} + \frac{C_{z,2}}{\rho^3}\cdots\right\}, \tag{2.2}$$

$$E_x^{total} = \frac{i\omega u_o I_o l_z e^{ik_o\rho}}{4\pi}\cos\phi\left\{\frac{(z'-z)}{\rho^2} - \frac{(z'+z)R_{TM}}{\rho^2} + \frac{C_{x,1}}{\rho^2} + \frac{C_{x,2}}{\rho^3}\cdots\right\}, \tag{2.3}$$

$$E_y^{total} = \frac{i\omega u_o I_o l_z e^{ik_o\rho}}{4\pi}\sin\phi\left\{\frac{(z'-z)}{\rho^2} - \frac{(z'+z)R_{TM}}{\rho^2} + \frac{C_{y,1}}{\rho^2} + \frac{C_{y,2}}{\rho^3}\cdots\right\}. \tag{2.4}$$

The first term in the brackets is the direct field; the second term is the geometrical-optics reflection field; and the rest of the terms accounts for higher order scattered fields—where the Cs denote unknown factors. Since incidence is near grazing angle, it is easy to show that $R_{TM} \approx -1$, $(1 - R_{TM}) \approx 2$, whereas $(1 + R_{TM})$ is a small quantity proportional to $1/\rho$. For the z-component of the field, it can be seen that the cancellation of the direct and geometrical-optics reflection term generates a $1/\rho^2$ resultant—which is of the same order as the next term in the expansion. Likewise, for the x and y components, the sum of the direct and geometrical-optics reflection also produces a term that is of the same order as the next higher order term. Similar analysis can be applied to a horizontal dipole. Thus, when the source and observation points are close to the interface (incidence at grazing angle), it is apparent that an accurate description of the field components necessitates the derivation of the higher order term that comes after the geometrical-optics reflection term.

The complete evaluation of the field quantities begins with the two-fold integral form of the dyadic Green's function. A change of variable is applied to obtain the integration in terms of k_ρ and Bessel functions. In integral form, the resulting

expressions—for which exact closed-form solutions do not exist—of the x, y, and z components of the scattered field are given in Appendix A. Since numerical computation of these expressions is slow and formidable due to the presence of singularities and the highly oscillatory behavior of the Bessel function at large distance ρ, approximate asymptotic solutions are sought. In a standard procedure, Hankel's functions of the first and second kind are used in extending the limits of integration to negative and positive infinity (in k_ρ-plane). By transforming the integration over to the complex w-plane by the change of variable $k_\rho = k_o \sin w$, and then substituting the asymptotic form of the Hankel's function for large arguments, the integrand can be written in the following form—to which the standard method of steepest descents can be applied:

$$E_{ij}^s(\rho,\phi,z) = \frac{-k_o^3 \eta_o I_o l_i}{16\pi}\sqrt{\frac{2}{ik_o\rho\pi}} \int_{-\frac{\pi}{2}+i\infty}^{\frac{\pi}{2}-i\infty} f_{ij}(w) e^{q(w)} dw, \tag{2.5}$$

where subscripts $i, j = x, y,$ or z and $q(w) = ik_o R cos(w - w_s)$. The saddle point at $w = w_s$ is defined by $q'(w_s) = 0$; therefore

$$\sin w_s = \frac{\rho}{R}, \tag{2.6}$$

$$\cos w_s = \frac{z + z'}{R}, \tag{2.7}$$

$$R^2 = \rho^2 + (z + z')^2. \tag{2.8}$$

After some manipulations and following the procedure of saddle point integration provided by [19], the j component of the saddle point contribution up to second order for a dipole pointed in the i direction can be written as

$$E_{ij}^{sp} = \frac{-k_o^3 \eta_o I_o l_i}{8\pi} e^{ik_o\rho} \cdot \left\{ f_{ij}(w_s)\left(\frac{1}{ik_o\rho}\right) + \frac{1}{2}\left[f_{ij}''(w_s) + \frac{f_{ij}(w_s)}{4}\right]\left(\frac{1}{ik_o\rho}\right)^2 \right\} \tag{2.9}$$

where the two terms represent the first and second saddle point expansion terms. The first saddle point expansion term is the geometrical-optics reflection term and the

second expansion term can be thought as a correction term that becomes dominant when the source and observation points are close to the interface. This correction term is also commonly known as the Norton wave [41]. After some lengthy algebraic manipulations, expressions for $f_{ij}(w)$ of (2.9) can be shown to be the following:

$$f_{zx} = -\frac{2}{k_o}\sin^{\frac{3}{2}} w\cos w R^{01}_{TM}(w)\cos\phi, \tag{2.10}$$

$$f_{zy} = -\frac{2}{k_o}\sin^{\frac{3}{2}} w\cos w R^{01}_{TM}(w)\sin\phi, \tag{2.11}$$

$$f_{zz} = \frac{2}{k_o}\sin^{\frac{5}{2}} w R^{01}_{TM}(w), \tag{2.12}$$

$$f_{xx,yy} = \sin^{\frac{1}{2}} w\cos w\left[R_-(w) \mp R_+(w)\cos(2\phi)\right], \tag{2.13}$$

$$f_{xy,yx} = -\sin^{\frac{1}{2}} w\cos w R_+(w)\sin(2\phi), \tag{2.14}$$

$$f_{xz} = \frac{2}{k_o}\sin^{\frac{3}{2}} w\cos w R^{01}_{TM}(w)\cos\phi, \tag{2.15}$$

$$f_{yz} = \frac{2}{k_o}\sin^{\frac{3}{2}} w\cos w R^{01}_{TM}(w)\sin\phi. \tag{2.16}$$

The mixed reflection coefficient, which is required for an x or y-directed dipole, is defined as

$$R_\pm(w) = \frac{R^{01}_{TE}(w)}{k_o\cos w} \pm \frac{\cos w R^{01}_{TM}(w)}{k_o}. \tag{2.17}$$

The TE and TM reflection coefficients are of the standard form:

$$R^{mn}_{TE}(w) = \frac{\sqrt{\varepsilon_{rm}-\sin^2 w}-\sqrt{\varepsilon_{rn}-\sin^2 w}}{\sqrt{\varepsilon_{rm}-\sin^2 w}+\sqrt{\varepsilon_{rn}-\sin^2 w}}, \tag{2.18}$$

$$R^{mn}_{TM}(w) = \frac{\varepsilon_{rn}\sqrt{\varepsilon_{rm}-\sin^2 w}-\varepsilon_{rm}\sqrt{\varepsilon_{rn}-\sin^2 w}}{\varepsilon_{rn}\sqrt{\varepsilon_{rm}-\sin^2 w}+\varepsilon_{rm}\sqrt{\varepsilon_{rn}-\sin^2 w}}. \tag{2.19}$$

The appearance of branch points at $w_b = \pm\sin^{-1}\sqrt{\epsilon_{r1}}$ entails the use of a two-sheeted Riemann surface in representing the w-plane; in order to satisfy the radiation condition, the path of integration of (2.5) is restricted to lie on the upper sheet ($\mathrm{Im}\sqrt{\varepsilon_{r1}-\sin^2 w} > 0$). The branch cut defined by $w_b = \sin^{-1}\sqrt{\epsilon_{r1}}$ may be crossed

by the steepest descent path and its contribution to the integral can be included by adding the following to the saddle point contribution [19]:

$$E_{ij}^{b} = \left(\frac{-k_o\eta_o I_o l_i}{8\pi}\right)\left(\sqrt{-2i}e^{-\frac{3}{2}i\arg(-ik_o\sqrt{1-\varepsilon_{r1}})}\right)\cdot \left(\frac{e^{ik_1\rho+ik_o\sqrt{1-\varepsilon_{r1}}(z+z')}}{\sqrt{\rho}\left|\rho\sqrt{1-\varepsilon_{r1}}-(z+z')\sqrt{\varepsilon_{r1}}\right|^{\frac{3}{2}}}\right)\lim_{w\to w_b}\sqrt{w-w_b}f_{ij}^{'}(w) \tag{2.20}$$

It can be readily verified [18, 19] that the poles of the integrand in (2.5) are not intercepted as the original integration path deforms to the steepest descent path. Depending on the permittivity of the lower medium (ϵ_{r1}), these poles (the zeros of the denominator of the reflection coefficients in (2.18) and (2.19)) may move into the vicinity of the saddle point; thus, the poles may come into effect indirectly and must be taken into account by carrying out a modified saddle point integration method. Simulation results, however, show that the ordinary saddle point integration as used here is sufficient for predicting the field contributions in the far field. The total field is then the sum of the direct, saddle point, and branch cut contributions:

$$E_{ij} = E_{ij}^{d} + E_{ij}^{sp} + U(w_s-\theta_b)E_{ij}^{b} \tag{2.21}$$

where $\theta_b = \mathrm{Re}\,(w_b) - \cos^{-1} sech\,[\mathrm{Im}\,(w_b)]$, and $U(\cdot)$ is the Heaviside step function. Calculation of (2.20) can be quite involved, but note that the branch cut contribution decays exponentially with ρ since the wave number k_1 is complex; therefore, at large ρ, the branch cut contribution can be considered as negligible.

For a two-layer medium, to account for higher order reflections that are transmitted into and then emerging from the dielectric layer, the total reflection coefficient is modified as follows [40]:

$$R_P(w) = R_P^{01} + \sum_{u=1}^{\infty} T_P^{01}\left(R_P^{12}\right)^u\left(R_P^{10}\right)^{u-1}T_P^{10}e^{i2udk_o\sqrt{\varepsilon_{r1}-\sin^2 w}}. \tag{2.22}$$

Using the relations

$$\begin{aligned} R_P^{mn} &= -R_P^{nm}; \\ T_P^{mn} &= 1 + R_P^{mn}, \end{aligned} \tag{2.23}$$

(2.22) can be re-written as

$$R_P(w) = \frac{R_P^{01} + R_P^{12} e^{i2dk_o\sqrt{\varepsilon_{r1} - \sin^2 w}}}{1 + R_P^{01} R_P^{12} e^{i2dk_o\sqrt{\varepsilon_{r1} - \sin^2 w}}}. \tag{2.24}$$

The subscript "P" is a place holder for the polarization—either TE or TM. The saddle point contribution for each higher order reflection ($u = 1, 2, ..., \infty$) in the summation series of (2.22) can be evaluated by using (2.9) after replacing the reflection coefficient term in $f_{ij}(w)$ with $T_P^{01}(R_P^{12})^u(R_P^{10})^{u-1}T_P^{10}e^{i2udk_o\sqrt{\varepsilon_{r1} - \sin^2 w}}$. Note that the higher order reflections lead to higher order poles for the terms in the summation series of (2.22); although they are still located outside of the steepest descent path, these poles are close enough that—at higher orders—they demand a more refined saddle point integration method even when ρ is relatively large; in order to circumvent this difficulty, calculations are made by following the normal mode approach in which the total aggregate reflection coefficient in (2.24) is inserted into (2.10)–(2.16) as a whole rather than as individuals in a series; this approach leads to satisfactory results in the far field even with the exclusion of the pole contributions—which are now supplied by the zeros of the denominator in (2.24) and must be located through numerical methods before their contributions can be included using a standard technique [19]. These pole contributions, depending on their locations on the complex plane, represent either distinct surface-wave modes or leaky modes [42–44]—both of which become less significant as the distance between source and observation points increases [19,45]. Also note that in the two-layer case there are branch points only at $w_b = \pm\sin^{-1}\sqrt{\varepsilon_{r2}}$ since the expression in (2.24) can be shown to be an even function

of $\sqrt{\varepsilon_{r1} - \sin^2 w}$. The branch point that can be intercepted is at $w_b = \sin^{-1}\sqrt{\varepsilon_{r2}}$; but since medium 2 (the ground layer) is highly lossy, the branch cut contribution falls off asymptotically according to $e^{ik_2\rho}$ and, hence, rapidly becomes much smaller than the algebraically decaying saddle point contribution.

2.2.2 Case 2 ($-d < z' < 0$ and $z > 0$)

Exact formulations for this case have been derived and can be found in Appendix A. Proceeding through the same procedure as before, the method of steepest descents is employed in obtaining the integral after transforming the integration to the w-plane. Multiple reflections occurring within the dielectric layer can be accommodated by defining the total transmission coefficient as the following:

$$T_P^{up}(w) = T_P^{10} \sum_{u=0}^{\infty} (R_P^{10} R_P^{12})^u e^{i2udk_o\sqrt{\varepsilon_{r1}-\sin^2 w}} = \frac{T_P^{10}}{1 + R_P^{01} R_P^{12} e^{i2dk_o\sqrt{\varepsilon_{r1}-\sin^2 w}}} \tag{2.25}$$

and

$$T_P^{down}(w) = T_P^{up} R_P^{12}. \tag{2.26}$$

The definition of (2.26) differs from that of (2.25) in that the former expression applies to waves containing an initial bounce off the dielectric layer/ground interface. It can be shown that the transmitted field E_{ij} for each order u can be written as

$$E_{ij,u}(\rho, \phi, z) = \frac{-k_o^3 \eta_o I_o l_i}{16\pi} \sqrt{\frac{2}{ik_o\rho\pi}} \int_{-\frac{\pi}{2}+i\infty}^{\frac{\pi}{2}-i\infty} f_{ij,u}(w) e^{q(w)} dw \tag{2.27}$$

where

$$q(w) = ik_o (\rho \sin w + z \cos w) \approx ik_o \rho \cos(w - w_s) \tag{2.28}$$

and the saddle point can be approximately defined by

$$\cos w_s \approx \frac{z}{\rho}. \tag{2.29}$$

The set of $f_{ij,u}(w)$ for an arbitrarily-oriented dipole can be shown to take the following forms:

$$f_{zx,u} = -\frac{2}{k_o}\frac{\sin^{\frac{3}{2}} w \cos^2 w}{\sqrt{\varepsilon_{r1} - \sin^2 w}} \cos\phi \left\{ T^{up}_{TM,u} e^{c_{up}(w)} + T^{down}_{TM,u} e^{c_{down}(w)} \right\}, \tag{2.30}$$

$$f_{zy,u} = -\frac{2}{k_o}\frac{\sin^{\frac{3}{2}} w \cos^2 w}{\sqrt{\varepsilon_{r1} - \sin^2 w}} \sin\phi \left\{ T^{up}_{TM,u} e^{c_{up}(w)} + T^{down}_{TM,u} e^{c_{down}(w)} \right\}, \tag{2.31}$$

$$f_{zz,u} = \frac{2}{k_o}\frac{\sin^{\frac{5}{2}} w \cos w}{\sqrt{\varepsilon_{r1} - \sin^2 w}} \left\{ T^{up}_{TM,u} e^{c_{up}(w)} + T^{down}_{TM,u} e^{c_{down}(w)} \right\}, \tag{2.32}$$

$$f_{xx,u} = \sin^{\frac{1}{2}} w \cos w \left\{ \left[T^{up}_{+} - T^{up}_{-} \cos(2\phi) \right] e^{c_{up}(w)} + \left[T^{down}_{-} - T^{down}_{+} \cos(2\phi) \right] e^{c_{down}(w)} \right\}, \tag{2.33}$$

$$f_{yy,u} = \sin^{\frac{1}{2}} w \cos w \left\{ \left[T^{up}_{+} + T^{up}_{-} \cos(2\phi) \right] e^{c_{up}(w)} + \left[T^{down}_{-} + T^{down}_{+} \cos(2\phi) \right] e^{c_{down}(w)} \right\}, \tag{2.34}$$

$$f_{xy,u} = f_{yx,u} = -\sin^{\frac{1}{2}} w \cos w \sin(2\phi) \left\{ T^{up}_{-} e^{c_{up}(w)} + T^{down}_{+} e^{c_{down}(w)} \right\}, \tag{2.35}$$

$$f_{xz,u} = -\frac{2}{k_o} \sin^{\frac{3}{2}} w \cos w \cos\phi \left\{ T^{up}_{TM,u} e^{c_{up}(w)} - T^{down}_{TM,u} e^{c_{down}(w)} \right\}, \tag{2.36}$$

$$f_{yz,u} = -\frac{2}{k_o} \sin^{\frac{3}{2}} w \cos w \sin\phi \left\{ T^{up}_{TM,u} e^{c_{up}(w)} - T^{down}_{TM,u} e^{c_{down}(w)} \right\}, \tag{2.37}$$

in which

$$c_{up}(w) = ik_o \sqrt{\varepsilon_{r1} - \sin^2 w}\, |z'|, \tag{2.38}$$

$$c_{down}(w) = ik_o \sqrt{\varepsilon_{r1} - \sin^2 w}(z' + 2d). \tag{2.39}$$

The designations "*up*" and "*down*" differentiate waves that are initially propagating upward and downward from the source. The mixed transmission coefficients have been written in the following form:

$$T^{up}_{\pm}(w) = \frac{T^{up}_{TE,u}}{k_o \sqrt{\varepsilon_{r1} - \sin^2 w}} \pm \frac{T^{up}_{TM,u} \cos w}{k_o}, \tag{2.40}$$

$$T^{down}_{\pm}(w) = \frac{T^{down}_{TE,u}}{k_o \sqrt{\varepsilon_{r1} - \sin^2 w}} \pm \frac{T^{down}_{TM,u} \cos w}{k_o}. \tag{2.41}$$

In the formulations above, $T_{P,u}^{up}$ and $T_{P,u}^{down}$ are the individual terms in the infinite series of (2.25) and (2.26), respectively. Instead of computing each order of transmission separately, the saddle point evaluation of (2.27) can be carried out using (2.9) as before by means of the normal mode approach—in which now the aggregate transmission coefficients in (2.25) and (2.26) are substituted into $f_{ij}(w)$ as one term. The difficulty mainly lies in taking the double derivative of $f_{ij}(w)$, but this can be overcome with the help of a symbolic math software. When the source and observation points are located in the vicinity of the interface, it is seen that both the first and second term in the saddle point expansion fall off as $1/\rho^2$; thus, as in Case 1, both expansion terms are necessary for accurate representation of the total field.

It is seen that the sign of the term $\sqrt{\varepsilon_{r1} - \sin^2 w}$ has no effect on the final result in computing the integral in (2.27); therefore, once again, the function $f_{ij}(w)$ is an even function of $\sqrt{\varepsilon_{r1} - \sin^2 w}$ and the only branch points on the complex w-plane are attributed to the term $\sqrt{\varepsilon_{r2} - \sin^2 w}$. (As a matter of fact, for general stratified media problems, in the normal mode approach, the branch points on the k_ρ plane are supplied only by the first and last layer [46]; the branch points of the first layer can be eliminated—as it has been done here—by translating the calculation onto the w-plane after the change of variable $k_\rho = k_o \sin w$. Thus, on the w-plane, the only branch points remaining are due to the last layer in the stratification.) Similar to Case 1, calculations are much simplified by ignoring contributions from the branch cut and the poles (which are provided by the zeros of the denominator of (2.25) and (2.26)); in the far field, this claim is justified since the saddle point contribution becomes the only dominant field component.

2.2.3 Case 3 ($-d < z' < 0$ and $-d < z < 0$)

As it has been shown in [24], when both the source and observation points are located inside medium 2, the direct and saddle point contributions decay exponentially as a function of the radial distance ρ since their propagation takes place in a lossy medium; the dominant contribution to the total field, as it turns out, comes from a branch cut contribution. Although a modal analysis can be used, a ray tracing approach provides a more insightful interpretation for this case. In the ray tracing approach, the effective reflection coefficient is expanded as a series before asymptotic evaluation is carried out separately for each term. In such an approach, both medium 1 and medium 2 would furnish branch cut contributions on the w-plane since now—for each individual order of reflection—the integrand in the field integral is no longer an even function of $\sqrt{\varepsilon_{r1} - \sin^2 w}$. Discarding the branch cut contribution arising from the branch point at $w_b = \sin^{-1}\sqrt{\varepsilon_{r2}}$ for the reason mentioned earlier, the only relevant and significant contribution, in the far field, comes from the branch cut contribution due to the branch point at $w_b = \sin^{-1}\sqrt{\varepsilon_{r1}}$. This branch cut contribution, which now no longer undergoes exponential decay, can be interpreted as a wave from the source that radiates upward to the dielectric/air interface at critical angle and then propagates along the interface (in air) before reaching the observation point at critical angle again. Since the majority of the propagation takes place in air, this field component—which has been labeled as the "lateral" wave—does not suffer the large path-loss experience by the direct and saddle point contributions. Through standard branch cut integration techniques, the three lowest orders of lateral waves

have been derived in [24] and are expressed in matrix form as the following ($z' > z$):

$$\vec{E}^b = \frac{-i\eta_1}{2\pi(1-1/\varepsilon_{r1})^{\frac{1}{4}}}\frac{e^{ik_o\rho}}{\sqrt{\rho}}\left\{\frac{e^{ik_1\sqrt{1-1/\varepsilon_{r1}}(|z'|+|z|)}}{\left[\sqrt{1/\varepsilon_{r1}}(|z'|+|z|)-\rho\sqrt{1-1/\varepsilon_{r1}}\right]^{\frac{3}{2}}}\overline{\overline{A}} \;+\right.$$
$$\frac{e^{ik_1\sqrt{1-1/\varepsilon_{r1}}(2d-|z'|+|z|)}}{\left[\sqrt{1/\varepsilon_{r1}}(2d-|z'|+|z|)-\rho\sqrt{1-1/\varepsilon_{r1}}\right]^{\frac{3}{2}}}\overline{\overline{A}}\cdot\overline{\overline{R}} \;+$$
$$\left.\frac{e^{ik_1\sqrt{1-1/\varepsilon_{r1}}(2d+|z'|-|z|)}}{\left[\sqrt{1/\varepsilon_{r1}}(2d+|z'|-|z|)-\rho\sqrt{1-1/\varepsilon_{r1}}\right]^{\frac{3}{2}}}\overline{\overline{A}}\cdot\overline{\overline{R}}\right\}\cdot I_o\vec{l} \qquad (2.42)$$

where $\overline{\overline{A}}$ and $\overline{\overline{R}}$ are symmetric dyads defined in [24]. The first term in (2.42) represents the direct lateral wave contribution; the second term is the contribution of the lateral wave generated from the image of the source in the ground plane; and the third term is the contribution of the direct lateral wave that has been reflected from the ground plane before reaching the observation point. It is seen that the lateral waves, and hence the total field, decrease as $1/\rho^2$—which is the same asymptotic behavior observed for the first two cases. For further details on the derivation and verification of (2.42), the reader is referred to [24].

2.3 Simulation Results

In this section, the field components for a vertical dipole and a horizontal dipole are calculated using the formulations derived in Section 2.2. The variation in radiation characteristics is also demonstrated as a function of the effective permittivities, thickness of the vegetation or snow layer, locations of the source and observation points, and frequency of operation. Before the analysis, it is necessary to verify the validity of the asymptotic expressions presented. Figures 2.2 and 2.3 show the total fields (scattered plus direct) of a vertical dipole of unity current moment operating at 30 MHz located on the z-axis at $z' = 0.4\lambda$ with the observation point

at $(\rho, \pi/3, 0.3\lambda)$. The middle dielectric layer has been chosen to have a thickness of 0.5λ; the effective permittivity of the ground, ϵ_{r2}, is set to be $8 + 6i$, which approximately corresponds to a soil composed of gray San Antonio clay loam with a density of 1.4 g/cm^3 and 5% moisture content [4]. The dielectric layer is assumed to be sparse vegetation ($\epsilon_{r1} = 1.01 + 0.01i$) in Figure 2.2 and dry snow with density of 0.5 g/cm^3 ($\epsilon_{r1} = 2.01 + 0.01i$) in Figure 2.3. Note the $1/\rho^2$ dependence of all the field components in the far field. The exact solutions are obtained through numerical integration of the expressions tabulated in Appendix A. Figures 2.4 and 2.5 show the fields for a horizontal dipole calculated using the same set of parameters, except now the dipole itself is located inside the dielectric layer at $z' = -0.4\lambda$. It can be seen that there is very good agreement (both in magnitude and phase) between the exact and asymptotically-evaluated values when ρ is large in all the cases. As it has been noted in Section 2.2, the validity of the formulations presented here depends on the assumption that exponentially-decaying components of the field can be discarded when ρ is large; for example, in Figure 2.5, the validity holds for $\rho \geq 30\lambda$—below which the branch cut and pole contributions must be included to accurately account for the total field as well as the interference patterns.

Having validated the accuracy of the asymptotic expressions, it is beneficial to investigate the region in which the Norton wave (or the second term in (2.9)) is dominant. It is expected that when the source or observation point (or both) is far from the dielectric/air interface, the geometrical-optics term would become the principal field contribution. Depending on the configuration and physical parameters of the problem, simulations confirm that geometrical-optics provides an accurate approximation as long as the source or observation point (or both) is greater than 2λ–3λ above the dielectric layer. A comparison of the asymptotic and geometrical-

optics approximations with the exact solutions is shown in Figure 2.6(a) and (b) for a vertical dipole as a function of the observation point's distance above the dielectric. The dipole's location is in air for the first figure but is in the dielectric for the second. Note that the geometric-optics term converges to the exact solution for large z but becomes a rather poor approximation as the observation point approaches the interface. An example of the relative magnitude of the Norton wave as compared to the geometrical-optics approximation is shown in Figure 2.7(a); the Norton wave is seen to be highly localized to the air/dielectric interface—hence, it is obvious why this wave contribution has been designated as a type of "surface" wave. From Figure 2.6, one can also see that the field intensity at the receiver can be increased by elevating the receiver higher above ground—this is often called the height-gain effect. In fact, for small elevations, the field intensity increases linearly with elevation, as shown in Figure 2.7(b) for a dipole embedded in the dielectric layer—a similar plot can be constructed for a dipole located in air.

It is also instructive to analyze how the field changes as a function of the thickness of the dielectric layer. As the thickness changes, interference patterns caused by the superposition of multiple reflections are observed; this is shown in Figure 2.8(a) for a vertical dipole located above a dielectric layer with $\epsilon_{r1} = 1.01+0.01i$ and $2.01+0.01i$. The observation point is fixed in the far field at $(100\lambda, \pi/3, 0.3\lambda)$ in both cases. It can be deduced that the magnitude of the field oscillates about the limit value for which $d \to \infty$ (one-layer medium) and the rate of oscillation is dependent upon the magnitude of the permittivity whereas the rate of the approach towards the limit value is determined by the loss tangent.

To fully consider the effects of the dielectric layer and the ground, the total field's dependence on the effective permittivities of the two media must also be examined.

For a vegetation layer, the effective dielectric constant is slightly greater than that of free space; on the other hand, for a snow layer, while the imaginary part of the permittivity is still small, the real part can be as large as 2.0–3.0, depending on the snow density and the moisture content. The field variations as a function of ϵ_{r1} for fixed dipole and observation point locations are shown in Figure 2.9. Note that the field strength can change considerably as a function of the real part of the permittivity; and, for the set of parameters used in this example, there can be a 15 to 20 dB difference between the field value of a vegetation layer and that of a snow layer. The complex semi-oscillatory behavior evident in Figure 2.9 can also be anticipated if the permittivity of the ground, ϵ_{r2}, is varied while holding that of the dielectric layer constant. A primary determinant of the permittivity of soil is the moisture content. In Figure 2.8(b), the effect of the moisture content on the total field is illustrated for a ground composed of gray San Antonio clay loam with a dry density of 1.4 g/cm^3; the value of the corresponding dielectric constant for each moisture level is obtained from the measurements done by Hipp [4]. It is obvious that the field strength can change quite noticeably as a function of the permittivity of the ground; in addition, it is interesting to note that the field strength, as the soil moisture content is elevated, decreases for a vegetation layer but increases for a snow layer.

To illustrate the frequency response of the present problem, a frequency dependent model must be used for the permittivities of the dielectric layer and ground. For the simulations that follow, the soil of the ground is again selected to be gray San Antonio clay loam with a density of 1.4 g/cm^3 (5% moisture content). The dielectric constant as a function of frequency of such a composition can be found in figures given by [4]. For a vegetation layer, the effective dielectric constant is calculated by using the

Polder-van Santen mixing formula, in which the host material is air and the inclusion being the vegetation material. The dielectric properties of the vegetation material are dependent upon the gravimetric moisture content, frequency, and temperature; an empirical formula in terms of these parameters has been derived in [2]. For a snow layer, if the snow is dry, then the real part of the effective dielectric constant can be considered to be independent of frequency and to be a function of the snow density only; the imaginary part is relatively small and on the order of 10^{-2} to 10^{-3}.

The results of the simulations are shown in Figure 2.10(a) and (b); the former is for a vegetation layer and the latter is for a dry snow layer; a ground with the soil parameters given above is used in both cases. The source is a vertical dipole located in air; two observation points are used: in air and in the vegetation or snow—hence, there are two graphs in each figure. In the frequency range of 30 MHz to 200 MHz, the relative dielectric constant of soil changes from $8.10 + 6.00i$ to $6.10 + 1.79i$, and that of the vegetation layer changes from $1.09 + 0.001i$ to $1.10 + 0.009i$ for 5% inclusion by volume and for a vegetation material at $27°C$ with 50% gravimetric moisture content. For the dry snow, with a density of $0.5\ g/cm^3$, the relative dielectric constant is $2.01 + 0.01i$ and is almost independent of frequency. Note that only the z-component of the electrical field is shown in the graphs, and the quantity has been normalized to frequency in order to set the power output of the transmitter to constant. As it is evident in these figures, the amplitudes of variation can be quite large; thus, in the design of low-power communication channels, the selected frequency of operation is a critical factor in determining the efficiency of the system.

2.4 Conclusion

In this study, the concept and relevance of Norton waves and lateral waves have been analyzed for the canonical problem of propagation in the presence of a two-layer medium representing a vegetation or snow-covered terrain. Through the method of steepest descents, asymptotic formulations for the total field of an arbitrarily-oriented electric dipole have been derived from exact expressions for dipole and observation point situated near the air/dielectric interface. By discarding the pole and branch cut contributions for configurations in which the dipole and observation point both are *not* embedded within the dielectric layer, the formulations are much simplified and reduce to an ordinary saddle point contribution. It should be emphasized that such a simplification can only be made when there is loss in the media of propagation; in the absence of loss, in order to be considered as an accurate and practical solution, the saddle point contribution must be supplemented with the proper branch cut and pole contributions—regardless of the magnitude of the radial distance between the transmitter and receiver. When the aforementioned simplification is exploited, it has been shown that the saddle point contribution becomes the dominant field component and it is composed of a geometrical-optics term and a Norton wave correction term that is highly localized to the air/dielectric interface. In addition, simulation results indicated that the field intensity and frequency response at the receiver have a strong dependence on the permittivities of the vegetation or snow layer and the ground. Although the transmitter has been restricted to an electric dipole throughout this study, extension to an arbitrary radiating source can be made by noting that the asymptotic form of the Green's function for each of the three cases discussed is related

to the derived expressions for the field components by a simple constant:

$$\overline{\overline{G}}(\vec{r}', \vec{r}) = \frac{1}{i\omega\mu_o} \begin{bmatrix} E_{xx} & E_{yx} & E_{zx} \\ E_{xy} & E_{yy} & E_{zy} \\ E_{xz} & E_{yz} & E_{zz} \end{bmatrix}. \tag{2.43}$$

Therefore, once the current distribution of an arbitrary source is known, an approximation to the far field pattern can be easily computed. Also, upon application of the reciprocity principle, it is straightforward to verify that

$$\overline{\overline{G}}(\vec{r}, \vec{r}') = \overline{\overline{G}}(\vec{r}', \vec{r})^T \tag{2.44}$$

where the superscript "T" indicates the transpose operation. Simply by using the relation stated in (2.44), the formulations can be extended for other standard configurations not explicitly treated in Section 2.2—for example, the dipole is located in air while the observation point is located inside the dielectric layer.

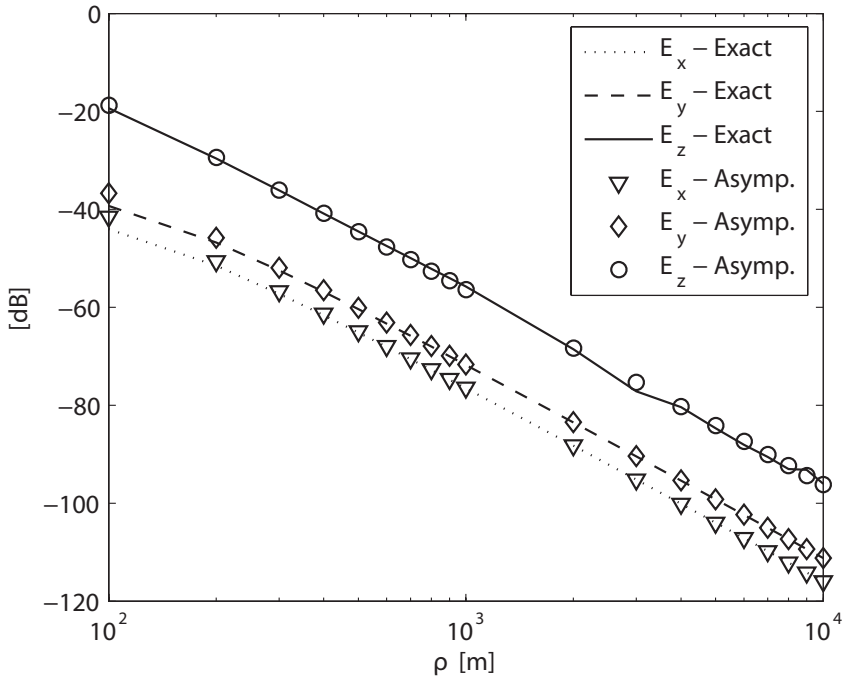

(a)

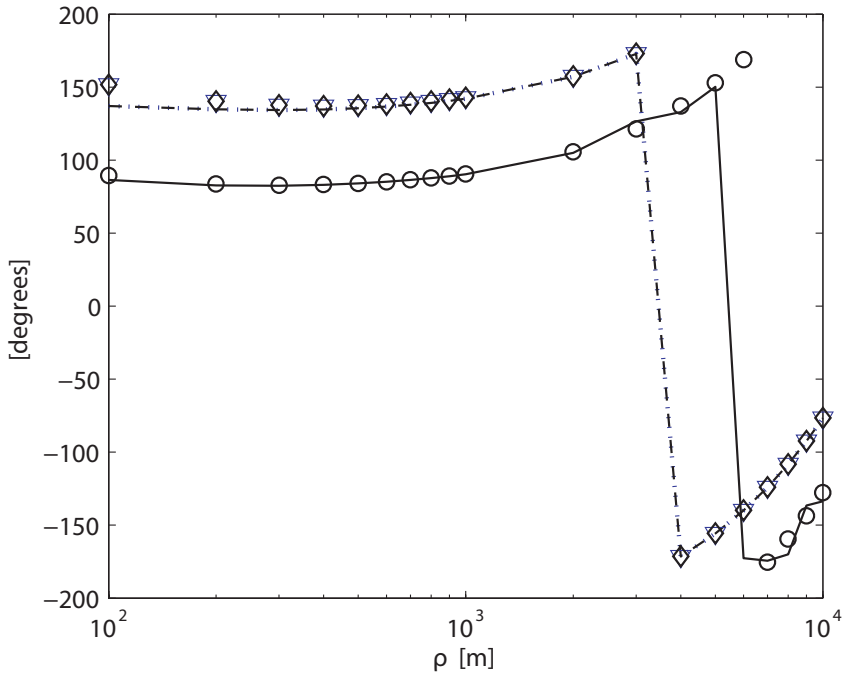

(b)

Figure 2.2: (a) Magnitude and (b) phase of the electric fields of a vertical dipole as a function of distance in the presence of a vegetation layer with $d = 0.5\lambda$. The dipole is located on z-axis at $z' = 0.4\lambda$ and the observation point is at $(\rho,\ \pi/3,\ 0.3\lambda)$; $f = 30$ MHz, $\epsilon_{r1} = 1.01 + 0.01i$, and $\epsilon_{r2} = 8 + 6i$.

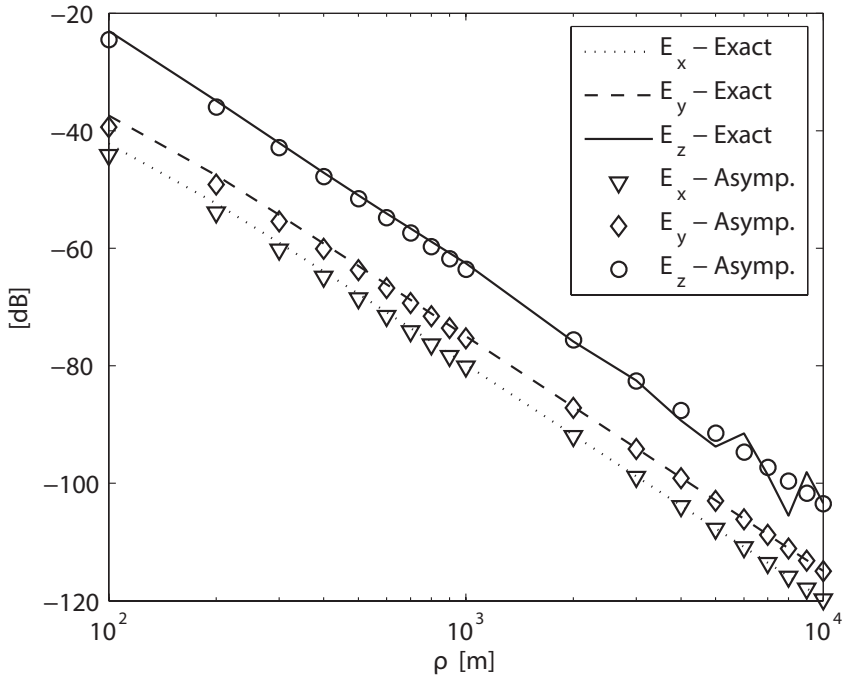

(a)

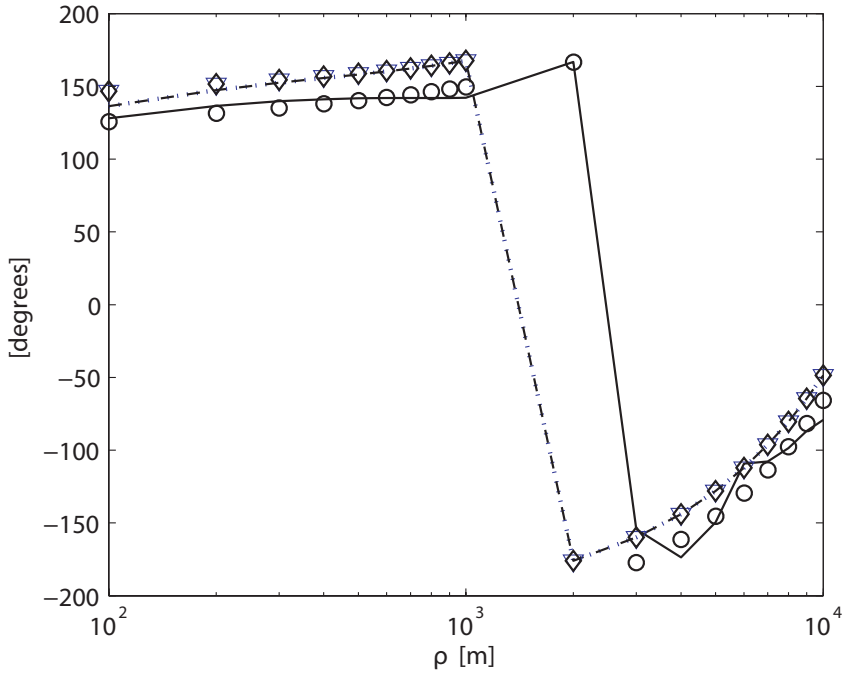

(b)

Figure 2.3: (a) Magnitude and (b) phase of the electric fields of a vertical dipole as a function of distance in the presence of a dry snow layer with $d = 0.5\lambda$. The dipole is located on z-axis at $z' = 0.4\lambda$ and the observation point is at $(\rho,\ \pi/3,\ 0.3\lambda)$; $f = 30$ MHz, $\epsilon_{r1} = 2.01 + 0.01i$, and $\epsilon_{r2} = 8 + 6i$. Note the poor quality of the numerical calculation for E_z at large distances, but the asymptotic solution is well-behaved.

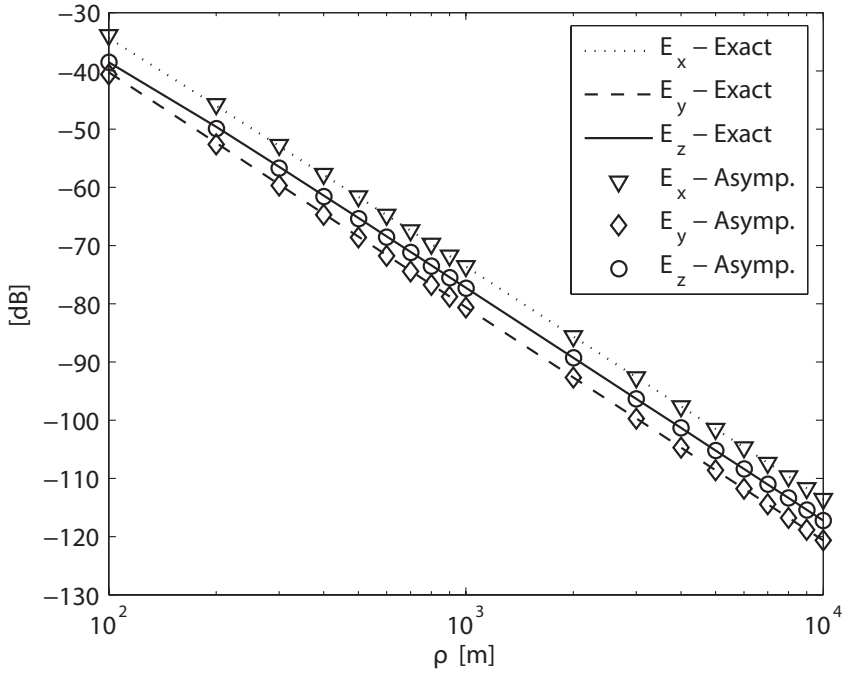

(a)

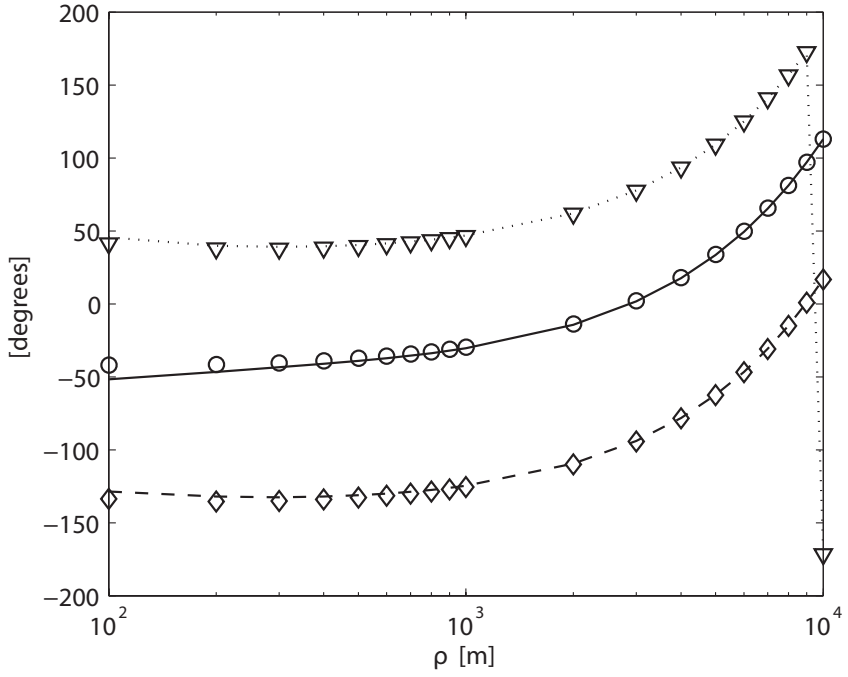

(b)

Figure 2.4: (a) Magnitude and (b) phase of the electric fields of a horizontal dipole as a function of distance in the presence of a vegetation layer with $d = 0.5\lambda$. The dipole is located on z-axis at $z' = -0.4\lambda$ and the observation point is at (ρ, $\pi/3$, 0.3λ); $f = 30$ MHz, $\epsilon_{r1} = 1.01 + 0.01i$, and $\epsilon_{r2} = 8 + 6i$.

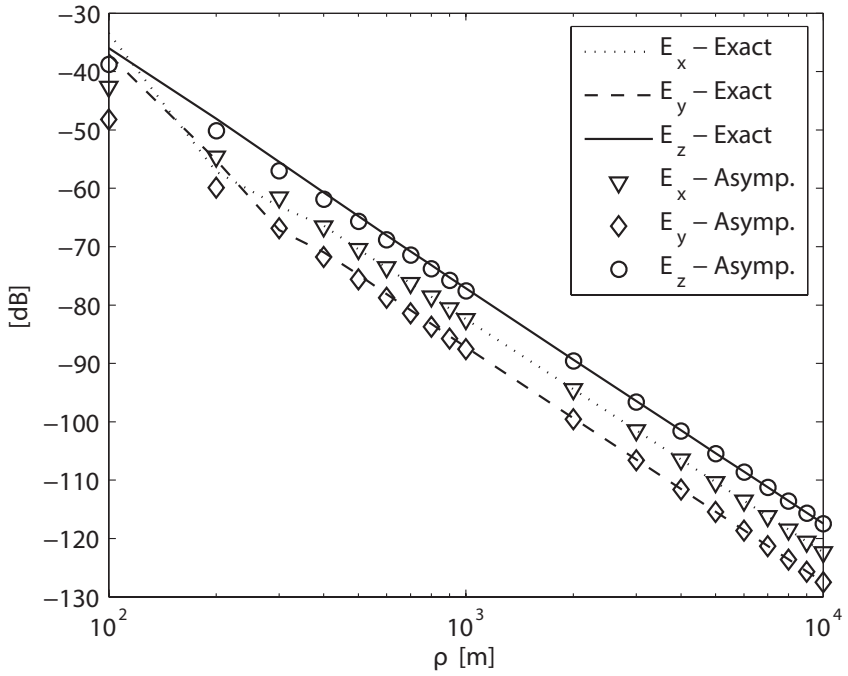

(a)

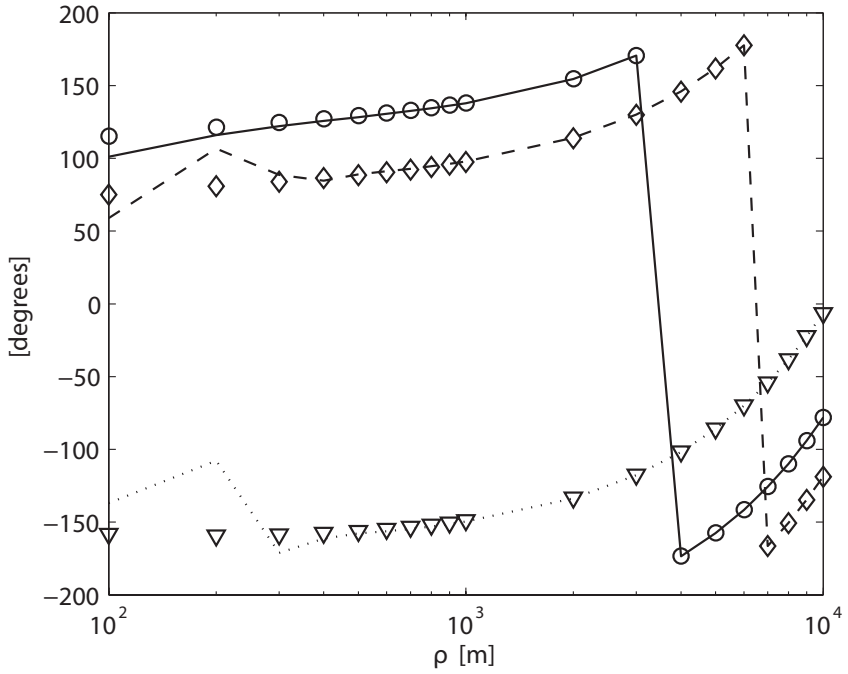

(b)

Figure 2.5: (a) Magnitude and (b) phase of the electric fields of a horizontal dipole as a function of distance in the presence of a dry snow layer with $d = 0.5\lambda$. The dipole is located on z-axis at $z' = -0.4\lambda$ and the observation point is at (ρ, $\pi/3$, 0.3λ); $f = 30$ MHz, $\epsilon_{r1} = 2.01 + 0.01i$, and $\epsilon_{r2} = 8 + 6i$.

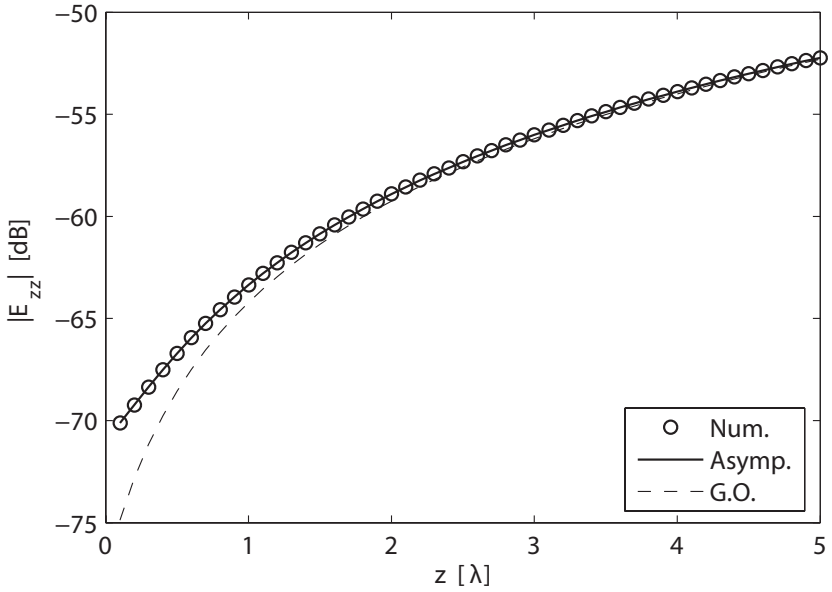

(a)

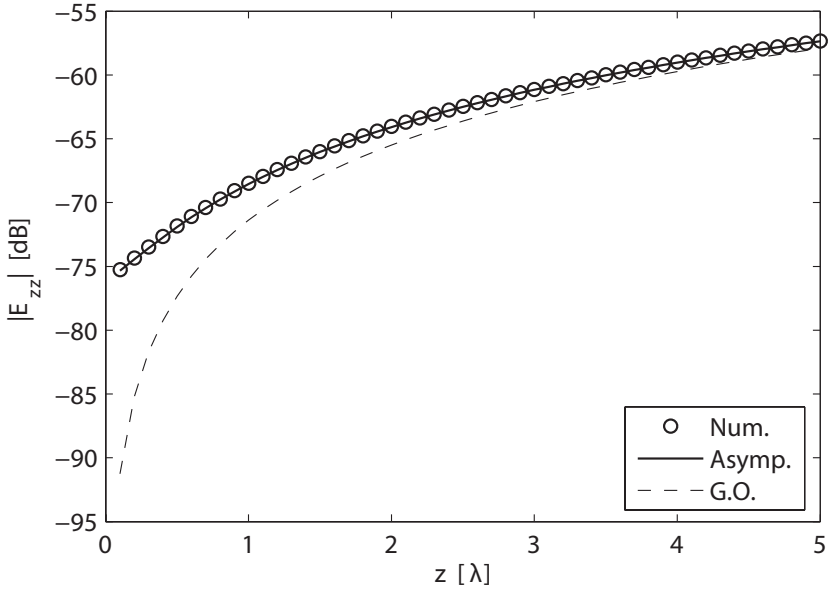

(b)

Figure 2.6: Comparison of asymptotic and geometrical-optics approximations with exact values obtained from numerical integration for a vertical dipole located at (a) $z' = 0.4\lambda$ and (b) $z' = -0.4\lambda$. Observation point is at $(200\lambda, \pi/3, z)$; $f = 30$ MHz, $\epsilon_{r1} = 1.01 + 0.01i$, $\epsilon_{r2} = 8 + 6i$, and $d = 0.5\lambda$.

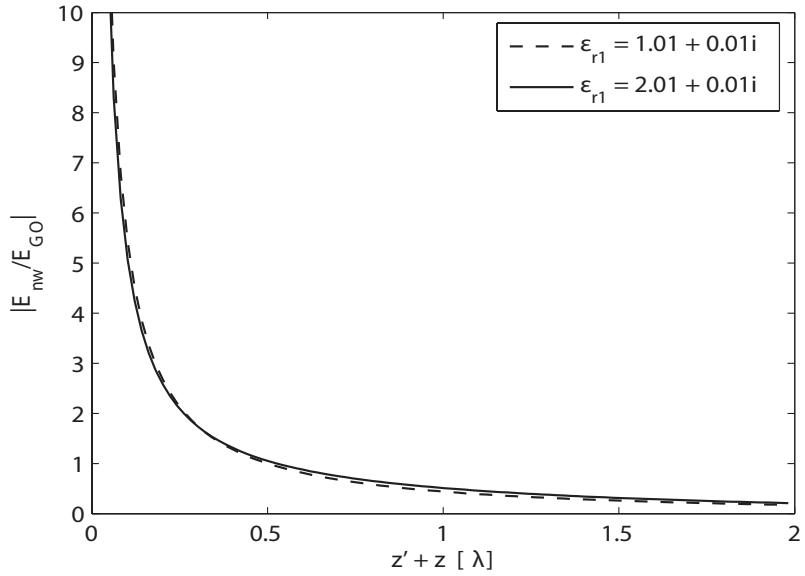

(a)

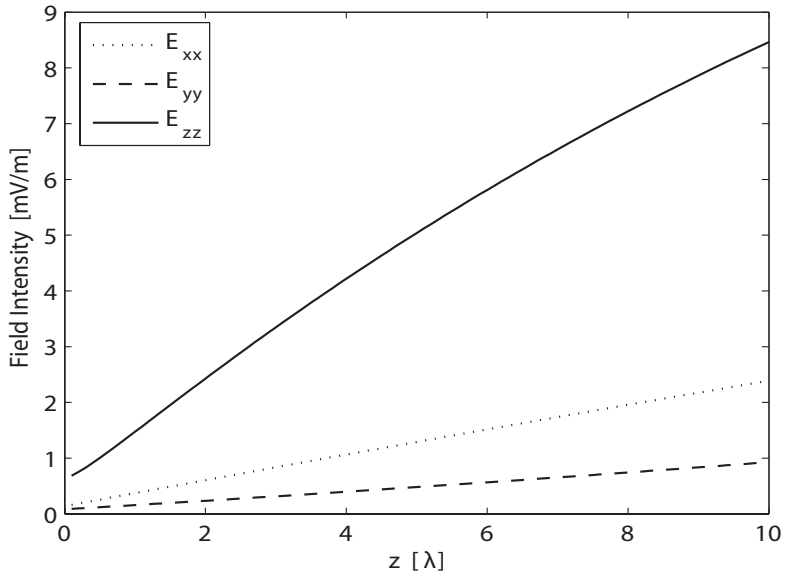

(b)

Figure 2.7: (a) Ratio of Norton wave to G.O. contribution for a vertical dipole. Source and observation points located above dielectric layer; $f = 30$ MHz, $\rho = 200\lambda$, $\epsilon_{r2} = 8 + 6i$, and $d = 0.5\lambda$. (b) Field intensity as a function of receiver height above dielectric/air interface for a dipole located inside the dielectric at $z' = -0.4\lambda$. Observation point is at $(100\lambda, \pi/3, z)$; $f = 30$ MHz, $\epsilon_{r1} = 1.01 + 0.01i$, $\epsilon_{r2} = 8 + 6i$, and $d = 0.5\lambda$.

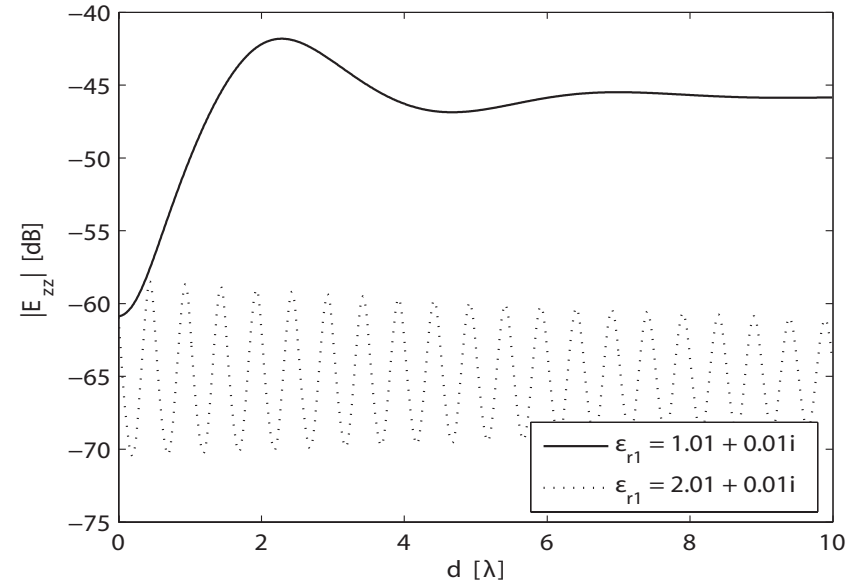

(a)

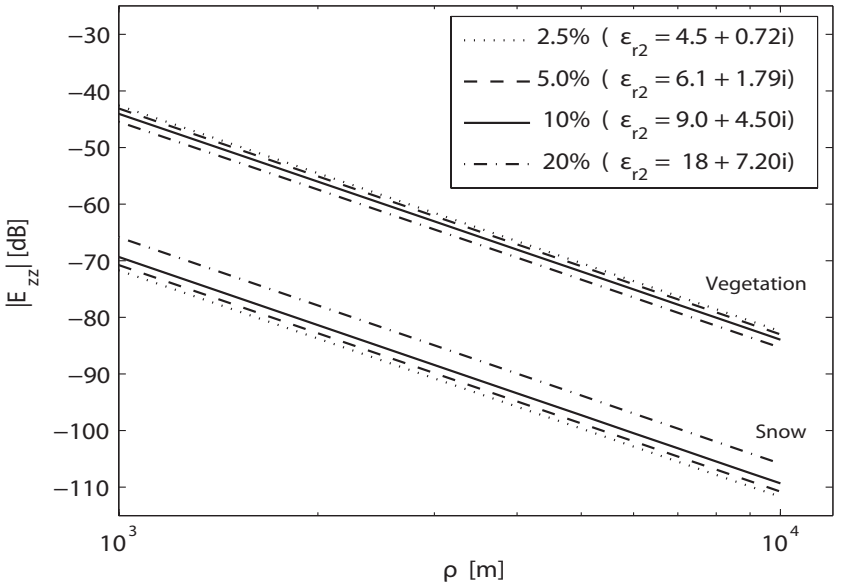

(b)

Figure 2.8: (a) Magnitude of E_z for a vertical dipole located above a dielectric layer with $\epsilon_{r1} = 1.01 + 0.01i$ and $2.01 + 0.01i$. Observation point is at $(100\lambda,\ \pi/3,\ 0.3\lambda)$; $f = 30$ MHz and $\epsilon_{r2} = 8 + 6i$. (b) Magnitude of E_z for a vertical dipole in the presence of a ground with various percentages of soil moisture content. The dipole is located inside the dielectric layer at $z' = -0.5\lambda$ and observation point is at $(\rho,\ \pi/3,\ 0.5\lambda)$; $f = 200$ MHz, $\epsilon_{r1} = 1.01 + 0.01i$ for vegetation layer, $\epsilon_{r1} = 2.01 + 0.01i$ for snow layer, and $d = 2.0\lambda$.

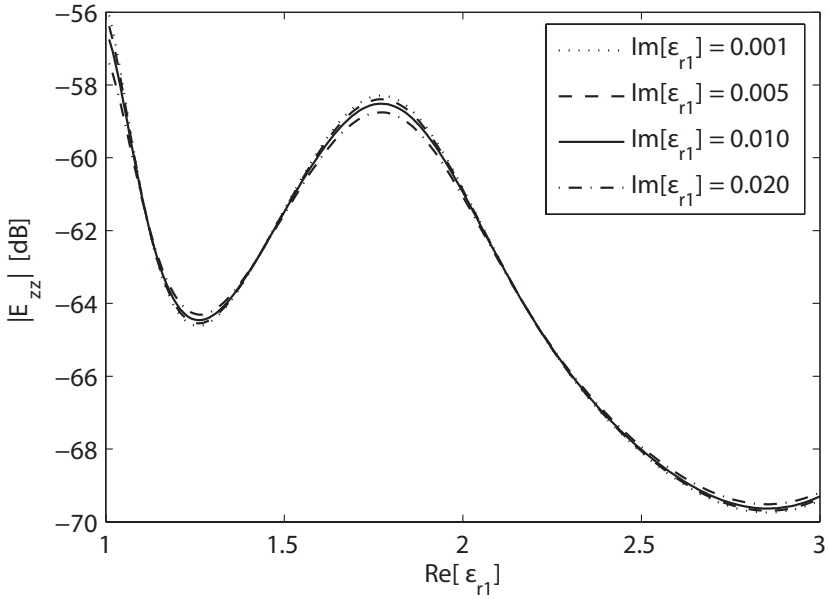

(a)

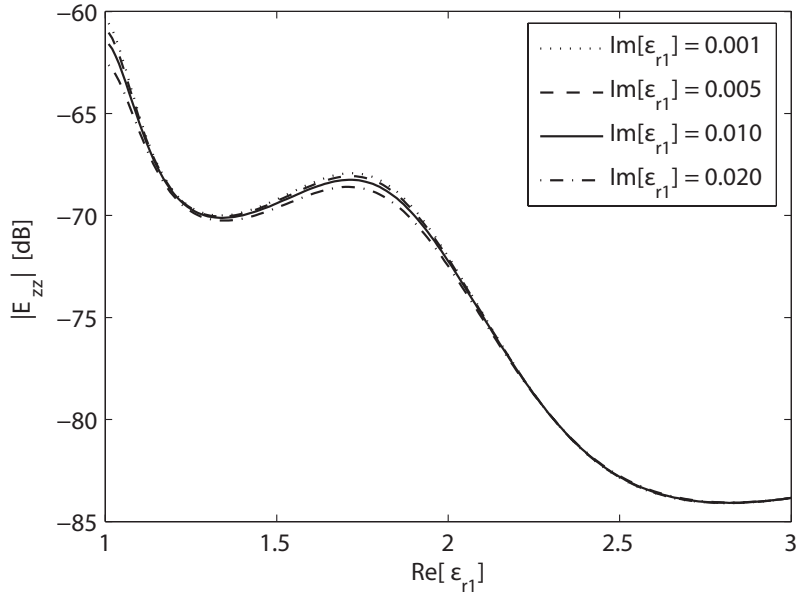

(b)

Figure 2.9: Electric field as a function of the effective permittivity of the dielectric layer for a vertical dipole. Dipole is located above the dielectric layer for (a) and within the dielectric layer for (b). Observation point is at $(100\lambda,\ \pi/3,\ 0.3\lambda)$, $f = 30$ MHz, $\epsilon_{r2} = 8 + 6i$, and $d = 0.5\lambda$.

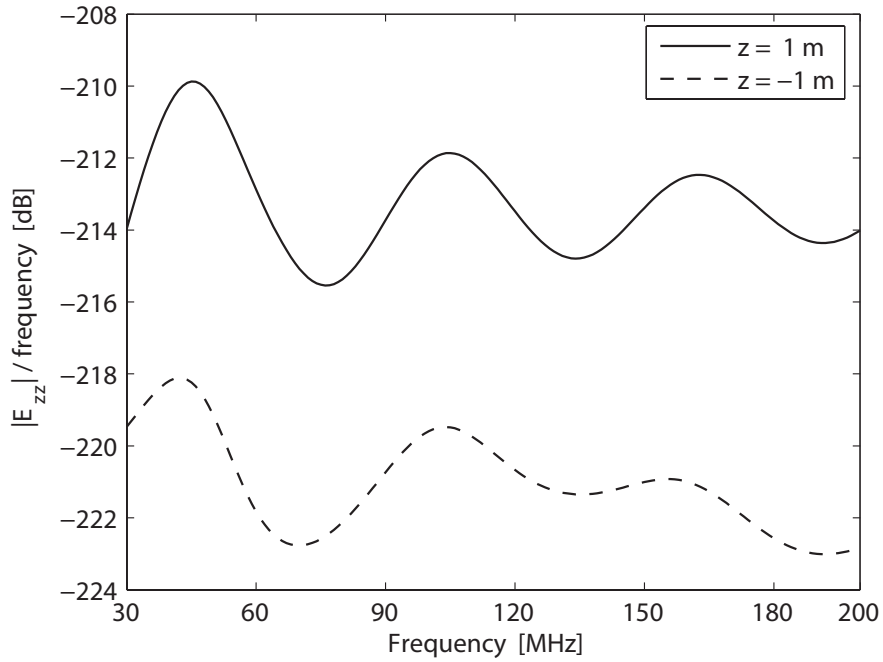

(a)

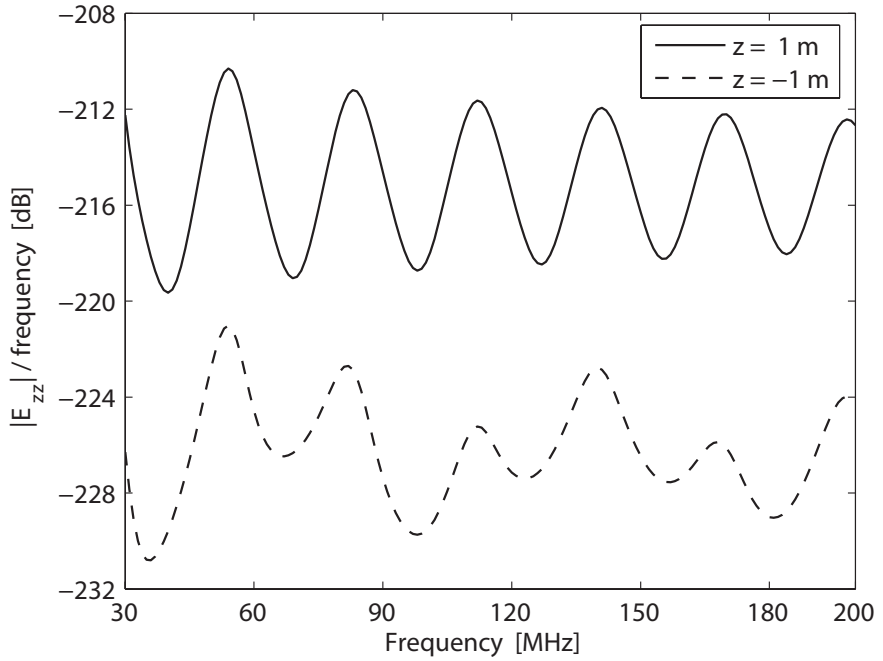

(b)

Figure 2.10: Frequency response for a vertical dipole in (a) a vegetation layer and (b) a snow layer. Dipole is located above the dielectric layer at $z' = 1$ m, observation point is at (1000 m, $\pi/3$, ± 1 m), and $d = 2$ m.

CHAPTER III

Modeling and Simulation of Near-Earth Propagation in Presence of a Truncated Vegetation Layer

3.1 Introduction

In the previous chapter, the problem of VHF wave propagation in the presence of a vegetated terrain was treated by replacing the physical medium with an effective homogeneous two-layer medium and then applying the asymptotic dyadic Green's function to compute the radiated field distribution of an electric-dipole with the assumption that the vegetation layer is infinite in extent in the two dimensions parallel to the ground. In practice, the effects of any discontinuity in the vegetation layer would have to be included to accurately model the path-loss between the transmitter and receiver. The geometry of a particular canonical problem of interest is illustrated in Figure 3.1, in which the vegetation layer extends to infinity in both directions along the x-axis and in the negative direction along the y-axis. An exact solution to this problem can be found through a full-wave numerical technique such as FDTD or—its variant—moving-window FDTD; however, for near-earth propagation problems in which the computational domain is large and the wave energy spreads out to the receiver at grazing-angles, a full-wave analysis is rather difficult to implement in an efficient and straight-forward manner with a high level of accuracy [47–50]. One salient feature of the field behavior near the air/ground interface

is the near cancellation of the direct and reflected waves at distant points from the transmitter; in order to capture this feature for low transmitter and receiver heights, an extremely stringent requirement must be placed on the precision of the calculation for the total field. To the best of the author's knowledge, the propagation effects of a truncated vegetation canopy have been analytically examined only by Tamir through a ray-tracing approach [21]; while Tamir's solution is simple to construct, its accuracy has not been fully verified. In this work, a semi-exact, analytical solution to the same problem is formulated by making use of the equivalence principle [51], [52]; specifically, the field at an observation point located in the far field of a truncated vegetation canopy is solved by performing a surface-field integration over the vertical 2D plane containing the truncation facet. Since the solution contains limits of integration that are infinite, the stationary phase approximation is applied as needed to achieve computationally-efficient solutions. In Section 3.2, the details of the formulation are presented; in Section 3.3, a comparison is made between the results obtained from the approach discussed herein and from the one outlined in Tamir's study, and the construction of an indoor experimental simulator for rapid channel characterization is described.

3.2 Analytical Formulations

As shown in Figure 3.1, the transmitter is assumed to be an infinitesimal electric dipole with effective current moment vector $I_o\vec{l} = I_o(l_x\hat{x} + l_y\hat{y} + l_z\hat{z})$ located inside the vegetation at $\vec{r}_o(x_o, y_o, z_o)$. The total field at the receiver, assuming the existence of an equivalent electric and magnetic current sheet located on the x-z plane, can be

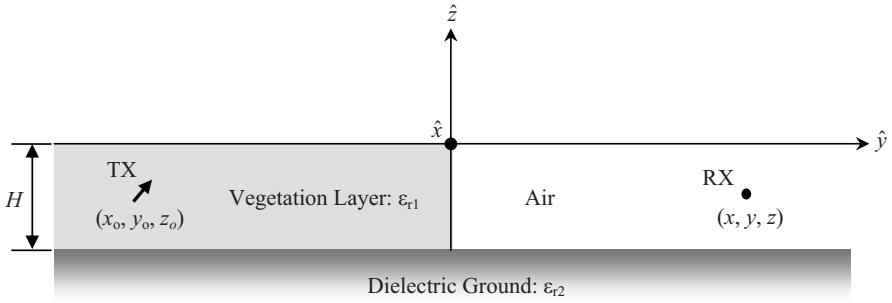

Figure 3.1: An electric dipole located inside a truncated vegetation layer of thickness H. The effective permittivities of the vegetation and the ground can be calculated using standard dielectric mixing or empirical models based on their respected compositions [2–4].

calculated as

$$\vec{E}(\vec{r}) = \int_{-H}^{+\infty}\int_{-\infty}^{+\infty} \left\{ \overline{\overline{G}}^{\,J}(\vec{r},\vec{r}') \cdot \hat{y} \times \nabla_{\vec{r}'} \times \vec{E}_o(\vec{r}',\vec{r}_o) - \overline{\overline{G}}^{\,M}(\vec{r},\vec{r}') \cdot \hat{y} \times \vec{E}_o(\vec{r}',\vec{r}_o) \right\} dx'dz', \tag{3.1}$$

where $\vec{r}(x,y,z)$ is the location of the receiver and $\vec{r}'(x',y',z')$ is that of the incremental sources on the plane of integration; also, in accordance with conventional notation, $\overline{\overline{G}}^{\,J}(\vec{r},\vec{r}')$ and $\overline{\overline{G}}^{\,M}(\vec{r},\vec{r}')$ are, respectively, the electric and magnetic dyadic Green's functions (in asymptotic form). Note that a typical ground is highly lossy, therefore it has been determined that the contributions from the sources residing below the ground plane ($z' < -H$) can be ignored. The propagation matrix $\overline{\overline{G}}^{\,J}(\vec{r},\vec{r}')$—relevant for the calculation of the radiated electric field from an electric current source located above a dielectric half-space—can be written as the sum of a free space part that accounts for the direct field and a reflected part that accounts for the presence of the ground:

$$\overline{\overline{G}}^{\,J}(\vec{r},\vec{r}') = \overline{\overline{G}}^{\,J}_{fs}(\vec{r},\vec{r}') + \overline{\overline{G}}^{\,J}_{r}(\bar{r},\vec{r}'). \tag{3.2}$$

It can be readily verified that reciprocity dictates

$$\begin{aligned} \overline{\overline{G}}^{\,M}(\vec{r},\vec{r}') &= \overline{\overline{G}}^{\,M}_{fs}(\vec{r},\vec{r}') + \overline{\overline{G}}^{\,M}_{r}(\vec{r},\vec{r}') \\ &= \left[-\nabla_{\vec{r}'} \times \overline{\overline{G}}^{\,J}_{fs}(\vec{r}',\vec{r})\right]^T + \left[-\nabla_{\vec{r}'} \times \overline{\overline{G}}^{\,J}_{r}(\vec{r}',\vec{r})\right]^T, \end{aligned} \tag{3.3}$$

where the superscript "T" denotes the transpose operation. Furthermore, since the first bracketed term of (3.3) can be interpreted as a stand-alone component relevant for a homogeneous medium (free space, in this case), symmetric properties generate the following simplifications:

$$\begin{aligned} \overline{\overline{G}}^{\,M}_{fs}(\vec{r},\vec{r}') &= \left[\overline{\overline{G}}^{\,M}_{fs}(\vec{r}',\vec{r})\right]^T = \left[-\nabla_{\vec{r}'}\times\overline{\overline{G}}^{\,J}_{fs}(\vec{r}',\vec{r})\right]^T \\ &= -\nabla_{\vec{r}}\times\overline{\overline{G}}^{\,J}_{fs}(\vec{r},\vec{r}'). \end{aligned} \tag{3.4}$$

The expression in (3.1) can now be re-written as the superposition of four terms:

$$\begin{aligned} \vec{E}(\vec{r}) = \int_{-H}^{+\infty}\int_{-\infty}^{+\infty} \Big\{ & \overline{\overline{G}}^{\,J}_{fs}(\vec{r},\vec{r}')\cdot\hat{y}\times\nabla_{\vec{r}'}\times\vec{E}_o(\vec{r}',\vec{r}_o) \\ & + \overline{\overline{G}}^{\,J}_{r}(\vec{r},\vec{r}')\cdot\hat{y}\times\nabla_{\vec{r}'}\times\vec{E}_o(\vec{r}',\vec{r}_o) \\ & - \overline{\overline{G}}^{\,M}_{fs}(\vec{r},\vec{r}')\cdot\hat{y}\times\vec{E}_o(\vec{r}',\vec{r}_o) \\ & - \overline{\overline{G}}^{\,M}_{r}(\vec{r},\vec{r}')\cdot\hat{y}\times\vec{E}_o(\vec{r}',\vec{r}_o) \Big\} dx'dz'. \end{aligned} \tag{3.5}$$

In (3.5), the exact form of $\overline{\overline{G}}^{\,J}_{fs}(\vec{r},\vec{r}')$ is known; an asymptotic form for $\overline{\overline{G}}^{\,J}_{r}(\vec{r},\vec{r}')$ has been derived in Chapter II to the second order to include the effects of the Norton wave component [41]. For a tenuous vegetation layer ($\epsilon_{r1}\approx 1$, which is satisfied for most foliage), the electric field $\vec{E}_o(\vec{r}',\vec{r}_o)$ over the integration plane (x-z plane) is approximated as the same as that of an infinite canopy configuration and can be calculated with the expressions given in Chapter II for an arbitrarily-oriented electric dipole: for $z'>0$, $\vec{E}_o(\vec{r}',\vec{r}_o)$ is the effective refracted field from the radiating dipole in the presence of the slab; for $-H<z'<0$, the primary contributions to $\vec{E}_o(\vec{r}',\vec{r}_o)$ come from lateral waves [24]; in view of the distinction between these two types of wave components, the integration domain in (3.1) is separated as follows:

$$\vec{E}(\vec{r}) = \int_{-H}^{0}\int_{-\infty}^{+\infty}\{\ \cdot\ \}\ dx'dz' \ + \ \int_{0}^{+\infty}\int_{-\infty}^{+\infty}\{\ \cdot\ \}\ dx'dz'. \tag{3.6}$$

The first term in (3.6) is evaluated by numerically integrating over the variable z' while performing a 1D stationary phase approximation over x'; the second term is evaluated by a full 2D stationary phase approximation. The exponential phase characteristic of each of the terms in (3.1) and (3.2) has been shown to be the following in Chapter II:

$$\overset{\approx}{G}{}^{J}_{fs}(\vec{r},\vec{r}') \propto e^{ik_o|\vec{r}-\vec{r}'|}; \tag{3.7}$$

$$\overset{\approx}{G}{}^{J}_{r}(\vec{r},\vec{r}') \propto e^{ik_o|\vec{r}-\vec{r}'+2(H+z')\hat{z}|}; \tag{3.8}$$

$$\vec{E}_o(\vec{r}',\vec{r}_o) \propto \begin{cases} e^{ik_o|\vec{r}'-\vec{r}_o+z_o\hat{z}|},\ z'>0; \\ e^{ik_o|\vec{\rho}'-\vec{\rho}_o|+ik_1(|z'|+|z_o|)\sqrt{1-\frac{1}{\varepsilon_{r1}}}},\ -H<z'<0, \text{ 1st order lateral wave}; \\ e^{ik_o|\vec{\rho}'-\vec{\rho}_o|+ik_1(2H-|z'|+|z_o|)\sqrt{1-\frac{1}{\varepsilon_{r1}}}}, -H<z'<0, \text{ 2nd order lateral wave}; \\ e^{ik_o|\vec{\rho}'-\vec{\rho}_o|+ik_1(2H+|z'|-|z_o|)\sqrt{1-\frac{1}{\varepsilon_{r1}}}}, -H<z'<0, \text{ 3rd order lateral wave}; \end{cases} \tag{3.9}$$

where

$$\vec{\rho} = x\hat{x} + y\hat{y}, \tag{3.10}$$

and the definitions for the three orders of lateral waves are provided in Chapter II and [24]. Each term in (3.5) can be evaluated independently of the others, and each can be cast in a generic form:

$$\vec{I} = \vec{I}_1 + \vec{I}_2 = \int_{-H}^{0}\int_{-\infty}^{+\infty} \vec{F}(x',z')e^{if(x',z')}dx'dz' + \int_{0}^{+\infty}\int_{-\infty}^{+\infty} \vec{F}(x',z')e^{if(x',z')}dx'dz'. \tag{3.11}$$

It is seen that integrals of the form in (3.11) is amendable to stationary phase evaluation. Following the procedure for stationary phase approximation as given by Felsen and Marcuvitz [19], the first integral in (3.11) becomes

$$\vec{I}_1 \approx \int_{-H}^{0} \vec{F}(x'_s,z')e^{if(x'_s,z')} \sqrt{\frac{2\pi}{\left|\frac{\partial^2 f(x',z')}{\partial x'^2}\Big|_{x'=x'_s}\right|}} e^{\pm i\frac{\pi}{4}}dz',\ \frac{\partial^2 f(x',z')}{\partial x'^2}\Big|_{x'=x'_s} \gtrless 0, \tag{3.12}$$

where the stationary point x'_s is defined by

$$\left.\frac{\partial f(x',z')}{\partial x'}\right|_{x'=x'_s} = 0. \tag{3.13}$$

(In (3.12), and henceforth, the ambiguity in sign is resolved by associating + with $>$ and $-$ with $<$.) The closed-form solution of the second integral in (3.11) can be found by expanding the phase function around the stationary point as a Taylor series and then evaluating the resulting canonical integral:

$$\begin{aligned}
\vec{I}_2 &\approx \vec{F}(x'_s,z'_s)e^{if(x'_s,z'_s)} \int_0^{+\infty}\int_{-\infty}^{+\infty} e^{\frac{i}{2}\left[(x'-x'_x)\frac{\partial}{\partial x'}+(z'-z'_s)\frac{\partial}{\partial z'}\right]^2 f(x',z')}dx'dz' \\
&\approx \vec{F}(x'_s,z'_s)e^{if(x'_s,z'_s)} \int_{-z'_s}^{+\infty}\int_{-\infty}^{+\infty} e^{\frac{i}{2}\left[ax''^2+2bx''z''+cz''^2\right]}dx''dz'',
\end{aligned} \tag{3.14}$$

where $z'_s > 0$ is assumed at the moment and

$$\begin{aligned}
a &= \left.\frac{\partial^2 f(x',z')}{\partial x'^2}\right|_{\substack{x'=x'_s\\z'=z'_s}} \\
b &= \left.\frac{\partial^2 f(x',z')}{\partial x'dz'}\right|_{\substack{x'=x'_s\\z'=z'_s}} \\
c &= \left.\frac{\partial^2 f(x',z')}{\partial z'^2}\right|_{\substack{x'=x'_s\\z'=z'_s}}
\end{aligned} \tag{3.15}$$

with

$$\begin{aligned}
x'' &= x' - x'_s; \\
z'' &= z' - z'_s.
\end{aligned} \tag{3.16}$$

The stationary point on the x'-z' plane is defined by

$$\begin{aligned}
\left.\frac{\partial f(x',z')}{\partial x'}\right|_{\substack{x'=x'_s\\z'=z'_s}} &= 0; \\
\left.\frac{\partial f(x',z')}{\partial z'}\right|_{\substack{x'=x'_s\\z'=z'_s}} &= 0.
\end{aligned} \tag{3.17}$$

The double integral in (3.14) can be shown to be the following:

$$\int_{-z_s'}^{+\infty}\int_{-\infty}^{+\infty} e^{\frac{i}{2}\left[ax''^2+2bx''z''+cz''^2\right]}dx''dz'' = \alpha\beta; \tag{3.18}$$

$$\alpha = \frac{\sqrt{\pi}e^{\pm i\frac{\pi}{4}}}{\sqrt{|ac-b^2|}},\ a \gtrless 0; \tag{3.19}$$

$$\beta = \sqrt{\pi}e^{\pm i\frac{\pi}{4}} + 2\int_{0}^{|\gamma|^{\frac{1}{2}}z_s'} e^{\pm it^2}dt,\ \gamma \gtrless 0,\ \gamma = \frac{1}{2a}(ac-b^2). \tag{3.20}$$

Therefore, the expression in (3.14) can be re-written as

$$\vec{I}_2 \approx \vec{F}(x_s', z_s')e^{if(x_s', z_s')}\alpha\beta,\ z_s' > 0. \tag{3.21}$$

If $z_s' < 0$, the second integral in (3.11) can be evaluated as

$$\begin{aligned}\int_{0}^{+\infty}\int_{-\infty}^{+\infty} \vec{F}(x', z')e^{if(x', z')}dx'dz' &= \int_{-\infty}^{+\infty}\int_{-\infty}^{+\infty} \vec{F}(x', z')e^{if(x', z')}dx'dz' \\ &- \int_{-\infty}^{0}\int_{-\infty}^{+\infty} \vec{F}(x', z')e^{if(x', z')}dx'dz'.\end{aligned} \tag{3.22}$$

The first integral on the right side of (3.22) can be evaluated using (3.21) with the replacement of z_s' by infinity in the expression for β and then noting that [53]

$$\int_{0}^{+\infty} e^{\pm it^2}dt = \frac{\sqrt{\pi}}{2}e^{\pm i\frac{\pi}{4}}. \tag{3.23}$$

It can be shown that the second integral on the right side of (3.22) can be evaluated using (3.21) as well, but with the replacement of z_s' by $|z_s'|$ in the expression for β.

To test the general validity of the proposed 2D stationary phase approximation as presented above for various receiver heights, the formulation is applied to the propagation problem over a simple half-space medium (Figure 3.1, in the absence of

the vegetation slab) for which an exact solution is known. After repositioning the x-y plane to coincide with the ground plane, the expression in (3.1) can be modified to

$$\vec{E}(\vec{r}) = \int_0^{+\infty}\int_{-\infty}^{+\infty}\Big\{\overset{\approx}{G}{}^{J}(\vec{r},\vec{r}')\cdot\hat{y}\times\nabla_{\vec{r}'}\times\Big[\vec{E}_{o,fs}(\vec{r}',\vec{r}_o)+\vec{E}_{o,r}(\vec{r}',\vec{r}_o)\Big]dx - \overset{\approx}{G}{}^{M}(\vec{r},\vec{r}')\cdot\hat{y}\times\Big[\vec{E}_{o,fs}(\vec{r}',\vec{r}_o)+\vec{E}_{o,r}(\vec{r}',\vec{r}_o)\Big]\Big\}dx'dz', \tag{3.24}$$

where the electric field on the plane of integration has been explicitly separated into a free space (direct) field and a reflected field to emphasize the different phase characteristics of the two components; asymptotic forms of the reflected field including the Norton wave have been derived and are given in Chapter II. Once again, the contributions from the sources located below the ground plane ($z' < 0$) have been ignored; also, note that the expression in (3.24) is exact, with the only approximations originating from the asymptotic nature of the values for the reflected field and the dyadic propagating matrices $\overset{\approx}{G}{}_r^{J}(\vec{r},\vec{r}')$ and $\overset{\approx}{G}{}_r^{M}(\vec{r},\vec{r}')$. The evaluation of (3.24) can be carried out by first writing each term in the integrand in the standard form shown in the second part of (3.11) and then systematically applying (3.14)–(3.23). For an electric dipole located above a perfectly conducting plane ($\epsilon_{r2} = 1 + i\infty$), very good agreement between the exact solution and the 2D stationary phase approximation is seen in Figures 3.2 and 3.3; however, for a dielectric ground, Figure 3.4 shows that the approximation does not adhere to the exact solution for observation points close to the air/ground interface. This inaccuracy can be attributed to the inability of the stationary phase approximation to fully capture the Norton wave components radiated by the equivalent electric and magnetic current sources residing on the part of the plane of integration very close to the ground; for this region, all the field components need be computed to a high order precision due to the substantial degree of

cancellation between the direct and reflected fields detected at the low observation point. To improve the level of accuracy of the approximate solution for low receiver heights, the second integral in (3.11) is evaluated using a 1D stationary approximation in the x-direction while numerical integration is carried out in the z-direction; this modified approach does indeed produce better results—as shown in Figures 3.5 and 3.6.

3.3 Simulation Results and Discussions

3.3.1 Numerical Simulations

After the effectiveness and limitations of the stationary phase approximation have been assessed, the field integration technique is applied to the truncated vegetation canopy configuration of Figure 3.1. The expression in (3.6) is evaluated by the following two methods: in the first method (SPA_{2D}), a full 2D stationary phase approximation is applied to the second double integral; in the second method (SPA_{1D}), a 1D stationary phase approximation is applied in the x-direction while numerical integration is used in the z-direction for the second double integral; in both methods, the first integral in (3.6) is calculated using a 1D stationary phase approximation with numerical integration. The results of the simulation for horizontal and vertical polarizations are displayed in Figures 3.7 and 3.8, respectively. Although the "height gain" effect is properly reproduced, the figures indicate that the first method does not generate the desired "leveling" effect—the flattening out of the field magnitude function (on a log-dB plot) as the height decreases toward the ground—that is evident, as it will be shown, in the results obtained from ray-tracing and from measurements for both polarizations. Since the receiver is located above a dielectric ground, the field amplitude should approach a limiting value as the height decreases to zero; however, this is not observed in the results from SPA_{2D}. The levels of approxima-

tion in SPA_{2D} can be reduced by utilizing a 1D stationary phase approximation—an application of which leads to the flattening of the curves readily seen in the results from SPA_{1D}; as verified in the previous section, this method can be used to avoid or correct the erroneous results manifesting at low receiver heights.

As mentioned in Section 3.1, a simplistic solution also exists for the current problem and has been formulated by Tamir in the form of a ray-tracing scheme [21]. In Tamir's approach, for an observation point located in the far field and to the right of the truncation edge, there are two regions of interest (Figure 3.9)—depending on the height of the receiving point. If the receiver is high above the bare ground (region A), the field is calculated as though the canopy is infinite while assuming that the truncation has negligible effect on the wave refracted toward the receiver. If the receiver is close to the ground (region B), the field is calculated according to the following procedure: the problem is first inverted through reciprocity arguments by interchanging the source and observation point locations (i.e., the dipole now is outside of the canopy and the observation point is inside); next, the field at the canopy edge—which includes the geometrical-optics ray and Norton wave components—is calculated; then, assuming all the impinging energy at the edge is coupled into lateral wave modes, the field arriving at the receiver is found by matching the field at the edge to that of lateral waves and subsequently extending those waves from the edge to the receiver. Detailed explanations of this ray-tracing approach and its pertinent formulations can be found in [21].

The variations of the electric field amplitude and phase as a function of receiver height calculated using Tamir's approach are superimposed upon those obtained through stationary phase considerations in Figures 3.7 and 3.8. Note that as discussed by Tamir, the transition height between region A and region B is estimated by

plotting the formulation valid in each respected region and then locating the intersection point of the two curves; this explains the apparent "discontinuity" in Tamir's solution demonstrated in Figures 3.7(b), 3.8(a), and 3.8(b) near the receiver height of 10λ. From Figures 3.7(a) and 3.8(a), it is seen that when the observation point is low, the received field for both polarizations in the current approach is generally smaller than that in Tamir's solution; this disagreement is anticipated since in the ray-tracing approach, all the energy arriving at the canopy edge is assumed to couple and assimilate *entirely* into a wave that propagates to the receiver, but in the field integration approach, such an assumption is not enforced. By comparing Figure 3.7(a) to Figure 3.8(a), it is evident that a horizontally-polarized wave can couple more effectively out of (or into) the vegetation medium than the vertically-polarized wave; this is also not surprising since the transmission coefficient for the vegetation/air transition for a horizontally-polarized wave is expected to be greater than that of the vertically-polarized wave for the slab configured as shown. Note that Tamir's and the stationary phase approaches may predict significantly different phase behaviors for the received field at low observation points, as it is shown in Figures 3.7(b) and 3.8(b). In view of the fact that the solution here (specifically, SPA_{1D}) is more akin to a full-wave solution, it is expected that the phase characteristics predicted therefrom are more accurate. When the observation point is far above the surface, both approaches lead to identical results in amplitude and phase—confirming that a refracted ray determines the principal field contribution and any diffraction effect from the vegetation slab discontinuity is negligible.

The lack of a formal closed-form solution to the problem at hand has forced approximations to be made—as it has been done both in this work and in Tamir's study. It should be mentioned that the procedure of the ray-tracing approach in

effect requires two successive assumptions to be made: for example, for a wave propagating into the canopy from the air region—first, the field at the truncation edge is calculated as though the canopy does not exist; second, the translation of the energy arriving at the edge and the subsequent extension to the generated lateral wave is carried out as though the canopy is infinite. In the solution of this work, the only assumption required to hold is that the field distributed on the plane of integration is nearly unperturbed by the canopy truncation.

3.3.2 Experimental Measurements

For a fixed set of intrinsic properties (ϵ, μ) and constant dipole current moment $I_o l$, it can be inferred from the Green's function of this problem that the field quantities (E, H) scale *exactly* as f^2 and the received power as f^4—assuming all the physical dimensions (thickness of vegetation layer H, radial distance ρ, source and observation point heights z' and z) are scaled with respect to the wavelength as well. Consequently, the *relative* radiation pattern of a transmitter is independent of the frequency of operation, and an alternate simulation method for the proposed problem (excluding a computationally-intensive full-wave analysis) can be developed by measuring the response of a scaled-replica of the propagation medium. The advantages of channel characterization using scaled measurement systems have been discussed in detail by Aryanfar and Sarabandi [54, 55]. A simple mock-up for the current canonical problem has been build and is displayed in Figure 3.10 along with the instrumentation setup. A typical dielectric ground is represented by a particle board with a dielectric constant (ϵ_{r1}) of $\sim 2.0 + 0.1i$, as determined by matching the measured and simulated field responses of propagation above an uncovered board; the vegetation canopy is modeled by a processed, low-density polyurethane foam layer with an effective dielectric constant (ϵ_{r2}) of $\sim 1.10 + 0.007i$, as determined by

measuring the resonance frequency and Q-factor of a circular cavity resonator filled with the foam. Note that in order to increase its dielectric loss to the level as stated above and comparable to that found in realistic foliage, the polyurethane foam was processed by immersing it in a 50/50 mixture of a common household paint and water and then was air-dried. In modeling the propagation properties of the three sides of the vegetation layer that extend to infinity, the foam block is designed to be tapered at those sides in an effort to minimize reflections arising from the presence of the truncations. To further reduce multi-path effects, the time-domain gating feature of the vector network analyzer (HP8720B) was used to isolate the primary wave component arriving at the receiver. The transmitting and receiving antennas are wire monopoles constructed with finite ground planes and are connected to the S_{11} and S_{21} ports of the network analyzer, respectively. The frequency response of the system is characterized at X-band (centered at 10 GHz), which allows the features in the propagation medium to be scaled by a factor of about ~ 33 to 333 for a VHF (30 MHz–300 MHz) wireless channel. Specifically, the network analyzer was set to sweep from 8 GHz to 12 GHz, sampling in intervals of 5 MHz; the signal response at the S_{21} port is interpreted as the power carried by the propagating wave.

In Figure 3.11 measurement results for both polarizations are compared with the simulation results computed using stationary phase considerations; the signal-to-noise-ratio of each measurement data point is ≥ 6 dB. Also, note there is a minimum height (0.25λ for V-pol. and 0.5λ for H-pol. in this experiment) at which useful measurements can be made since the receiving antenna cannot be placed arbitrarily close to the dielectric ground plane. Good agreement between the measured data and the calculated results is seen in Figure 3.11; note that the calculated results assume a point source transmitter and a perfectly homogeneous vegetation layer; the main

cause for the differences between the two sets of results can be attributed to possible inhomogeneities occurring within the simulated foliage as a result of the uneven mixing of foam and paint. Unfortunately, as indicated in Figure 3.11, the measurements cannot unequivocally validate the existence of the discrepancy between the numerical results in this study and those in Tamir's for low receiver heights. Nevertheless, the practicality of the experimental simulator as described above is obvious since the set up can be quickly built and assembled into various configurations much more complicated than the canonical case treated here; for example, multiple blocks of foam can be arranged to represent a vegetation layer containing multiple discontinuities or truncations; it would be difficult to implement either a ray-tracing or field integration technique to such a complicated scenario to model all the propagation mechanisms accurately, but simulation data can be acquired rapidly (and cheaply) from an experimental set up.

3.4 Conclusion

A coherent model for simulating radiation emanating from a transmitter embedded within a truncated vegetation layer has been discussed. The field at an observation point located in the far field outside of the vegetation is calculated by integrating the surface fields over an imaginary 2D plane containing the truncated face of the vegetation layer; the resulting double integral is evaluated using the method of stationary phase. It is seen that for large receiver heights, a very efficient full 2D stationary phase approximation can lead to accurate results; however, for an observation point located in the vicinity of the ground, in order to correctly capture the Norton waves radiating from the fictitious equivalent sources situated on the plane of integration close to the ground, the modified approach in the form

of a 1D stationary phase approximation augmented with numerical integration is more appropriate. The approach as outlined here has been compared with a simple ray-tracing approach put forth previously by Tamir. Simulation results show that the current approach generally predicts fields that are slightly smaller in magnitude than those calculated by means of ray-tracing for low receiver heights—indicating diffraction at the truncation edge is important for those heights and, consequently, dis-supporting the postulation that all the energy of a propagating wave couples completely across the canopy discontinuity. Also presented is an X-band experimental simulator in which the wireless channel is characterized by measuring the response of a scaled-replica of the propagation medium.

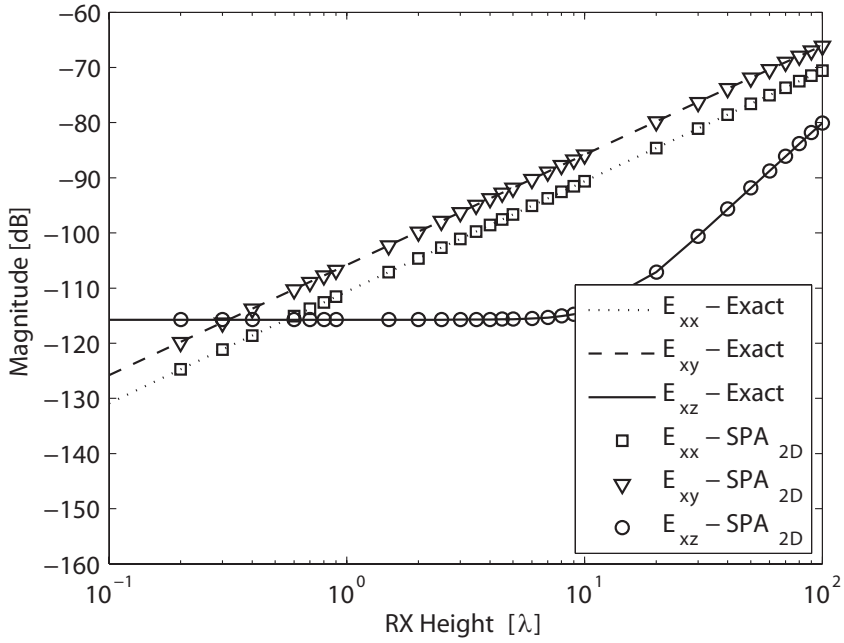

(a)

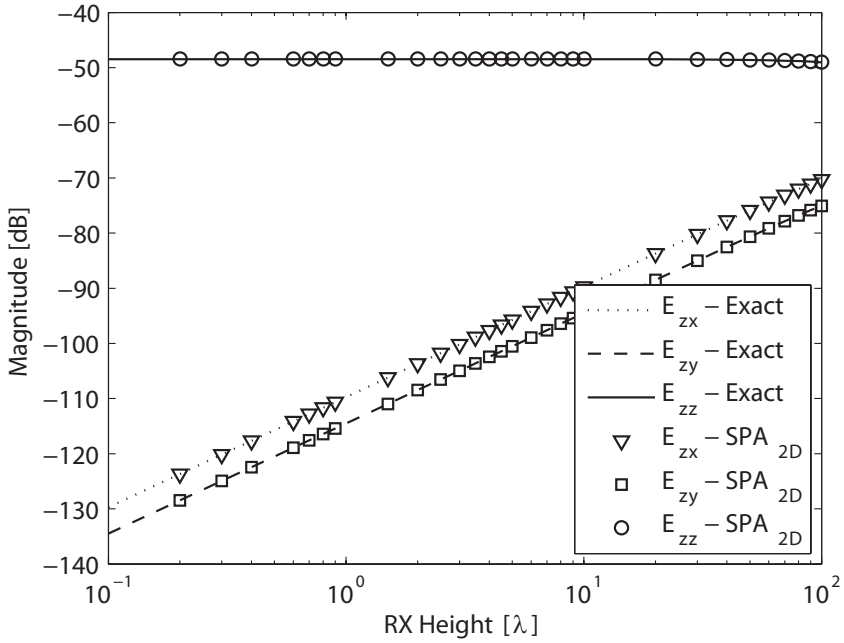

(b)

Figure 3.2: Electric field patterns as a function of receiver height for (a) horizontal and (b) vertical dipole located at (0, -200λ, 0.5λ) above a perfectly conducting ground plane; observation point is at (866.0λ, 500.0λ, z), and $f = 30$ MHz. Excellent agreement is evident between the exact solution calculated using image theory and the 2D stationary phase approximation (SPA_{2D}) for all field components.

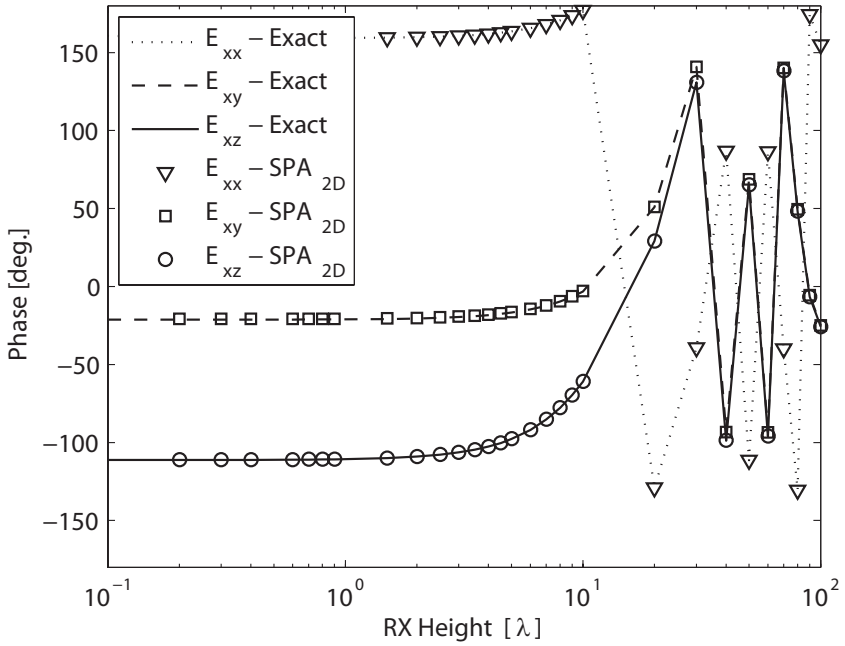

(a)

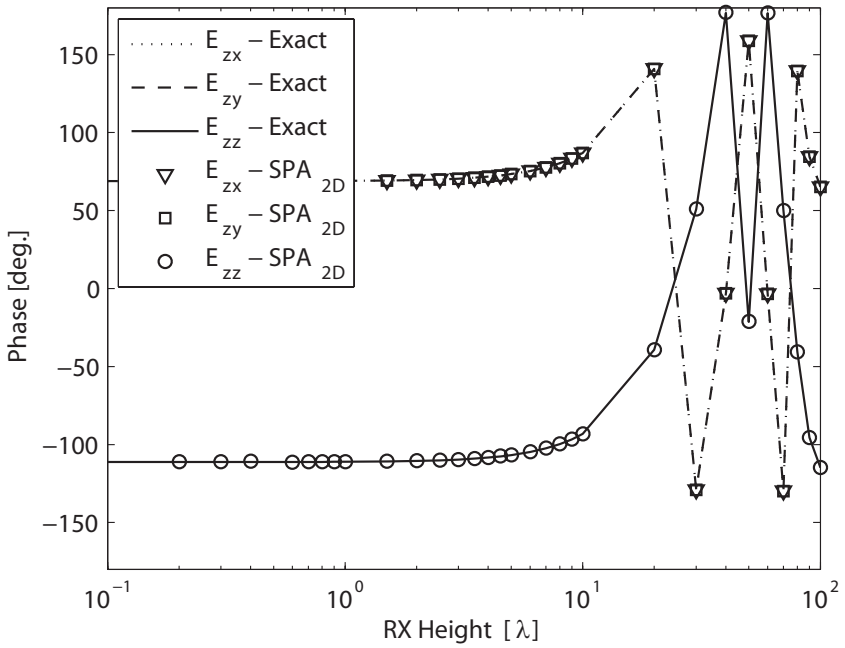

(b)

Figure 3.3: Electric field phase patterns as a function of receiver height for (a) horizontal and (b) vertical dipole for the same set of simulation parameters as those in Figure 3.2.

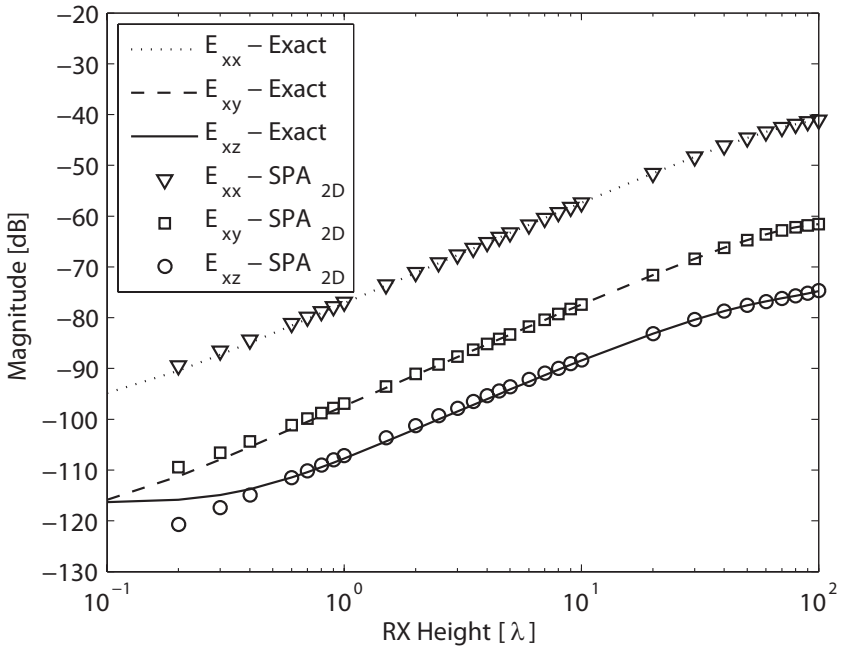

(a)

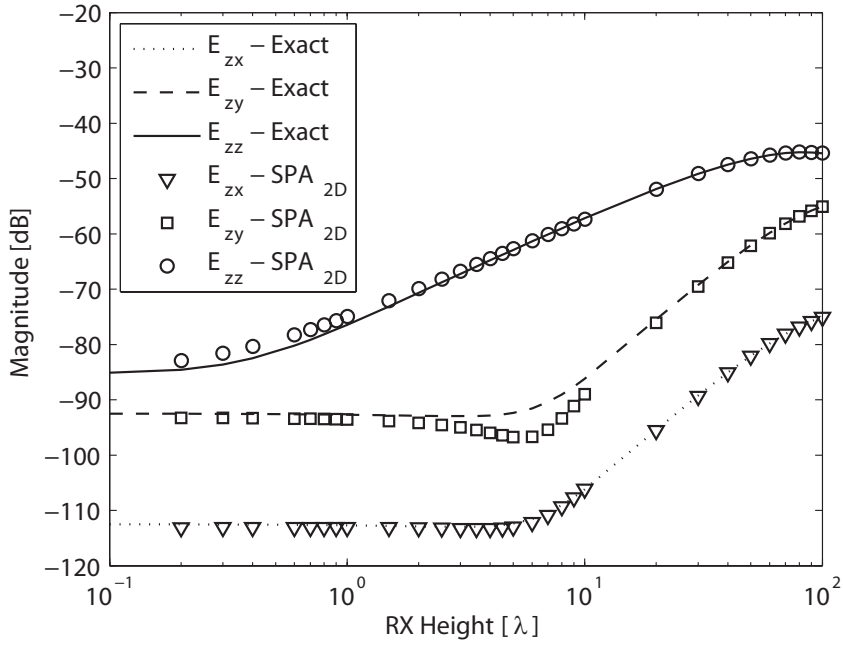

(b)

Figure 3.4: Electric field patterns as a function of receiver height for (a) horizontal and (b) vertical dipole located at $(0, -200\lambda, 0.5\lambda)$ above a dielectric ground plane with $\epsilon_{r2} = 4 + 2i$; observation point is at $(29.85\lambda, 298.5\lambda, z)$, and $f = 30$ MHz. For the set of parameters used in this simulation, SPA_{2D} begins to lose accuracy if receiver height is below approximately 10λ for V-pol. and 1λ for H-pol.

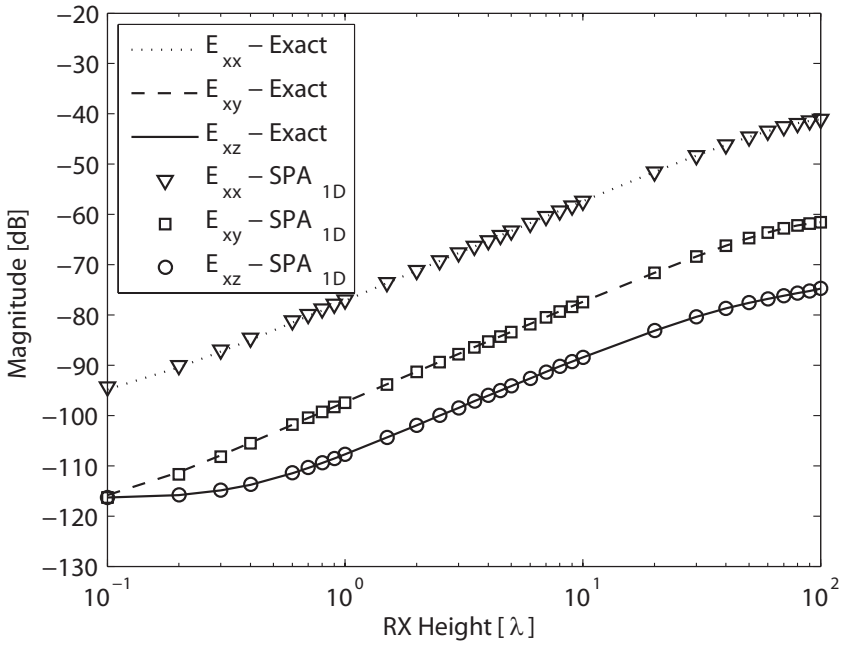

(a)

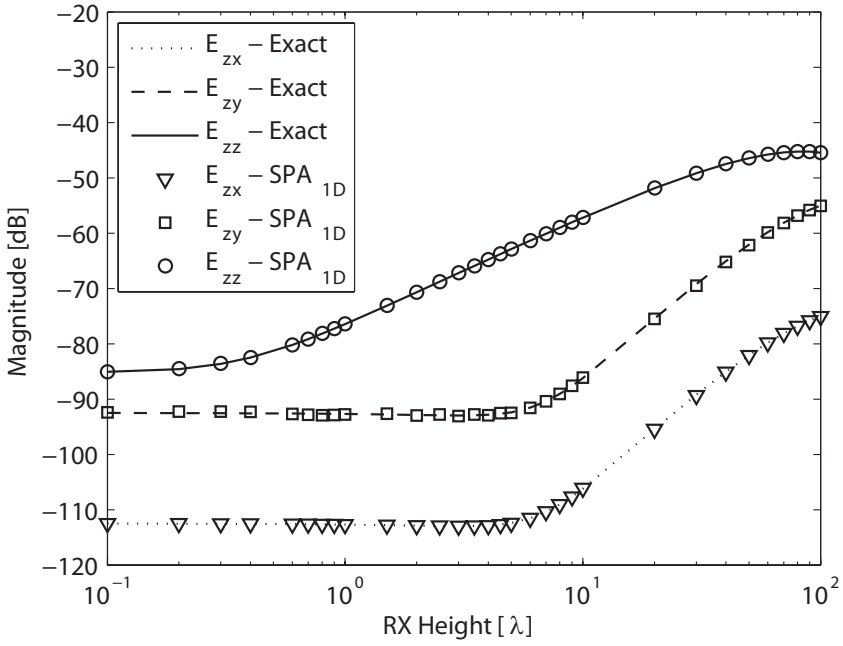

(b)

Figure 3.5: Electric field patterns as a function of receiver height for (a) horizontal and (b) vertical dipole located above a dielectric ground plane for the same set of parameters as that of Figure 3.4. A 1D stationary phase approximation (SPA_{1D}) with numerical integration is used to improve accuracy for low receiver heights.

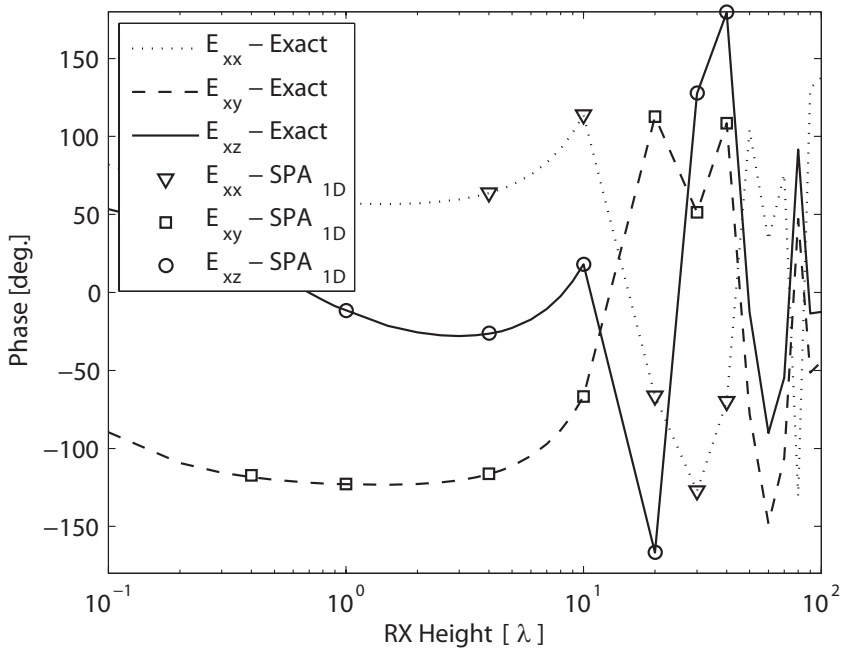

(a)

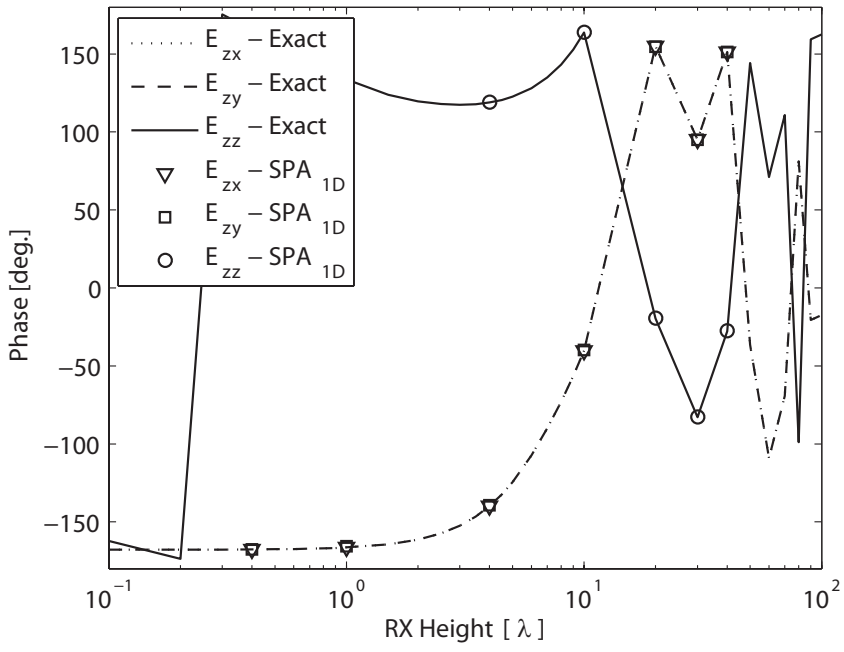

(b)

Figure 3.6: Electric field phase patterns as a function of receiver height for (a) horizontal and (b) vertical dipole located above a dielectric ground plane for the same set of parameters as that of Figure 3.5.

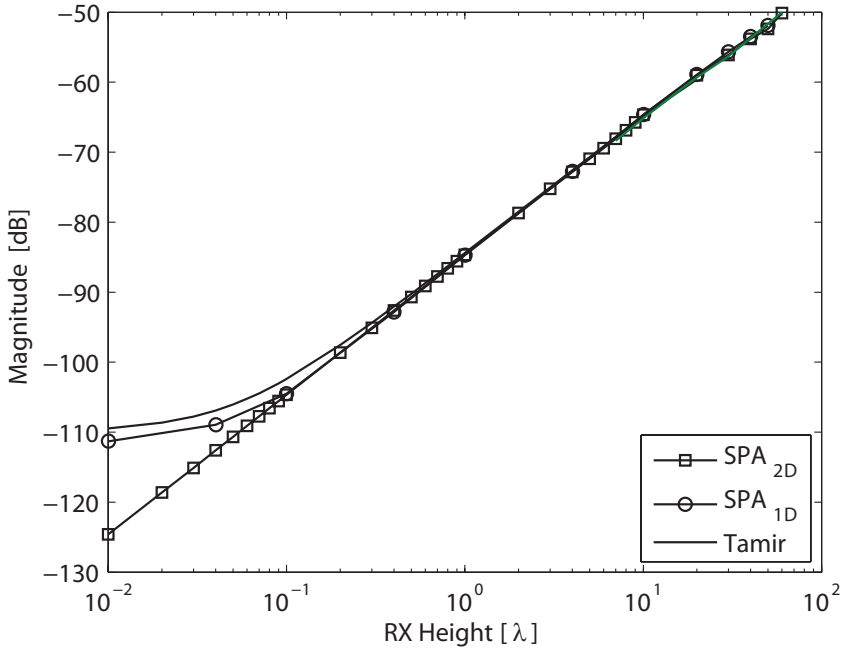

(a)

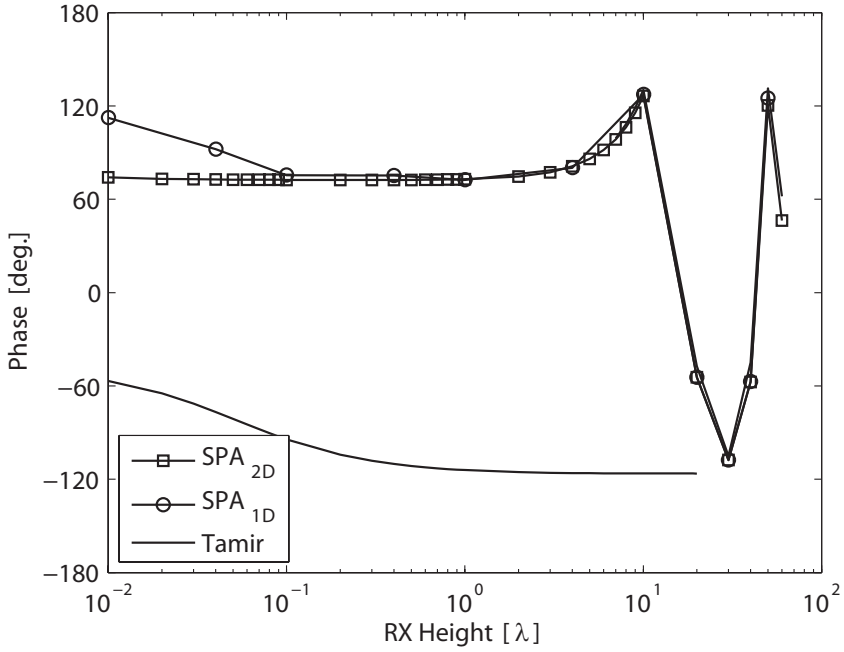

(b)

Figure 3.7: A comparison between Tamir's solution and the surface-field integration solution: shown is the variation of the (a) amplitude and (b) phase of the received field (E_{xx}) as function of receiver height for horizontal polarization. The horizontal dipole is located at (0, -200λ, -0.3λ) inside a truncated vegetation layer of thickness $H = 0.5\lambda$ with $\epsilon_{r1} = 1.01 + 0.03i$ covering a dielectric ground plane with $\epsilon_{r2} = 8 + 6i$; observation point is to the right of the truncation at (29.85λ, 298.5λ, z), and $f = 30$ MHz.

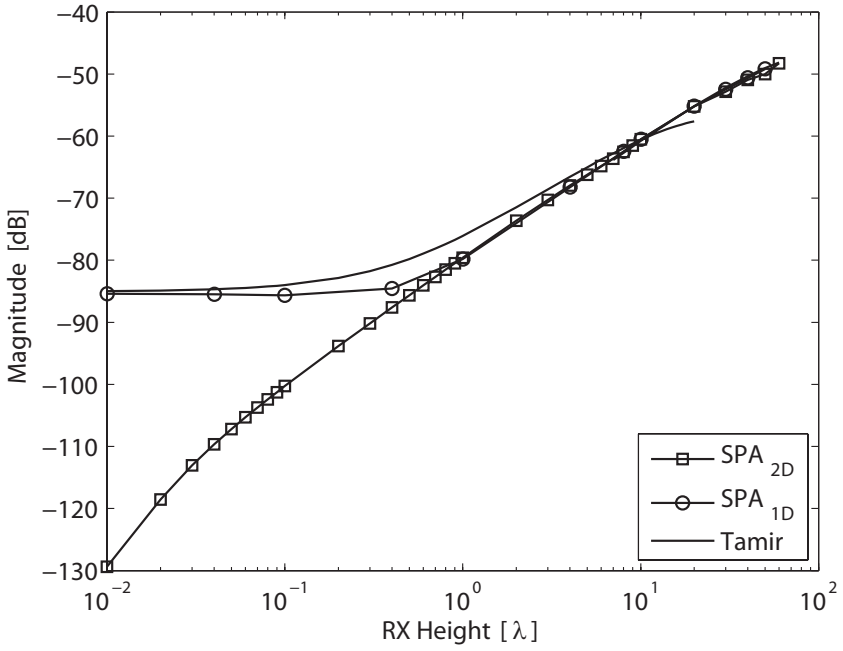

(a)

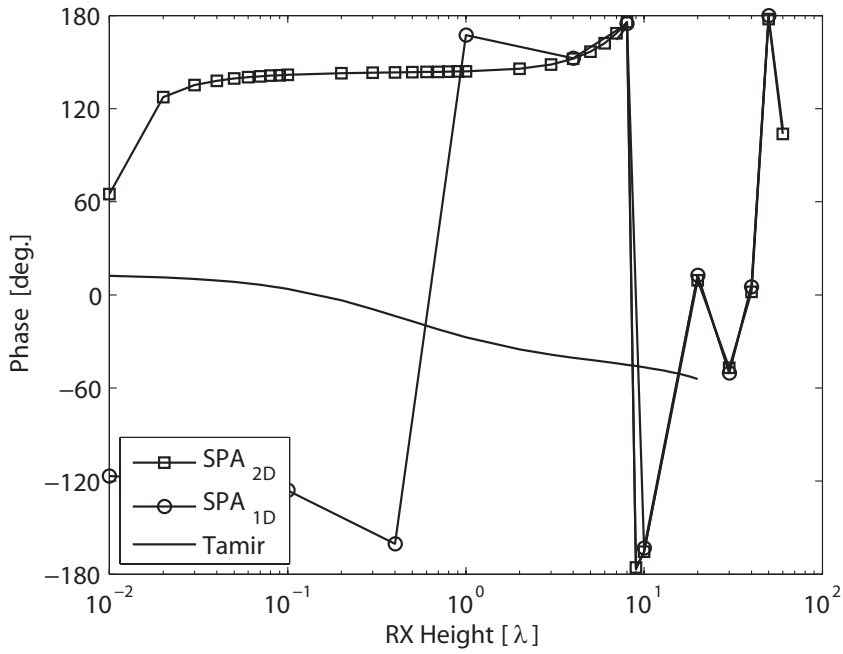

(b)

Figure 3.8: A comparison between Tamir's solution and the surface-field integration solution: shown is the variation of the (a) amplitude and (b) phase of the received field (E_{zz}) as function of receiver height for vertical polarization. The locations of the dipole and observation point and other parameters are the same as those in Figure 3.7.

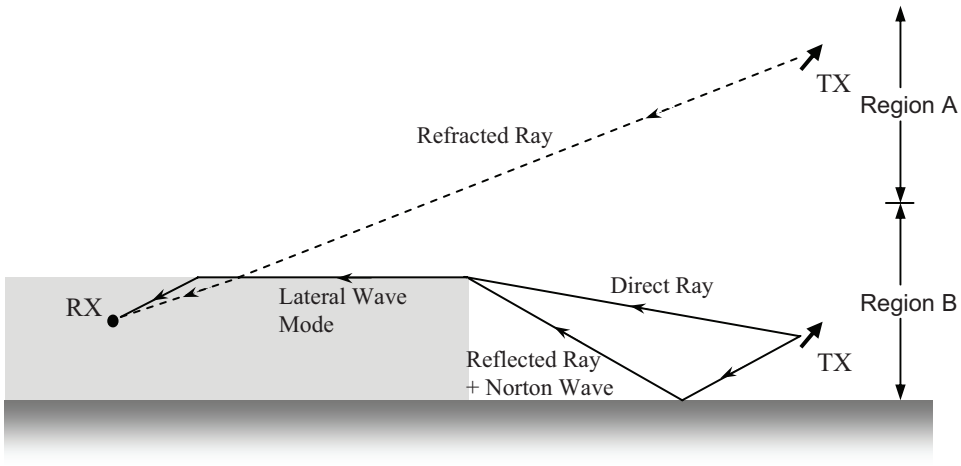

Figure 3.9: Illustration of Tamir's ray-tracing approach for calculating the field radiated by a dipole embedded in a vegetation layer. The positions of the transmitter and receiver have been switched by applying the reciprocity theorem.

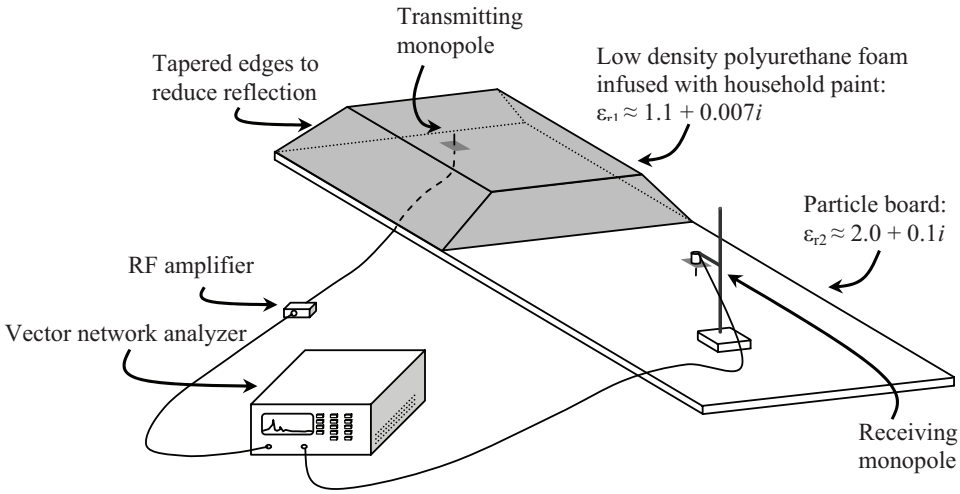

Figure 3.10: X-band scaled propagation measurement model for simulating radiation from a source located inside a truncated vegetation slab.

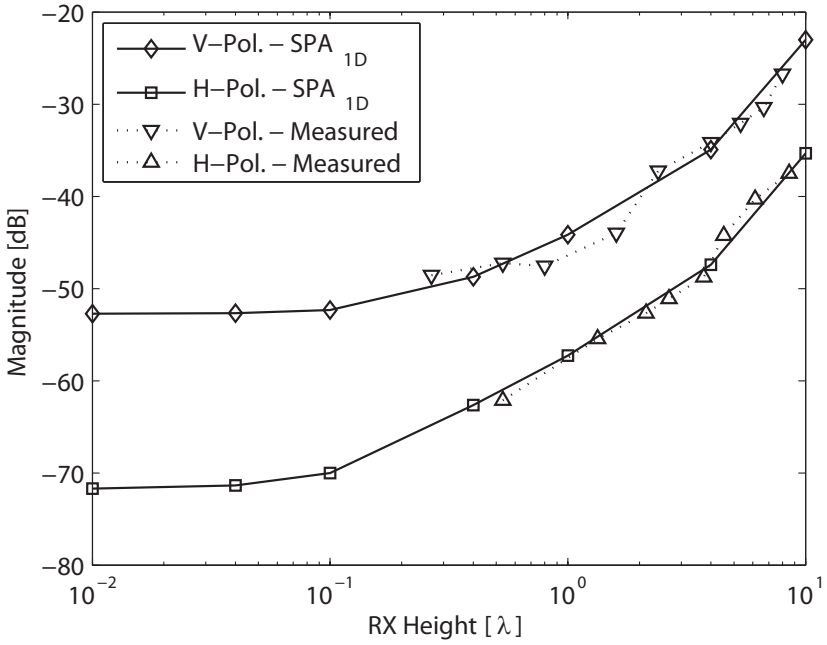

Figure 3.11: Comparison of calculated results (at 300 MHz, using SPA_{1D}) with measurements (S_{21} at 10 GHz) for both polarizations; the measured data points are normalized with respect to the calculated values for a height of 20λ, where the predictions from ray-tracing and field integration are expected to match. The transmitting monopole is embedded within the foam block at a height of 0.3λ; the distance between the transmitter and truncation plane is 95λ and the distance between the truncation plane and receiver is 38.5λ. The dimensions of the foam block (as shown in Figure 3.10) representing the vegetation slab are $\sim 100\lambda \times 43.6\lambda \times 3.2\lambda$.

CHAPTER IV

Simulation of Near-Ground Long-Distance Radiowave Propagation over Terrain Using Nyström Method with Phase Extraction Technique and FMM-Acceleration

4.1 Introduction

As discussed in Chapter I, in supporting signal coverage prediction for specialized systems such as near-ground wireless communication and sensor networks in which the transmitter and receiver are in extreme proximity to the ground, available studies have been limited to the reliance on site-specific, empirical-based models; however, the practicality of these models is restricted as they cannot be applied to general radio configurations and propagation environments. Specifically, for the problem of propagation over an irregular terrain, the interaction between the radiowave and the terrain is often a complicated function of surface profile statistics and ground composition and, therefore, cannot be easily deduced from measurement databases; furthermore, the unique properties of near-earth propagation limit the usefulness of conventional analytical techniques such as ray-tracing and physical optics. As such, when improved solution accuracy is required—especially for low-power systems and networks, full-wave simulation routines—despite their computational inefficiency and because of their generality—are often needed to assess near-earth propagation parameters. A variety of numerical algorithms have been proposed by many workers

over the years toward the treatment of wave propagation over a generalized terrain. Commonly implemented full-wave simulators include the parabolic equation method, finite difference method, and boundary integral equation solver—the last of these has been the most chronicled in literature and is upon which the current chapter is based.

Some of the integral equation-based propagation fast solvers include the fast far field approximation (FAFFA) [56], tabulated interactions method (TIM) [57], [58], adaptive integral method (AIM) [59], and fast multipole method (FMM) [60], [61]. For terrain simulations with large number of unknowns, these method of moments (MoM)-based routines derive their efficiency in essence by speeding up the matrix-vector products in the solution process through the substitution of far field point-to-point interactions with group-to-group interactions. For example, in a conventional MoM iterative solver with no acceleration, the memory and computational cost scale as $\mathcal{O}(N^2)$—where N is the total number of solution unknowns, as compared to $\mathcal{O}(N^{1.5})$ in a single-level FMM and $\mathcal{O}(N \log N)$ in a multi-level FMM. Thus, fast algorithms can—to some extent—circumvent the computational barriers (excessive storage and computer operations) inhibiting the efficiency of the solver and in turn make long-distance propagation simulations more manageable for ordinary computer platforms. Existing schemes as implemented, unfortunately, are low-order in terms of solution convergence (e.g., a twofold improvement in solution accuracy requires a twofold increase in density of solution unknowns), but the need for high-order implementation is critical for propagation problems involving large-scale terrains due to the substantial number of solution unknowns and the necessity to capture path-loss variations precisely in shadow regions. The premiere advantage of high-order schemes is that they can allow the attainment of the solution, for a given level of desired accuracy, with fewer unknowns as compared to low-order schemes. For non-

singular kernels, it is well known that the classical Nyström method [62], a quadrature integration-based scheme, provides a simple and error-controllable method to achieve high-order approximation to the solutions of boundary integral equations; the asymptotic error expansion of this solver for linear integral equations can be found in [63]. For singular kernels, this method has been extended using a local-correction technique by Canino, *et al.* [31] for applications involving the electromagnetic Helmholtz equation; as demonstrated in [31], this modified Nyström method (locally-corrected Nyström—LCN) has the capability of realizing controllable exponential solution error convergence in the form of $\mathcal{O}\left(h^{N_q}\right)$—where h is the surface discretization scale and N_q the Nyström order. Given its inherent fast, controllable convergence behavior and other desirable properties [31], the Nyström method has been applied to irregular terrain propagation simulations in the author's previous study [64].

To further reduce the number of unknowns in the solution, the physical phase propagation information can be deduced and included in the structure of the solver in advance. In [65], an asymptotic phasefront extraction (APE) approach is applied to an iterative physical optics method for modeling the scattering of perfectly conducting objects; an introduction of the APE into the combined field integral equation via a MoM approach is made in [66] to simulate perfectly conducting cylinders of arbitrary cross-sections. In these studies, as well as in others including [67–70], the general technique is based on properly choosing a basis function for the solution with the rapidly-varying phase progression component included; hence, in effect, only a slowly-varying residual function is being explicitly solved.

In this work, a 2D surface integral equation-based Nyström solver in which a phase extraction technique is utilized to reduce the number of surface unknowns is featured. As forward scattering is the dominant mechanism at the near-ground re-

gion, the associated rapidly-varying phase components of the integral equation kernel and solution unknowns are deduced and isolated in advance and subsequently built into the solver. The structure of this solver, as compared to the regular LCN method, is presented in Section 4.2; the inclusion of this solver into the FMM framework is also discussed. Applications of the solver to near-ground propagation simulations over irregular terrain profile are carried out in Section 4.3, within which convergence properties are examined for different integral equation formulations, viz.: the magnetic field integral equation, the electric field integral equation, and the PMCHWT formulation; in addition, the effects of terrain properties such as ground permittivity and roughness on solver convergence are analyzed.

4.2 Formulations

With excitation provided by a radiating source, the induced electric and magnetic currents on the terrain surface (Figure 4.1) can be found using a surface integration method. For example, the Poggio, Miller, Chang, Harrington, Wu, and Tsai (PMCHWT) [71–73] integral formulation on the surface $s(x)$ is of the form

$$\begin{aligned} \hat{n} \times \vec{E}_{inc} &= -\hat{n} \times \left[\left(\eta_1 \boldsymbol{L_1} + \eta_2 \boldsymbol{L_2} \right) \vec{J}(t) - \left(\boldsymbol{T_1} + \boldsymbol{T_2} \right) \vec{M}(t) \right]; \\ \hat{n} \times \vec{H}_{inc} &= -\hat{n} \times \left[\left(\boldsymbol{T_1} + \boldsymbol{T_2} \right) \vec{J}(t) + \left(\eta_1^{-1} \boldsymbol{L_1} + \eta_2^{-1} \boldsymbol{L_2} \right) \vec{M}(t) \right]; \end{aligned} \tag{4.1}$$

where $\eta_{v=1,2}$ is the medium impedance and $\boldsymbol{L_v}$ and $\boldsymbol{T_v}$ are the linear operators

$$\begin{aligned} \boldsymbol{L_v} \vec{u} &= i \left(k_v + k_v^{-1} \nabla \nabla \cdot \right) \left(g_v * \vec{u} \right); \\ \boldsymbol{T_v} \vec{u} &= \nabla \times \left(g_v * \vec{u} \right); \end{aligned} \tag{4.2}$$

with $*$ as the convolution notation, k_v the medium wavenumber, and g_v the scalar Green's function

$$g_v = \frac{i}{4} H_0^{(1)} \left(k_v \rho \right), \tag{4.3}$$

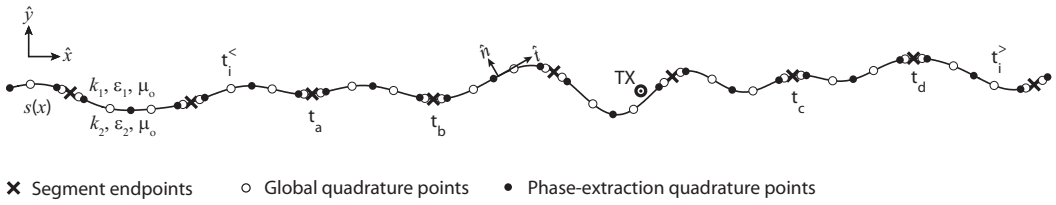

Figure 4.1: Terrain surface and parameter definitions.

in which ρ denotes the radial distance between the source and observation points.

4.2.1 Regular LCN

Discretizing the surface into N_s segments and placing N_q testing points within each segment lead to a matrix system for solving the currents $\vec{J}(t)$ and $\vec{M}(t)$, where t is the surface parametric variable. In the framework of the Nyström method based on Gaussian-Legendre quadrature, the operation of $\boldsymbol{L_v}$ or $\boldsymbol{T_v}$ on the currents can be cast in the generic matrix form of

$$\int_{s(x)} K(t_i, t')\,\vec{u}(t')\,dt'\,|_{i=1,2,..,N} = \boldsymbol{K}\boldsymbol{W}\vec{u} = (\boldsymbol{K_{lc}} + \boldsymbol{K_{nlc}})\,\boldsymbol{W}\vec{u} \tag{4.4}$$

in which $\vec{u}$ on the right side is now a vector of length $N = N_s N_q$ sampling the total unknown current (either $\vec{J}(t)$ or $\vec{M}(t)$) at the global quadrature points—or testing locations—t_i; $\boldsymbol{W}$ is a diagonal matrix of quadrature weights corresponding to the current points; $\boldsymbol{K_{nlc}}$ (non-locally corrected)—an interaction matrix relating the non-local current points to the total observed fields at the testing points—is a direct evaluation of the kernel $K(t, t')$, i.e.,

$$K_{nlc}^{ij}\,\big|_{t_j \notin \text{ local seg. of } t_i} = K(t_i, t_j)|_{i,j=1,2,...,N}\,, \tag{4.5}$$

and the entries of $\boldsymbol{K_{lc}}$ (locally-corrected, or the block diagonal portion of $\boldsymbol{K}$) for each segment local to t_i are filled by a local-correction scheme described as follows:

$$K_{lc}\,\big|_{t_j \in \text{ local seg. of } t_i} = \boldsymbol{w}^{-1}\left(\boldsymbol{p}^T\right)^{-1}\vec{\psi}; \tag{4.6}$$

where, with $p_x(\cdot)$ denoting a Legendre polynomial of order x spanning the local segment,

$$\psi_{m=0,1,...,N_q-1} = \int\limits_{\text{local seg. of } t_i} K(t_i, t')\, p_m(t')\, dt'; \tag{4.7}$$

$$p_{\alpha\beta}\big|_{\alpha,\beta=0,1,...,N_q-1} = p_\beta(t_\alpha)\,|_{t_\alpha \in \text{ local seg. of } t_i}\ ; \tag{4.8}$$

and $\boldsymbol{w}$ is the sub-block matrix of $\boldsymbol{W}$ corresponding to the local segment being integrated. In this work, the local-correction region is taken as the self-segment (containing t_i) and its two adjacent segments.

An application of the Nyström method as outlined above is tantamount to approximating the unknown current function on each surface segment with a linear combination of Legendre polynomials in obtaining a fast converging solution through the use of quadrature integration. Expression (4.4) can also be rewritten as

$$\boldsymbol{KW}\vec{u} = \boldsymbol{KWP}\vec{a}, \tag{4.9}$$

where $\vec{a}$ is simply the multiplication coefficients of the polynomials and $\boldsymbol{P}$ is a block diagonal matrix in which the elements of the kth ($k = 1, 2, ..., N_s$) diagonal block $\boldsymbol{p_k}$ are given by

$$p_{\alpha\beta}\big|_{\alpha,\beta=0,1,...,N_q-1} = p_\beta(t_\alpha)\,|_{t_\alpha \in \text{ seg. } k}\ . \tag{4.10}$$

4.2.2 Phase-Extracted LCN

In traditional Galerkin MoM methods, 10 to 20 unknowns per linear wavelength is needed to achieve an accurate solution. An application of the regular Nyström method as outlined can lead to a reduction in the number of unknowns. Assuming propagation is mostly in the paraxial direction, to reach a solution with even fewer unknowns, the fast-varying components of both the current and kernel functions are extracted and built into the solver in advance. The surface is discretized into N_s

segments and N_q quadrature points are populated on each segment as in the regular Nyström method; the current on each segment is assumed to be of the form

$$\sum_{n=0}^{N_q-1} a_n p_n(t)\, e^{\pm ik_1 t}. \tag{4.11}$$

By considering the phase dependencies of the current and kernel as indicated in Figure 4.1, the matrix filling routine in the phase extraction method for the non-local region is carried out as follows:

for $t_i > t'$,

$$\begin{aligned} t' \in [t_a, t_b] \Rightarrow \int\limits_{[t_a,t_b]} K^{>}(t_i,t')p_n(t')e^{-ik_1t'}dt' &= \int\limits_{[t_a,t_b]} \left[\frac{K^{>}(t_i,t')}{e^{-ik_vt'}}\right] p_n(t')e^{-i(k_v+k_1)t'}dt' \\ &= \sum_{m=0}^{M_q^{><}-1} w_m^{><} \frac{K^{>}(t_i,t_m)}{e^{-ik_vt_m}}; \end{aligned} \tag{4.12}$$

$$\begin{aligned} t' \in [t_c, t_d] \Rightarrow \int\limits_{[t_c,t_d]} K^{>}(t_i,t')p_n(t')e^{+ik_1t'}dt' &= \int\limits_{[t_c,t_d]} \left[\frac{K^{>}(t_i,t')}{e^{-ik_vt'}}\right] p_n(t')e^{-i(k_v-k_1)t'}dt' \\ &= \sum_{m=0}^{M_q^{>>}-1} w_m^{>>} \frac{K^{>}(t_i,t_m)}{e^{-ik_vt_m}}; \end{aligned} \tag{4.13}$$

for $t_i < t'$,

$$\begin{aligned} t' \in [t_a, t_b] \Rightarrow \int\limits_{[t_a,t_b]} K^{<}(t_i,t')p_n(t')e^{-ik_1t'}dt' &= \int\limits_{[t_a,t_b]} \left[\frac{K^{<}(t_i,t')}{e^{+ik_vt'}}\right] p_n(t')e^{+i(k_v-k_1)t'}dt' \\ &= \sum_{m=0}^{M_q^{<<}-1} w_m^{<<} \frac{K^{<}(t_i,t_m)}{e^{+ik_vt_m}}; \end{aligned} \tag{4.14}$$

$$\begin{aligned} t' \in [t_c, t_d] \Rightarrow \int\limits_{[t_c,t_d]} K^{<}(t_i,t')p_n(t')e^{+ik_1t'}dt' &= \int\limits_{[t_c,t_d]} \left[\frac{K^{<}(t_i,t')}{e^{+ik_vt'}}\right] p_n(t')e^{+i(k_v+k_1)t'}dt' \\ &= \sum_{m=0}^{M_q^{<>}-1} w_m^{<>} \frac{K^{<}(t_i,t_m)}{e^{+ik_vt_m}}. \end{aligned} \tag{4.15}$$

The superscript notations $>$ and $<$ are used to differentiate the two cases $t_i > t'$ and $t_i < t'$; similarly, the superscript double notations $><$, $>>$, $<<$, and $<>$ are used

to differentiate the four possible phase dependencies of the integrand as listed above. The specialized weights w_m for each case (4.12)–(4.15) over the kth source segment are deduced by testing the integrand with Legendre polynomials:

$$\vec{w}_k = \left(\boldsymbol{p}^T\right)^{-1} \vec{\psi}; \tag{4.16}$$

$$\psi_{m=0,1,...,M_q-1} = \int\limits_{\text{seg. } k} p_m\left(t'\right) p_n\left(t'\right) e^{\pm i(k_v \pm k_1)t'} dt'; \tag{4.17}$$

$$p_{\alpha\beta}\left|_{\alpha,\beta=0,1,...,M_q-1} = p_\beta\left(t_\alpha\right)\right|_{t_\alpha \in \text{ seg. } k}. \tag{4.18}$$

Evaluating (4.16)–(4.18) for $n = 0, 1, ..., N_q - 1$ over the source segment establishes the matrix $\boldsymbol{w_k}$ of dimensions M_q (where M_q is used to generically represent either $M_q^{><}$, $M_q^{>>}$, $M_q^{<<}$, or $M_q^{<>}$) by N_q, and the multiplication of this matrix with a source coefficient vector can be interpreted as the transformation of N_q continuous source functions (without the phase variation term) into M_q discrete source points (positioned at the phase-extraction quadrature points t_m). Note that in general the number of phase-extraction points can be made adaptive, depending on the local variations of the terrain surface containing the segment being integrated. Simulations show that the choice of $M_q = N_q$ is sufficient to consistently achieve good results; as such, this process of deducing the specialized quadrature weights does not need to be repeated for every surface segment; instead, it only needs to be calculated once for each case of (4.12)–(4.15) as the procedure can be re-normalized with respect to the segment interval.

As done similarly in the regular Nyström method, matrix filling for a source segment in the local-correction region of t_i is found by explicit integrations of the source functions:

$$K_{lc}\left|_{t_j \in \text{ local seg. of } t_i} = \int\limits_{\text{local seg. of } t_i} K\left(t_i, t'\right) p_n\left(t'\right) e^{\pm i k_1 t'} dt'\right|_{n=0,1,...,N_q-1}. \tag{4.19}$$

Carrying out the matrix filling process for all testing points t_i over the surface generates the following generic matrix system for computing the operation of $\boldsymbol{L_v}$ or $\boldsymbol{T_v}$ on the currents:

$$\boldsymbol{K}\vec{a} = \left(\boldsymbol{K_{lc}} + \boldsymbol{K_{nlc}^{>}}\boldsymbol{P_{phase}^{>}}\boldsymbol{P_{w}^{>}} + \boldsymbol{K_{nlc}^{<}}\boldsymbol{P_{phase}^{<}}\boldsymbol{P_{w}^{<}}\right)\vec{a}; \tag{4.20}$$

the first term within the parenthesis is the diagonal block of $\boldsymbol{K}$, and second and third terms are the lower and upper triangular portions, respectively. The above operation tracks the interactions among $M = N_s M_q$ source points and $N = N_s N_q$ observation points. The diagonal matrix $\boldsymbol{P_{phase}}$ corrects the phase of the source points on the surface with a multiplication by $e^{\pm ik_1 t_m}$; $\boldsymbol{P_w}$ is a block diagonal matrix with the kth block given by $\boldsymbol{w_k}$; and $\boldsymbol{K_{nlc}}$ is given by direct evaluations of the kernel:

$$K_{nlc}^{ij}\Big|_{t_j \notin \text{ local seg. of } t_i} = K\left(t_i, t_j\right)|_{i=1,2,\ldots,N; j=1,2,\ldots,M}\ . \tag{4.21}$$

Therefore, in the phase extraction based routine, unlike in the regular Nyström routine, separate sets of surface points are needed to position the radiating and observation points. For the special case of $M_q = N_q$, these two sets of points are the same; in general, however, depending on the values of $M_q^{><}$, $M_q^{>>}$, $M_q^{<<}$, $M_q^{<>}$, and N_q, they do not have to coincide.

To speed up the matrix-vector product operation of (4.20), the kernel matrix $\boldsymbol{K_{nlc}}$ is further decomposed into a near field and a far field component. The near field component is computed as shown in (4.21); the far field component is calculated using the fast multipole method; specifically, the source segments and points are divided into interaction groups, and the far field interactions among the discrete points at t_i and t_j are calculated based on the factorization of the Green's function using the addition theorem [60], [61]:

$$H_0^{(1)}\left(k_v \rho_{ij}\right) = \vec{\beta}_{il'}^{d}\boldsymbol{\tau}_{l'l}\vec{\beta}_{lj}^{a}, \tag{4.22}$$

where ℓ' and ℓ represent the indexes of the group centers and

$$\beta_{lj}^{a}\Big|_{q=1,2,\ldots,Q} = e^{+ik_v\rho_{\ell j}\cos\left(\alpha_q-\phi_{\ell j}\right)}\ ; \tag{4.23}$$

$$\beta_{i\ell'}^{d}\Big|_{q=1,2,\ldots,Q} = e^{-ik_v\rho_{i\ell'}\cos(\alpha_q-\phi_{i\ell'})}\ ; \tag{4.24}$$

$\boldsymbol{\tau_{\ell'\ell}}$ is a diagonal matrix with the diagonal elements given by

$$\sum_{c=-C}^{C} H_0^{(1)}\left(k_v\rho_{\ell'\ell}\right) e^{-ik_v c\left(\phi_{\ell'\ell}-\alpha_q+\frac{\pi}{2}\right)}\Big|_{q=1,2,\ldots,Q}\ , \tag{4.25}$$

with C being the truncation number in the addition theorem and $Q = 2C + 1$ can be interpreted as the number of plane waves used to approximate the field of a source point. In a single-level FMM implementation, the operation of the far field component of the different types of kernel matrices on an arbitrary source vector is then calculated as a sequential product involving sparse matrices:

$$\boldsymbol{K_{nlc}^{ff}}\vec{x} = \boldsymbol{\beta^d T \beta^a}\vec{x}, \tag{4.26}$$

where $\boldsymbol{\beta^a}$, $\boldsymbol{T}$, and $\boldsymbol{\beta^d}$ represent—in FMM terminology—the matrices of plane wave aggregation, translation, and disaggregation, respectively. As the matrices $\boldsymbol{P_{phase}}$ and $\boldsymbol{P_w}$ are diagonally-dominant and with $M_q = N_q$, the overall complexity of the matrix-vector product operation (4.20) in the phase extraction routine can be readily shown to be the same as that of the original FMM routine, i.e., $\mathcal{O}(N^{1.5})$. The detailed definitions for the various parameters within the FMM framework are not presented here explicitly but can be found in works [60], [61].

4.3 Numerical Results

The regular and phase-extracted locally-corrected Nyström methods as presented in the previous section are applied to wave propagation prediction over irregular terrain profiles in this section.

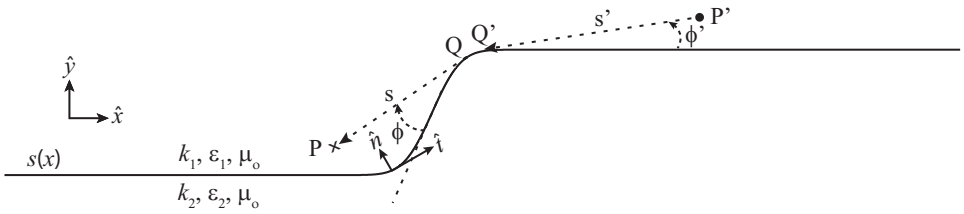

Figure 4.2: S-shaped terrain surface.

4.3.1 Standard Example

As an initial step, the validity and convergence properties of the regular LCN are examined for a canonical shape (circular cylinder); these results are displayed in Appendix B; next, this algorithm is applied to the terrain profile of Figure 4.2. The surface length L is selected to be 1000λ with $s(x) = 30\,erf(0.03x)$; the simulation frequency is 300 MHz and $\epsilon_2 = (2 + i)\epsilon_o$. Since no exact solution exists for this problem, the reference used for convergence validation is the solution calculated with a very fine discretization. The $\mathcal{O}\left(h^{N_q}\right)$ asymptotic convergence behaviors of the solver as functions of the average number of surface unknowns are shown in Figures 4.3 and 4.4: each curve in Figure 4.3 is obtained by holding the discretization scale $h = L/N_s$ constant while changing the Nyström order N_q—similar to the terminology set forth in [31], this can be called N_q-refinement; the vice versa is performed in Figure 4.4—this is known as h- or N_s-refinement. The relative error of the solution vector is defined as

$$E_{rel} = \frac{\|\vec{u} - \vec{u}_{ref}\|_2}{\|\vec{u}_{ref}\|_2}. \tag{4.27}$$

In Figures 4.3 and 4.4, the y-axis can be re-interpreted as the average number of digits of precision in the solution vectors. Note that although this is a double-precision code, the exponential fall of the relative error flattens out at ~ 8 digits due to precision loss in floating point operations. It is seen that (for this set of simulation results shown) 8 digits of precision can be reached with as few as 8 surface

points per wavelength. The code is written in Matlab script and implemented on a Linux machine with a 2.6 GHz AMD Opteron processor and 16 GB of RAM. For a simulation with 32000 total unknowns, the total runtime (setup plus iterative solve) is ~ 3800 seconds and the required memory is ~ 1.6 GB.

4.3.2 Diffraction Coefficient Extraction

The developed algorithm can be an efficient utility for extracting diffraction coefficients to complement standard ray-tracing routines. Consider the transmitting and receiving points configured as displayed in Figure 4.2, the difficulty in extending existing UTD methods to this problem largely stems from the absence of an accurate method for characterizing the diffracted fields guided by the smooth dielectric convex interface along surface segment $\overset{\frown}{Q'Q}$. For the region dipping slightly into the shadow region (i.e., when $\overset{\frown}{Q'Q}$ is small), an asymptotic model in terms of creeping wave modes originally developed for circular dielectric cylinders can be applied to compute the diffracted field as

$$H_{z,1}^{diff,asymp}(\phi',\phi) \approx \sum_{m=1}^{\infty} \frac{e^{+ik_1 s'}}{\sqrt{s'}} D_m(Q') A_m(Q') \cdot e^{(+ik_1 \overset{\frown}{Q'Q} - \alpha_m)} D_m(Q) A_m(Q) \frac{e^{+ik_1 s}}{\sqrt{s}}, \tag{4.28}$$

in which the effective attenuation constant over $\overset{\frown}{Q'Q}$ is a function of the modal eigenvalue σ_m and surface curvature ρ_c [74]:

$$\alpha_m = \int_{\overset{\frown}{Q'Q}} \frac{\sigma_m}{\rho_c} \left(\frac{k_1 \rho_c}{2} \right)^{\frac{1}{3}} e^{-i\frac{\pi}{6}} \, dt'. \tag{4.29}$$

For large $\overset{\frown}{Q'Q}$, only the first ($m = 1$) mode survives. The definitions for the modal eigenvalue and other accompanying quantities in (4.28) are found in [74]. For sake of simplicity, only the creeping wave-excited diffracted field located beyond the shadow boundaries is analyzed in this work. Note that the heuristic expression in (4.28) is

not rigorously valid for obtaining fields in the deep shadow regions (i.e., for large $Q\widehat{\ }Q$) since the creeping wave modal parameters for a dielectric surface—unlike those for a perfectly conducting one—are functions of the surface curvature and thus give rise to modal scattering and inter-modal coupling as the modes travel along the curvature-varying segment $Q\widehat{\ }Q$. Currently there is neither an analytical nor heuristic approach for accurately handling these scattering and coupling mechanisms as pertaining to creeping waves propagating along dielectric convex surfaces; by noting that the decaying factor in (4.29) needs to be modified for general curvature profiles, here it is suggested that a correction can be derived numerically to account for these effects for observation points in the deep shadow regions. For large $Q\widehat{\ }Q$, the decaying factor is expected to be the same over the portion of the wave path (along the surface) that is common to a given set of incident angles; consequently, a normalized correction function $C_{norm}(\phi)$ can be sampled through a single run of the numerical code with the placing of an excitation source at the lowest desired ϕ'_{ref} while computing the fields over the entire range of observation angles beyond the shadow boundary up to minimum angle ϕ_{ref} deep in the shadow region. Once this has been accomplished, for use with sources placed at other incident angles ϕ' ($> \phi'_{ref}$), the correction function can be unnormalized by multiplying it with the ratio of the exact field to the asymptotic uncorrected field for the case when the source is at ϕ_{ref} and the observation at ϕ'; note that the set of exact field values can be tabulated in advance with a second run of the numerical simulator. Symbolically, the procedure is summarized as

$$H_{z,1}^{diff,corr}(\phi',\phi) = H_{z,1}^{diff,asymp}(\phi',\phi,m=1)\cdot C_{norm}(\phi)\frac{H_{z,1}^{diff,exact}(\phi_{ref},\phi')}{H_{z,1}^{diff,asymp}(\phi_{ref},\phi',m=1)}. \tag{4.30}$$

In effect, to obtain the diffraction coefficients for all incident and observation an-

gles (in the shadow), only two runs of the numerical code are required: the first to obtain $C_{norm}(\phi)$ and the second to obtain $H_{z,1}^{diff,exact}(\phi_{ref}, \phi')$; however, these functions must be re-simulated as the frequency, the terrain dielectric property, or the terrain profile changes. Figure 4.5 shows the results of using (4.30) for computing the creeping wave-excited diffracted field component for various source incident angles.

4.3.3 Arbitrary Terrain Profiles

Without the loss of generality, a zero-mean surface profile obeying Gaussian statistics $\{\sigma, c_l\}$—where σ is the rms height and c_l the correlation length—is assumed and generated from its randomized power spectral density by following the procedure outlined in [75]. It is impractical to use $s(x)$ (regardless of whether the function is random or deterministic) directly because of the necessity for rapid generation and inter-translation of surface height, length, and slope parameters. Therefore, an approximate form for $s(x)$ which facilitates efficient computation of these routines must be employed. The approximate $s(x)$ in this solver is reconstructed from a sampled set of $s(x)$ using the approximate prolate spheroidal wave function (APSWF) as the basis. It has been shown that the APSWF interpolant can be exploited to approximate a band-limited function with an exponential error bound [76] and is superior to classical polynomial interpolants; as a consequence, the solver exhibits exponential convergence in terms of surface discretization error. In the following results, to avoid dealing with the singular behavior of the current solution at the surface edges, only the portion of the solution located away from the open edges is being used for error convergence analysis. (Alternately, a tapered excitation source can be employed to avoid direct illumination of the edges; for example, a complex source beam which approximates the Gaussian beam is used in [64] for this purpose.)

The asymptotic convergence behaviors of the solvers as functions of the average

number of surface unknowns are shown in Figures 4.6 and 4.7. The surface parameters are $\{\sigma, c_l\} = \{1\lambda, 5\lambda\}$, with $L = 500\lambda$, $\epsilon_2 = (1.5 + 0.2i)\epsilon_o$, and the frequency is at 300 MHz. The relative error of the solution vector is again defined as (4.27), and the reference solution used for comparison is obtained by solving the problem with a very fine surface discretization and high density of unknowns.

The high-order convergent behavior of the regular locally-corrected Nyström method is demonstrated. Specifically, the error decays approximately as $\mathcal{O}\big(h^{N_q}\big)$, as readily seen in Figure 4.7. However, the actual slopes of the decay are slower than predicted; for example, for both the electric and magnetic currents, the actual exponents are approximately 5.6, 7.6, and 9, respectively, for $N_q = 6$, 8, and 10; this observation is consistent with what has been reported in [31]. Because of the exponential error convergence behavior, Figure 4.6 shows that faster convergence is achieved by using a larger discretization scale. Note that, as in the results of Section 4.3.1, the exponential fall of the relative error flattens out at ~ 8 to 9 digits due to precision loss in floating point operations.

The results obtained from the phase-extracted Nyström method are superimposed upon those from the regular method in Figures 4.6 and 4.7. It is seen that the asymptotic convergence rate of the phase-extracted solver is comparable to that of the regular solver for both h- and N_q-refinement; the benefit of extracting the fast-varying solution component is also evident: the relative error for each case is dramatically reduced, especially for small number of unknowns. The exponential convergence behavior $\mathcal{O}\big(h^{N_q}\big)$ is similarly observed in Figure 4.7. As illustrated in Figure 4.6, the phase-extraction technique is more advantageous for larger surface discretization scales; this is expected since a set of polynomials complete up to order N_q can approximate the same fast-varying function less accurately over a larger sur-

face interval than over a smaller interval. As the surface discretization becomes finer, Figure 4.6 shows that the relative errors calculated from phase-extraction approach closer to those from the regular routine (for large surface unknown density). The actual amplitudes of the induced magnetic and electric surface currents are plotted in Figure 4.8 for the aforementioned surface profile. Even with as few as an average of one unknown per wavelength, the solution from the phase-extracted solver is seen to follow the "true" (reference) solution accurately, including in the terrain shadow regions. In this example, $N_s = 125$ and $M_q = N_q = 4$; since the phase variation of the currents near the small region around the source location is strictly not of $e^{\pm ik_1 t}$ dependence, a higher segmentation density is used in that region to speed up convergence; this adaptive segmentation scheme, however, does not change the overall complexity of the solver, as the average number of unknowns is nearly unaffected for large surface profiles. Note that, alternatively, because the current variation is slow around the source region, a mixed solver could be applied in which a regular LCN method is used for the source region while a phase-extracted solver is used for the rest of the profile.

The convergence of the phase-extracted solver for two ground dielectric constants, $\epsilon_2 = (1.5 + 0.2i)\epsilon_o$ and $\epsilon_2 = (3.0 + 0.5i)\epsilon_o$, is shown in Figure 4.9; the convergence is seen to be comparable for the two cases. To analyze the validity of the paraxial approximation, the convergence properties of the phase-extracted solver are shown in Table 4.1 for various surface rms heights. As expected, the performance of the new solver degrades as rms slope increases; the loss of accuracy is primarily due to the fact that backscattering phenomena become more significant in the deep terrain shadows; that is, the currents are no longer of purely $e^{\pm ik_1 t}$ dependence; nevertheless, even with such as a simple approximation, the phase-extraction approach is seen to

		Number of Unknowns / λ					
		0.5	1	1.5	2	2.5	3
$\sigma = 1\lambda$	Regular LCN	21.9	8.91	8.07	8.95	6.17	3.31
	Phase-Extracted LCN	0.762	0.207	4.30e-2	6.77e-3	1.09e-3	4.56e-04
$\sigma = 2\lambda$	Regular LCN	36.2	10.6	12.1	10.9	7.00	3.42
	Phase-Extracted LCN	3.15	1.86	0.790	0.369	0.142	4.56e-2
$\sigma = 3\lambda$	Regular LCN	43.1	20.1	14.3	12.7	10.5	5.98
	Phase-Extracted LCN	5.85	5.29	3.51	2.00	1.84	0.956

Table 4.1: Performance of regular and phase-extracted LCN solvers for varying surface roughness; shown is the average error in dB as compared to the reference solution; $L = 500\lambda$; $N_s = 125$; $c_l = 5\lambda$; $M_q = N_q$.

be able to speed up solution convergence for relatively very rough terrain profiles.

The convergence behaviors of different integral formulations are compared next. The propagation problem has been treated using the PMCHWT formulation thus far; two other commonly used formulations include the EFIE and the MFIE as given by

EFIE:

$$\begin{aligned} \hat{n} \times \vec{E}_{inc} &= -\frac{1}{2}\vec{M}(t) - \hat{n} \times \left[\eta_1 \boldsymbol{L_1} \vec{J}(t) - \boldsymbol{T_1} \vec{M}(t)\right]; \\ \vec{0} &= +\frac{1}{2}\vec{M}(t) - \hat{n} \times \left[\eta_2 \boldsymbol{L_2} \vec{J}(t) - \boldsymbol{T_2} \vec{M}(t)\right]; \end{aligned} \tag{4.31}$$

MFIE:

$$\begin{aligned} \hat{n} \times \vec{H}_{inc} &= +\frac{1}{2}\vec{J}(t) - \hat{n} \times \left[\boldsymbol{T_1} \vec{J}(t) + \eta_1^{-1} \boldsymbol{L_1} \vec{M}(t)\right]; \\ \vec{0} &= -\frac{1}{2}\vec{J}(t) - \hat{n} \times \left[\boldsymbol{T_2} \vec{J}(t) + \eta_2^{-1} \boldsymbol{L_2} \vec{M}(t)\right]. \end{aligned} \tag{4.32}$$

The convergence of the surface currents for the three integral formulations is

tracked in Figures 4.10 and 4.11. From the results of the phase-extracted solver, it is seen that the electric current calculated with the MFIE has better accuracy than the one calculated with the other two formulations, whereas the convergence of the magnetic current is similar among the three formulations. The improved accuracy in the electric current of the MFIE can be attributed to the fact that this solver does not contain the hypersingular kernel (i.e., the kernel for calculating electric field from electric current) which appears in the EFIE and PMCHWT. (For perfect conductors, it has been observed in [77] that the MFIE is superior to EFIE in terms of convergence.) The above observations, however, are less apparent in the results of the regular LCN solver.

4.4 Conclusion

A high-order accurate solver has been investigated for wave propagation applications in this chapter. Mainly, a modified Nyström solver derived with a phase extraction technique has been described for near-ground radiowave propagation prediction in the presence of irregular terrain profiles. The convergence properties of this new solver—which is called the phase-extracted LCN—have been examined and compared to those of the regular LCN; it is seen that the solver not only retains the high-order convergence that is characteristic of the regular LCN but also exhibits significantly smaller start-up error. The incorporation of the new solver into the fast multipole method also has been discussed. By applying this new method, in combination with an adaptive surface segmentation routine for the surface region near the source, as few as one to two average unknowns per wavelength is adequate in obtaining accurate solutions to propagation over gently-undulating, random terrain profiles; therefore, the solver can provide additional reduction in number of solution

unknowns and speed-up in computational efficiency as compared to the regular LCN. Although the phase extraction in the manner as presented stipulates the solution to follow a simple phase-dependence, the solver is seen to outperform the regular LCN for highly irregular terrain profiles as well.

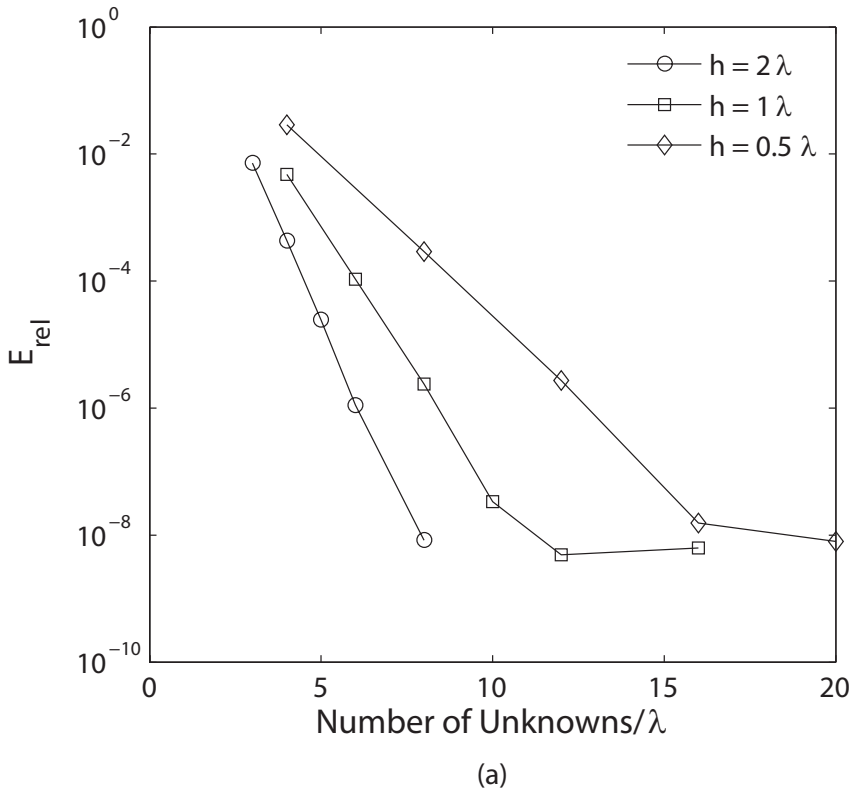

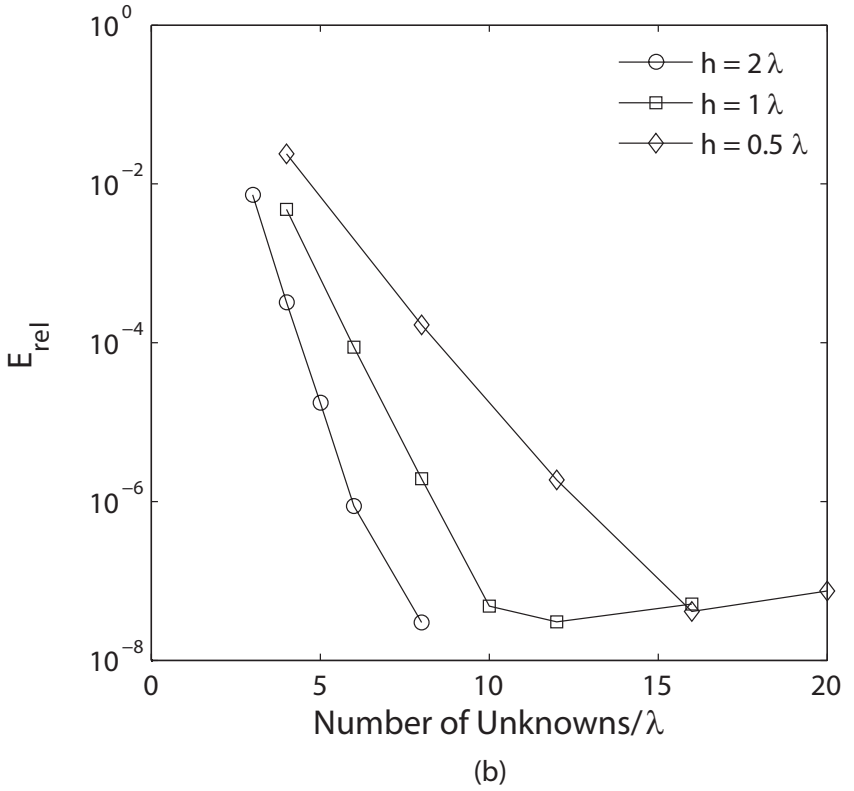

Figure 4.3: Error convergence (N_q-refinement) for (a) electric current and (b) magnetic current.

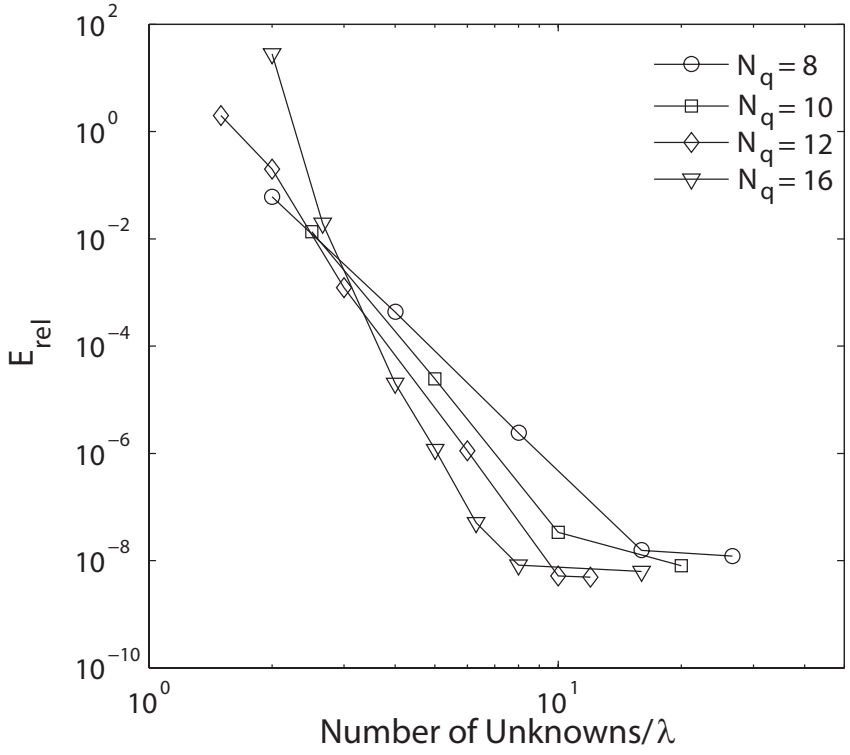

(a)

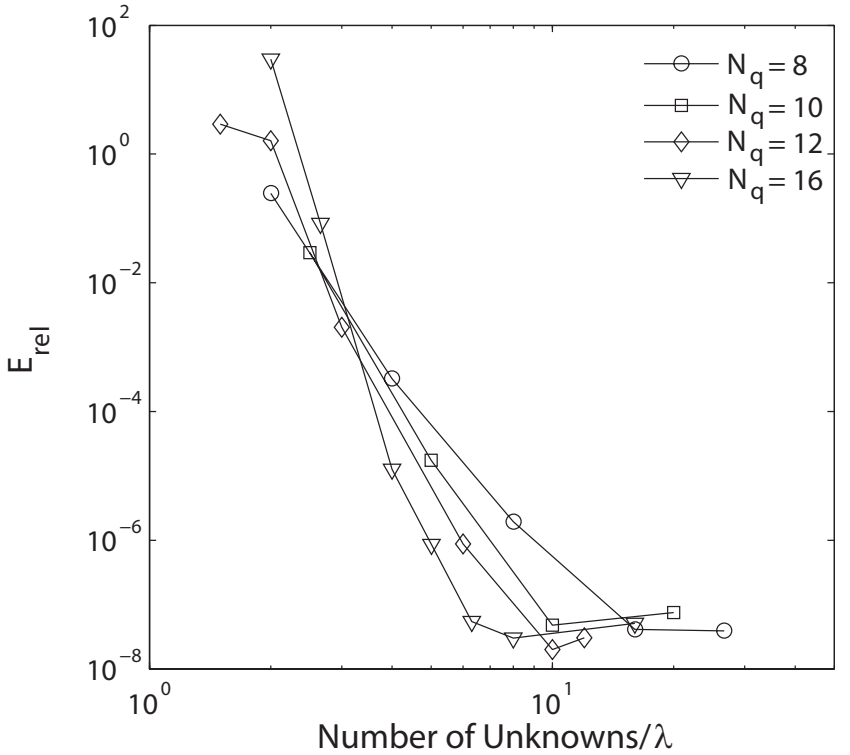

(b)

Figure 4.4: Error convergence (h-refinement) for (a) electric current and (b) magnetic current.

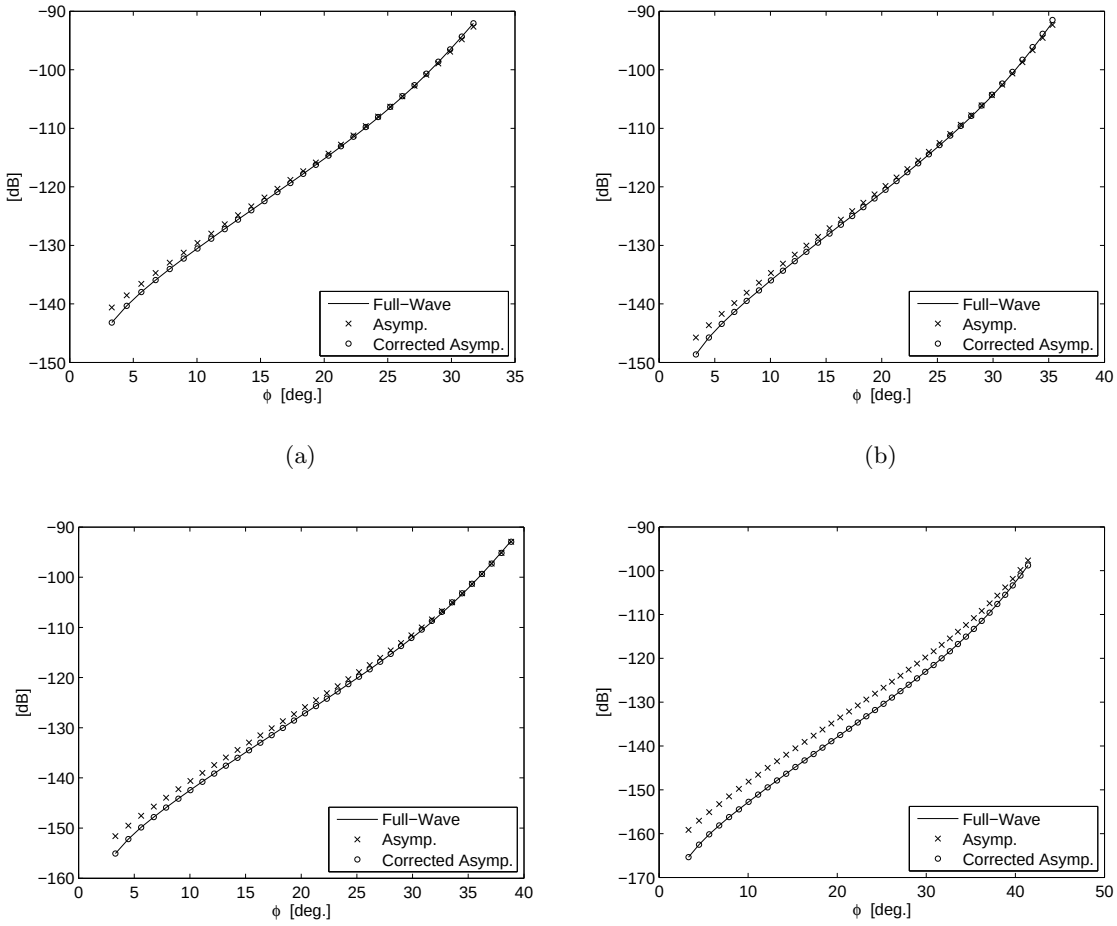

Figure 4.5: Comparison of diffracted field obtained using numerical, heuristic-asymptotic, and corrected heuristic-asymptotic approaches—(a) $\phi' = 13.26°$; (b) $\phi' = 9.78°$; (c) $\phi' = 6.10°$; (d) $\phi' = 2.18°$.

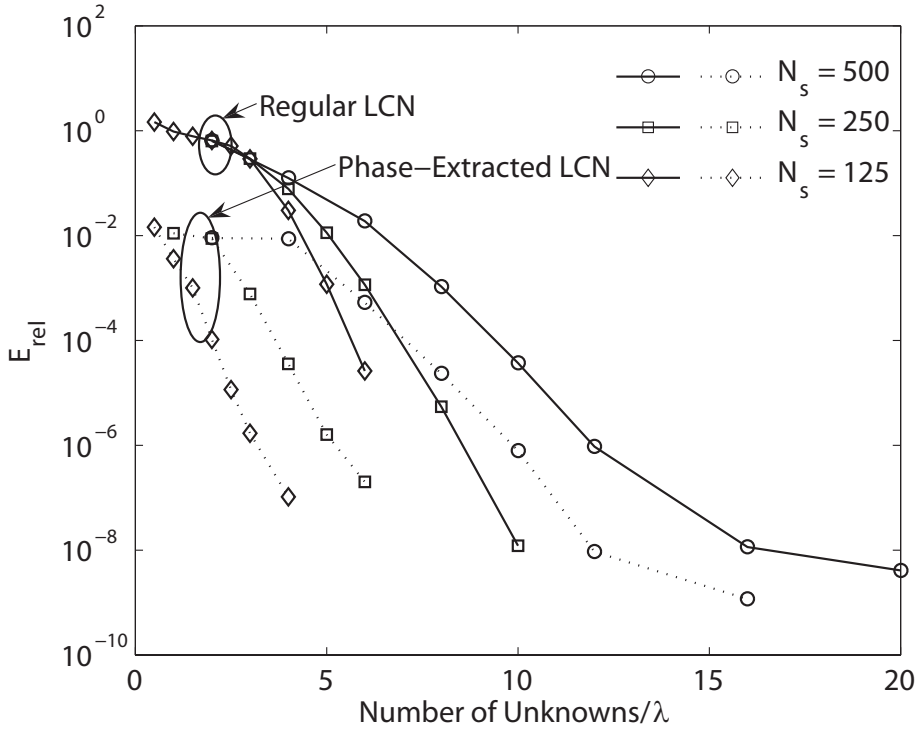

(a)

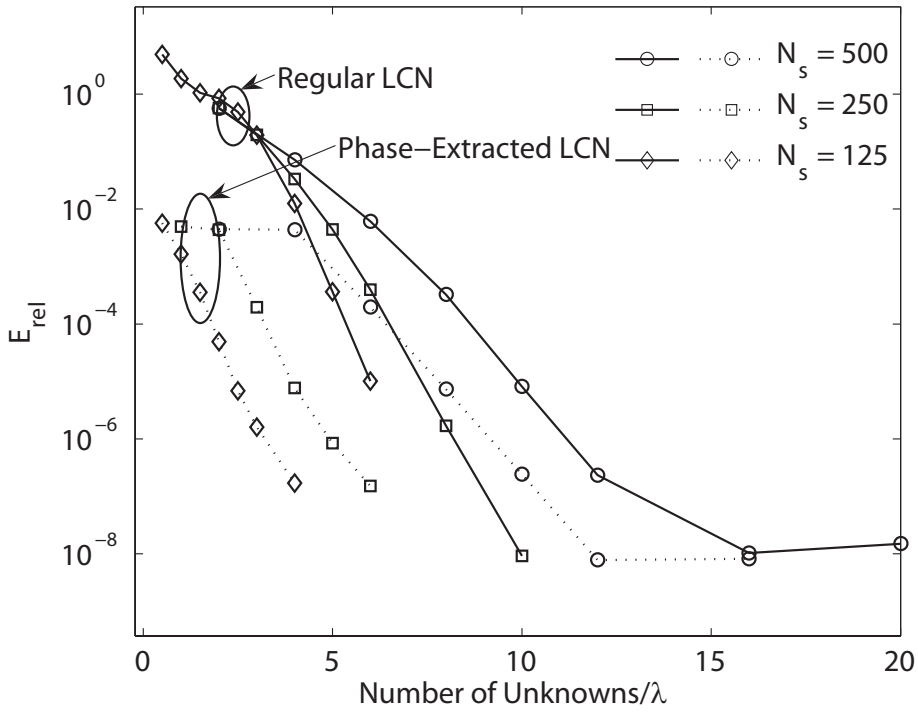

(b)

Figure 4.6: Solution relative error for (a) electric and (b) magnetic current with varying Nyström order N_q and constant discretization scale h at 1λ ($N_s = 500$), 2λ ($N_s = 250$), and 4λ ($N_s = 125$); $L = 500\lambda$; $M_q = N_q$.

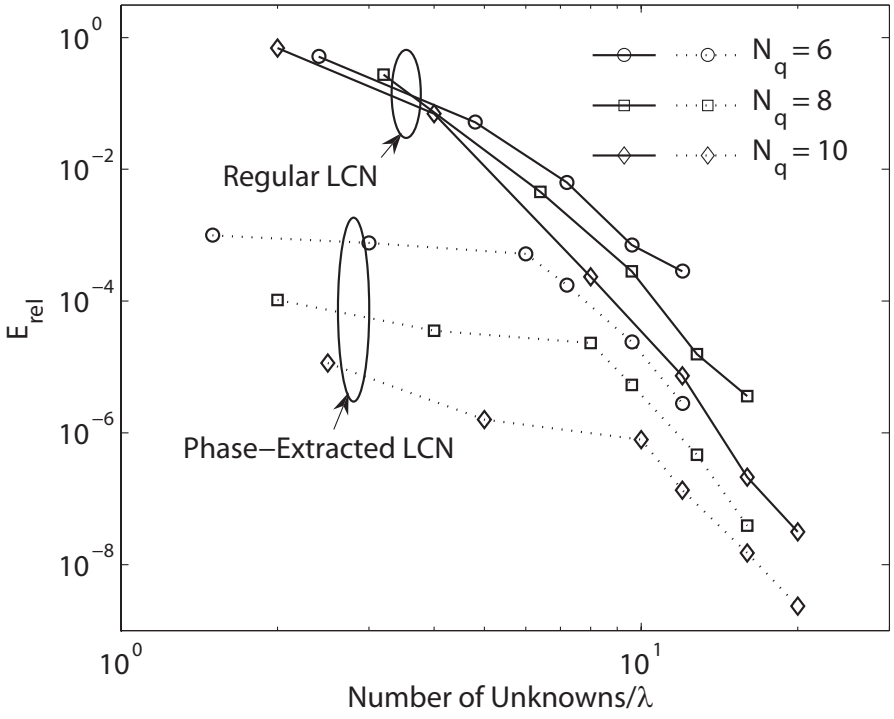

(a)

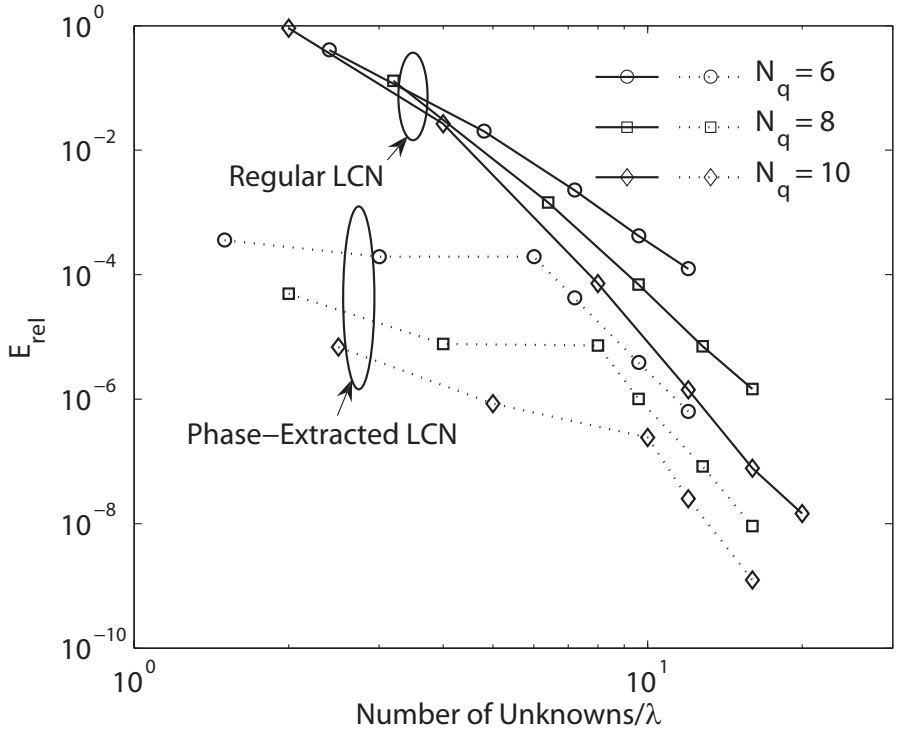

(b)

Figure 4.7: Solution relative error for (a) electric and (b) magnetic current with varying discretization scale h and constant Nyström order N_q at 6, 8, and 10; $L = 500\lambda$; $M_q = N_q$.

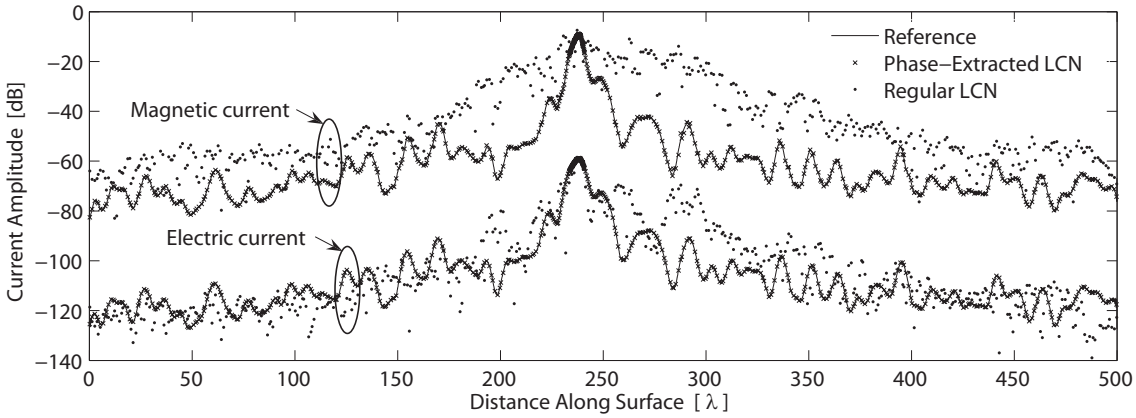

Figure 4.8: Comparison of solutions from regular and phase-extracted LCN methods with an average of one unknown per wavelength; $N_s = 125$ and $M_q = N_q = 4$; surface is Gaussian with rms height $= 1\lambda$ and correlation length $= 5\lambda$; $L = 500\lambda$; $\epsilon_2 = (1.5 + 0.2i)\epsilon_o$; frequency = 300 MHz.

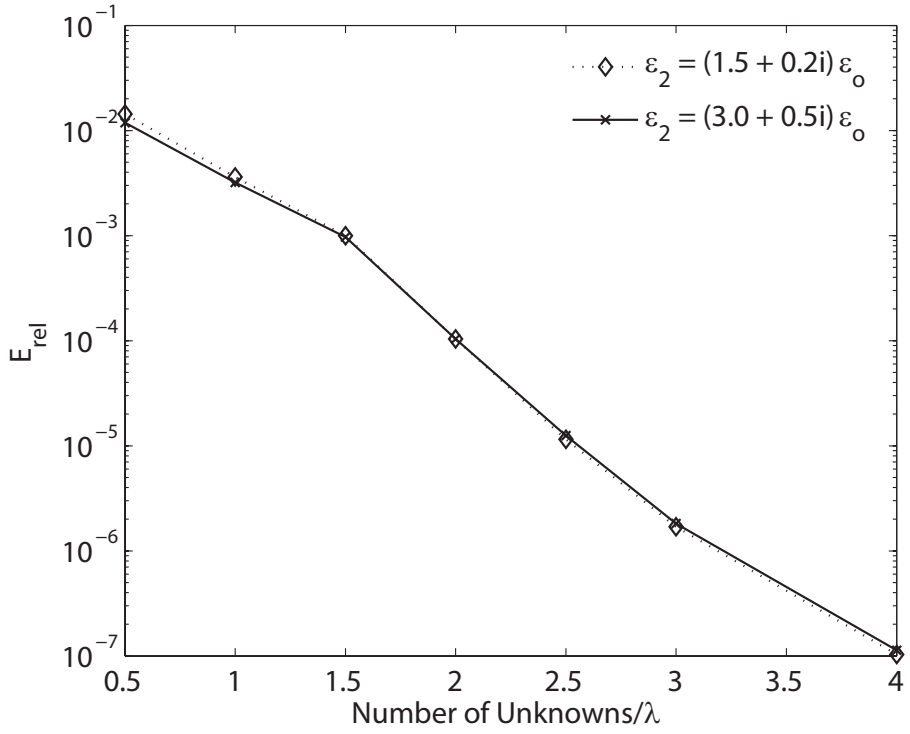

(a)

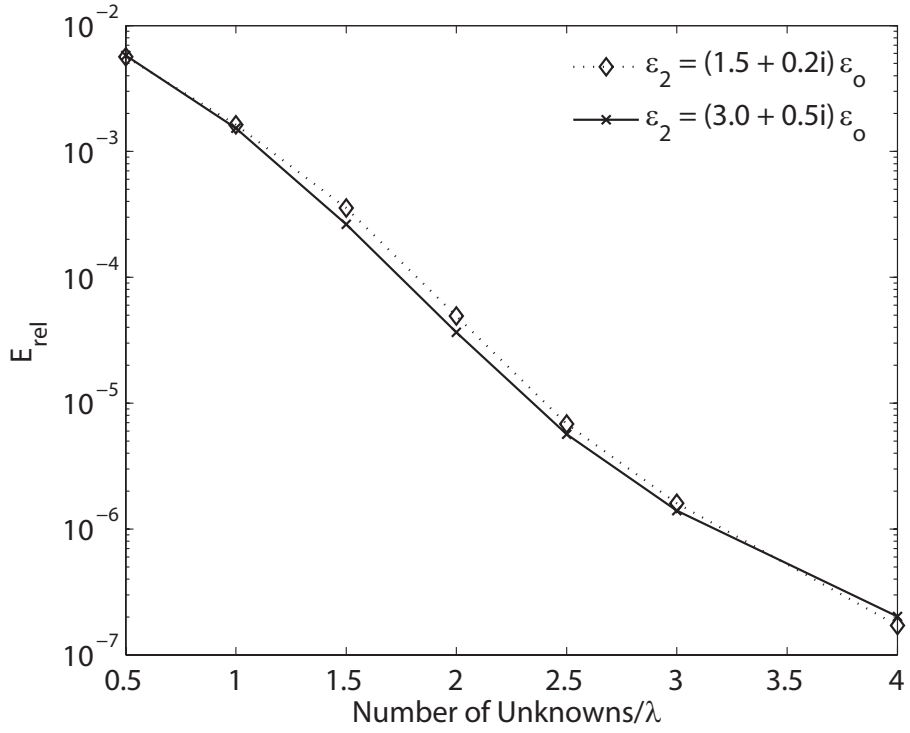

(b)

Figure 4.9: Comparison of solutions—(a) electric current and (b) magnetic current—from phase-extracted LCN method for $\epsilon_2 = (1.5 + 0.2i)\epsilon_o$ and $\epsilon_2 = (3.0 + 0.5i)\epsilon_o$; $L = 500\lambda$; $N_s = 125$; $M_q = N_q$.

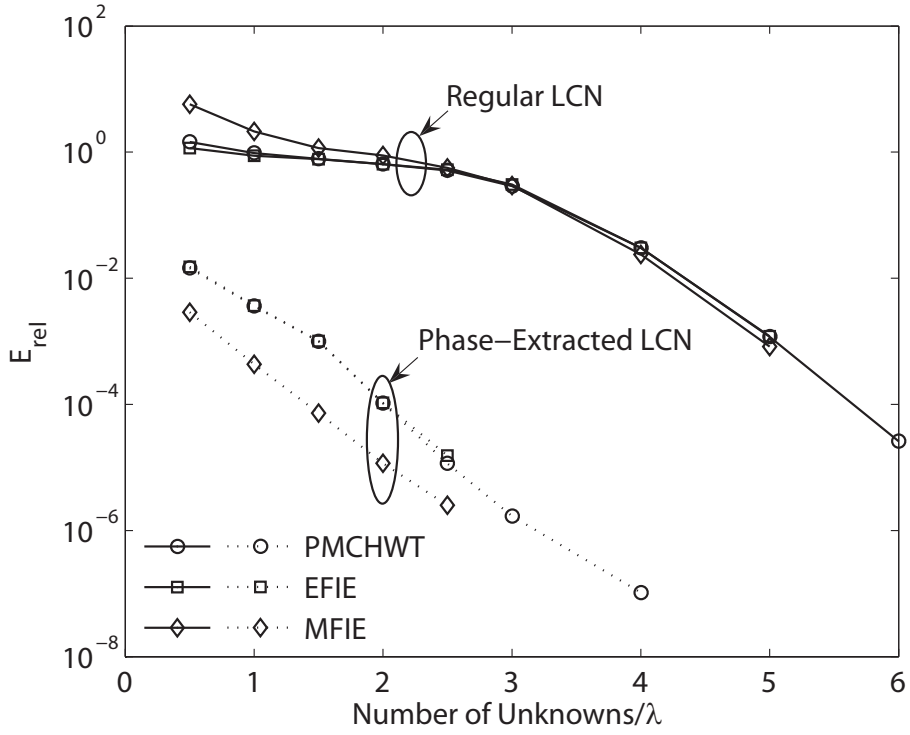

(a)

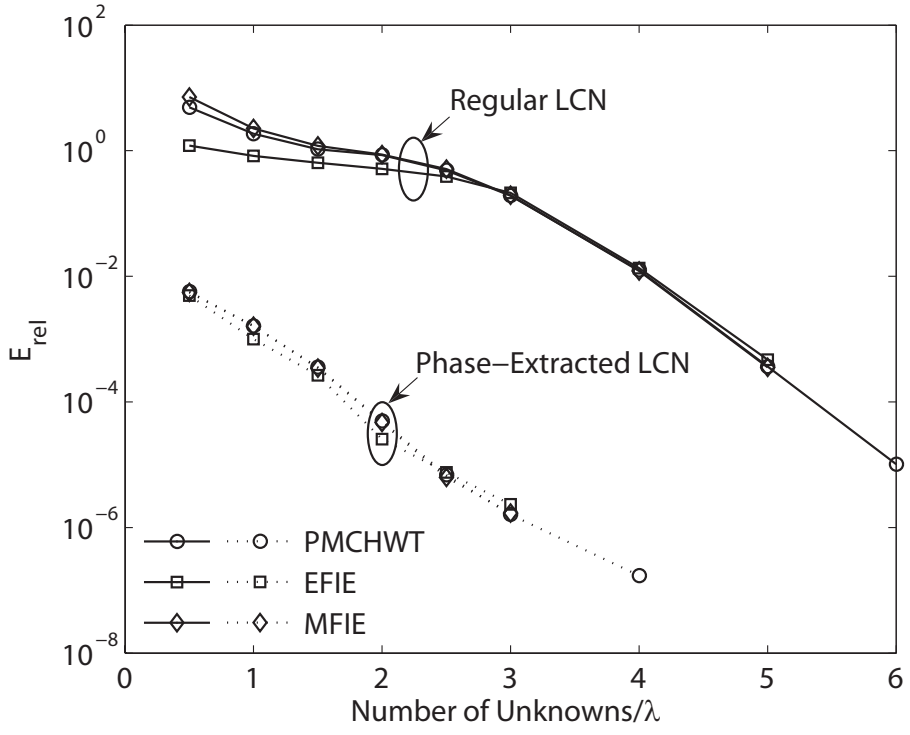

(b)

Figure 4.10: Comparison of solutions—(a) electric current and (b) magnetic current—from phase-extracted LCN method based on PMCHWT, EFIE, and MFIE; $\epsilon_2 = (1.5 + 0.2i)\epsilon_o$; $L = 500\lambda$; $N_s = 125$; $M_q = N_q$.

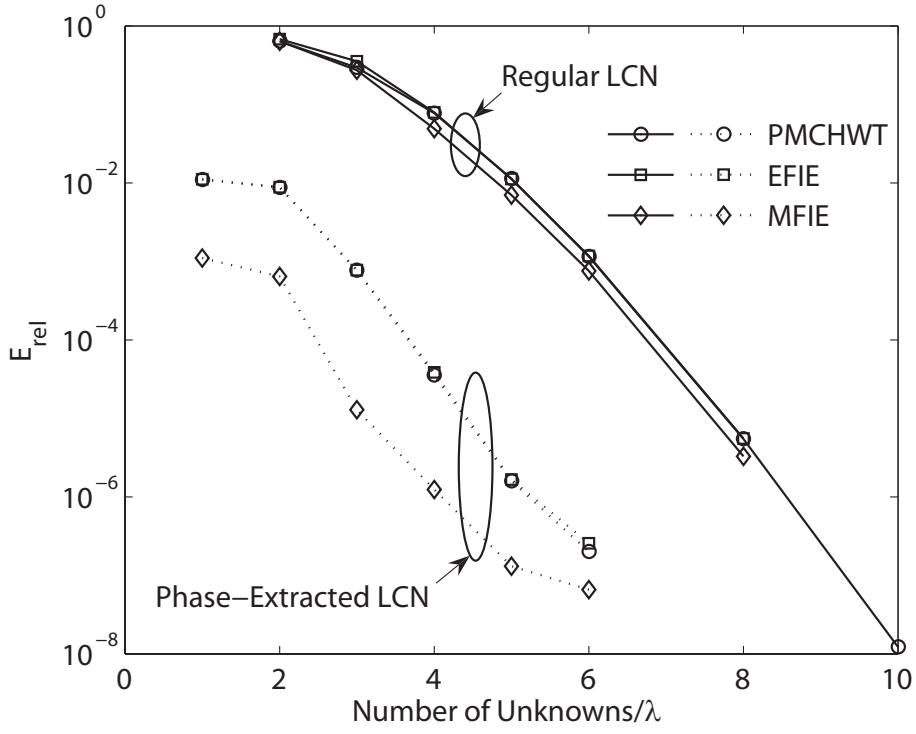

(a)

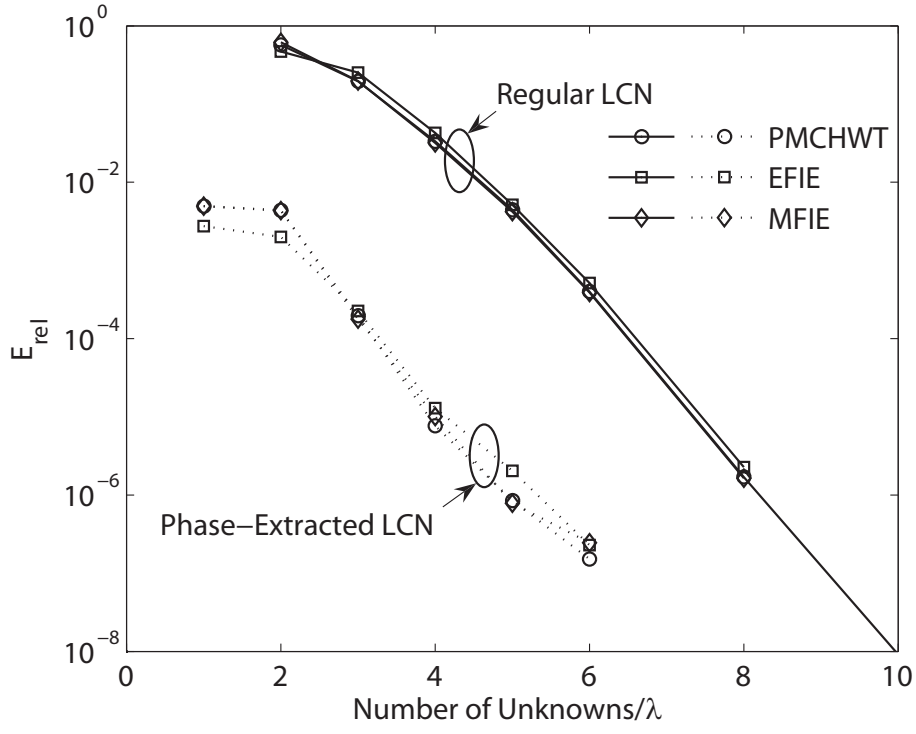

(b)

Figure 4.11: Comparison of solutions—(a) electric current and (b) magnetic current—from phase-extracted LCN method based on PMCHWT, EFIE, and MFIE; $\epsilon_2 = (1.5 + 0.2i)\epsilon_o$; $L = 500\lambda$; $N_s = 250$; $M_q = N_q$.

CHAPTER V

An Approximate Numerical Model for Simulation of Long-Distance Near-Ground Radiowave Propagation over Random Terrain Profiles

5.1 Introduction

For analyzing the electromagnetic effects of a randomly-rough terrain, an assortment of analytical models has been proposed in the remote sensing community for the computation of radar scattering response. These methods include various perturbation methods [78–81] and the Kirchhoff approximation [82]; each of these methods has its own range of validity determined by the statistics of the terrain surface; unfortunately, these methods have been found to be inaccurate for grazing-angle scattering scenarios. Furthermore, as these approaches have been developed under the assumption of plane wave interactions, there remains the unsolved issue of how they should be properly utilized or modified for near-ground propagation problems in which the dominant mode of interaction is surface waves.

As mentioned in Chapter IV, in view of the limitations of analytical deterministic methods, numerical algorithms have been developed for simulating radiowave propagation over an irregular terrain. For random rough surfaces, the quasi-planar structure of the surface can be further exploited to expedite the solution process and has led to the introduction of the steepest descent FMM (SDFMM) [83]. In the cur-

rent work, the near-grazing propagation condition is taken advantage of in obtaining a fast and efficient numerical routine through the replacement of the intermediate terrain section between the transmitter and observation point with a planar section. A domain decomposition of the resultant profile enables the fast Fourier transform (FFT) to be used to carry out the matrix-vector products for the planar section, which has a block-Toeplitz MoM representation. In what follows, first the basic steps of the algorithm are described, then the validity of the planar approximation and domain decomposition procedure is examined through Monte Carlo simulations.

5.2 Algorithm Development

The initial set up of the algorithm is based on the regular LCN as expressed by (4.1)–(4.10). For near-ground propagation, it is conjectured here that the coherent and incoherent signal powers at the receiver are primarily determined by the statistics of the random surface surrounding the transmitter and receiver; therefore, a simplified—though approximate—model is obtained by replacing the terrain surface far from the transmitter and receiver with a planar section while keeping the rough regions in the vicinity of the transmitter and receiver unchanged (Figure 5.1). This is a reasonable assumption since the terrain surface in the far field basically interacts with the transmitter and receiver through grazing-incident fields; therefore, this portion of the surface appears to be electrically flat to these fields. The development of this simplified model is as follows. The original terrain surface is decomposed into three separate sections as illustrated in Figure 5.1; the planar section has an effective height as defined by

$$h_{eff} = \left\langle \frac{s\left(x\right) + \left|s\left(x\right)\right|}{2} \right\rangle, \tag{5.1}$$

where the angle brackets denote the averaging operation. Subsequently, the boundary

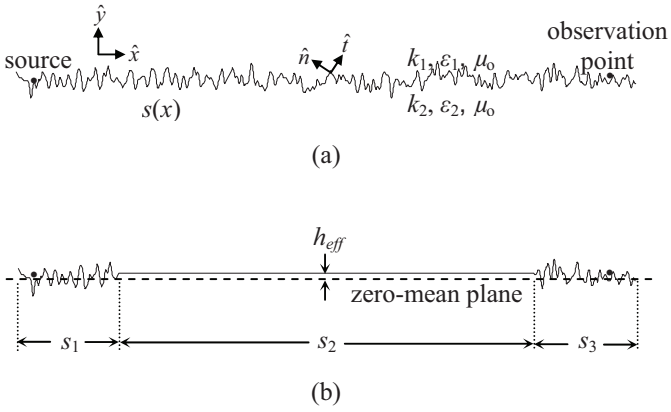

Figure 5.1: (a) Original zero-mean random profile; (b) Three-sub-domain simplified profile.

integral equation solver aforementioned is applied over the entire simplified profile. In accordance to the Nyström method framework, the resulting matrix equation relating the convolution of the kernels with the current unknowns to the tangential excitation field quantities is of the form

$$\begin{bmatrix} \boldsymbol{K_{E,J}} & \boldsymbol{K_{E,M}} \\ \boldsymbol{K_{H,J}} & \boldsymbol{K_{H,M}} \end{bmatrix} \begin{bmatrix} \tilde{J} \\ \tilde{M} \end{bmatrix} = \begin{bmatrix} E_{tan}^{inc} \\ H_{tan}^{inc} \end{bmatrix}. \tag{5.2}$$

In (5.2), the kernel evaluations at the quadrature points are represented by the sub-matrices $\boldsymbol{K_{u,v}}$ $(u = E, H; v = J, M)$, each of dimensions $N_s N_q \times N_s N_q$; and the quadrature weights have been embedded within the current unknowns as indicated by the tilde notation. The interactions of the flat section (s_2) with itself are captured within the central portion of each $\boldsymbol{K_{u,v}}$ and can be shown to be a block-Toeplitz matrix $\boldsymbol{T_{u,v}}$ of dimensions $N_f N_q \times N_f N_q$, where N_f is the number of segments used to discretize the flat section. Note that each sub-block ($N_q \times N_q$) of $\boldsymbol{T_{u,v}}$ does not in general have a Toeplitz structure. As the majority of the original profile has been replaced with a flat section, the amount of memory needed to store the matrices $\boldsymbol{K_{u,v}}$ has been significantly reduced since only the first block column and row of $\boldsymbol{T_{u,v}}$ need to be tabulated. The computational complexity in solving the matrix system (5.2)

can also be simplified by using a recursive forward marching scheme described as follows:

1. The current vectors $\tilde{J} = [\tilde{J}_1, \tilde{J}_2, \tilde{J}_3]$ and $\tilde{M} = [\tilde{M}_1, \tilde{M}_2, \tilde{M}_3]$ are initialized to zero. (The subscript index identifies the surface section on which the current is located.)
2. Each iteration then consists of the following steps:

   For $i = 1$ to 3

   (a) If $i \neq 2$, calculate the currents $\tilde{J}_i$ and $\tilde{M}_i$ simultaneously over the rough section near either the transmitter or observation point using (5.2) by enforcing boundary conditions (4.1) for $\vec{r} \in s_i$; since the sub-matrices touched by this operation are small, a direct solver is used.

   (b) If $i = 2$, calculate the currents $\tilde{J}_2$ and $\tilde{M}_2$ over the flat section using (5.2) by enforcing (4.1) for $\vec{r} \in s_2$. Note that the two integral equations in (4.1) are decoupled (i.e., $\boldsymbol{T_{E,M}} = \boldsymbol{T_{H,J}} = 0$); therefore, $\tilde{J}_2$ and $\tilde{M}_2$ can be solved separately. This step could involve the inversion of $\boldsymbol{T_{E,J}}$ and $\boldsymbol{T_{H,M}}$; however, an iterative solver is used here with the block-Toeplitz matrix-vector products provided by an efficient FFT routine constructed in [84].

   (c) Update $\tilde{J}$ and $\tilde{M}$.

3. Re-iterate via step 2.

The recursive routine above continues until the relative norm of the error vector between successive iterations falls below a pre-determined tolerance level (for exam-

ple, 10^{-5} is the value usually employed for the simulation scenarios presented in the next section).

5.3 Numerical Validation and Results

Monte Carlo simulations of propagation over random terrain surfaces are run to validate the accuracy of the proposed three-sub-domain model. Figures 5.2 and 5.3 show the comparison—for both polarizations—between solutions of the original rough surface profile (Figure 5.1(a)) and the simplified profile (Figure 5.1(b)) in terms of the coherent and incoherent received powers (i.e., power mean and variance); note that good agreement (within 1 dB) is observed between the two sets of results. In these calculations, the source is either a magnetic line source (vertical polarization) or an electric line source (horizontal polarization) fixed at a distance 560λ away from the observation point; both the source and observation point are at a height of 3.6λ above the terrain zero-mean plane. The middle 400λ section of the rough terrain between the source and observation point is replaced with a flat section in the simplified model. Only LOS paths are examined in the figure by generating realizations of Gaussian random surfaces such that the direct wave is unobstructed; albeit not shown here, similar good agreement is observed for the different field components of NLOS paths as well. The locations of the junction between the rough and flat sections are varied on the order of a wavelength to dampen artificial coherent effects; the transitions also have been smoothed to reduce the occurrence of sharp edge diffractions. In these simulations and those that follow, the operational frequency is at 300 MHz and the dielectric constant of the terrain soil is set to be $\epsilon_2 = (8 + 6i)\epsilon_o$; the Nyström method parameters are $N_q = 6$ and $h = 1\lambda$.

To verify the convergence of the recursive forward marching scheme as applied to

	TE_z			TM_z		
Iteration	E_x	E_y	H_z	H_x	H_y	E_z
1	14.57	3.852E-1	6.087E-1	1.698	6.623E-2	9.473E-2
2	4.721	1.247E-1	1.968E-1	4.452E-1	1.696E-2	2.470E-2
3	1.532	4.039E-2	6.390E-2	1.045E-1	3.954E-3	5.767E-3
4	5.001E-1	1.316E-2	2.087E-2	2.352E-2	8.821E-4	1.284E-3
5	1.642E-1	4.318E-3	6.855E-3	5.053E-3	1.852E-4	2.684E-4

Table 5.1: Maximum percent error in the recursive forward marching solution as referenced to the entire domain solution (simplified profile is used in the calculations).

the simplified model, a comparison is made between the solutions calculated using the entire profile and the domain decomposed profile. The field values at an observation line positioned 3.6λ above the zero-mean are computed, and the maximum percent error for each field component at each iteration is tracked and is shown in Table 5.1. Very fast convergence is seen due to the low level of backward scattering coupling among the sub-domains; in this set of simulations, for example, a maximum error of less than one percent is guaranteed with only four iterations. The algorithm is implemented via Matlab script on a Linux machine with a 2.6 GHz AMD Opteron processor and 6 GB of available RAM; for a rough surface with a surface length of 1100λ, the amount of memory needed is 1 GB (as opposed to 7.7 GB for conventional MoM); the setup time (for matrix filling) is 15 minutes and each iteration takes about 1 minute.

After considering its accuracy and convergence characteristics, the solver is applied to study near-ground propagation for rough terrain environments with different surface statistics. These simulation results are featured in Figures 5.4 and 5.5. As plotted in Figure 5.4 (where a LOS path is assumed), the path-loss increases with terrain rms height as expected. However, the signal strength also has considerable dependence on the surface correlation length for fixed rms height as shown in Figure 5.5: the path-loss is seen to increase as the correlation length is reduced. This

behavior can be understood by noticing that as the average surface peak-to-peak distance decreases, more of the ground reflected wave component is successfully guided forward along the surface toward the observation location; therefore, a more drastic coherent cancellation occurs between the direct and reflected waves. It is interesting to note that the same type of correlation length dependence appears for NLOS propagation as well—as evident in Figure 5.6 (where it is also seen that the ratio of the incoherent to coherent components of the wave has risen significantly as compared to the LOS case). The NLOS simulations assume that the transmitting and receiving points are always located at the zero-mean plane and the surface realizations are generated such that these points are always above the surface profile. For NLOS situations, the wave guided on top of the terrain peaks is similar to a lateral wave [24] since the transmitting and receiving points can be interpreted as being submerged within a ground with some mean effective height. Even if the actual terrain *rms* height remains constant, as the terrain correlation length decreases, this *effective* surface height is raised; therefore, the lateral wave experiences more attenuation as it propagates through the vertical distance between the transmitting and receiving points and the *effective* surface top.

5.4 Conclusion

Exploiting the near-grazing propagation condition, a new efficient numerical algorithm for predicting near-ground radiowave propagation over random rough terrain has been developed. Conjecturing that the signal statistics at the receiver are primarily determined by the statistics of the terrain surface surrounding the transmitter and receiver, a physically flat section is used to replace the intermediate rough section located between the transmitter and receiver, therefore reducing the original

problem into a simplified and more tractable one for which the solution is subsequently obtained using a recursive forward marching domain decomposition scheme. The accuracy of the simplified model has been demonstrated through Monte Carlo simulations and the convergence of the forward marching scheme also has been examined. Though the development is contingent upon the assumption of 2D surface and field variations, the model as presented herein is valuable nevertheless for gaining insights into some of the important physical propagation mechanisms relevant to near-ground signal-strength prediction scenarios.

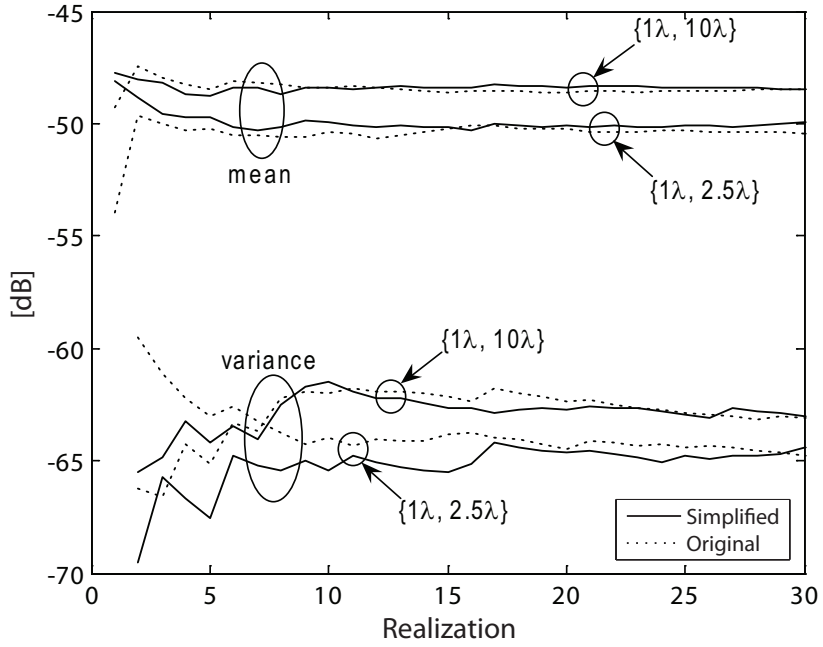

Figure 5.2: Received power as computed using simplified and original models for vertical polarization. The random rough surface parameters are indicated as $\{\sigma, c_l\}$.

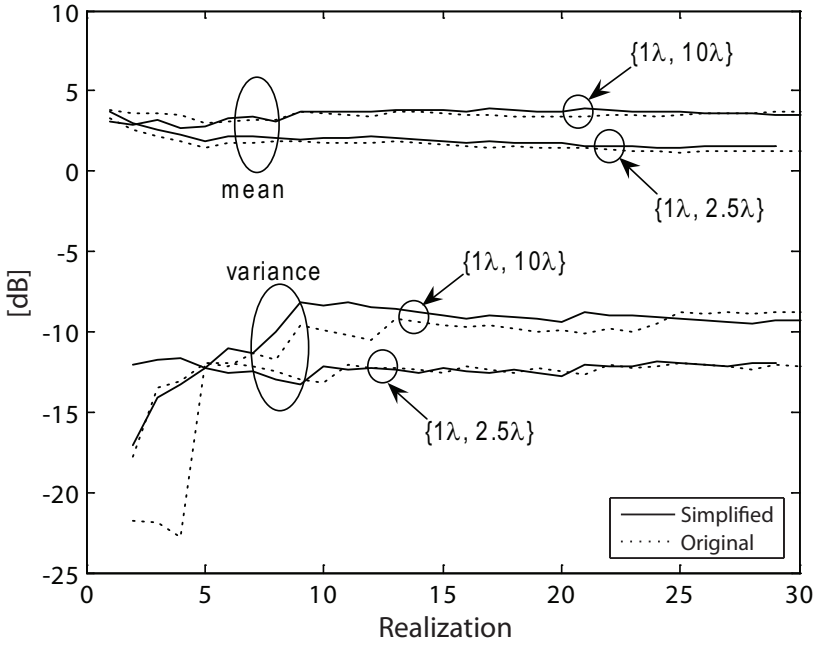

Figure 5.3: Received power as computed using simplified and original models for horizontal polarization. The random rough surface parameters are indicated as $\{\sigma, c_l\}$.

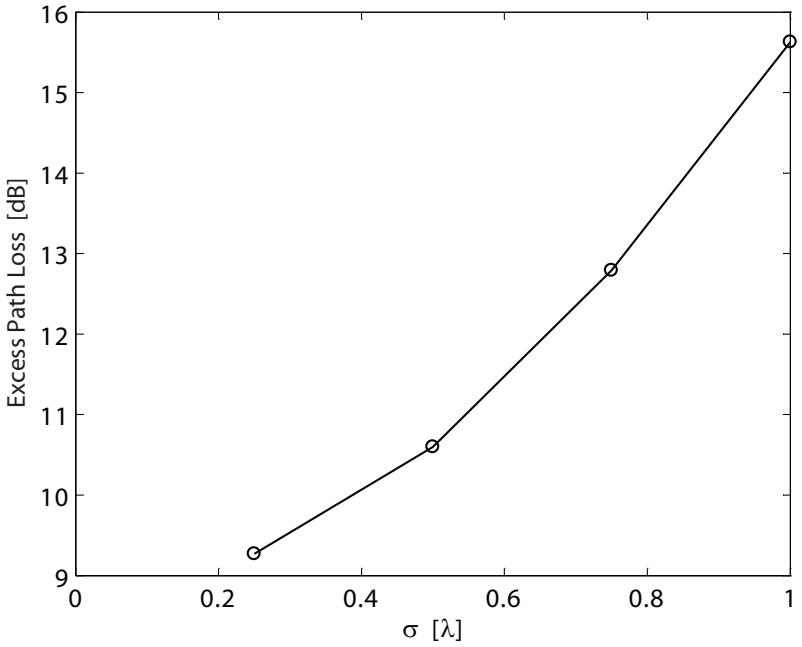

Figure 5.4: Excess path loss (over free space loss) for vertically-polarized LOS paths as function of terrain rms height.

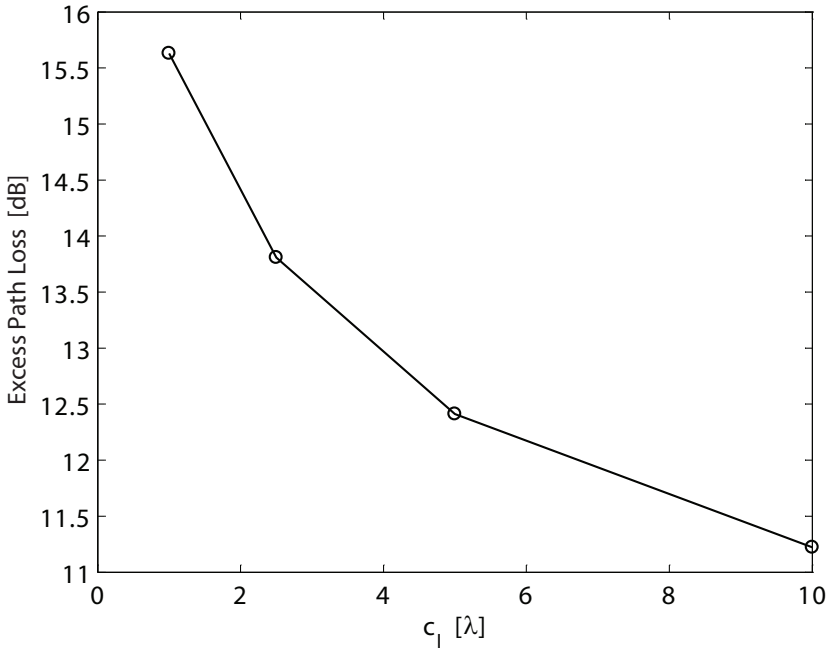

Figure 5.5: Excess path loss (over free space loss) for vertically-polarized LOS paths as function of terrain correlation length.

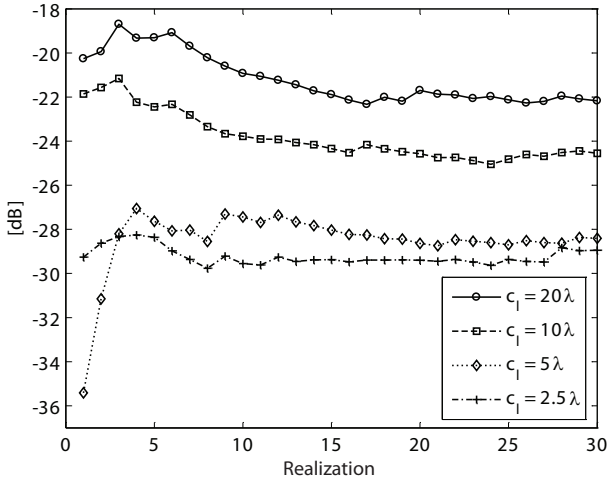

(a)

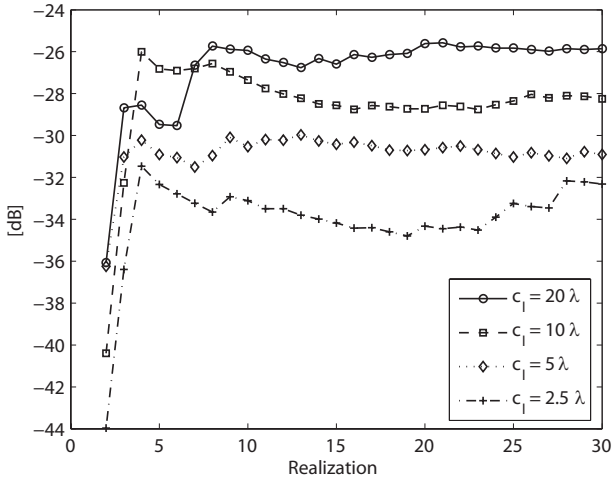

(b)

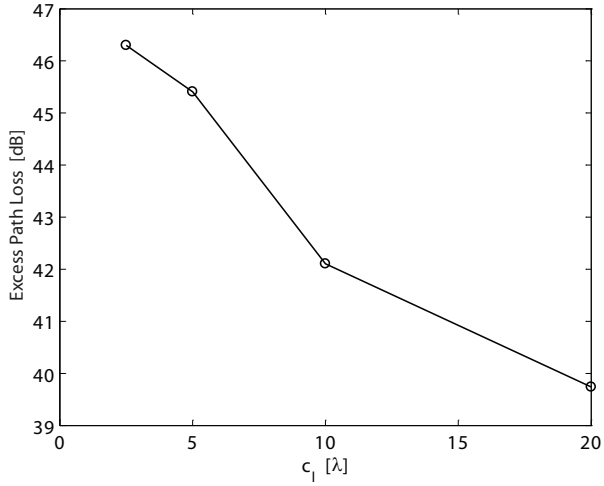

(c)

Figure 5.6: Vertically-polarized NLOS propagation response: (a) mean of field; (b) variance of field; (c) path-loss. Distance between source and observation point is 600λ and $\sigma = 1\lambda$.

CHAPTER VI

On the Effective Low-Grazing Reflection Coefficient of Random Terrain Roughness

6.1 Introduction

For propagation over a rough terrain, the statistical properties of the surface (height profile probability density function, surface autocorrelation function or roughness spectrum) have a direct impact on the statistics of the propagating signal. In the near field, the LOS space wave (when it is unobstructed) from the transmitting antenna provides the primary contribution to the total received signal, as coherent reflection is reduced by the random scattering effects. However, over a long distance, as the propagation path approaches the grazing condition, in accordance with the Rayleigh criterion, the surface appears electrically smooth again and coherent cancellation between the direct and ground scattered signal is re-established. These qualitative observations are consistent with the simulation results of the preceding chapters; specifically, as it has been shown in Chapter V, the far field propagation loss increases with corrugation *rms* height as expected but also shows considerable dependence on the surface correlation length (Figure 5.5); furthermore, at grazing propagation, it is no longer proper to calculate coherent signal statistics by a *complete* replacement of the rough surface with a smooth surface at the original surface's physical mean height, for now the *effective* height is a function of both sur-

face rms height and correlation length. Although the numerical models presented in Chapters IV and V have proven to be efficient simulators in dealing with the near-ground channel, it is also convenient to quantitatively capture the aforementioned observations—which have not been sufficiently addressed and explained in existing literature—in analytical formulations.

Owing to the random multi-scattering processes inherent in an undulating terrain environment, a radio signal has both coherent and incoherent components, each contributing to the total channel transfer characteristics. In considering the effects of random roughness, an equivalent coherent reflection coefficient can be produced—according to physical optics—by supplementing the Fresnel reflection coefficient for a flat surface with a phase correction factor ξ:

$$R^{eff} = R^i \xi = R^i \left\langle e^{-2ik^i_{0z} f(x)} \right\rangle . \tag{6.1}$$

The ensemble average can be calculated based on the probability distribution function (PDF) of the surface profile $z = f(x)$; for instance, assuming a normally distributed surface profile, the correction factor reduces to the Ament approximation, $\xi_A = e^{-\frac{1}{2}(2k_o\sigma\cos\theta)^2}$, which has been incorporated into ray-tracing routines by other workers for predicting reflection loss due to surface roughness. Note that Ament derived his result from an integral equation approach formulated for a PEC surface on which the value of the induced surface current is estimated to be independent of surface elevation [32]; the same result for ξ_A can also be reached using the Kirchhoff, or tangent-plane, approximation [85]. Another commonly used form of the correction factor has been derived by Miller and Brown, who originally considered the reflection effects of an ocean surface modeled as a collection of sinusoidal waves with Gaussian distribution in amplitude and uniform distribution in phase [33, 34]; although the Miller-Brown approximation, $\xi_{MB} = \xi_A I_o\left(\frac{1}{2}\left(2k_o\sigma\cos\theta\right)^2\right)$, has been shown to be in

better agreement with experimental results [86] (as compared to the Ament approximation), the theoretical validity of applying such a PDF specific to ocean surfaces for terrain propagation problems has yet to be investigated.

While being simple to implement, both ξ_A and ξ_{MB} as given above are not valid for grazing angle propagation as (6.1) (and the Kirchhoff approximation itself) does not include terrain self-shadowing effects. The fraction of the surface that is illuminated by the incident rays can be estimated and the surface PDF can be modified to include a shadowing factor before insertion into (6.1) [87]; the subsequent expression for the effective reflection coefficient, however, maybe in a complicated integral form that is dependent upon the choice of an "optimal" shadowing PDF [88]. Alternatively, instead of defining the effective reflection coefficient directly, an equivalent impedance for the rough surface can be calculated based on the surface statistical properties [89]. The shadowing PDF and the equivalent impedance approaches have been shown to provide improvement over the traditional Ament and Miller-Brown formulations; however, these approaches still do not consider the implications of surface wave effects and have not been tested for near-ground propagation scenarios.

In this chapter, in order to arrive at an analytical representation for the effects of terrain roughness on the near-ground channel, a new closed-form expression for the effective reflection coefficient is presented. The basis of the derivation is founded on the perturbation approach applied to a volumetric integral equation as introduced by Sarabandi and Chiu [35] for remote sensing applications involving modeling the general scattering coefficients of rough surfaces with inhomogeneous dielectric profiles. Here, expressions for the coherent effective reflection coefficient are derived for the 2D problem; the accuracy of these expressions is validated using the numerical simulator outlined in Chapter IV for 2D excitation sources of vertical and horizon-

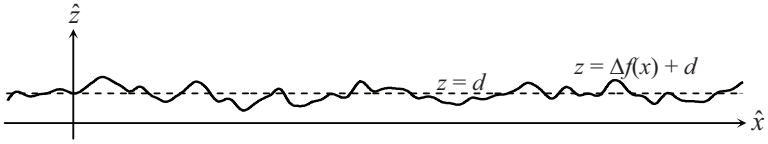

Figure 6.1: Propagation geometry; the rough terrain is characterized by relative dielectric constant ϵ_{r1} and normalized variation profile $f(x)$, which has zero-mean and stationary statistics.

tal polarizations. Extensions to—and simulation results for—3D sources are also provided.

6.2 Theoretical Background

The perturbation approach set forth in [35] is briefly reviewed here; for a detailed discussion of the derivation of this method, the reader is referred to the original work. In formulating the response of the dielectric surface, a volumetric integral equation is first formed, relating the scattered field to the fictitious polarization current induced in the rough layer region ($0 < z < \Delta f(x) + d$); after taking the Fourier transform of the expansion of the integral equation about the surface elevation $z = d$, with the assumption that the polarization current can be written as a perturbation series in terms of the perturbation parameter Δ, an iterative set of relations is generated from which the current can be found to arbitrary order. Essentially, the zeroth-order current gives the induced current of the flat interface geometry, and higher-order terms represent the corrections necessary to account for the presence of surface fluctuations about the mean at $z = d$. Though the validity of the original formulations in [35] has been confirmed for $\Delta \ll \lambda$, it is shown here that, in the context of near-grazing propagation, the reflection coefficient derived herein is even applicable for surface variations (*rms* height) on the order of λ or more; the main reason for such an extended region of validity has its roots in the fact that only the normal component of the wave vector (i.e., $k_z = \frac{2\pi}{\lambda_z}$) "sees" the surface roughness. Also, it should be noted

that in contrast to other existing perturbation methods (e.g., small perturbation method—SPM [78]), the perturbation series of interest here is expanded in terms of the volumetric current instead of the surface current or tangential fields; therefore, this method offers the advantage of being readily modifiable for the analysis of a surface with an inhomogeneous vertical dielectric profile.

6.2.1 Horizontal Polarization—2D

With an excitation of the form $\vec{E}^i = e^{-ik_{0z}^i z + ik_x^i x}\hat{y}$, following the procedure delineated in [35], the Fourier transform of the polarization current within the rough layer, in the 2D case, can be shown to reduce to the following forms:

$$\tilde{\vec{J}}_{total}\left(k_x, z\right) = \sum_{N=0}^{\infty} \Delta^N \tilde{\vec{J}}_N\left(k_x, z\right), \tag{6.2}$$

where each order of the current is given by

$$\tilde{\vec{J}}_0\left(k_x, z\right) = 2\pi\delta\left(k_x - k_x^i\right) J_{h,y} e^{-ik_{1z}^i z}\hat{y}; \tag{6.3}$$

$$\tilde{\vec{J}}_N\left(k_x, z\right) = \frac{ik_o^2\left(\varepsilon_{r1} - 1\right)e^{-ik_{1z}z}}{\left(k_{0z} + k_{1z}\right)e^{-ik_{1z}d}} \left\{\tilde{\vec{V}}_N\left(k_x, z\right)\cdot\hat{y}\right\}\hat{y}; \tag{6.4}$$

and

$$J_{h,y} = -i\omega\epsilon_o\left(\varepsilon_{r1} - 1\right)\frac{2k_{0z}^i e^{-ik_{0z}^i d}}{\left(k_{0z}^i + k_{1z}^i\right)e^{-ik_{1z}^i d}}; \tag{6.5}$$

$$\begin{aligned}\tilde{\vec{V}}_N\left(k_x, z\right) &= \sum_{n=0}^{N-1}\sum_{m=0}^{N-n-1} \frac{\binom{N-n-1}{m}\left(ik_z\right)^m}{(N-n)!} \\ &\quad \cdot\frac{\partial^{N-n-m-1}}{\partial z^{N-n-m-1}}\tilde{\vec{J}}_n\left(k_x, d\right) *^{N-n}_{\otimes} F\left(k_x\right)\left(\frac{1}{2\pi}\right)^{N-n};\end{aligned} \tag{6.6}$$

and $*^{N-n}_{\otimes}$, as defined in [35], is taken as the convolution of the function with itself $N-n$ times.

The field response can then be calculated from the polarization current using the Fourier transforms of the flat-interface, half-space dyadic Green's function, $\tilde{\tilde{G}}\left(k_x, z, z'\right)$,

and that of the surface profile, $F(k_x)$:

$$\begin{aligned}\vec{E}^s(x,z) &= R_h^i \vec{E}^i + \frac{i\omega\mu_o}{2\pi}\int_{-\infty}^{+\infty}\Bigg\{\sum_{N=0}^{\infty}\Delta^N\int_0^d \approx{G}(k_x,z,z')\cdot\tilde{\vec{J}}_N(k_x,z')\,dz' \\ &\quad + \sum_{N=1}^{\infty}\Delta^N\sum_{n=0}^{N-1}\sum_{m=0}^{N-n-1}\frac{\binom{N-n-1}{m}}{(N-n)!}\frac{\partial^m}{\partial z'^m}\approx{G}(k_x,z,d) \\ &\quad \cdot\left\{\frac{\partial^{N-n-m-1}}{\partial z'^{N-n-m-1}}\tilde{\vec{J}}_N(k_x,d) * \overset{N-n}{\otimes} F(k_x)\right\}\left(\frac{1}{2\pi}\right)^{N-n}\Bigg\}e^{ik_x x}dk_x,\end{aligned} \tag{6.7}$$

in which R_h^i is the horizontal polarization reflection coefficient for a flat interface located at $z = 0$. Taking the ensemble average of (6.7), after much manipulation and making use of the identities

$$\langle F(k_x) * F(k_x)\rangle = 4\pi^2\delta(k_x); \tag{6.8}$$

$$\left\langle F(k_x-k_x')\,F\left(k_x'-k_x^i\right)\right\rangle = 2\pi\delta\left(k_x-k_x^i\right)W(k_x-k_x'); \tag{6.9}$$

where $W(\cdot)$ is the power spectral density of the surface $f(x)$, the total coherent scattered field to the second order ($N = 2$) reduces to

$$\vec{E}^s = R_h^{i,eff}e^{ik_{0z}^i z + ik_x^i x}\hat{y}, \tag{6.10}$$

with

$$\begin{aligned}R_h^{i,eff} &= \Bigg\{R_h^i + \frac{\Delta^2}{2}k_o^2(\varepsilon_{r1}-1)(1-{R_h^i}^2) \\ &\quad -\frac{\Delta^2}{2}\left[k_o^2(\varepsilon_{r1}-1)\right]^2(1+R_h^i)\frac{\Omega_y\left(k_\rho^i\right)}{\pi\left(k_{0z}^i+k_{1z}^i\right)}\Bigg\}e^{-i2dk_{0z}^i}.\end{aligned} \tag{6.11}$$

The function $\Omega_y\left(k_\rho^i\right)$ is given by

$$\Omega_y\left(k_\rho^i\right) = \int_{-\infty}^{+\infty}\frac{1}{(k_{0z}'+k_{1z}')}W(k_\rho^i-k_x')dk_x'. \tag{6.12}$$

Note that (6.11) is essentially accurate up to $N = 3$ since it can be shown that the coherent averages of the odd-order terms in (6.7) is zero—assuming $f(x)$ is zero-mean Gaussian. The definitions for k_{0z}^i, k_{1z}^i, and k_ρ^i above are consistent with those for comparable forms found in Chapter II and Appendix A.

In general, functions of the form (6.12) are evaluated numerically in this study. Assuming a Gaussian correlation function for the surface, i.e., $W(k_x') = c_l\sqrt{\pi}e^{-\frac{c_l^2 k_x'^2}{4}}$, the integral in (6.12) is fast convergent, especially for large correlation lengths, as most of the contribution to the integral comes from the path near $k_x' = k_\rho^i$. When k_ρ^i is not close to the branch point k_o, an analytical approximation to (6.12) can be found simply by first replacing the first term in the integrand with its Taylor series expansion, and then integrating the resulting expression exactly using the identity

$$\int_{-\infty}^{+\infty} t^n e^{-\alpha t^2} dt = \begin{cases} \frac{n!\sqrt{\pi}}{\left(\frac{n}{2}\right)!2^n \alpha^{\frac{n+1}{2}}}, n = \text{even}; \\ 0, n = \text{odd}. \end{cases} \tag{6.13}$$

For near-grazing propagation, evaluation of (6.12) at $k_\rho^i \to k_o$ is needed; in deriving a closed-form formulation for the integral, a more complete procedure [90, 91] must be taken owing to the presence of the branch point at k_o. (For realistic ground conditions, here it is assumed that the branch point k_1 does not lie near the real axis.) After multiplying the numerator and denominator of the integrand by $(k_{0z}' - k_{1z}')$, the integral is separated into two components: one containing k_{1z}'—which is regular over the entire path of integration; and the other containing k_{0z}'—which, after some manipulations (namely, after the changing of variable $t = k_x' - k_\rho^i$, expanding the part of the integrand that does not include the branch point t_a near $t = 0$, and then another changing of variable $u = \sqrt{2\alpha}\,(t - t_a)$), is expressible in terms of parabolic cylinder functions. Therefore, the lower order terms in the series expansion for

$\Omega_y\left(k_\rho^i\right)$ are

$$\begin{aligned}\Omega_y\left(k_\rho^i\right) \approx \left(\tfrac{c_l\sqrt{\pi}}{k_o^2-k_1^2}\right)\Bigg\{\sqrt{\tfrac{\pi}{\alpha}}\left(-\left[k_1^2-k_\rho^{i\,2}\right]^{\frac{1}{2}}+\tfrac{k_1^2}{4\alpha\left[k_1^2-k_\rho^{i\,2}\right]^{\frac{3}{2}}}\right)\\ +\tfrac{ie^{-\alpha t_a^2}}{\sqrt{2\alpha}}\left(\tfrac{[t_a-t_b]^{\frac{1}{2}}}{\left(\sqrt{2\alpha}\right)^{\frac{1}{2}}}\Psi_{\frac{1}{2}}+\tfrac{1}{2[t_a-t_b]^{\frac{1}{2}}\left(\sqrt{2\alpha}\right)^{\frac{3}{2}}}\Psi_{\frac{3}{2}}-\tfrac{1}{8[t_a-t_b]^{\frac{3}{2}}\left(\sqrt{2\alpha}\right)^{\frac{5}{2}}}\Psi_{\frac{5}{2}}\right)\Bigg\},\end{aligned} \tag{6.14}$$

where

$$\Psi_m = \sqrt{2\pi}e^{-i\frac{m\pi}{2}}e^{\frac{\alpha t_a^2}{2}}D_m\left(-i\sqrt{2\alpha}t_a\right); \tag{6.15}$$

$$\alpha = \frac{c_l^2}{4}; \tag{6.16}$$

t_a and t_b are the zeros of $\left(k_o^2-\left(t+k_\rho^i\right)^2\right)$, $t_a > t_b$; and $D_m(\cdot)$ denotes the parabolic cylinder function. In deriving (6.14), a second order Taylor series expansion is used for the integral component containing k_{1z}' and for the aforementioned term not containing the branch point t_a. As $k_\rho^i \to k_o$, the following simplification can be used:

$$D_m(0) = \frac{2^{\frac{m}{2}}\sqrt{\pi}}{\Gamma\left(\frac{1-m}{2}\right)}. \tag{6.17}$$

Figure 6.2 shows the validity of expression (6.14).

6.2.2 Vertical Polarization—2D

Following a procedure similar to that given in Section 6.2.1, but now with excitation as $\vec{H}^i = e^{-ik_{0z}^i z + ik_x^i x}\hat{y}$, the polarization current simplifies to

$$\tilde{\vec{J}}_0(k_x,z) = 2\pi\delta\left(k_x-k_x^i\right)\left(J_{v,x}\hat{x}+J_{v,z}\hat{z}\right)e^{-ik_{1z}^i z}; \tag{6.18}$$

$$\tilde{\vec{J}}_{N,x}(k_x,z) = \frac{ik_o k_{1z}\left(\varepsilon_{r1}-1\right)e^{-ik_{1z}z}}{\left(\varepsilon_{r1}k_{0z}+k_{1z}\right)e^{-ik_{1z}d}}\left\{\tilde{\vec{V}}_N(k_x,z)\cdot\frac{\left(k_z\hat{x}+k_x\hat{z}\right)}{k_o}\right\}\hat{x}; \tag{6.19}$$

$$\tilde{\vec{J}}_{N,z}(k_x,z) = \frac{ik_o k_\rho\left(\varepsilon_{r1}-1\right)e^{-ik_{1z}z}}{\left(\varepsilon_{r1}k_{0z}+k_{1z}\right)e^{-ik_{1z}d}}\left\{\tilde{\vec{V}}_N(k_x,z)\cdot\frac{\left(k_z\hat{x}+k_x\hat{z}\right)}{k_o}\right\}\hat{z}; \tag{6.20}$$

where

$$J_{v,x} = i\left(\varepsilon_{r1}-1\right)\frac{2k_{0z}^i k_{1z}^i e^{-ik_{0z}^i d}}{\left(\varepsilon_{r1}k_{0z}^i+k_{1z}^i\right)e^{-ik_{1z}^i d}}; \tag{6.21}$$

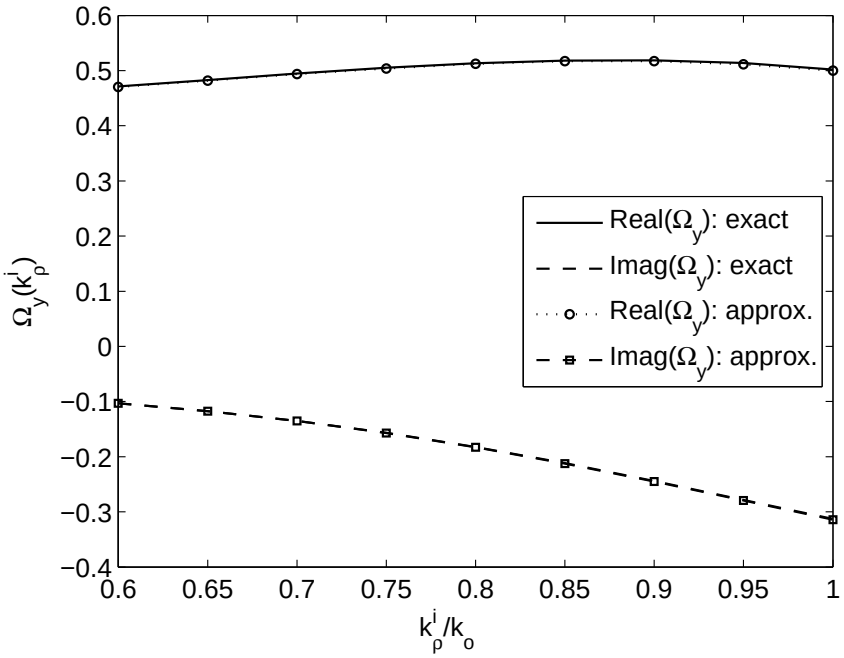

(a)

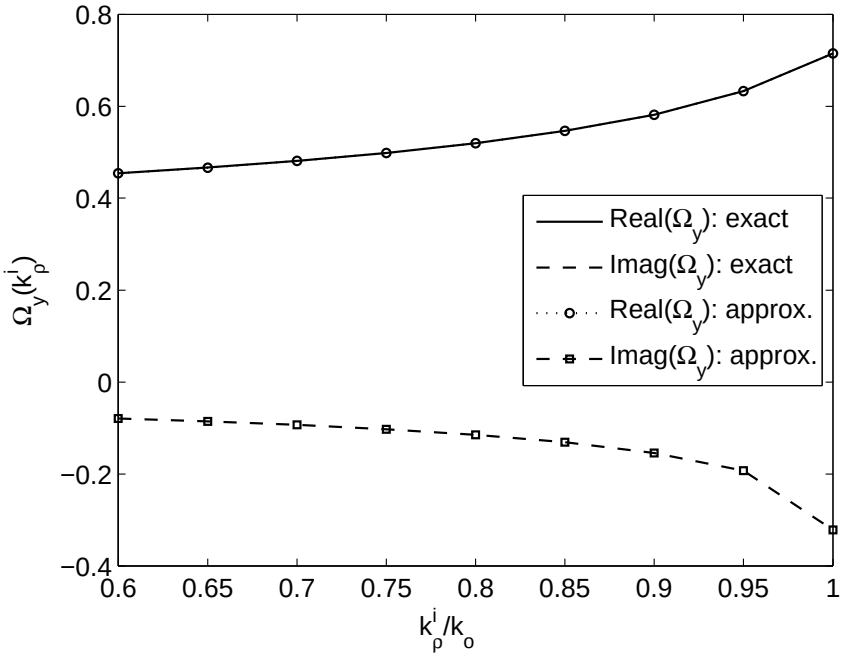

(b)

Figure 6.2: Comparison between (6.12) and (6.14): (a) $k_o c_l = 2\pi$; (b) $k_o c_l = 40\pi$; $\epsilon_{r1} = 2 + i$; $f = 300$ MHz.

$$J_{v,z} = i\left(\varepsilon_{r1}-1\right)\frac{2k_{0z}^{i}k_{x}^{i}e^{-ik_{0z}^{i}d}}{\left(\varepsilon_{r1}k_{0z}^{i}+k_{1z}^{i}\right)e^{-ik_{1z}^{i}d}}; \tag{6.22}$$

and $\tilde{\vec{V}}_N\left(k_x,z\right)$ is the same as (6.6). From (6.7)–(6.9), the effective reflection coefficient defined by $\vec{H}^s = R_v^{i,eff}e^{ik_{0z}^{i}z+ik_x^{i}x}\hat{y}$ can be shown to be

$$\begin{aligned} R_v^{i,eff} \;=\; & \left\{ R_v^i - \frac{\Delta^2}{2}k_o^2\left(\varepsilon_{r1}-1\right)\left(1-R_v^{i\,2}\right)\right. \\ & -\Delta^2\left(\varepsilon_{r1}-1\right)\frac{k_\rho^{i\,2}}{\left(\varepsilon_{r1}k_{0z}^{i}+k_{1z}^{i}\right)}\left[\left(R_v^i-1\right)k_{0z}^{i}-\left(R_v^i+1\right)k_{1z}^{i}\right] \\ & -\frac{\Delta^2}{2}\left(\varepsilon_{r1}-1\right)^2\frac{1}{\left(\varepsilon_{r1}k_{0z}^{i}+k_{1z}^{i}\right)} \\ & \left.\cdot\left[\left(R_v^i-1\right)k_{0z}^{i}\frac{\Omega_x\left(k_\rho^i\right)}{\pi}+\left(R_v^i+1\right)k_\rho^{i}\frac{\Omega_z\left(k_\rho^i\right)}{\pi}\right]\right\}e^{-i2dk_{0z}^{i}}; \end{aligned} \tag{6.23}$$

in which R_v^i is the Fresnel reflection coefficient for vertical polarization for a flat surface located at $z=0$ and

$$\Omega_x\left(k_\rho^i\right) = \int_{-\infty}^{+\infty}\frac{k_{1z}'}{\varepsilon_{r1}k_{0z}'+k_{1z}'}\left(k_{1z}^{i}k_{0z}'+k_\rho^{i}k_x'\right)W\left(k_\rho^i-k_x'\right)dk_x'; \tag{6.24}$$

$$\Omega_z\left(k_\rho^i\right) = \int_{-\infty}^{+\infty}\frac{k_\rho'}{\varepsilon_{r1}k_{0z}'+k_{1z}'}\left(k_{1z}^{i}k_{0z}'+k_\rho^{i}k_x'\right)W\left(k_\rho^i-k_x'\right)dk_x'. \tag{6.25}$$

Approximate analytical forms can also be found for the functions (6.24) and (6.25), as it has been done for (6.12). Note that in contrast to the 3D case shown below, for non-oblique (to y-axis) incidence, no cross-polarization component for the polarization current is generated; thus, no depolarization effects are observed for the 2D problem.

Unlike the results from geometrical optics approximations (the Ament and Miller-Brown formulations), (6.11) and (6.23) show that the amount of correction to the reflection coefficient is dependent on the polarization. Also, the correction factor is a complex number as opposed to a purely real number as specified by geometrical optics; the complete statistics of the rough surface are taken into account through the parameter Δ and the function $W\left(\cdot\right)$.

6.3 Simulation Results

In order to validate the accuracy and convergence of the perturbation-derived effective reflection coefficients as given in the previous section, the perturbation method is applied to the constant perturbation function $f(x) = -1$, resulting in a flat interface problem with a well-defined exact solution; thus, in this case, the deterministic coherent field in (6.7) can be found to arbitrary order N. Figure 6.3 shows the error in the computed scattered field as functions of perturbation order for a TM line radiator located above a half-space with a varying interface as specified by the parameter Δ. Since the wave vectors responsible for the interaction at grazing angle are almost entirely parallel to the horizontal plane of the surface (i.e., $k_z \ll \lambda$), the variation of the polarization current in z is small; therefore, even in the presence of significant roughness (large Δ), the first few orders of the current are adequate in capturing the scattering characteristics of the surface. (The application of the perturbation method for analyzing grazing propagation behavior above a dielectric sinusoidal surface is included in Appendix D.)

6.3.1 Validation with Monte Carlo Simulations

In this section, the effective reflection coefficients derived in Section 6.2 are employed for characterizing the near-grazing radiation properties of 2D sources located above a rough surface. The radiators of interest here include the electric and magnetic line sources, free space fields of which are given by

$$\left\{ \vec{E}_{e.\ line}\left(x,z\right), \vec{H}_{m.\ line}\left(x,z\right) \right\} = \int_{-\infty}^{+\infty} \hat{y}\left\{E_o, H_o\right\} e^{ik_x^i x - ik_{0z}^i z} dk_x^i, \tag{6.26}$$

with

$$E_o = \frac{k_o Z_o}{4\pi k_{0z}^i} e^{ik_{0z}^i z' - ik_x^i x'}; \tag{6.27}$$

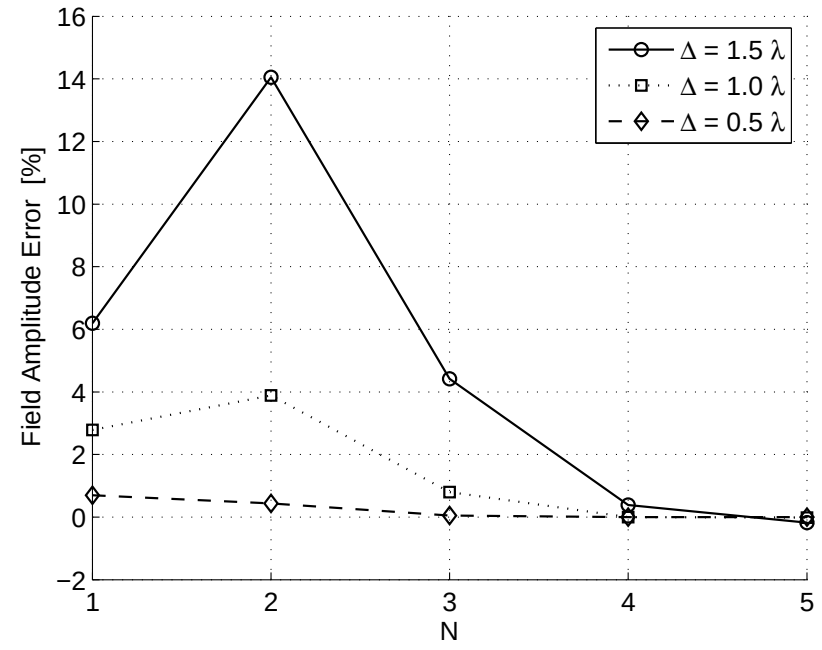

(a)

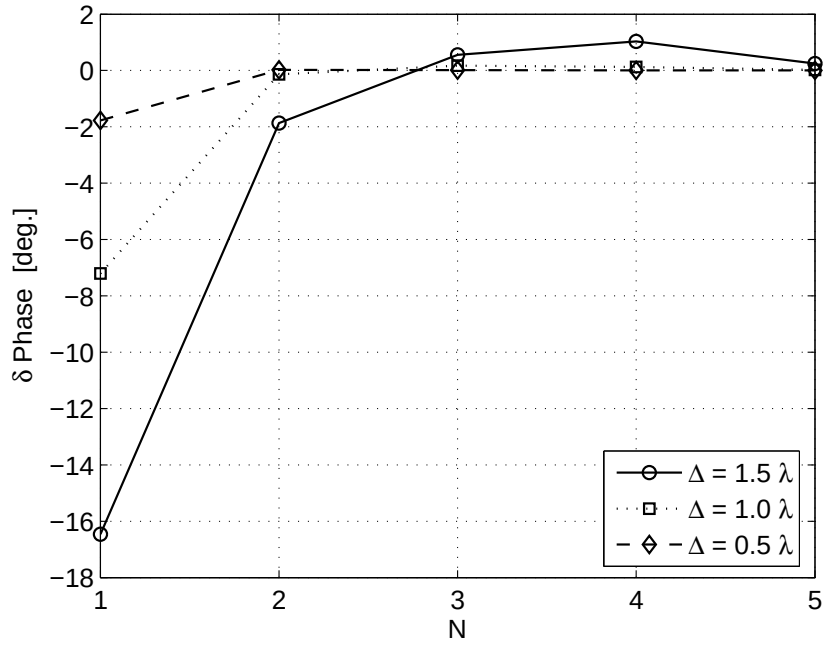

(b)

Figure 6.3: Convergence as functions of Δ for perturbation solution applied to flat interface geometry: (a) percent error in field amplitude and (b) error in phase as compared to exact Sommerfeld solution; $d = 2.1\lambda$; $z' = 3.5\lambda$; $z = 2.5\lambda$; the source is a TM line source; distance between source and observation point = 100λ.

$$H_o = -\frac{k_o Y_o}{4\pi k_{0z}^i} e^{ik_{0z}^i z' - ik_x^i x'}; \tag{6.28}$$

$$k_{0z}^i = \sqrt{k_o^2 - k_x^{i\,2}}; \tag{6.29}$$

and (x', z') denotes the location of the source; the scattered field due to the ground appears as

$$\left\{ \vec{E}^s_{e.\ line}(x,z), \vec{H}^s_{m.\ line}(x,z) \right\} = \int_{-\infty}^{+\infty} \hat{y} \left\{ E_o, H_o \right\} \left\{ R_h^{i,eff}, R_v^{i,eff} \right\} e^{ik_x^i x + ik_{0z}^i z} dk_x^i. \tag{6.30}$$

For observation points in the far field, the second order asymptotic method as introduced in Chapter II can be applied for the evaluation of (6.30). After the transformation $k_x^i = k_o \sin w$, saddle point integration leads to

$$\begin{aligned} \left\{ \vec{E}^s_{e.\ line}(x,z), \vec{H}^s_{m.\ line}(x,z) \right\} &\approx \hat{y} \left\{ \frac{k_o Z_o}{4\pi}, -\frac{k_o Y_o}{4\pi} \right\} \sqrt{\frac{2\pi}{ik_o\rho}} \\ \cdot \Bigg[\left\{ \tilde{R}_h^{i,eff}(w_s), \tilde{R}_v^{i,eff}(w_s) \right\} &+ \frac{1}{ik_o\rho} \Bigg(\frac{1}{2} \left\{ \tilde{R}_h^{i,eff\prime\prime}(w_s), \tilde{R}_v^{i,eff\prime\prime}(w_s) \right\} \\ &+ \frac{1}{8} \left\{ \tilde{R}_h^{i,eff}(w_s), \tilde{R}_v^{i,eff}(w_s) \right\} \Bigg) \Bigg]; \end{aligned} \tag{6.31}$$

where $\rho = \sqrt{(x-x')^2 + (z+z'-2d)^2}$; $\left\{ \tilde{R}_h^{i,eff}, \tilde{R}_v^{i,eff} \right\}$ is the expression in (6.11) and (6.23) without the $e^{-i2dk_{0z}^i}$ term; and the saddle point w_s is

$$w_s = \tan^{-1}\left(\frac{x-x'}{z+z'-2d} \right). \tag{6.32}$$

Figures 6.4–6.6 show the comparison of the total fields computed from the perturbation solution and from Monte Carlo simulations; very good agreement is seen in both the field amplitude and phase. The variation of the signal intensity as function of surface correlation length is shown in Figure 6.7; for constant σ, the signal intensity decreases with c_l, consistent with the discussions of Chapter V; this result can be attributed to the shadowing effect, the dependence upon c_l of which is more apparent

at grazing angles; this is seen in Figure 6.8, which plots $\Omega_y\left(k_\rho^i\right)$ as function of the saddle point angle; similar curves for $\Omega_x\left(k_\rho^i\right)$ and $\Omega_z\left(k_\rho^i\right)$ in the vertical polarization case can be generated.

6.3.2 Extension to 3D

Having validated the accuracy of the perturbation-derived, rough-surface effective reflection coefficients in the 2D case, their complementary 3D forms are presented in this section. Since the analytical procedure is analogous to that of the 2D case, only the direct results are shown below.

For a horizontally-polarized incident wave $\vec{E}^i = e^{i\vec{k}_i\cdot\vec{r}}\hat{h}$—where $\hat{h} = \frac{\vec{k}_i\times\hat{z}}{\left|\vec{k}_i\times\hat{z}\right|}$, $\vec{k}_i = k_x^i\hat{x} + k_y^i\hat{y} - k_{0z}^i\hat{z}$, the effective reflection coefficient is

$$\begin{aligned} R_h^{i,eff} &= \left\{ R_h^i + \frac{\Delta^2}{2}k_o^2\left(\varepsilon_{r1}-1\right)\left(1-R_h^{i\,2}\right)\right. \\ &\quad \left. -\Delta^2 k_o^2\left(\varepsilon_{r1}-1\right)^2\left(1+R_h^i\right)\frac{\Omega_h\left(k_x^i,k_y^i\right)}{\left(2\pi\right)^2\left(k_{0z}^i+k_{1z}^i\right)}\right\}e^{-i2dk_{0z}^i}; \end{aligned} \tag{6.33}$$

where

$$\begin{aligned} \Omega_h\left(k_x^i,k_y^i\right) &= \int_{-\infty}^{+\infty}\int_{-\infty}^{+\infty}\left\{\frac{k_o^2}{k_{0z}'+k_{1z}'}\cdot\left(\frac{k_x^ik_x'+k_y^ik_y'}{k_\rho^ik_\rho'}\right)^2\right. \\ \left.+\frac{k_{0z}'k_{1z}'}{\varepsilon_{r1}k_{0z}'+k_{1z}'}\cdot\left(\frac{k_y^ik_x'-k_x^ik_y'}{k_\rho^ik_\rho'}\right)^2\right\}&W\left(k_x^i-k_x',k_y^i-k_y'\right)dk_x'dk_y'; \end{aligned} \tag{6.34}$$

and, for a surface with Gaussian height distribution and correction function,

$$W\left(k_x',k_y'\right) = c_l^2\pi e^{-\frac{c_l^2\left(k_x'^2+k_y'^2\right)}{4}}. \tag{6.35}$$

For a vertically-polarized incident wave $\vec{E}^i = e^{i\vec{k}_i\cdot\vec{r}}\hat{v}$—where $\hat{v} = \frac{\hat{h}\times\vec{k}_i}{k_o}$, the coeffi-

cient becomes

$$\begin{aligned} R_v^{i,eff} &= \Bigg\{ R_v^i - \frac{\Delta^2}{2} k_o^2 \left(\varepsilon_{r1} - 1\right) \left(1 - R_v^{i\,2}\right) \\ &\quad -\Delta^2 \left(\varepsilon_{r1} - 1\right) \frac{k_\rho^{i\,2}}{\left(\varepsilon_{r1} k_{0z}^i + k_{1z}^i\right)} \left[\left(R_v^i - 1\right) k_{0z}^i - \left(R_v^i + 1\right) k_{1z}^i\right] \\ &\quad -\frac{\Delta^2}{(2\pi)^2} k_o^2 \left(\varepsilon_{r1} - 1\right)^2 \frac{1}{\left(\varepsilon_{r1} k_{0z}^i + k_{1z}^i\right)} \\ &\quad \cdot \left[\left(1 - R_v^i\right) \Omega_{v,1}\left(k_x^i, k_y^i\right) + \left(1 - R_v^i\right) \Omega_{v,2}\left(k_x^i, k_y^i\right) \right. \\ &\quad \left. + \left(1 + R_v^i\right) \Omega_{v,3}\left(k_x^i, k_y^i\right)\right] \Bigg\} e^{-i2dk_{0z}^i}; \end{aligned} \tag{6.36}$$

with

$$\begin{aligned} \Omega_{v,1}\left(k_x^i, k_y^i\right) &= \int_{-\infty}^{+\infty} \int_{-\infty}^{+\infty} \left\{ \frac{-k_{0z}^i k_{1z}^i}{k_{0z}' + k_{1z}'} \cdot \left(\frac{k_x^i k_x' + k_y^i k_y'}{k_\rho^i k_\rho'} \right)^2 \right\} \\ &\quad \cdot W\left(k_x^i - k_x', k_y^i - k_y'\right) dk_x' dk_y'; \end{aligned} \tag{6.37}$$

$$\begin{aligned} \Omega_{v,2}\left(k_x^i, k_y^i\right) &= \int_{-\infty}^{+\infty} \int_{-\infty}^{+\infty} \left\{ \frac{-k_{0z}^i k_{1z}'}{\varepsilon_{r1} k_{0z}' + k_{1z}'} \cdot \right. \\ &\quad \left. \cdot \frac{\left[k_{1z}^i k_{0z}' \left(k_x^i k_x' + k_y^i k_y'\right) + \left(k_\rho^i k_\rho'\right)^2\right] \left(k_x^i k_x' + k_y^i k_y'\right)}{\left(k_o k_\rho^i k_\rho'\right)^2} \right\} \\ &\quad \cdot W\left(k_x^i - k_x', k_y^i - k_y'\right) dk_x' dk_y'; \end{aligned} \tag{6.38}$$

$$\begin{aligned} \Omega_{v,3}\left(k_x^i, k_y^i\right) &= \int_{-\infty}^{+\infty} \int_{-\infty}^{+\infty} \left\{ \frac{k_{1z}^i k_{0z}' \left(k_x^i k_x' + k_y^i k_y'\right) + \left(k_\rho^i k_\rho'\right)^2}{k_o^2 \left(\varepsilon_{r1} k_{0z}' + k_{1z}'\right)} \right\} \\ &\quad \cdot W\left(k_x^i - k_x', k_y^i - k_y'\right) dk_x' dk_y'. \end{aligned} \tag{6.39}$$

In the 3D case, cross-polarization current and field components are also generated;

for horizontally-polarized incidence, the coefficient of the vertically-polarized field is

$$\begin{aligned} R_{vh}^{i,eff} &= \left\{ -\Delta^2 k_o^2 \left(\varepsilon_{r1}-1\right)^2 \frac{1}{\left(2\pi\right)^2 \left(k_{0z}^i + k_{1z}^i\right)} \right. \\ &\quad \cdot \Big[\left(1-R_v^i\right) \Omega_{vh,1}\left(k_x^i, k_y^i\right) + \left(1-R_v^i\right) \Omega_{vh,2}\left(k_x^i, k_y^i\right) \\ &\quad \left. + \left(1+R_v^i\right) \Omega_{vh,3}\left(k_x^i, k_y^i\right) \Big] \right\} e^{-i2dk_{0z}^i}; \end{aligned} \tag{6.40}$$

with

$$\begin{aligned} \Omega_{vh,1}\left(k_x^i, k_y^i\right) &= \int_{-\infty}^{+\infty}\int_{-\infty}^{+\infty} \left\{ \frac{k_o k_{0z}^i}{k_{0z}' + k_{1z}'} \cdot \frac{\left(k_x^i k_x' + k_y^i k_y'\right)\left(k_y^i k_x' - k_x^i k_y'\right)}{\left(k_\rho^i k_\rho'\right)^2} \right\} \\ &\quad \cdot W\left(k_x^i - k_x', k_y^i - k_y'\right) dk_x' dk_y'; \end{aligned} \tag{6.41}$$

$$\begin{aligned} \Omega_{vh,2}\left(k_x^i, k_y^i\right) &= \int_{-\infty}^{+\infty}\int_{-\infty}^{+\infty} \left\{ \frac{-k_{0z}^i k_{0z}' k_{1z}'}{k_o\left(\varepsilon_{r1} k_{0z}' + k_{1z}'\right)} \cdot \frac{\left(k_x^i k_x' + k_y^i k_y'\right)\left(k_y^i k_x' - k_x^i k_y'\right)}{\left(k_\rho^i k_\rho'\right)^2} \right\} \\ &\quad \cdot W\left(k_x^i - k_x', k_y^i - k_y'\right) dk_x' dk_y'; \end{aligned} \tag{6.42}$$

$$\Omega_{vh,3}\left(k_x^i, k_y^i\right) = \int_{-\infty}^{+\infty}\int_{-\infty}^{+\infty} \left\{ \frac{k_{0z}'\left(k_y^i k_x' - k_x^i k_y'\right)}{k_o\left(\varepsilon_{r1} k_{0z}' + k_{1z}'\right)} \right\} \cdot W\left(k_x^i - k_x', k_y^i - k_y'\right) dk_x' dk_y'. \tag{6.43}$$

Similarly, for vertically-polarized incidence, the coefficient of the horizontally-polarized field is

$$\begin{aligned} R_{hv}^{i,eff} &= \left\{ -\Delta^2 k_o^2 \left(\varepsilon_{r1}-1\right)^2 \frac{1}{\left(2\pi\right)^2 \left(\varepsilon_{r1} k_{0z}^i + k_{1z}^i\right)} \right. \\ &\quad \left. \cdot \left(1+R_h^i\right) \left[\Omega_{hv,1}\left(k_x^i, k_y^i\right) + \Omega_{hv,2}\left(k_x^i, k_y^i\right) \right] \right\} e^{-i2dk_{0z}^i}; \end{aligned} \tag{6.44}$$

with

$$\begin{aligned} \Omega_{hv,1}\left(k_x^i, k_y^i\right) &= \int_{-\infty}^{+\infty}\int_{-\infty}^{+\infty} \left\{ \frac{k_o k_{1z}^i}{k_{0z}' + k_{1z}'} \cdot \frac{\left(k_x^i k_x' + k_y^i k_y'\right)\left(k_x^i k_y' - k_y^i k_x'\right)}{\left(k_\rho^i k_\rho'\right)^2} \right\} \\ &\quad \cdot W\left(k_x^i - k_x', k_y^i - k_y'\right) dk_x' dk_y'; \end{aligned} \tag{6.45}$$

$$\Omega_{hv,2}\left(k_x^i, k_y^i\right) = \int_{-\infty}^{+\infty}\int_{-\infty}^{+\infty}\left\{\frac{k'_{1z}}{k_o\left(\varepsilon_{r1}k'_{0z}+k'_{1z}\right)} \cdot\frac{\left[k_{1z}^i k'_{0z}\left(k_x^i k'_x+k_y^i k'_y\right)+\left(k_\rho^i k'_\rho\right)^2\right]\left(k_y^i k'_x-k_x^i k'_y\right)}{\left(k_\rho^i k'_\rho\right)^2}\right\} \cdot W\left(k_x^i-k'_x, k_y^i-k'_y\right)dk'_x dk'_y. \quad (6.46)$$

The radiation pattern of a dipole source can be computed by inserting the effective reflection coefficients listed above into the half-space asymptotic formulations (2.9)–(2.17) from Chapter II; in order to justify this procedure, it is important to mention that all the forms of $\Omega\left(k_x^i, k_y^i\right)$ are functions of k_ρ^i only; this can be seen with the change of variable $k'_x = k''_\rho\cos\gamma'' + k_x^i$, $k'_y = k''_\rho\sin\gamma'' + k_y^i$, $k_x^i = k_\rho^i\cos\gamma^i$, $k_y^i = k_\rho^i\sin\gamma^i$, and subsequently realizing that the equivalent forms for Ω are expressible in the azimuthal parameters as $f\left(\cos\left(\gamma^i-\gamma''\right), \sin\left(\gamma^i-\gamma''\right)\right)$.

Figures 6.9 and 6.10 show the propagation loss for the dipole source (positioned on the z-axis) as functions of distance and surface statistics.

6.4 Conclusion

In view of the limited practicality of existing closed-form expressions for analyzing the scattering characteristics of random rough surfaces as relevant to the near-earth radio channel, a new set of expressions for the coherent effective reflection coefficients is presented in this work. The basis of the derivation is founded upon the volumetric current-based perturbation approach originally prescribed in [35]. In applying the results of this study to compute the radiation of 2D and 3D sources, it is noted that even in the presence of significant roughness, a coherent cancellation still occurs between the LOS signal and the ground scattered signal in the far field, establishing a ground wave important in long-distance transmission. The signal strength also

has a strong dependence on surface correlation statistics; however, for most realistic terrain surfaces of interest, it is seen that the roughness may only weaken the ground wave by up to $\approx$ 5–6 dB as compared to the smooth interface case.

As the initial step in the perturbation approach assumes that the plane wave providing the excitation is impinging upon the rough surface from free space, the formulations introduced for the effective reflection coefficients are valid only for transmitter locations located above the mean surface height ($z = d$). Nevertheless, because of the generality of the outlined perturbation approach, it is conjectured here that a similar procedure can be applied in deriving the polarization current and the scattered signal for NLOS propagation paths and even for when the radio terminals are embedded within the ground. In addition, few modifications are needed in adapting the formulations to solve the problem in which a ground with an inhomogeneous or stratified dielectric profile is situated below the rough layer region; the essential adjustment is done by replacing the flat-interface reflection coefficients within the expressions for the polarization currents with their equivalent counterparts for the inhomogeneous profile.

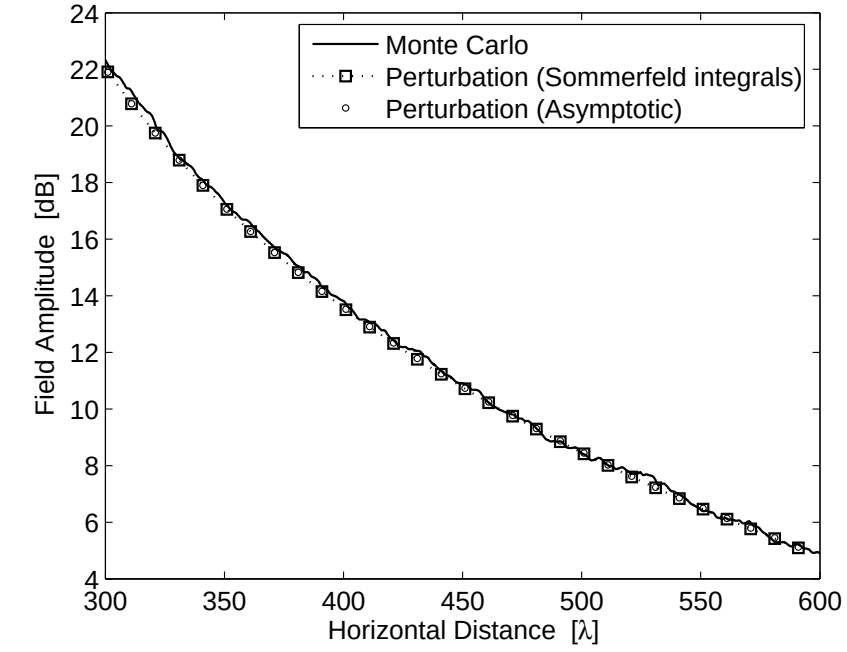

(a)

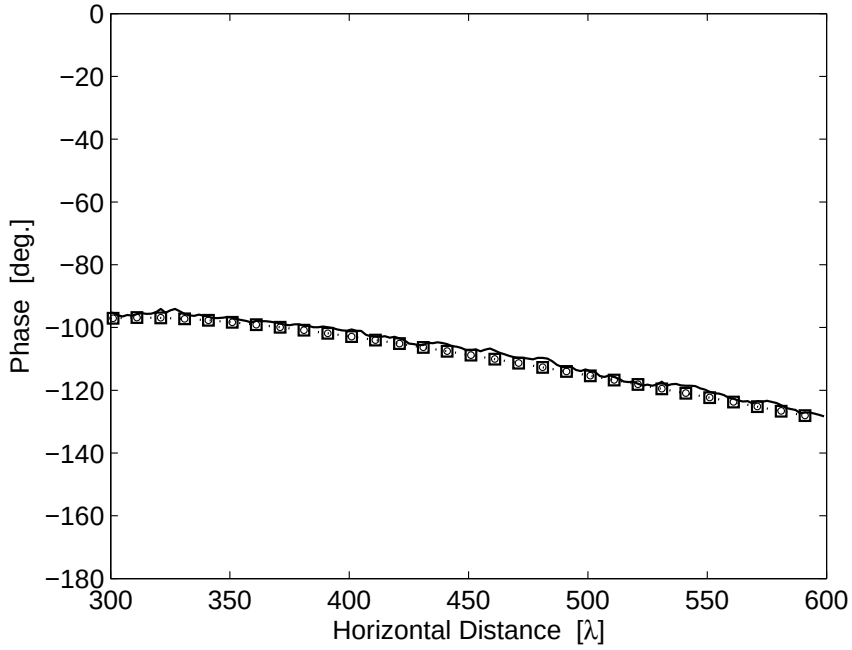

(b)

Figure 6.4: Total field (E_y) of TM line source located above a dielectric random surface with $k_o\sigma = \pi$ and $k_o c_l = 10\pi$; $d = 2\lambda$; $x' = 200\lambda$; $z' = 4.9\lambda$; $z = 4.3\lambda$; $\epsilon_{r1} = 2 + i$; $f = 300$ MHz.

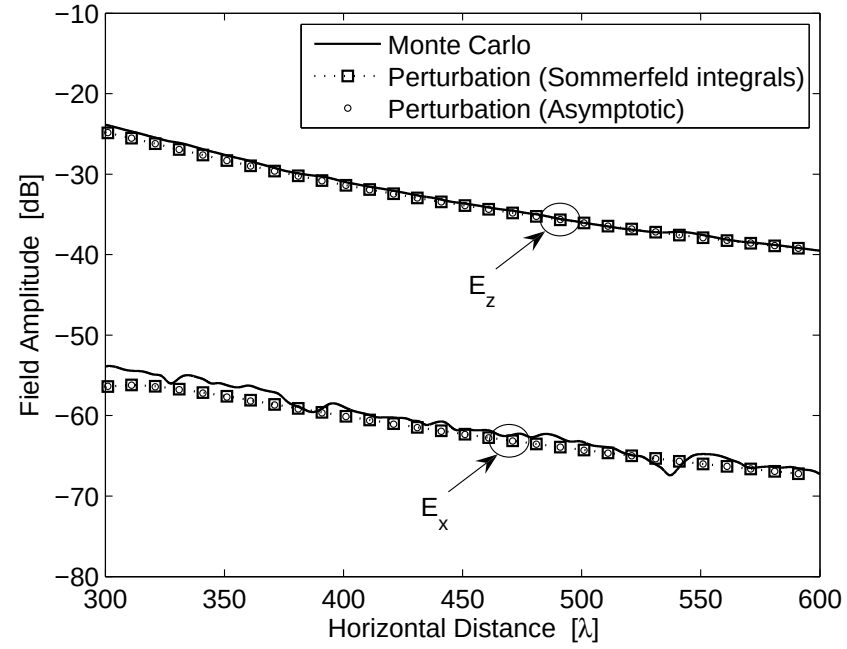

(a)

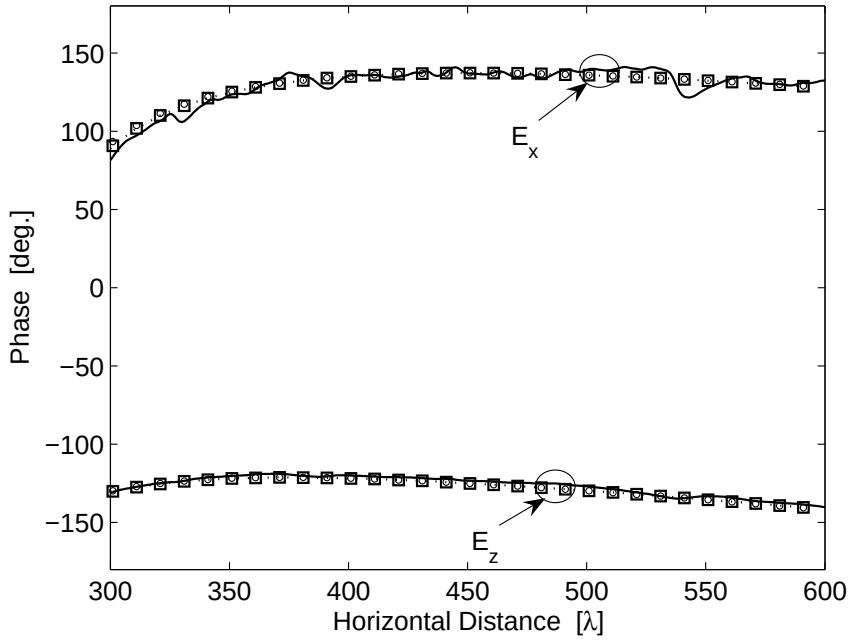

(b)

Figure 6.5: Total field of TE line source located above a dielectric random surface with $k_o\sigma = 2\pi$ and $k_o c_l = 40\pi$; $d = 4\lambda$; $x' = 200\lambda$; $z' = 8.4\lambda$; $z = 8\lambda$; $\epsilon_{r1} = 2 + i$; $f = 300$ MHz.

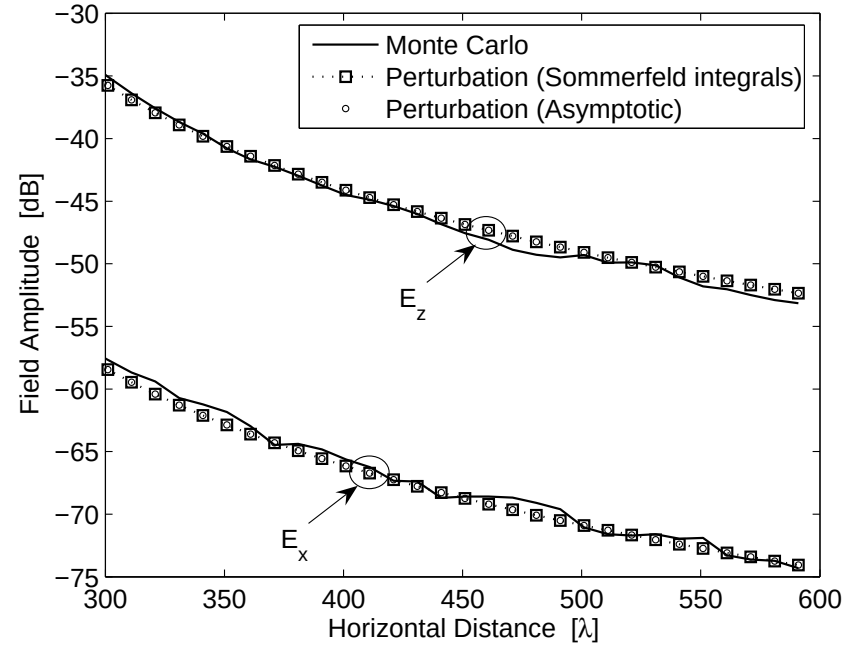

(a)

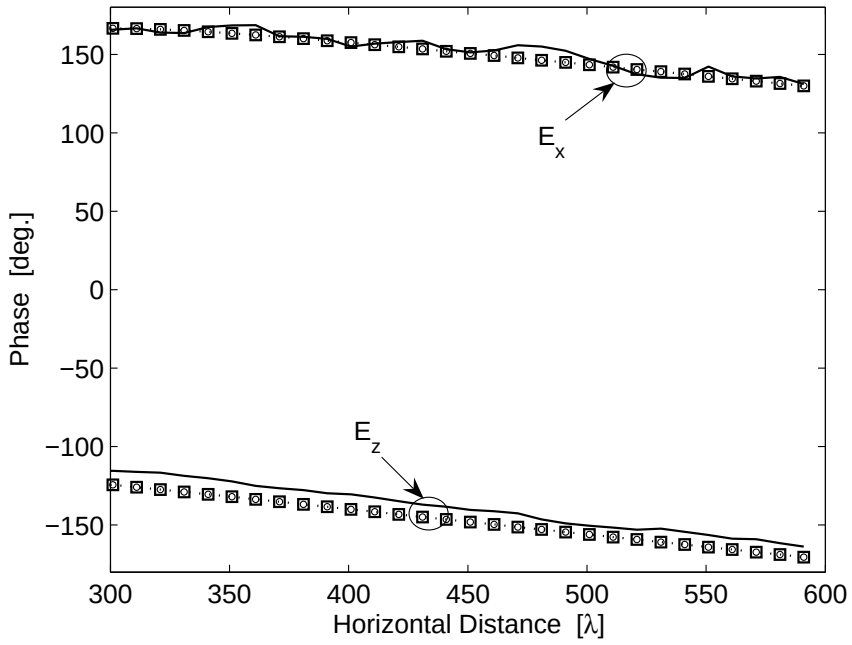

(b)

Figure 6.6: Total field of TE line source located above a dielectric random surface with $k_o\sigma = 2\pi$ and $k_o c_l = 40\pi$; $d = 4\lambda$; $x' = 200\lambda$; $z' = 6\lambda$; $z = 6\lambda$; $\epsilon_{r1} = 8 + 6i$; $f = 300$ MHz.

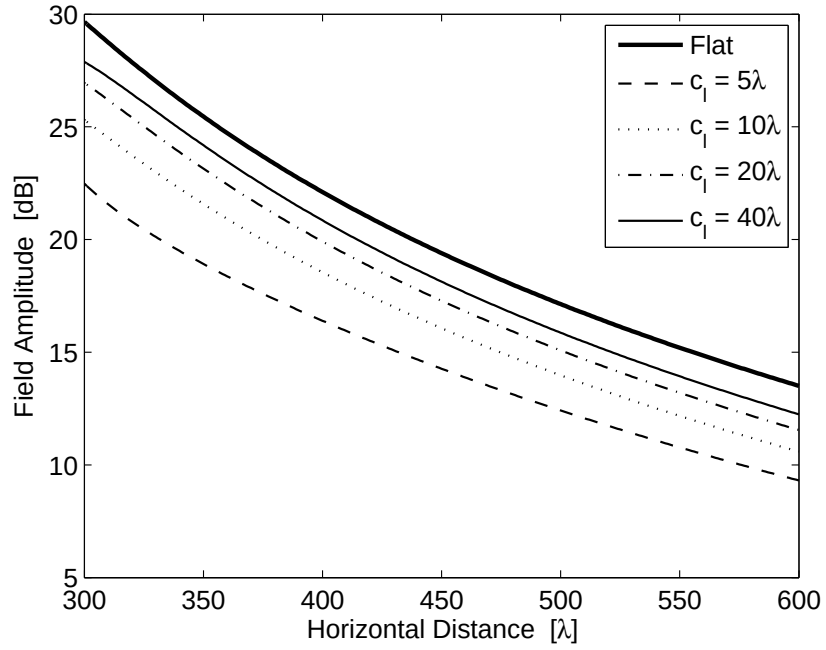

(a)

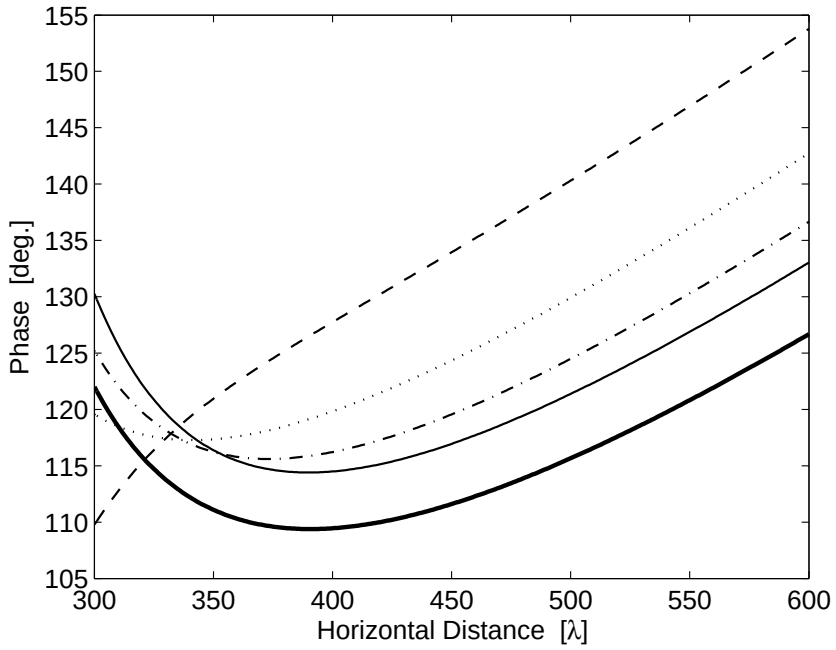

(b)

Figure 6.7: Total field of TM line source above a rough surface as functions of surface correlation length and distance; $\sigma = 1\lambda$; $d = 4\lambda$; $x' = 200\lambda$; $z' = z = 8\lambda$; $\epsilon_{r1} = 2 + i$; $f = 300$ MHz.

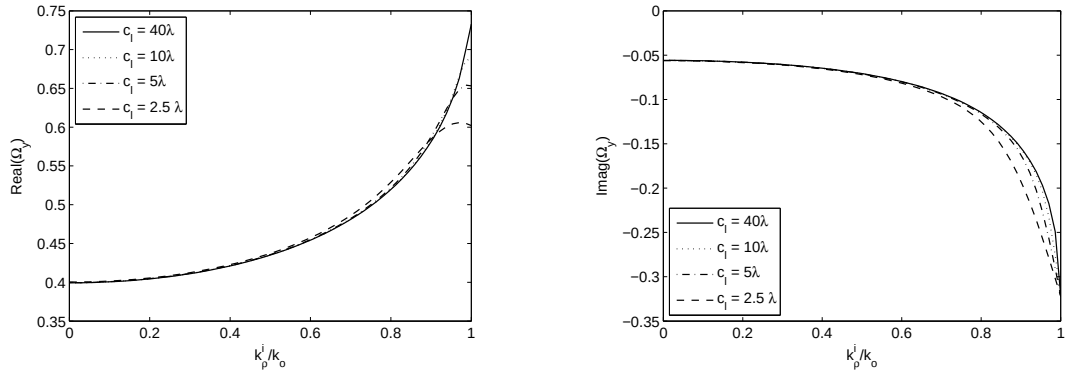

(a)

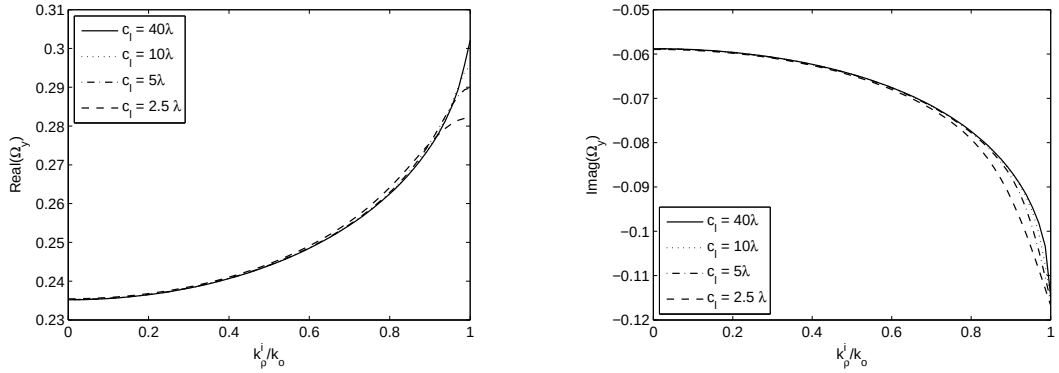

(b)

Figure 6.8: Variation of $\Omega_y\left(k_\rho^i\right)$ as functions of correlation length and w_s—(a) $\epsilon_{r1} = 2+i$; (b) $\epsilon_{r1} = 8+6i$.

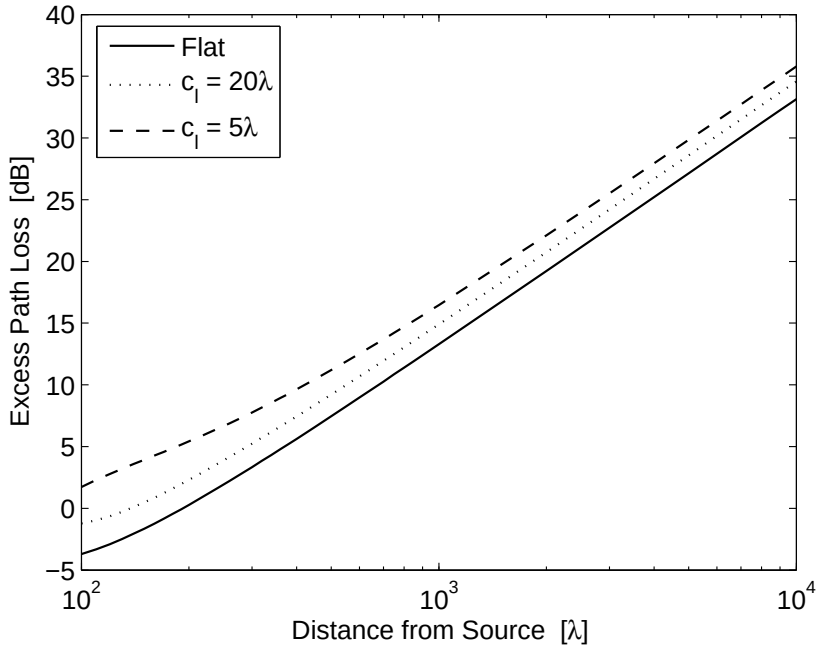

(a)

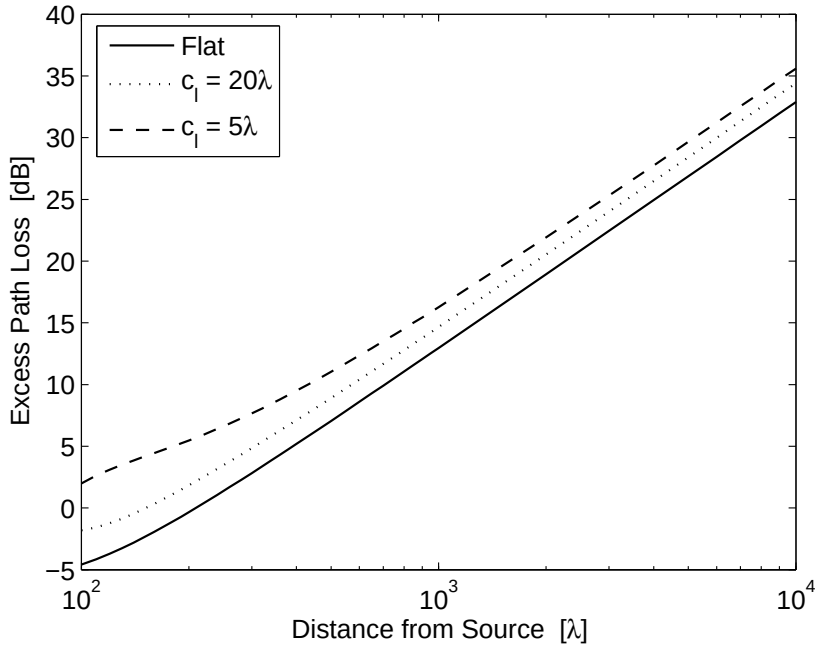

(b)

Figure 6.9: Excess path-loss of (a) vertical dipole and (b) horizontal dipole ($\hat{x}$-directed) located above a dielectric random surface with $k_o\sigma = 2\pi$; $d = 4\lambda$; $z' = 8.4\lambda$; $z = 8\lambda$; $\epsilon_{r1} = 2+i$; $f = 300$ MHz; observation point is above the y-axis.

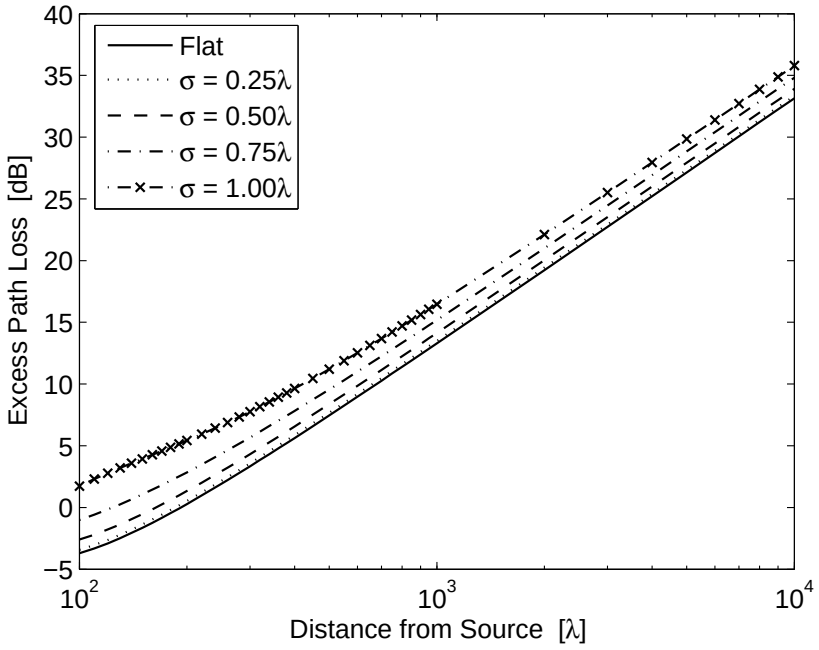

(a)

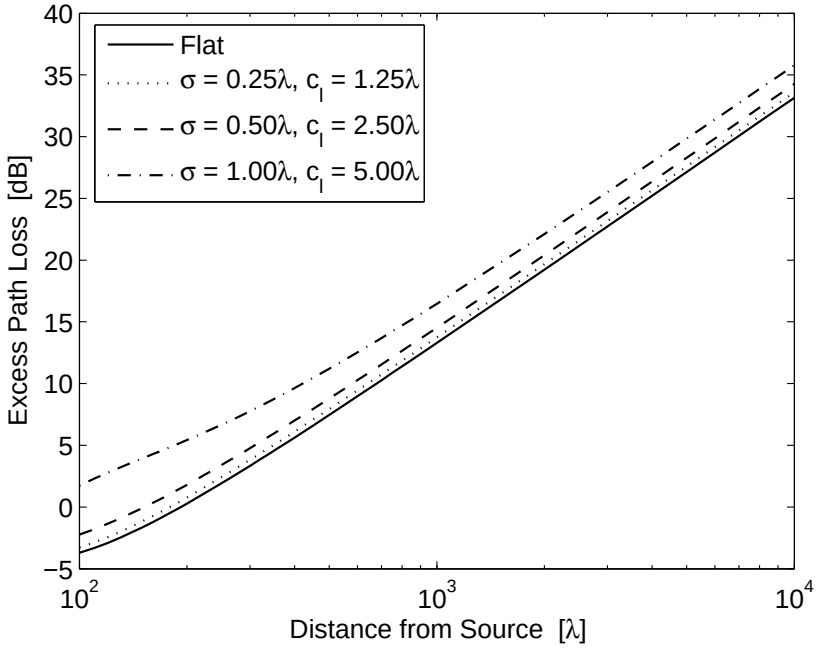

(b)

Figure 6.10: Excess path-loss of vertical dipole located above a dielectric random surface with $d = 4\lambda$; $z' = 8.4\lambda$; $z = 8\lambda$; $\epsilon_{r1} = 2 + i$; $f = 300$ MHz: (a) constant correlation length at $k_o c_l = 10$; (b) constant rms slope.

CHAPTER VII

Terminal-to-Terminal Hybrid Full-Wave Simulation of Low-Profile, Electrically-Small, Near-Ground Antennas

7.1 Introduction

Whereas an immense volume of literature has been devoted to characterizing radiation properties such as input impedance and current distribution of wire antennas located above, partly submerged, or fully submerged in a realistic earth [92–104], only few attempts have been made in explicitly comparing the system performances among these or other types of grounded antennas, especially for electrically-small radiators. Nevertheless, the vast quantity of existing studies in this subject underscores the importance of ground proximity effects in designing antennas pertaining to a gamut of applications including ground penetrating radars, geophysical sensing, landmine detection, telemetry, near-earth and subsurface communication systems, and others. For UGS surveillance applications, since the overall transceiver module must be as inconspicuous as possible to elude detection, the antennas should be low-profile, or even implanted within the ground; furthermore, since the preferred frequency of operation is at the VHF band to attain maximum range coverage, these antennas must be electrically-small as well. To facilitate optimal performance for an UGS network, an optimal antenna design must be selected.

To gain an initial insight into the scope of the problem treated in this chapter,

consider the four basic transmitting/receiving systems—consisting of ideal vertical or horizontal infinitesimal dipoles located adjacent to the air/ground interface—shown in Figure 7.1. For coherent wave propagation over flat ground, it is well known that vertically polarized waves experience less attenuation than horizontally polarized waves. For a simple dipole antenna placed directly over a dielectric ground, it can be shown that the electric field strength in the far field from a vertical dipole is superior to that from a horizontal dipole; the superiority in performance of the vertical dipole transmitter can be explained through symmetry, reciprocity, and boundary condition arguments. After noting that the far field component of interest at the receiver in the VV system is E_{zz} and in the HH system is E_{xx} and realizing that when the same two configurations are repositioned to immediately below the interface, lateral wave propagation (Chapter II, [24]) would impose the constraint that $E^*_{zz} = E^*_{xx}$ (the asterisk notation is reserved for quantities of interest in the lower medium), it can be shown

$$E_{zz} = \varepsilon_{rg}^2 E_{xx} = \varepsilon_{rg}^2 E^*_{xx} = \varepsilon_{rg}^2 E^*_{zz}. \tag{7.1}$$

Although the derived result is only applicable for the prescribed idealized systems located adjacent to the interface (while assuming identical current excitations at the transmitting terminals), it nevertheless—in simplistic terms—leads once again to the intuitive conclusion that VV outperforms HH, VV^*, and HH^*—with the relevant factor of proportionality among the systems determined by the permittivity of the ground. Of course, in order to fully characterize and compare the performances of the above systems, the impedance mismatch and the actual radiated and received powers at the transmitting and receiving terminals must be taken into account; in addition, careful consideration must be exercised in placing the receiver in the direction of maximum radiation intensity of the transmitter, as the radiation pattern

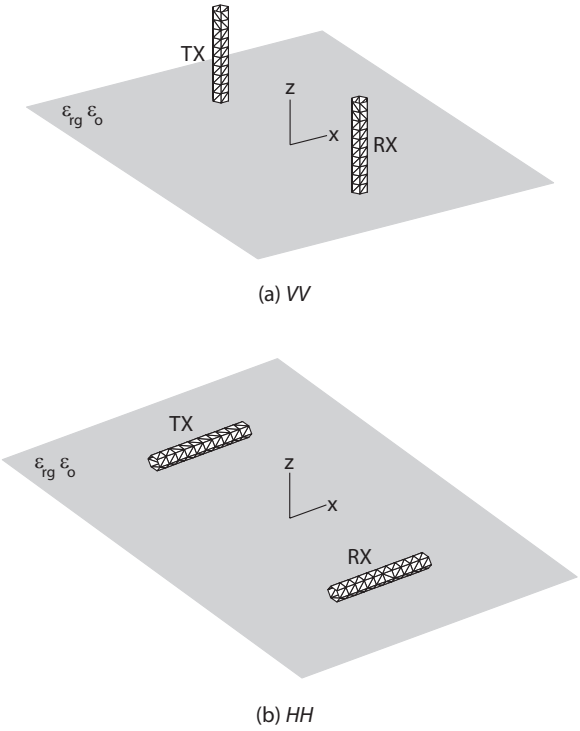

Figure 7.1: Idealized V-pol. and H-pol. transmitting and receiving dipole pairs located immediately above the air/ground interface: (a) VV and (b) HH. The notations VV^* and HH^* are used herein when the pairs are repositioned immediately below the interface.

of an antenna can dramatically change due to the presence of the ground.

Consequently, for a complete understanding of the performance of any transmitter/receiver pair, it is necessary to undertake a full-wave analysis in this problem; the following three-step procedure is proposed: (1) the current distribution on the transmitting antenna near ground is calculated through method of moments (MoM) considerations; (2) then the radiated field pattern of the transmitting antenna is characterized in the far field by propagating the fields using very accurate second order asymptotic formulations; (3) finally, the induced current distribution on the receiving antenna near ground is calculated through MoM considerations again. In carrying out step three above, it is noted that the incident field on the receiving antenna may not be strictly of a TEM (Transverse ElectroMagnetic) wave. For example, for a vertical impulse current source, when both the source and observation

points are located at or very close to the interface above a dielectric ground and are separated by a radial distance ρ, the total radiated field is the superposition of the direct, geometrical optics reflected, and Norton wave fields and is given by Chapter II:

$$E_z = \frac{i\omega\mu_o}{4\pi}\frac{e^{ik_o\rho}}{\rho}\left\{1 + R_v - \frac{i}{2k_o\rho}\left[R_v'' - \frac{9}{4}R_v\right]\right\};$$

$$E_x = \frac{\omega\mu_o}{4\pi}\frac{e^{ik_o\rho}}{\rho^2}\cos\phi\left\{\frac{R_v'}{k_o}\right\};$$

$$E_y = \frac{\omega\mu_o}{4\pi}\frac{e^{ik_o\rho}}{\rho^2}\sin\phi\left\{\frac{R_v{}'}{k_o}\right\};$$

where R_v is the vertical polarization reflection coefficient and the single and double primes indicate differentiation as defined in Chapter II; it is seen that in general the total field does not form a pure plane (TEM) wave since E_ρ is non-zero; similar results are relevant for a horizontal current source. Although existing simulation software packages can provide MoM modeling for an arbitrary antenna structure, they can only calculate the induced current on the structure for an incident field in the form of plane waves. For near-earth wave propagation problems, in which source and observation points could be in extreme proximity to the ground surface and the dominant wave contribution is non-geometrical-optics in nature, generic simulation software packages are handicapped by their inability to generate accurate results at the receiving end; as an additional drawback, the computational domain in standard simulation tools is limited to a relatively small volume that cannot encompass both the transmitting and a distant receiving antenna.

The proposed full-wave hybrid approach and the necessary formulations for the MoM analysis of general antenna structures used in this study are outlined in Section 7.2, along with a discussion on the efficient evaluation of the Green's functions for a half-space. In Section 7.3, numerical results for the performance of different

antenna systems including the dipole, loop, ordinary circular slot, and cavity-back circular slot are compared in terms of input impedance, radiation pattern, and input/output power efficiency.

7.2 Formulations for Numerical Analysis

A detailed description of the full-wave hybrid approach for analyzing grounded antenna performance is provided in this section.

7.2.1 MPIE-MOM

To calculate the radiating and induced currents at the transmitting and receiving antennas, a MoM procedure is solved through the use of a standard form of the electric field integral equation. For an arbitrary field impinging upon a perfectly conducting structure, the mixed potential integral equation (MPIE) in terms of vector potential $\vec{A}$ and scalar potential Φ is given by the following:

$$\hat{n} \times \left[\vec{E}_{inc}(\vec{r}) + \vec{E}_{scat}(\vec{r})\right] = 0, \vec{r} \in \text{antenna surface } s; \tag{7.2}$$

$$\vec{E}_{scat}(\vec{r}) = i\omega\vec{A}(\vec{r}) - \nabla\Phi(\vec{r}); \tag{7.3}$$

where

$$\vec{A}(\vec{r}) = \int_s \overline{\overline{G}}^A(\vec{r},\vec{r}') \cdot \vec{J}_s(\vec{r}')d\vec{r}'; \tag{7.4}$$

$$\Phi(\vec{r}) = \frac{1}{i\omega}\int_s G^{\Phi}(\vec{r},\vec{r}')\nabla' \cdot \vec{J}_s(\vec{r}')d\vec{r}'. \tag{7.5}$$

The dyadic and scalar Green's functions have been derived [105–107] for the case when the region of interest is the upper medium of the half-space in Figure 7.1:

$$\overline{\overline{G}}^A(\vec{r},\vec{r}') = \frac{\mu_o}{4\pi}\left\{ g_{fs}\overline{\overline{I}} + \begin{bmatrix} 0 & 0 & g_{xz} \\ 0 & 0 & g_{yz} \\ -g_{xz} & -g_{yz} & -2Kg_i \end{bmatrix} + \begin{bmatrix} I_{xx} & 0 & I_{xz} \\ 0 & I_{xx} & I_{yz} \\ -I_{xz} & -I_{yz} & I_{zz} \end{bmatrix} \right\}; \tag{7.6}$$

$$G^{\Phi}(\vec{r},\vec{r}') = \frac{1}{4\pi\varepsilon_o}\left\{g_{fs} + Kg_i + I_{\Phi}\right\}; \tag{7.7}$$

where $\overline{\overline{I}}$ is the unity matrix and

$$g_{fs,i} = \frac{e^{ik_o R_{fs,i}}}{R_{fs,i}}; \tag{7.8}$$

$$g_{xz} = -K\cos\phi\left[\frac{1}{\rho}e^{ik_o(z+z')} - \frac{(z+z')}{\rho}g_i\right]; \tag{7.9}$$

$$g_{yz} = -K\sin\phi\left[\frac{1}{\rho}e^{ik_o(z+z')} - \frac{(z+z')}{\rho}g_i\right]; \tag{7.10}$$

$$\begin{aligned} R_{fs} &= \sqrt{\rho^2+(z-z')^2}; \\ R_i &= \sqrt{\rho^2+(z+z')^2}; \\ K &= \frac{1-\varepsilon_{rg}}{1+\varepsilon_{rg}}. \end{aligned} \tag{7.11}$$

In the above expressions, the quantities denoted by subscripts "fs" and "i" correspond to free space and image components, respectively. The Sommerfeld integrals (Is) needed to complete (7.6) and (7.7) are defined in Appendix E. A set of expressions similar to (7.6)-(7.11) can be derived for the case when the region of interest is the lower medium of the half-space.

After meshing the antenna structure with triangular facets (Figure 7.2), by expanding the unknown surface current density $\vec{J}_s$ as a summation of Rao-Wilton-Glisson (RWG) basis functions [108, 109] and then testing (7.2) with the same type of functions, a matrix equation is formed, enabling the calculation of the surface current distribution throughout the antenna structure. A procedure similar to the one shown in [108] can be used for setting up the matrix equation; and, with the introduction of normalized area coordinates, the face-pair combination evaluation can be implemented to speed up the impedance matrix filling process by eliminating redundant computational routines inherent in the edge-pair combination evaluation.

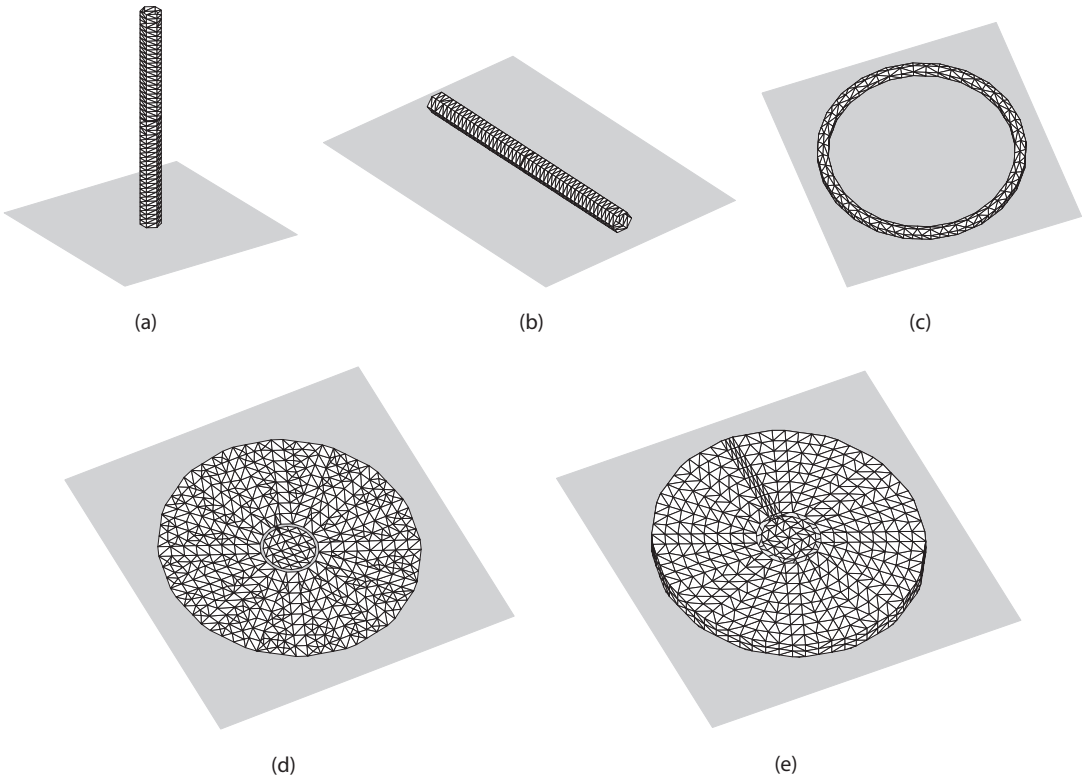

Figure 7.2: (a) Vertical dipole; (b) horizontal dipole; (c) horizontal loop; (d) ordinary circular slot; (e) cavity-backed circular slot; the dimensions of each geometry are given in Table 7.1. Note that the cavity-backed circular slot structure protrudes above the air/ground interface.

For a voltage-source excited antenna, a delta-gap model is assumed for the excitation vector in the matrix equation; in this model, an incident field only exists over the triangular patches spanning the gap location. For a more general incident field, the value of the incident field is assumed to be constant over each patch and equal to its value at the patch's centroid. Also, impedance loading of the antenna at the feed point can be treated by regarding the unknown voltage across the load as an equivalent incident field at the delta-gap [110].

7.2.2 Approximation for Green's Functions

Note that two primary difficulties are encountered when calculating the impedance matrix elements using (7.6) and (7.7). One is due to the singularities that would

emerge in the expressions g_{fs}, g_i, g_{xz}, and g_{yz} for certain impedance elements; however, singularity extraction techniques have been used successfully in obtaining closed-form solutions to the so-called self-terms [111–113]; also, a quadrature routine can be employed in computing the elements containing g_{xz} and g_{yz} even in the presence of singularities. The second difficulty concerns the calculation of the impedance matrix elements in the presence of the Sommerfeld integrals (E.1)–(E.5); implementing an exact routine to calculate the impedance matrix elements would necessitate the evaluation of a triple integral; to expedite the matrix filling process, different common schemes are available in efficiently calculating the Sommerfeld integrals—either by speeding up the convergence rate of the integrals or approximating the integrals with closed-form expressions. Since the Sommerfeld integrals are slowly convergent (especially for small $(z + z')$) along the original path on the real-axis, a deformed path (e.g., steepest descent path) can be exploited to achieve faster convergence. To avoid repeated calculation of the same integrals, another class of methods uses a precompute/tabulate/interpolate routine in which the values of the integrals at a finite number of sampled spatial locations are calculated in advance (using convergence acceleration techniques) and then are stored in a database to serve as a base set for interpolation by the MoM procedure. In this study, the method of discrete complex images (DCIM) is employed to approximate all the Sommerfeld integrals with closed-form analytical expressions; thus, by eliminating the innermost of the triple integral, the remaining double integral can be carried out readily using a standard quadrature algorithm. After mapping the integrands of (E.1)–(E.5) as a sum of N exponentials of the form $\sum_{v=1}^{N} \alpha_v e^{ik_{oz}\beta_v}$ on the complex k_{oz}-plane using the Generalized Pencil of Function (GPOF) method [114–117], either of the following two identities is applied in approximating the resulting simplified Sommerfeld integrals in canonical

forms:

$$\int_0^\infty \frac{i}{k_{oz}} e^{ik_{oz}(z+z')} J_o(k_\rho \rho) k_\rho dk_\rho = \frac{e^{ik_o R_i}}{R_i}; \tag{7.12}$$

$$\int_0^\infty e^{ik_{oz}(z+z')} J_1(k_\rho \rho) k_\rho^2 dk_\rho = \frac{\rho(z+z')e^{ik_o R_i}}{R_i^5} \left[3 - 3ik_o R_i - k_o^2 R_i^2\right]. \tag{7.13}$$

Following the recipe given above, the five Sommerfeld integrals of interest have been approximated with an error of less than 1% in this study; Figures 7.3 and 7.4 show a comparison between the exact values of these Sommerfeld integrals and the approximations provided by the method of discrete complex images with $N = 9$. In a particular propagation medium, note that each set of complex images is only valid in a particular spatial and spectral domain—in other words, each set affords accurate estimation only over a limited range of ρ, $(z + z')$, and frequency. (Formally, unlike that of (7.12), the right side of (7.13) is not in the proper form to be labeled as a "complex image" contribution; nonetheless, the name "method of discrete images" will continue to be adopted when referring to this technique.)

In examining (7.6) and (7.7), it can be seen that for a structure supporting purely horizontal currents (e.g., ordinary circular slot), only two Sommerfeld integrals—(E.1) and (E.2)—are needed in setting up the matrix equation. Furthermore, for a general 3D structure, it has been observed that the non-diagonal components (i.e., the directionally-mixed response terms G_{xz}^A, G_{zx}^A, G_{yz}^A, and G_{zy}^A) of the dyadic Green's function have only minor contributions to the total impedance matrix.

7.2.3 Half-Space Asymptotic Field Propagator

Once the current distribution has been obtained from the MPIE-MoM, the radiation properties of a transmitting antenna can be characterized by applying an appropriate propagation model in accordance with the geometry and physical properties of the propagation medium. For a current source located over a flat ground

surface, a second order asymptotic approximation can be derived from an exact solution in computing the radiated fields; the formulations necessary for this step can be deduced from the expressions given in Chapter II specialized to a half-space medium. At the receiving terminal, in order to maximize its response to the stimulating incident field, the receiving antenna is connected a load conjugately matched to its input impedance. Note that mutual coupling effects have been neglected by placing the receiver in the far field region of the transmitter.

It should be mentioned that although the hybrid MoM and asymptotic propagator approach as outlined above has been described only for antennas located above the air/ground interface, an equally valid and conceptually similar set of formulations and procedures exists for the subsurface case. The only major deviation results from the fact that when the antennas are submerged in a lossy medium, the mode of propagation taken by the fields is in the form of lateral waves instead of Norton waves (Chapter II, [24]); hence, the asymptotic propagator should be modified accordingly.

7.3 Numerical Results and Discussions

There are two sources of complications in the attempt to characterize the performance of an antenna in the presence of a lossy dielectric ground: (1) the effect of dielectric loading on the antenna's ability to radiate and receive power and (2) the effect of the ground on the radiation pattern. In a lossless, homogeneous medium, it is desirable to maximize an antenna's ability to radiate *real* power for a given unit of excitation (or for a given magnitude of current) at the feed point. This ability to radiate is conveniently captured by the input resistance (R_{in}) of a lossless antenna since a measure of the amount of power radiated is always consistent—either from the point of view of the excitation source supplying the power or from that of an

imaginary sphere surrounding the antenna and intercepting the outward-propagating power. As a result, the value of R_{in} of the transmitter directly indicates the magnitude of stimulation available at the receiver—assuming the receiver itself is properly positioned and oriented with respect to the transmitter. The proximity to a ground not only modifies an excitation source's ability to inject energy into an antenna but also—since energy is absorbed by the lossy dielectric—diminishes the usefulness of R_{in} as a performance indicator; alas, a larger R_{in} may only signify that more energy is coupled into the ground but furnish little information on the actual far field power deliverable to a receiver. Given the difficulty of defining practical parameters such as effective radiation resistance, gain, and antenna efficiency in the presence of a lossy environment, a quantity called the relative communication efficiency (RCE)—which is calculated as the ratio of the input power at a reference antenna to that at a test antenna when the same field strength is to be observed for both—has been introduced to serve as a figure of merit for evaluating different antenna systems [118, 119]. In this work, a similar but slightly different quantity for comparison purposes is defined while taking into account the response of the receiver; since the simulations carried out in this study assume that the same type of antenna is always used at both the transmitting and receiving ports, a system efficiency factor (f_e) can be established by simply calculating the ratio of the maximum power received at the receiving terminal to the total power delivered to the transmitting terminal. To maximize the received power, the receiving antenna is placed in the direction of maximum radiation intensity of the transmitter and—as already mentioned—is conjugately matched as well.

Now the four basic dipole transmitting/receiving systems put forward in Section 7.1 can be analyzed in a more precise and satisfying manner using the full-wave

Configuration	Antenna Dimensions	I_{in} (normalized)	Z_{in} [Ω]	P_{in} (normalized)	$P_{rec,max}$ (normalized)	f_e [dB] = $P_{rec,max}/P_{in}$ (normalized)
Dipole – *VV*	Length = $0.1\lambda_0$ Wire Radius = $10^{-4}\lambda_0$	1	13.8-1818.8*j*	1	1	0
Dipole – *HH* $\phi = 0^o$	Length = $0.1\lambda_0$ Wire Radius = $10^{-4}\lambda_0$	4.7	259.1-285.9*j*	4.14×10^{2}	1.05×10^{-2}	-46.0
Dipole – *HH* $\phi = 90^o$	Length = $0.1\lambda_0$ Wire Radius = $10^{-4}\lambda_0$	4.7	259.1-285.9*j*	4.14×10^{2}	1.32×10^{-4}	-65.0
Dipole – *VV**	Length = $0.1\lambda_0$ Wire Radius = $10^{-4}\lambda_0$	11.6	126.0-93.5*j*	1.22×10^{3}	3.91×10^{-4}	-64.9
Dipole – *HH** $\phi = 0^o$	Length = $0.1\lambda_0$ Wire Radius = $10^{-4}\lambda_0$	7.2	188.6-168.9*j*	7.01×10^{2}	3.78×10^{-2}	-42.7
Dipole – *HH** $\phi = 90^o$	Length = $0.1\lambda_0$ Wire Radius = $10^{-4}\lambda_0$	7.2	188.6-168.9*j*	7.01×10^{2}	4.61×10^{-4}	-61.8
Loop	Circumference = $0.1\lambda_0$ Wire Radius = $10^{-4}\lambda_0$	7.7	33.5+232.9*j*	1.44×10^{2}	8.27×10^{-5}	-62.4
Ordinary Circular Slot (OCS)	Slot Circumference = $0.1\lambda_0$ Slot Width = $3\times10^{-3}\lambda_0$ Overall Circumference = $0.5\lambda_0$	38.0	37.1-30.3*j*	3.90×10^{3}	9.11×10^{-4}	-66.3
Cavity-Backed Circular Slot (CBCS)	Slot Circumference = $0.1\lambda_0$ Slot Width = $3\times10^{-3}\lambda_0$ Overall Circumference = $0.5\lambda_0$ Cavity Height = $0.005\lambda_0$	8.7	1.3-210.0*j*	6.89	2.13×10^{-2}	-25.1
—	Slot Circumference = $0.1\lambda_0$ Slot Width = $3\times10^{-3}\lambda_0$ Overall Circumference = $0.5\lambda_0$ Cavity Height = $0.01\lambda_0$	6.5	0.5-281.6*j*	1.55	1.70×10^{-1}	-9.6
—	Slot Circumference = $0.1\lambda_0$ Slot Width = $3\times10^{-3}\lambda_0$ Overall Circumference = $0.5\lambda_0$ Cavity Height = $0.02\lambda_0$	5.5	0.2-328.0*j*	4.94×10^{-1}	1.30×10^{-1}	-5.8

Table 7.1: Performance parameters for various low-profile antenna configurations as normalized to the vertical dipole; distance between geometrical centers of transmitter and receiver is $100\lambda_0$; $f = 300$ MHz.

hybrid approach developed in Section 7.2. The results of the simulations for a typical ground with $\epsilon_{rg} = 8 + 6i$ are provided in Table 7.1. Whereas the radiation pattern of the vertical dipole is omni-directional, that of a horizontal dipole can change significantly depending on the properties of the ground; as displayed in Figure 7.5, for a horizontal dipole aligned along the x-axis, the direction of maximum radiation can be along either the x- or y-axis; using the formulations from Chapter II, it can be shown that the following relation exists between the fields at azimuthal locations $\phi = 0°$, $180°$ and $\phi = 90°$, $270°$:

$$E_{xx}^{\phi=0°,180°} = (1 - \varepsilon_{rg}) E_{xx}^{\phi=90°,270°}. \tag{7.14}$$

Thus, when the condition $|1 - \varepsilon_{rg}| \leq 1$ holds, the maximum (of E_{xx}) remains at

$\phi = 90°$, $270°$—as it is in free space; otherwise, the maximum is at $\phi = 0°$, $180°$—which is true for most realistic ground. According to (7.1), comparing the power performances, a -40 dB ($|\varepsilon_{rg}|^4$) difference separating VV from the other three configurations is expected; however, locating the results for VV, HH ($\phi = 90°$), VV^*, and HH^* ($\phi = 90°$) in Table 7.1, the actual difference is seen to be around -62 dB to -65 dB instead; the discrepancy is anticipated since the latter values include the effects of dielectric loss at the transmitting and receiving terminals, as the antenna near-field power that is normally reactive in a lossless medium is now being dissipated as real power. By re-arranging the horizontal dipoles in an end-to-end (or in-line) fashion (Figure 7.6) for optimal reception (with the proportional factor in (7.1) replaced by $\epsilon_{rg}^2/(1-\epsilon_{rg})$), the performances of the HH and HH^* configurations improve to -46 dB and -42.7 dB, respectively. (In this example, HH^* outperforms HH since while the *physical* length of the dipole is kept constant at 0.1 free space wavelength ($0.1\lambda_0$), the effective *electrical* length of the dipole is larger when it is in the ground.)

Given that the magnitudes of ϵ_{rg}^2 and $\epsilon_{rg}^2/(1-\epsilon_{rg})$ are larger than unity for a realistic ground, the performance of the VV configuration would always be superior to those of other dipole configurations—even if near-field dielectric losses are ignored. The performance parameters of another low-profile antenna, the horizontal circular loop, are included in Table 7.1. Because an electrical loop is mostly a magnetic element with positive stored reactive power in its near field region, it has the advantage of being less vulnerable to the dielectric loss of the ground; however, cancellation between the actual loop current and its image is responsible for the rather poor performance observed; of course, similar image cancellation occurs for the horizontal dipole as well. Note that when an antenna is placed adjacent to the ground surface,

it appears electrically larger and therefore its input impedance is forced to adjust accordingly; specifically, for electrically-small antennas, compared to the free space values, the resistance is increased whereas the reactance becomes less negative for a capacitive terminal (e.g., a two-terminal dipole) and more positive for an inductive terminal (e.g., loop). (Proper matching techniques are needed to maximize the practicality of the antennas connecting to an actual transceiver system but are not discussed here.) As mentioned, the enhancement in the input resistance of the transmitter, however, may not directly translate into higher received power at the receiver since the proximity to a lossy ground may cause a shift in the antenna's balance of near-field stored reactive power and real dissipated power, which now must include the effects of dielectric loss. It is worth mentioning that by insulating the antennas, a purely reactive region in the immediate vicinity of the current source can be re-established, thereby reducing the amount of dielectric loss; coated wire antennas immersed in an homogeneous conducting medium have been examined, for example, in [120] and [121]; modifications are needed, however, if the detailed analysis presented in these studies is to be extended to the present half-space problem.

The superior performance of the VV system is attributed to the boundary condition effect, as mentioned in Section 7.1, and also the height gain effect—a consequence of the fact that the current distributions of the system are elevated off the ground. Accordingly, the key for optimization is to mimic the properties of the vertical dipole with a low-profile design. The theoretical equivalent of a vertical dipole is a small circular slot—assuming a constant magnetic loop current can be established in the slot. Although the analysis of a circular slot on an infinite perfectly conducting plane above a dielectric space has been carried out in a number of studies, including [122] and [123], the results of conventional studies cannot be readily applied to

the present problem since the interest for the radiation pattern is no longer in the main-beam (or bore-sight, $\theta = 0°$) direction but rather in the edge ($\theta = 90°$) radiation direction, which demands the effects of a finite-sized conducting plane to be taken into account in an extremely accurate manner that is achievable only through the use of a full-wave numerical method. Also, the focus of most existing studies is on resonant slots operating with a slot circumference of 1λ; the radiation properties of an electrically-small slot located over a lossy ground have not been thoroughly investigated for near-earth propagation scenarios.

The geometry of an ordinary circular slot (OCS) antenna used in this work is shown in Figure 7.2; the antenna's radiation patterns are shown in Figures 7.7 and 7.8, with the simulation results displayed in Table 7.1. The unexpected poor performance of the OCS can be explained by realizing that the assumption of vertical dipole equivalence only holds for the case when the perfectly conducting ground plane is infinite in extend. In practice, when the conducting plane is finite, the radiation from the equivalent magnetic loop currents flowing in opposite directions and located on the top and bottom sides of the antenna ground plane would nullify each other (at $\theta = 90°$). Note that while an increase in the size of the ground plane may contribute an enhancement to the radiation pattern in the boresight direction, inferior performance would remain in the edge radiation direction, which is the critical region of interest for near-earth propagation problems. In order to circumvent the finite-ground-plane deficiency inherent in simple slot loop antennas and to achieve a better vertical dipole equivalent, the radiation from the bottom side of the open slot must be shielded with a cavity, thereby allowing the top magnetic loop current to radiate more effectively and omni-directionally. The resulting radiation patterns for the cavity-backed circular slot (CBCS) antenna are shown in Figures 7.7 and 7.8;

it is seen that the CBCS can provide a much better imitation of the vertical dipole than the OCS while maintaining a planar, low-profile architecture. The enhanced performance of the CBCS can also be attributed to its ability to support a vertical current density on the sidewall of its cavity: by radiating and receiving using J_z and E_z, the CBCS—as evident from Table 7.1—can achieve a much higher efficiency factor than the other low-profile alternatives. From the viewpoint of an electric current interpretation, the cavity-backed circular slot is similar to the vertical dipole except that the vertical current density is now distributed along a circular band instead of along a vertical line. Radiation from the top and bottom covers of the cavity is minimal since the currents flowing on each are in opposite directions. The use of the cavity also brings about an additional functional advantage: through a suppression of radiation in the backside, dielectric loss in the near-field region of the antenna is reduced substantially; this is reflected in the CBCS's small radiation resistance, which is characteristic of electrically-small antennas in free space. An efficiency factor of -9.6 dB is achieved for a CBCS with a cavity height of, for instance, $0.01\lambda_0$; this "gain" can be enhanced by increasing the cavity height; by doubling the cavity height to $0.02\lambda_0$, simulation results indicate that the efficiency factor is increased to -5.8 dB. It should be mentioned that although the results herein do not account for the ohmic loss of the antennas, a model for including finite conductivity in the computations can be established by using the Leontovich boundary condition in the MPIE-MoM formulation [124–126]. As the significance of this loss is also dependent upon the specific methodology utilized to transform these structures into resonant radiators, it is preferable to incorporate ohmic loss considerations during the fabrication process.

7.4 Conclusion

A numerical investigation into the radiation properties of electrically-small, low-profile, near-ground antennas has been presented in this study with the introduction and development of a full-wave hybrid approach based partly on a MPIE-MoM method and partly on an higher-order asymptotic wave simulator; in far field near-earth wave propagation problems, such a rigorous terminal-to-terminal, power tracking approach is necessary since the interaction between the transmitting and receiving antennas principally occurs at near-grazing angles, a region where the predominate wave contribution is non-geometrical-optics. The discrete complex image method has been applied to achieve efficient MoM computational routines. By calculating the ratio of the receiving power to the total radiated power, a system efficiency factor is employed as a figure of merit in facilitating performance comparison in the presence of ground proximity effects for various low-profile alternatives to the standard vertical dipole. Among the low-profile structures analyzed, the electrically-small cavity-backed circular slot antenna has been identified as the best low-profile replacement for the vertical dipole.

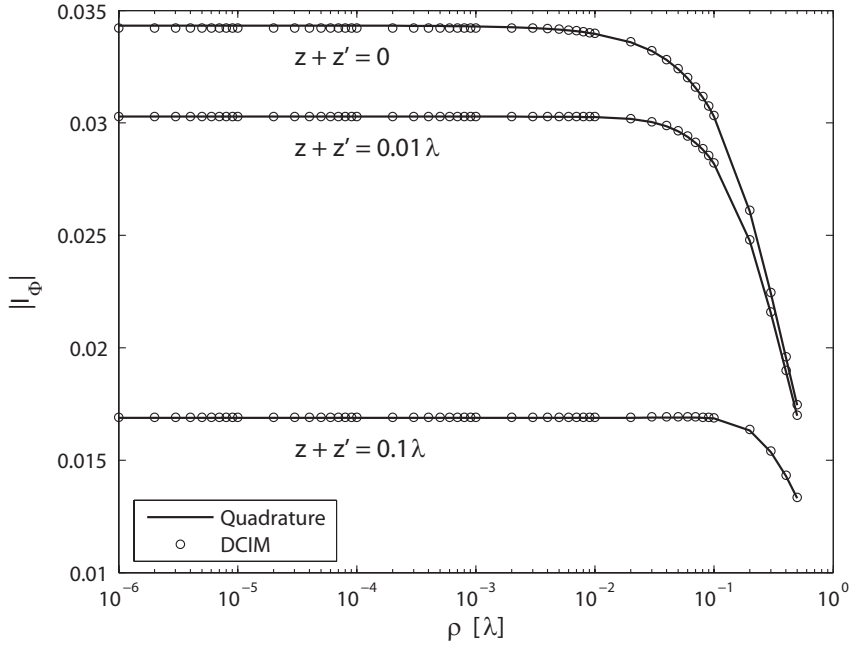

(a)

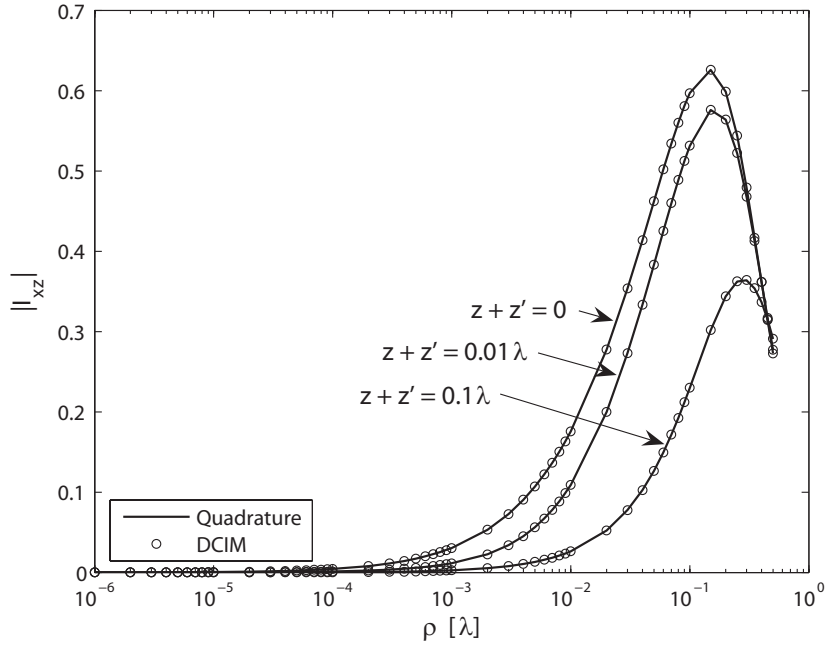

(b)

Figure 7.3: Comparison between exact and complex-image approximated values for Sommerfeld integrals (a) I_Φ and (b) I_{xz} as functions of radial distance ρ from source point. Observe that I_{yz} and I_{xz} differ only in terms of the azimuth variable. For the set of simulations shown, $N = 9$, $f = 300$ MHz, and $\epsilon_{rg} = 8 + 6i$.

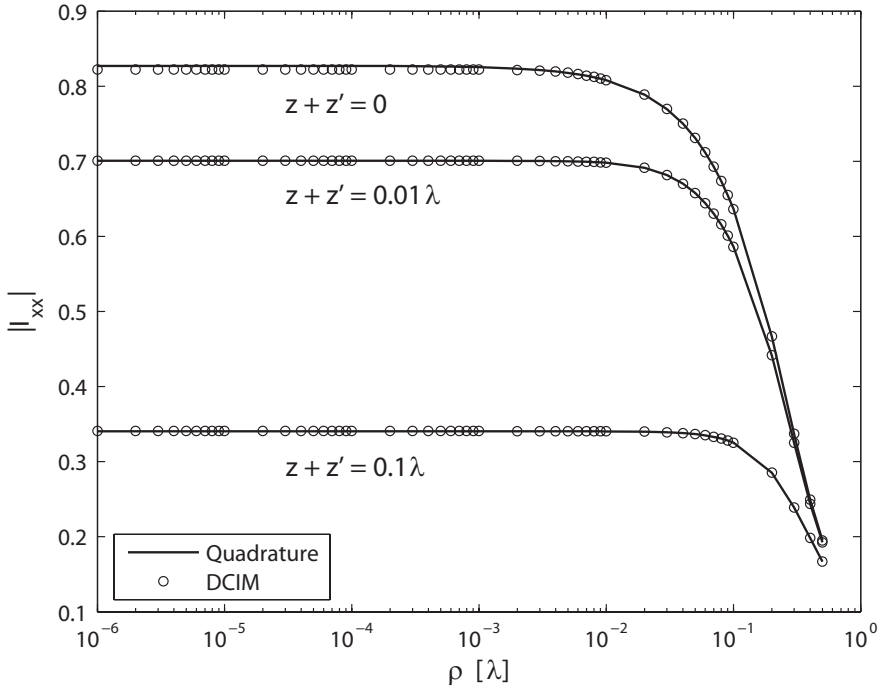

(a)

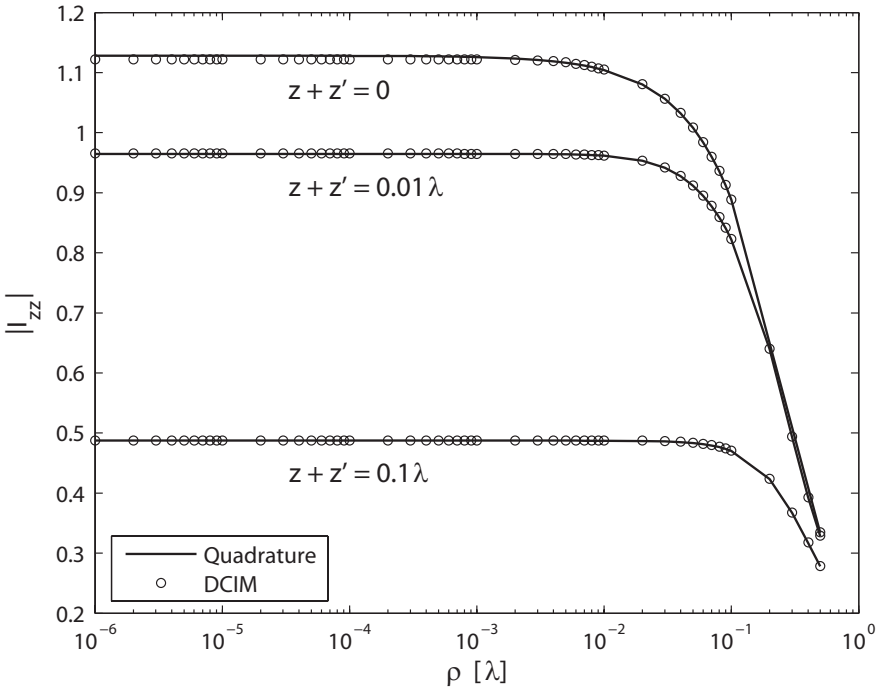

(b)

Figure 7.4: Comparison between exact and complex-image approximated values for Sommerfeld integrals (a) I_{xx}, and (b) I_{zz} as functions of radial distance ρ from source point. As in Figure 7.3, $N = 9$, $f = 300$ MHz, and $\epsilon_{rg} = 8 + 6i$.

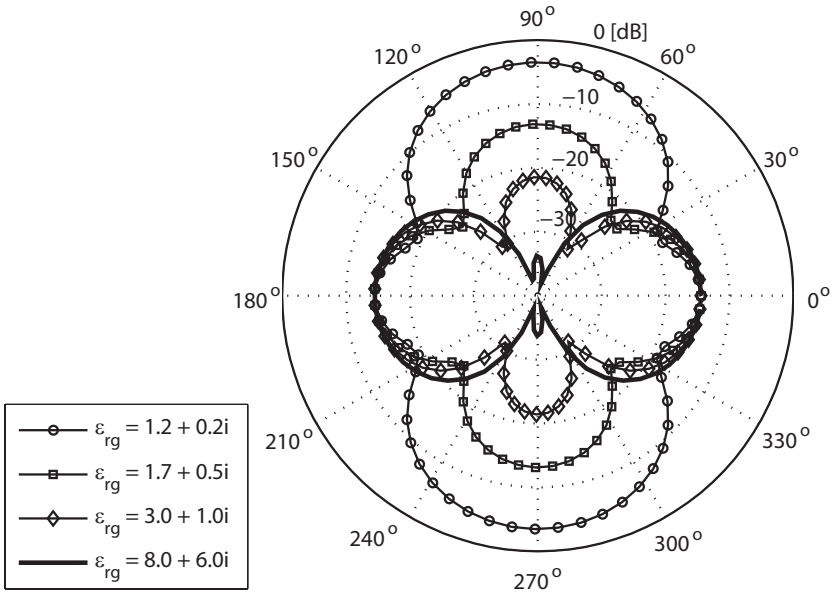

Figure 7.5: Normalized azimuthal (ϕ) radiation patterns (E_{xx} only, in dB) in the far field for an ideal horizontal dipole pointed toward $\phi = 0°$ for various ground permittivities; both source and observation points are directly on the ground surface.

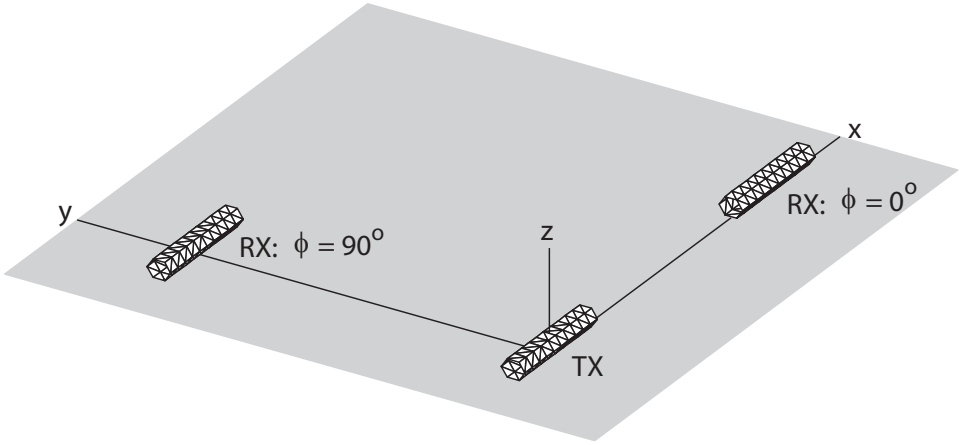

Figure 7.6: Two configurations for HH located slightly above the $z = 0$ plane (z^+). ϵ_{rg} for half-space $z < 0$ is $8 + 6i$. Maximum power is received when receiver is at $\phi = 0°$. HH^* configurations are obtained by moving the antennas to z^-.

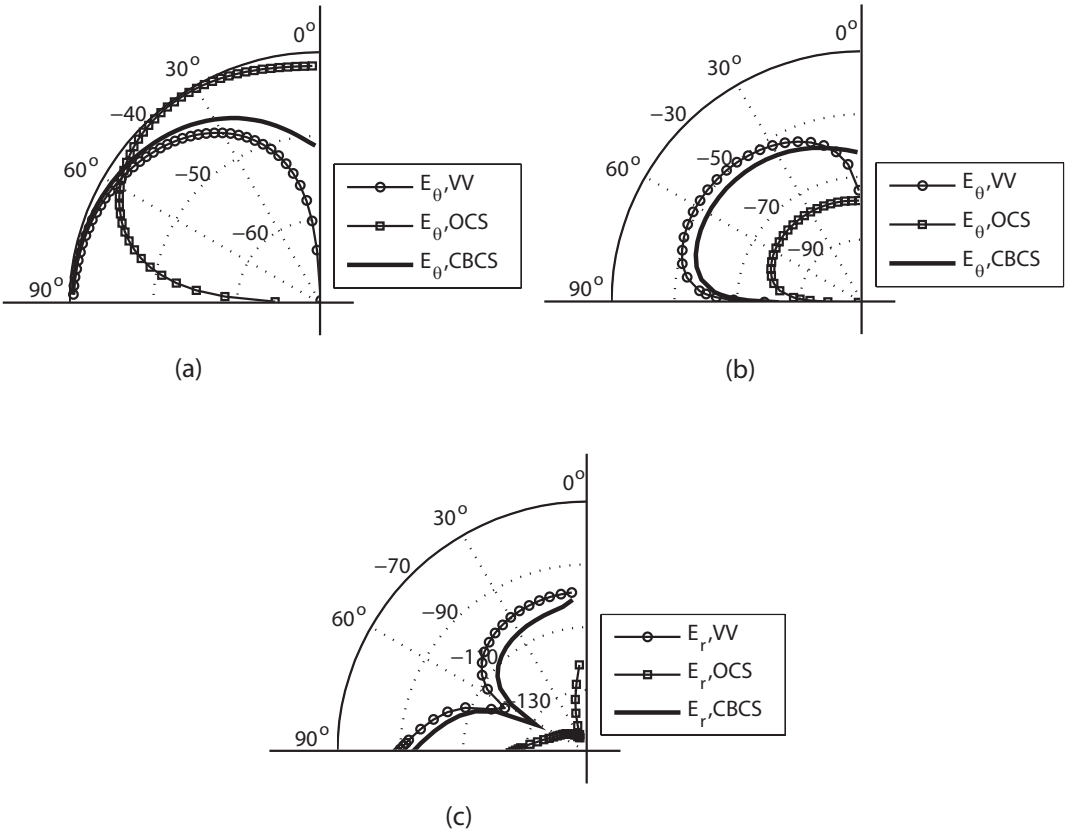

Figure 7.7: Normalized elevation (θ) radiation patterns (in dB) for vertical dipole, ordinary circular slot, and cavity-backed circular slot: (a)—free space; (b) and (c)—above a ground with $\epsilon_{rg} = 8 + 6i$. The main interest in this study is the behavior at elevation angle $\theta \approx 90°$.

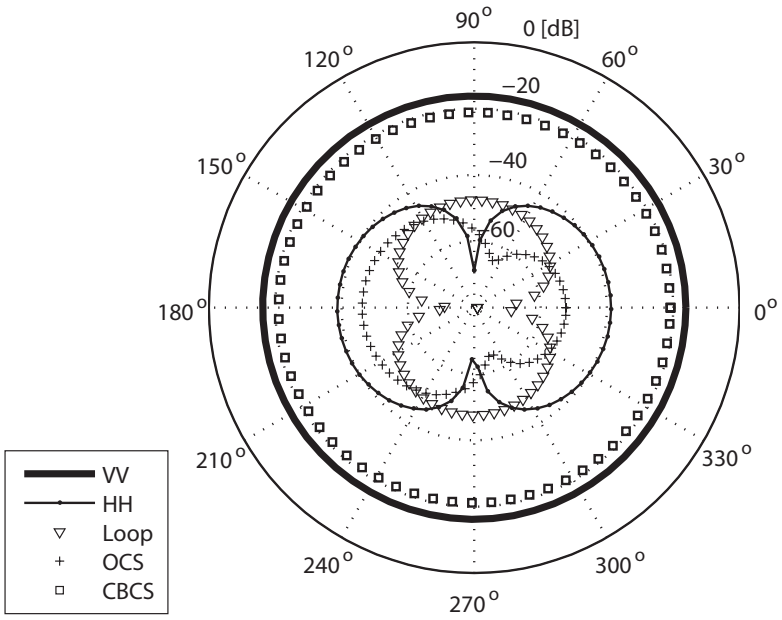

Figure 7.8: Normalized azimuthal (ϕ) radiation patterns (total field, in dB) in the far field at $\theta = 90°$ for different low profile antennas as compared to the standard vertical dipole; both observation point and antenna are directly on the ground surface ($\epsilon_{rg} = 8 + 6i$); also, the H-dipole is pointed toward $\phi = 0°$.

CHAPTER VIII

Conclusion

Accurate solutions to an important set of problems relevant to the prediction of radiowave propagation in the near-ground environment have been presented. The propagation domain of interest is defined by natural terrain features; the derivation of the solutions includes analytical, numerical, statistical, and experimental approaches. The topics of discussion are summarized below, followed by a list of suggestions for future studies.

8.1 Research Summary

The first part of this work describes the effects of vegetation and snow layers on the near-ground radio channel. In Chapter II, the presence of a continuous dielectric covering is considered by modeling the propagation environment as a homogeneous two-layer medium. Complete second order asymptotic far field expressions are provided for arbitrary transmitting and receiving terminal locations. The roles and importance of different contour integral contributions (i.e., branch cut, pole, saddle point) are explained. It is seen that, for near-grazing propagation, a Norton wave term analogous to that observed in the half-space configuration is the dominant signal contribution either when the transmitter and receiver are both located above the dielectric layer or when one is above and the other is within the layer; this surface

wave, which is supplied by the higher order component of the saddle point contribution, must be included to correct the geometrical optics reflected field when the locations of interest are localized within one to two wavelengths of the air/dielectric interface. Of course, as it has been clarified by previous works, the lateral surface wave (supplied by the branch cut) is the principal signal contribution when both radio terminals are embedded within the vegetation or snow layer. Instead of a ray or image method, a normal mode approach is employed for cases when the lateral wave is not the dominant contribution; in this approach, the residue contributions, which can be physically interpreted as guided modes in the form of either pole-surface waves or leaky waves, are seen to provide negligible contribution in the far field. Simulation results computed using the derived field expressions indicate that the signal intensity and signal frequency response at the receiver have a strong dependence on the permittivities of the vegetation or snow layer and of the ground.

Noting that a vegetation layer may not be infinite in extend in the horizontal direction, the higher order asymptotic model developed in Chapter II is subsequently applied in analyzing the effects of a discontinuity in the dielectric layer. The basis of the method introduced in Chapter III is a field integration approach derived from the Kirchhoff-Fresnel principle and essentially provides a first order approximation. The specific treatment assumes the transmitter is inside the foliage layer and the receiver is positioned on the opposite side of the truncation plane with respect to the transmitter location. The far field radiation pattern is calculated by integrating the surface fields over 2D plane containing the truncation facet of the foliage; after separating the relevant wave components on the spatial integration plane according to their distinct phase variations, the encountered double integral is evaluated using the method of stationary phase. Validation of the solution of this canonical problem

is provided through comparisons with the results of a half-space configuration, a ray-tracing routine developed by Tamir, and an experimental approach carried out using a scaled-replica of the propagation geometry. In analyzing the field patterns as a function of receiver height, it is seen that while a full 2D stationary phase approximation can lead to accurate results for a receiver located high above the ground, a modified approach in the form of a 1D stationary phase approximation augmented with numerical integration in the vertical direction is more appropriate for a receiver located in the near-ground region. The established approach shows improvements over the existing ray-tracing technique in that fewer explicit assumptions are built into the solution process. It is also noted that signal intensity measurements taken from the scaled-replica of the truncated layer show good agreement with the theoretical calculations.

In both Chapters II and III, the terrain surface is assumed to be smooth; the effects of terrain irregularities encountered along the propagation path, however, must be included for a complete description of the radio channel. In the second portion of this work, in view of the fact that the near-ground propagation characteristics of an undulating terrain cannot be accurately captured using standard analytical models, a 2D surface integral equation-based solver is developed for path-loss prediction. The high-order routine implemented in Chapter IV allows the attainment of solutions with a smaller number of unknowns as compared to conventional low-order solvers. Upon further enhancement—namely, with acceleration facilitated by the fast multipole method and with faster convergence provided by a phase extraction technique, the implementation becomes an attractive tool for signal coverage prediction over large terrain profiles. It is shown that by applying this solver, when combining with an adaptive surface segmentation routine, as few as one to two average unknowns per

wavelength is adequate in obtaining accurate solutions for a gently-varying terrain; this significantly reduces the memory storage and computational expense for the simulation of long-distance propagation effects. The controllable exponential convergence behavior of the solver has been demonstrated; the utilization of the solver for creeping wave diffraction analysis also has been carried out.

In Chapter V, in order to assess the significance of small random terrain roughness as pertaining to LOS and NLOS propagation, the numerical simulator developed in Chapter IV is modified through an exploitation of the quasi-planar nature of the terrain surface. The original terrain profile is replaced by an equivalent simplified profile that is more amenable to fast routines; specifically, the profile is decomposed into three sections, with the middle portion non-local to the transmitter and receiver locations being replaced by a physically flat surface (with an effective height) over which the interactions can be cast in block-Toeplitz matrix form, while the sections local to the transmitter and receiver remain unchanged. This model implies that the primary statistics of the received signal are predominately dictated by the statistics of the rough terrain local to the transmitter and receiver. Subsequently, propagation over the equivalent profile is solved using a recursive forward marching scheme based on the surface integral equation solver put forth in Chapter IV, with efficiency speed-up achieved by applying FFT in carrying out the block-Toeplitz matrix-vector multiplies. The convergence of the recursive routine has been demonstrated, and results from Monte Carlo simulations for LOS and NLOS links have shown that the equivalent model provides accurate estimations to signal statistics such as coherent and incoherent received powers.

The investigation of the effects of terrain roughness on near-ground propagation is continued in Chapter VI. In spite of the fact that a variety of analytical and

numerical routines have been proposed by other workers for the general treatment of the scattering properties of rough surfaces, much disagreement remains in the solution of the problem for near-grazing scenarios [127]. In striving to analytically describe the near-grazing propagation of signals from 2D and 3D radiators, an existing perturbation approach is exploited to formulate closed-form expressions for the coherent rough surface reflection coefficients; although the perturbation approach is originally intended for analyzing the scattering coefficients of a ground with scale of roughness much smaller than the wavelength, it is shown through Monte Carlo simulations that the effective reflection coefficients reported in Chapter VI are applicable for near-ground path-loss prediction even when the surface variation (*rms* height) is on the order of a wavelength or more.

While the focus of the first two portions of this work is on radiowave propagation issues, the subject of interest in the last section is the analysis of the radio link system efficiency with the inclusion of antenna performance metrics. In Chapter VII, an investigation into the simulation of low-profile, electrically-small antennas for near-ground operations is undertaken. Systems with above-surface and sub-surface link terminals are simulated in the presence of a flat ground interface using a hybrid full-wave approach consists of a MPIE-MoM routine for modeling the antenna structure and a higher order asymptotic propagator for tracking the wave energy across the ground surface; the method of discrete images are applied to approximate the half-space Sommerfeld integrals. The rigorous terminal-to-terminal, power tracing approach as outlined is necessary since the interaction between the transmitting and receiving antennas principally occurs at near-grazing angles, a condition at which the predominate wave contribution is non-geometrical-optics. Transceiver systems utilizing different types of near-ground antenna structures including the dipole, loop,

ordinary circular slot, and cavity-backed circular slot have been characterized; the impact of ground proximity effects on system parameters such as antenna input impedance, radiation pattern, overall path-loss, and transceiver efficiency also has been illustrated.

8.2 Recommendations for Future Studies

The propagation solutions as featured in this work can serve as fundamental blocks for analyzing more complicated propagation scenes. As the demand for accurate realistic propagation tools increases, extensions or modifications of these solutions can be made to support future research in the areas listed below.

8.2.1 Analytical Treatment of Foliage-Covered Terrain with Undulating Interfaces

In Chapter II, the canonical two-layer problem is modeled with the assumption that both the vegetation and ground interfaces are smooth. The effects of a Gaussian random vegetation interface have been addressed by [24], wherein it is shown that—for radio terminals situated within a forest canopy—the lateral wave is not drastically affected by surface roughness even when the *rms* height is on the scale of the signal wavelength. The distorted Born approximation for solving the volumetric integral equation as described in [24] can be similarly applied to study configurations in which both the transmitter and receiver are located above the rough canopy interface or one of them is below. The near-grazing condition would once again necessitate a second order asymptotic analysis. Within the formulation setup in spectral form, the coherent reflection coefficients as conveyed by (6.33) and (6.36) can be used in evaluating the significance of the rough ground interface.

8.2.2 Numerical Treatment of Foliage-Covered Terrain with Undulating Interfaces

A numerical simulation of the propagation of ground waves in the presence of a foliage-covered irregular terrain profile can be attained by extending the high-order surface integral equation solver prescribed in Chapter IV to the two-layer geometry. The machineries within the solver such as phase extraction and the fast multipole method can be employed here as well to achieve accurate and computationally-efficient solutions. The principal wave mechanism of interest in this case is the lateral wave; specifically, the effects of the highly undulating ground and foliage profiles on this wave mode need to be clarified.

8.2.3 Kirchhoff-Huygens Method for Multiple Foliage Layer Discontinuities

The first order approximation as proposed in Chapter III for modeling a truncated vegetation layer can be cascaded in succession to develop a forward marching scheme for analyzing propagation across multiple vegetation slabs. The full 2D stationary phase approximation can be used as previously described in determining the dominant wave paths for points of interaction located high above the ground. For field points located close to the ground, as the propagation of the fields from one integration plane to the next may be interpreted as a convolution, appropriate FFT routines can be adopted to speed up the forward marching procedure. As in the single truncation problem, the results of the overall model can be verified against measurements taken from a scaled-replica of the propagation domain.

8.2.4 Effective Reflection Properties of Rough Surfaces in NLOS Radio Links

The perturbation approach as followed in Chapter VI is valid for the characterization of LOS radio channels through an expansion of the perturbation current in a series about the solution for a flat slab; the excitation signal is assumed to be inci-

dent from above the slab. For treating the NLOS case, a slight modification to the formalism is required as the transmitter or receiver (or both) may be located below the physical mean elevation of the roughness. When only the receiver is situated below the mean, the perturbation current as found previously remains unchanged and only the Green's function in the expression for deriving the scattered fields needs to be replaced; when the transmitter is embedded within the slab, the zeroth current can be readily obtained by applying the flat-interface two-layer problem formulations from Case 3 of Chapter II; subsequently, the higher order currents can be recursively deduced as in Chapter VI. The incoherent power encountered in the NLOS configuration should also be computed as it may be significant as compared to the coherent component.

8.2.5 Near-Ground Antenna Performance Evaluation in Generalized Environments

The hybrid antenna modeling technique put forward in Chapter VII can be generalized to handle arbitrary terrain conditions. For example, for antennas located inside a foliage layer with a flat interface, the asymptotic routine from Chapter II can be used to propagate the far field signal from one antenna to another; at the transmitting and receiving terminals, the proper Green's functions for a layered-media should be inserted into the MoM procedure for calculating the induced currents. For irregular profiles, the formulations from Section 8.2.1 above—once they have been developed—could facilitate the inclusion of rough-interface effects into the computation of the antenna far field radiation pattern; however, in this case, to ensure that the MoM procedure remains tractable, it may be necessary to approximate the layer interfaces local to the antennas as smooth surfaces.

APPENDICES

APPENDIX A

Supplement to Chapter II

A.1 Integral Solutions for Case 1 ($z' > 0$ and $z > 0$)

Exact expressions for the electric field of a dipole radiating in the presence of a two-layer medium are derived from the dyadic Green's function. If the arbitrarily-oriented dipole is located on the z-axis at (0, 0, z') with the current moment vector $I_o\vec{l} = I_o(l_x\hat{x} + l_y\hat{y} + l_z\hat{z})$, it can be shown that—for Case 1—the general equation for the scattered electric field at observation point (ρ,ϕ,z), with $z' > z$, can be written as

$$E_{ij}^s = -\frac{\omega\mu_o I_o l_i}{8\pi}\int_0^\infty f_{ij}(k_\rho)e^{ik_{oz}(z+z')}dk_\rho \tag{A.1}$$

where the function in the integrand is dependent upon the dipole orientation and the field component of interest (x, y, or z):

$$f_{zx}(k_\rho) = \frac{-2ik_\rho^2}{k_o^2}R_{TM}(k_\rho)J_1(k_\rho\rho)\cos\phi, \tag{A.2}$$

$$f_{zy}(k_\rho) = \frac{-2ik_\rho^2}{k_o^2}R_{TM}(k_\rho)J_1(k_\rho\rho)\sin\phi, \tag{A.3}$$

$$f_{zz}(k_\rho) = \frac{2k_\rho^3}{k_{oz}k_o^2}R_{TM}(k_\rho)J_0(k_\rho\rho), \tag{A.4}$$

$$f_{xx,yy}(k_\rho) = k_\rho[R_-(k_\rho)J_0(k_\rho\rho) \pm R_+(k_\rho)J_2(k_\rho\rho)\cos(2\phi)], \tag{A.5}$$

$$f_{xy,yx}(k_\rho) = k_\rho R_+(k_\rho)J_2(k_\rho\rho)\sin(2\phi), \tag{A.6}$$

$$f_{xz}(k_\rho) = \frac{2ik_\rho^2}{k_o^2} R_{TM}(k_\rho) J_1(k_\rho \rho) \cos\phi, \tag{A.7}$$

$$f_{yz}(k_\rho) = \frac{2ik_\rho^2}{k_o^2} R_{TM}(k_\rho) J_1(k_\rho \rho) \sin\phi. \tag{A.8}$$

The total reflection coefficient is given by

$$\begin{aligned} R_P &= R_P^{01} + T_P^{01} T_P^{10} \sum_{u=1}^{\infty} (R_P^{10})^{u-1} (R_P^{12} e^{i2k_{1z}d})^u \\ &= R_P^{01} + \frac{[1-(R_P^{01})^2] R_P^{12} e^{i2k_{1z}d}}{1 + R_P^{01} R_P^{12} e^{i2k_{1z}d}} \\ &= \frac{R_P^{01} + R_P^{12} e^{i2k_{1z}d}}{1 + R_P^{01} R_P^{12} e^{i2k_{1z}d}}, \end{aligned} \tag{A.9}$$

and the mixed reflection coefficient is

$$R_\pm(k_\rho) = \frac{R_{TE}(k_\rho)}{k_{oz}} \pm \frac{R_{TM}(k_\rho) k_{oz}}{k_o^2}, \tag{A.10}$$

where the simple reflection coefficients for a wave going from layer m to layer n are the following:

$$R_{TE}^{mn} = \frac{k_{mz} - k_{nz}}{k_{mz} + k_{nz}}, \tag{A.11}$$

$$R_{TM}^{mn} = \frac{\varepsilon_{rn} k_{mz} - \varepsilon_{rm} k_{nz}}{\varepsilon_{rn} k_{mz} + \varepsilon_{rm} k_{nz}}. \tag{A.12}$$

The wavenumber is represented by k_u ($u = 0$, 1, or 2) and

$$k_{uz} = \sqrt{k_u^2 - k_\rho^2}. \tag{A.13}$$

The direct field must be added to the scattered field to obtain the total field. If $z' < z$, relation (2.44) should be applied.

A.2 Integral Solutions for Case 2 ($-d < z' < 0$ and $z > 0$)

When the dipole is inside the dielectric layer and the observation point is in air, the derivation for the total field is more complicated but is not much different from

that for the first case. Simple manipulations of the dyadic Green's function give the transmitted field as

$$E_{ij} = -\frac{\omega\mu_o I_o l_i}{8\pi}\int_0^\infty f_{ij}(k_\rho)e^{ik_{oz}z}dk_\rho, \tag{A.14}$$

where the set of $f_{ij}(k_\rho)$ functions can be shown to be

$$f_{zx}(k_\rho) = \frac{-2ik_\rho^2 k_{oz}}{k_o^2 k_{1z}}[T_{TM}^{up}e^{ik_{1z}|z'|} + T_{TM}^{down}e^{ik_{1z}(2d+z')}]J_1(k_\rho\rho)\cos\phi, \tag{A.15}$$

$$f_{zy}(k_\rho) = \frac{-2ik_\rho^2 k_{oz}}{k_o^2 k_{1z}}[T_{TM}^{up}e^{ik_{1z}|z'|} + T_{TM}^{down}e^{ik_{1z}(2d+z')}]J_1(k_\rho\rho)\sin\phi, \tag{A.16}$$

$$f_{zz}(k_\rho) = \frac{2k_\rho^3}{k_{1z}k_o^2}[T_{TM}^{up}e^{ik_{1z}|z'|} + T_{TM}^{down}e^{ik_{1z}(2d+z')}]J_0(k_\rho\rho), \tag{A.17}$$

$$\begin{aligned} f_{xx,yy}(k_\rho) = k_\rho\{&[T_+^{up}e^{ik_{1z}|z'|} + T_-^{down}e^{ik_{1z}(2d+z')}]J_0(k_\rho\rho) \\ &\pm[T_-^{up}e^{ik_{1z}|z'|} + T_+^{down}e^{ik_{1z}(2d+z')}]J_2(k_\rho\rho)\cos(2\phi)\}, \end{aligned} \tag{A.18}$$

$$f_{xy,yx}(k_\rho) = k_\rho\{T_-^{up}e^{ik_{1z}|z'|} + T_+^{down}e^{ik_{1z}(2d+z')}\}J_2(k_\rho\rho)\sin(2\phi), \tag{A.19}$$

$$f_{xz}(k_\rho) = \frac{2ik_\rho^2}{k_o^2}[-T_{TM}^{up}e^{ik_{1z}|z'|} + T_{TM}^{down}e^{ik_{1z}(2d+z')}]J_1(k_\rho\rho)\cos\phi, \tag{A.20}$$

$$f_{yz}(k_\rho) = \frac{2ik_\rho^2}{k_o^2}[-T_{TM}^{up}e^{ik_{1z}|z'|} + T_{TM}^{down}e^{ik_{1z}(2d+z')}]J_1(k_\rho\rho)\sin\phi. \tag{A.21}$$

The various transmission coefficients are defined below:

$$T_\pm^{up}(k_\rho) = \frac{T_{TE}^{up}(k_\rho)}{k_{1z}} \pm \frac{T_{TM}^{up}(k_\rho)k_{oz}}{k_o^2}, \tag{A.22}$$

$$T_\pm^{down}(k_\rho) = \frac{T_{TE}^{down}(k_\rho)}{k_{1z}} \pm \frac{T_{TM}^{down}(k_\rho)k_{oz}}{k_o^2}, \tag{A.23}$$

$$T_P^{up} = T_P^{10}\sum_{u=0}^{\infty}(R_P^{10}R_P^{12}e^{i2k_{1z}d})^u = \frac{T_P^{10}}{1+R_P^{01}R_P^{12}e^{i2k_{1z}d}}, \tag{A.24}$$

$$T_P^{down} = R_P^{12}T_P^{10}\sum_{u=0}^{\infty}(R_P^{10}R_P^{12}e^{i2k_{1z}d})^u = \frac{R_P^{12}T_P^{10}}{1+R_P^{01}R_P^{12}e^{i2k_{1z}d}}. \tag{A.25}$$

APPENDIX B

Supplement to Chapter IV

The high-order convergence properties of the Nyström method are demonstrated in this section by simulating the 2D plane wave response of a canonical problem—i.e., a circular cylinder (radius = 1λ); the EFIE (4.31) and MFIE (4.32) are applied for the PEC and PMC cases while the PMCHWT (4.1) formulation is applied for the dielectric case. Figures B.1–B.8 are for TE; Figures B.9–B.12 are for TM. The relative error E_{rel} is defined by (4.27), with the reference solution represented by the eigenfunction solution. Note that the required integral kernels have been regularized before the application of the Nyström method; integration routines needed for the local-correction scheme have been carried out with the aid of the Gaussian quadrature rule constructed by Ma *et al.* [128] for integrands containing a logarithmic singularity.

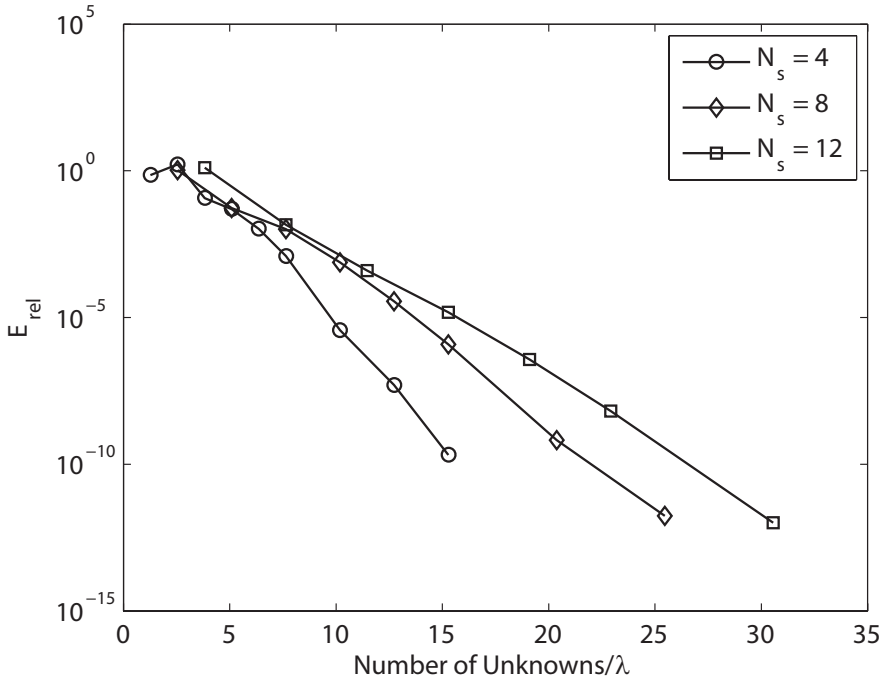

(a)

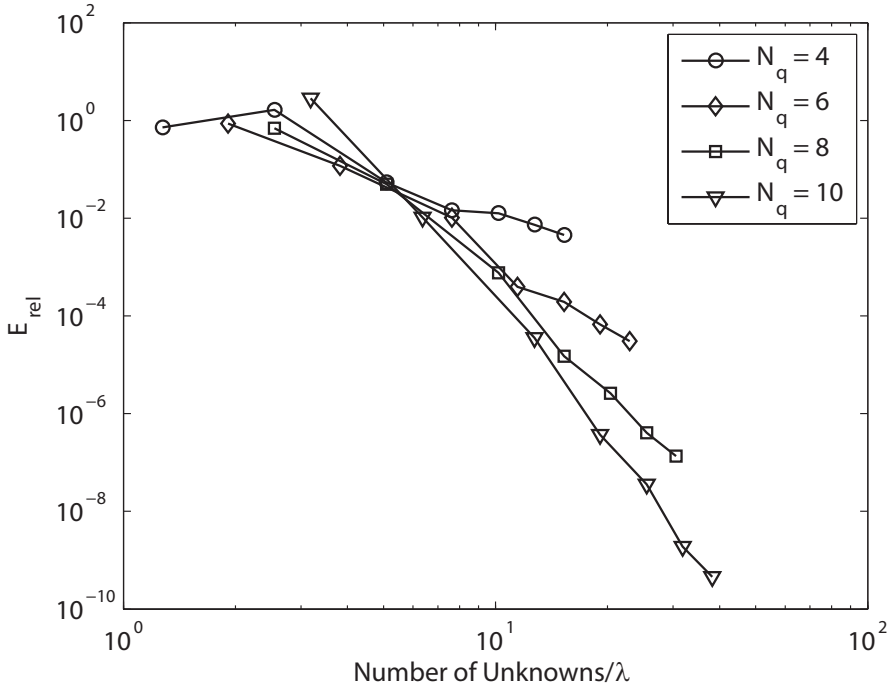

(b)

Figure B.1: TE, PEC, EFIE: (a) N_q-refinement; (b) h-refinement.

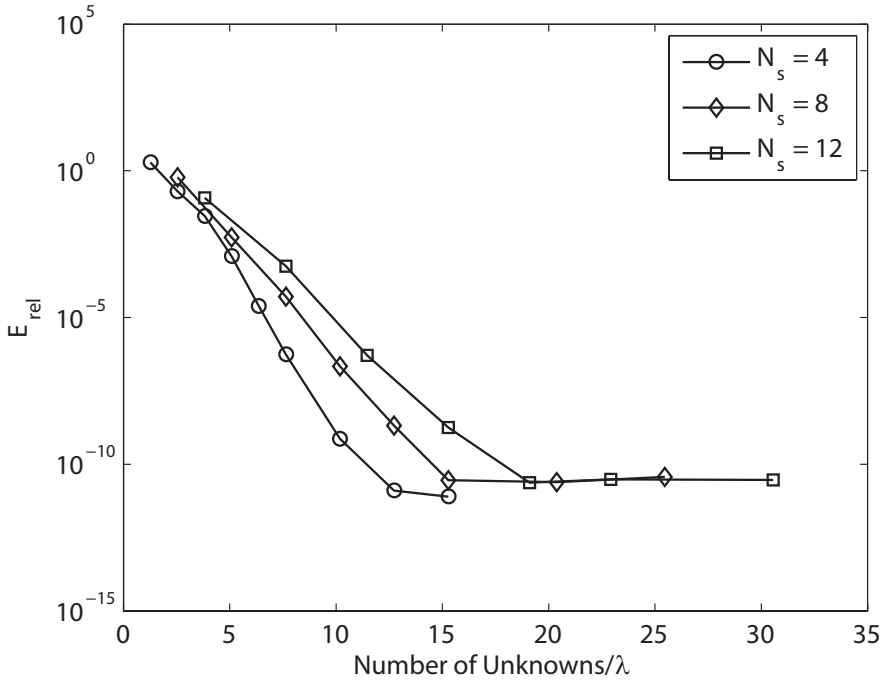

(a)

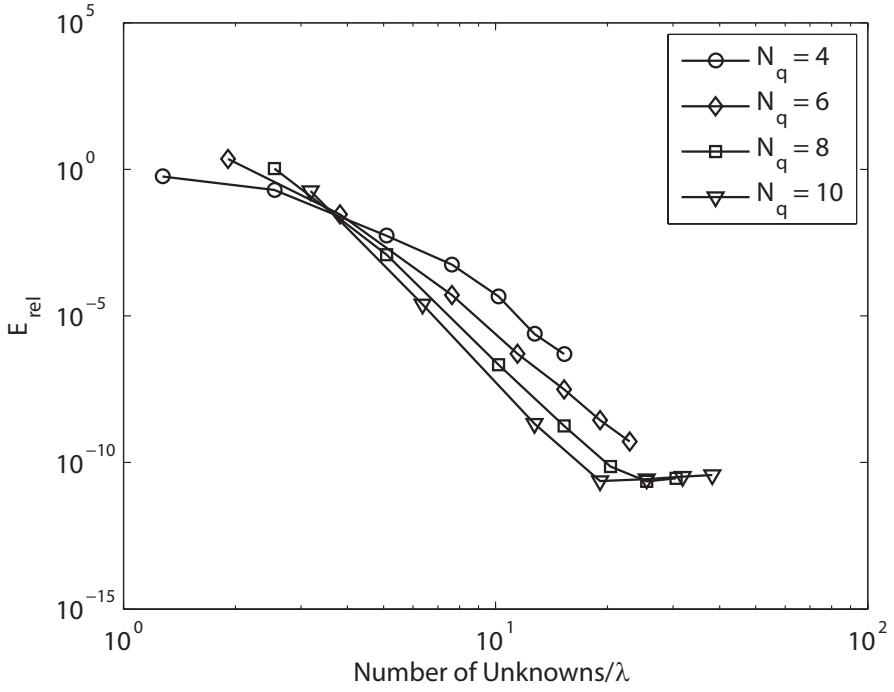

(b)

Figure B.2: TE, PEC, MFIE: (a) N_q-refinement; (b) h-refinement.

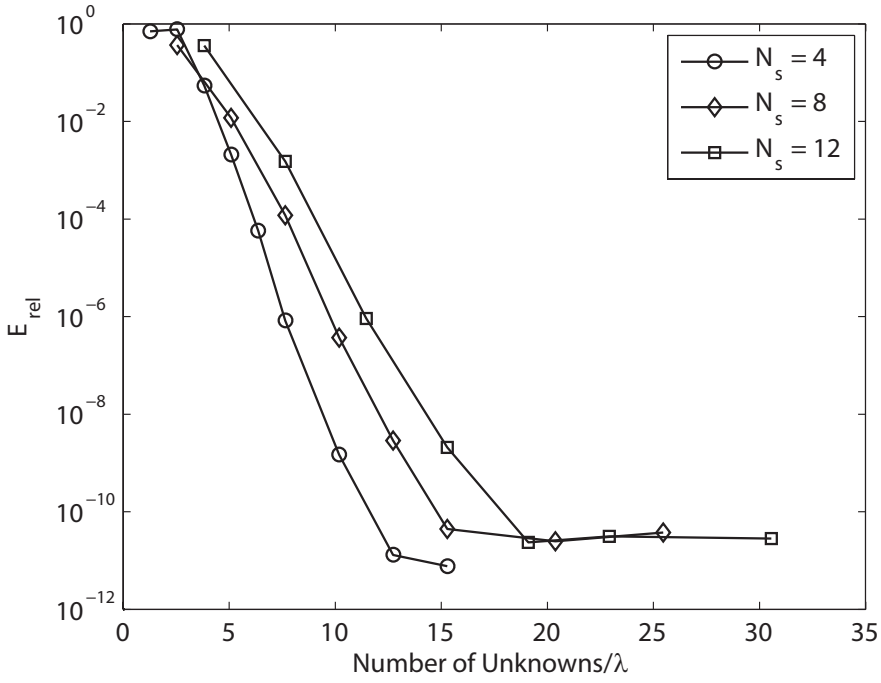

(a)

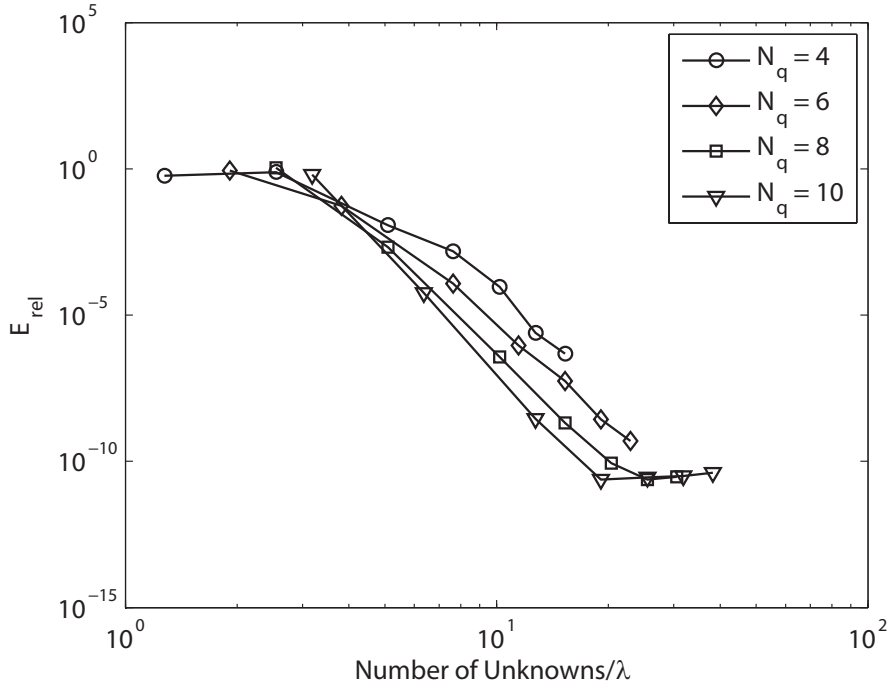

(b)

Figure B.3: TE, PMC, EFIE: (a) N_q-refinement; (b) h-refinement.

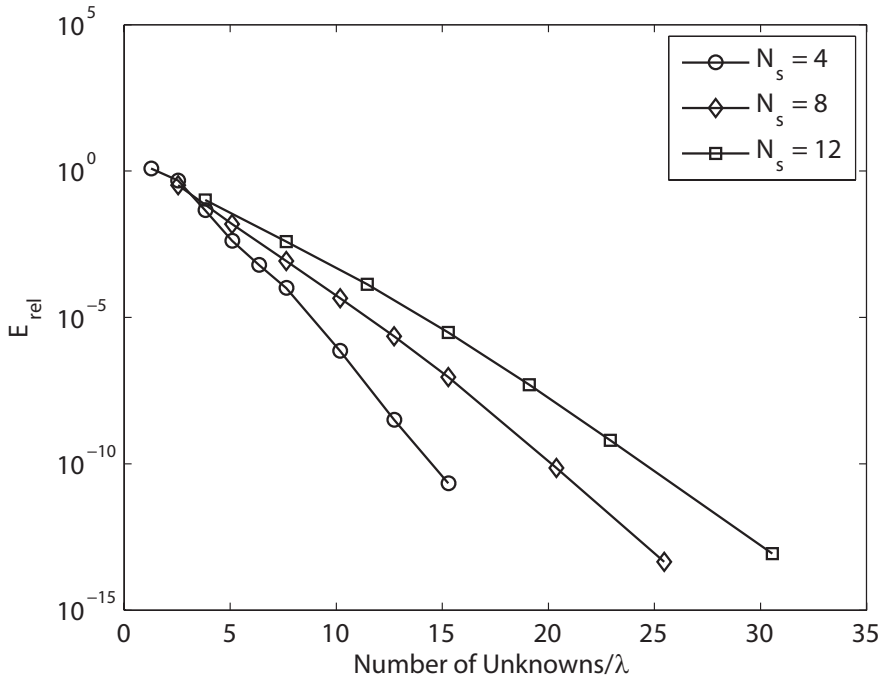

(a)

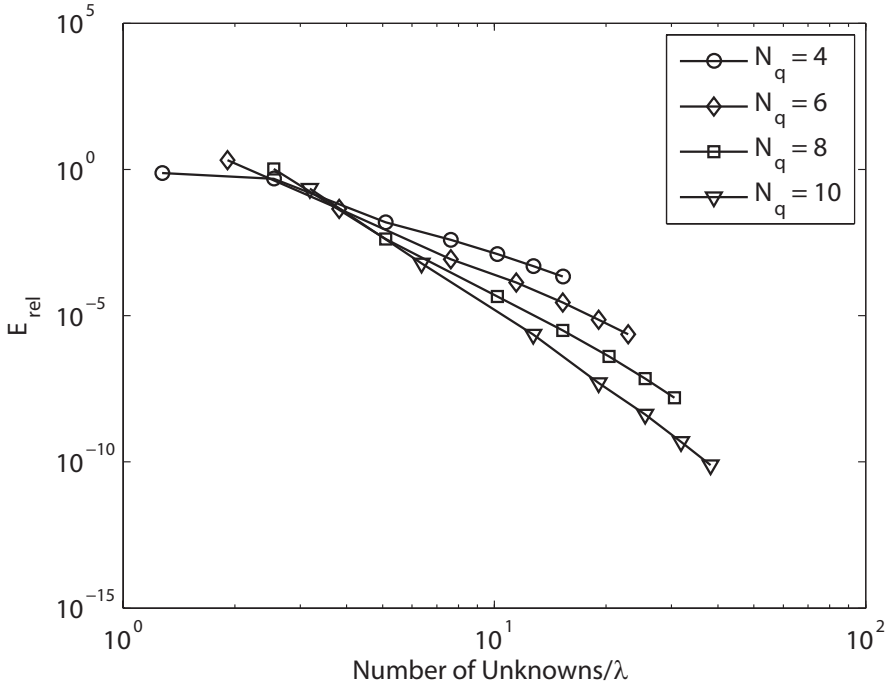

(b)

Figure B.4: TE, PMC, MFIE: (a) N_q-refinement; (b) h-refinement.

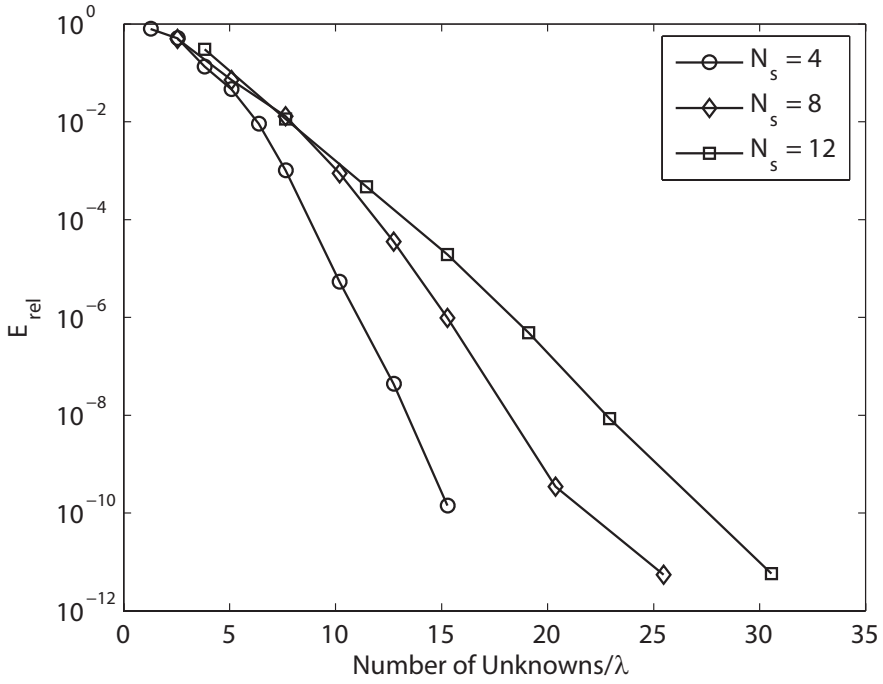

(a)

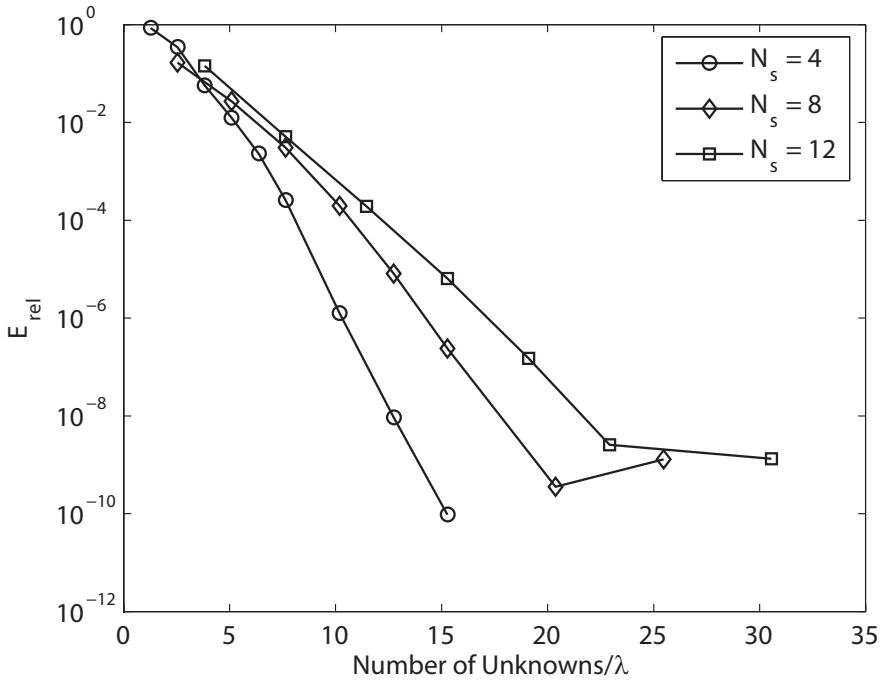

(b)

Figure B.5: TE, dielectric ($\epsilon_r = 2+i$), PMCHWT, N_q-refinement: (a) electric current; (b) magnetic current.

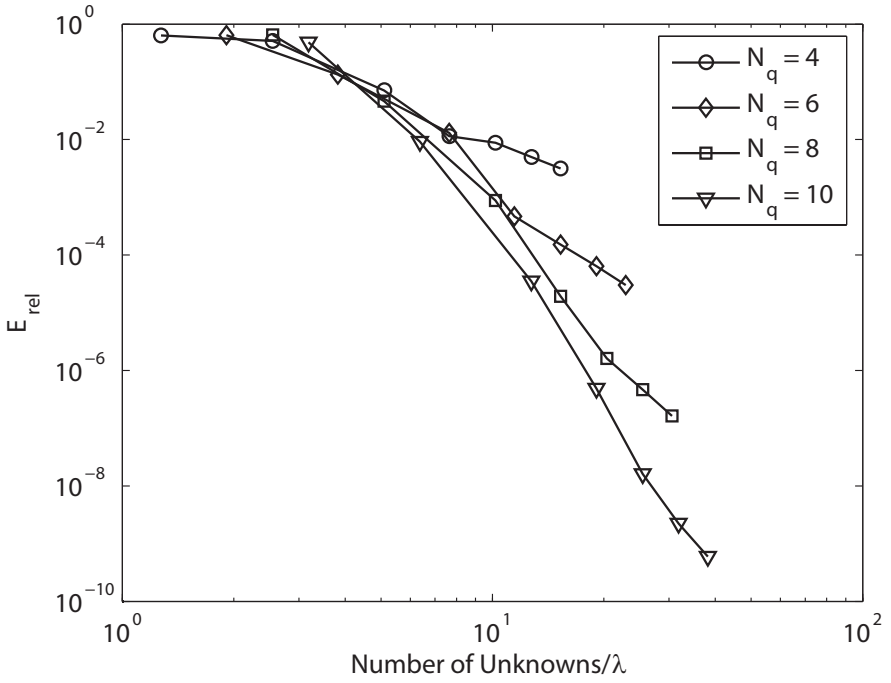

(a)

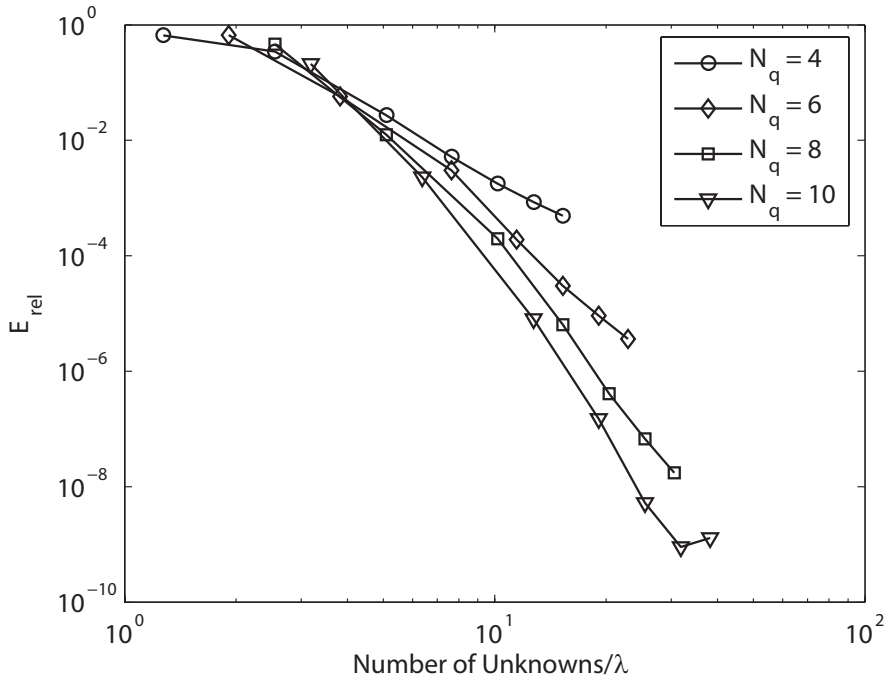

(b)

Figure B.6: TE, dielectric ($\epsilon_r = 2 + i$), PMCHWT, h-refinement: (a) electric current; (b) magnetic current.

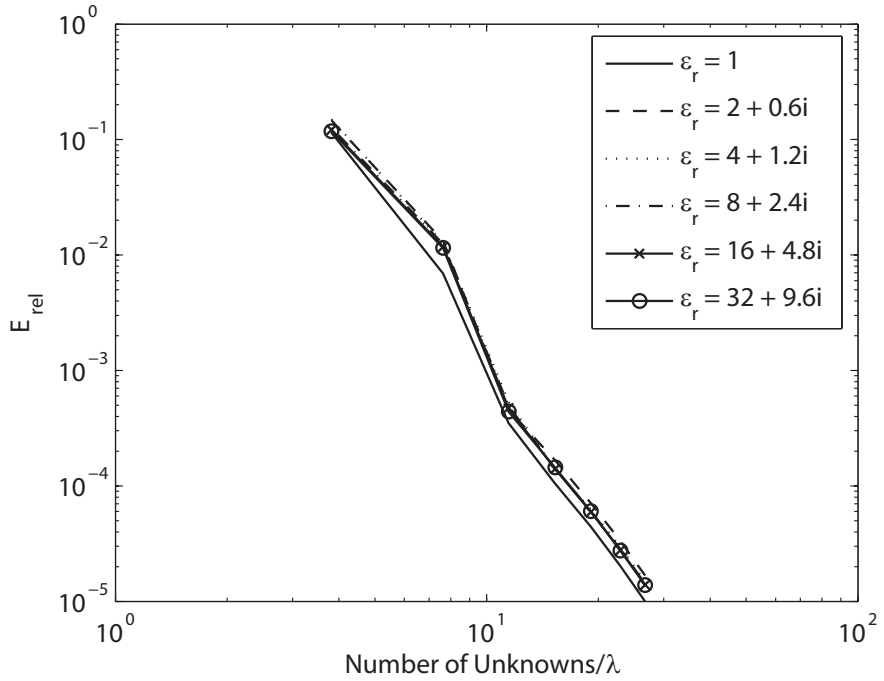

(a)

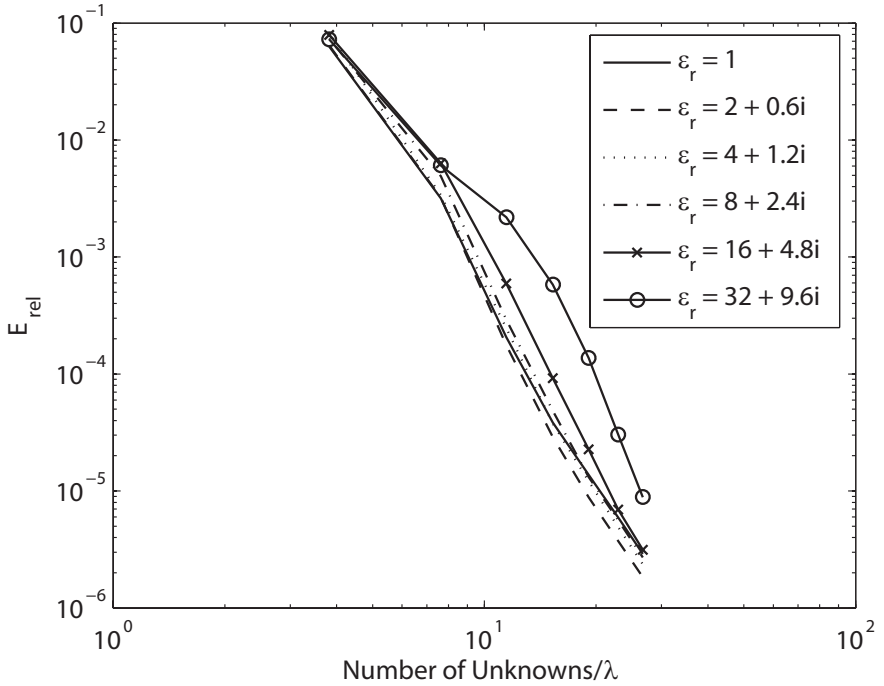

(b)

Figure B.7: TE, dielectric, PMCHWT, $N_q = 6$: (a) electric current; (b) magnetic current.

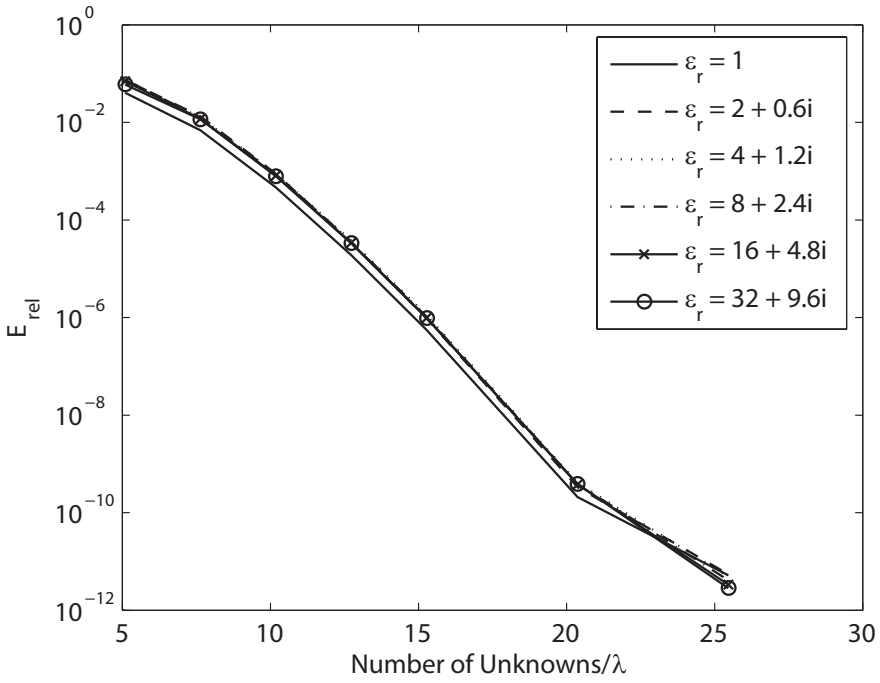

(a)

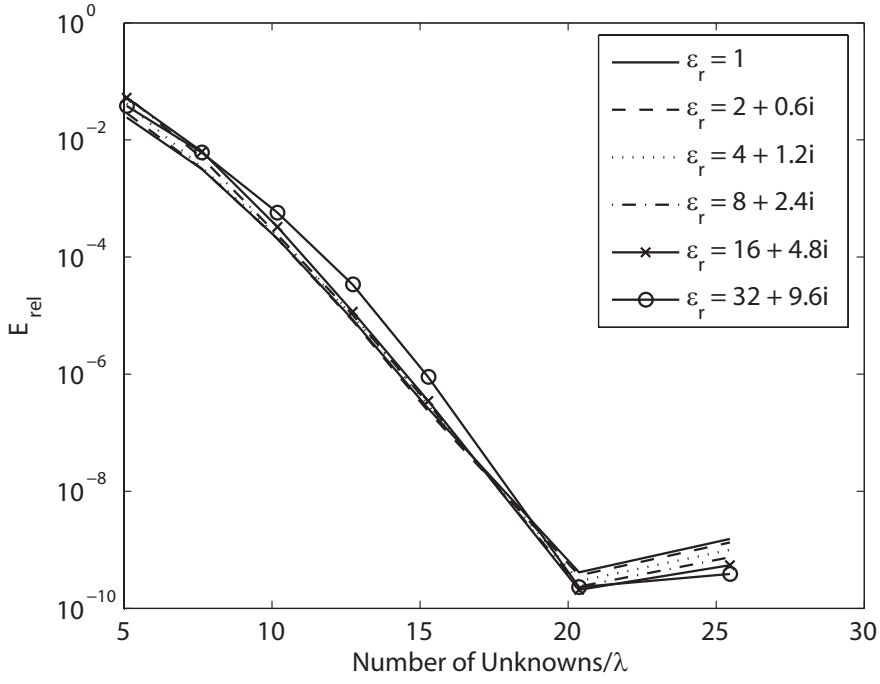

(b)

Figure B.8: TE, dielectric, PMCHWT, $N_s = 8$: (a) electric current; (b) magnetic current.

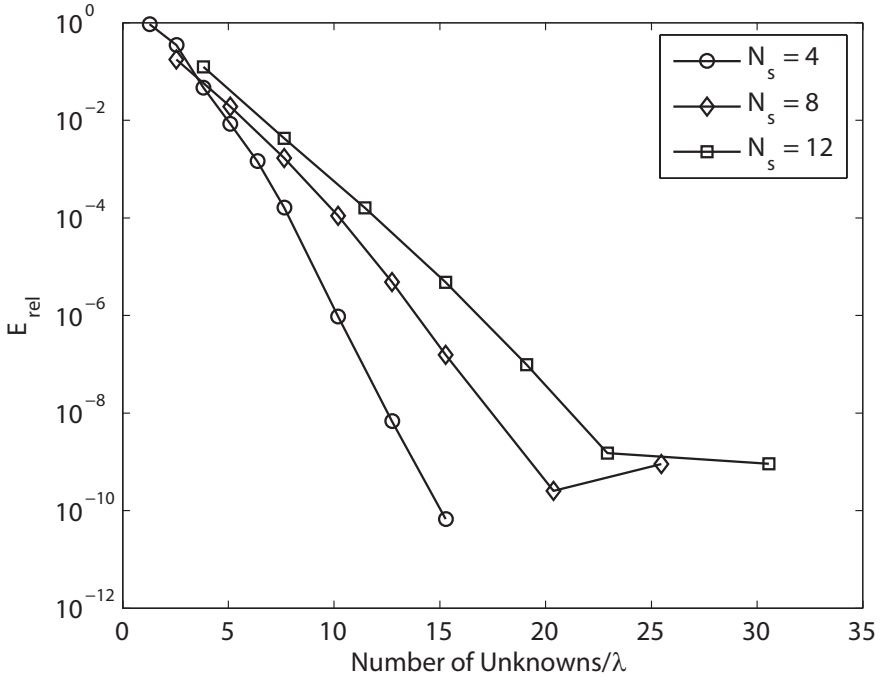

(a)

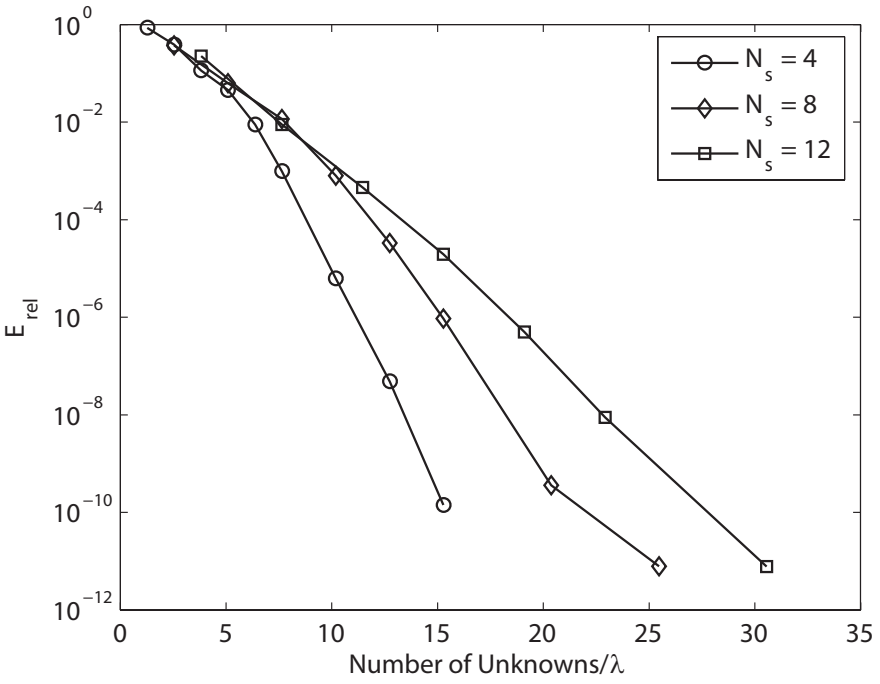

(b)

Figure B.9: TM, dielectric ($\epsilon_r = 2+i$), PMCHWT, N_q-refinement: (a) electric current; (b) magnetic current.

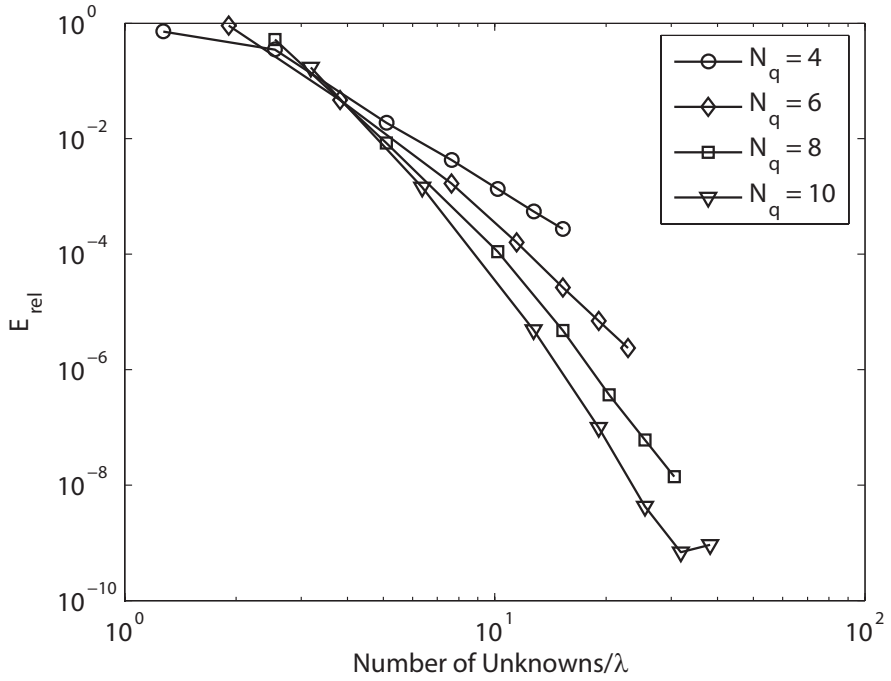

(a)

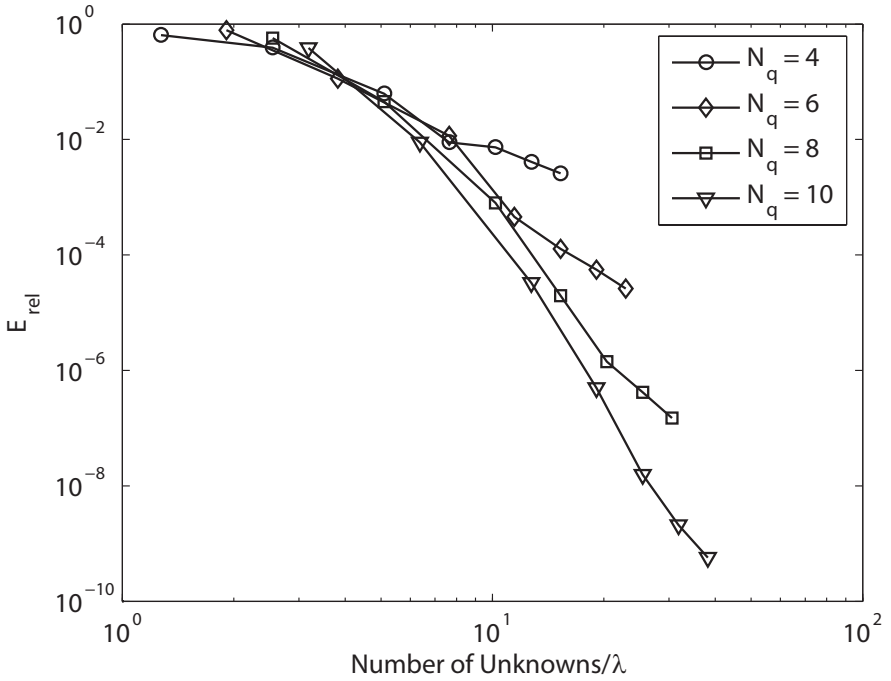

(b)

Figure B.10: TM, dielectric ($\epsilon_r = 2+i$), PMCHWT, h-refinement: (a) electric current; (b) magnetic current.

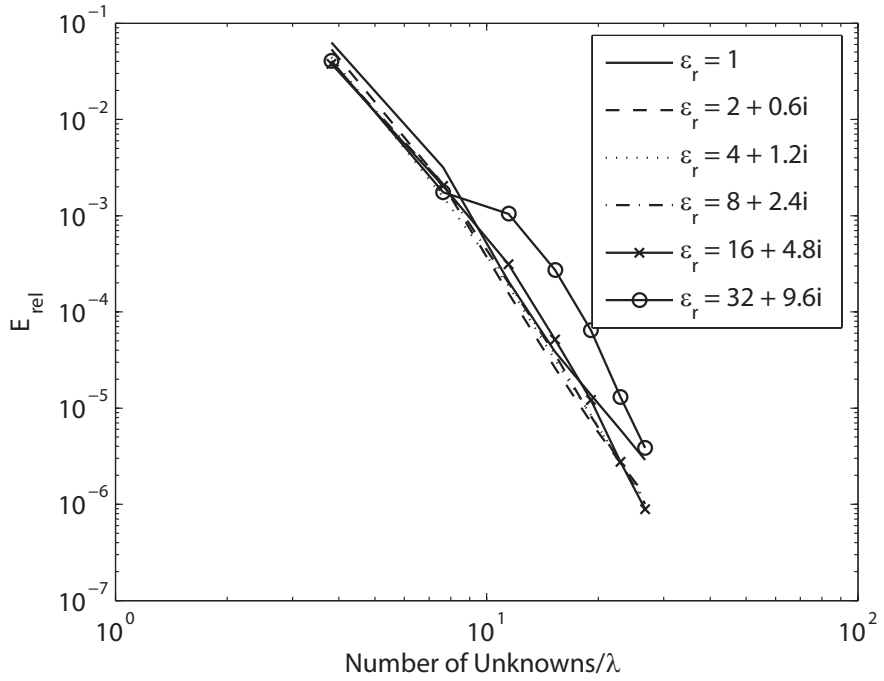

(a)

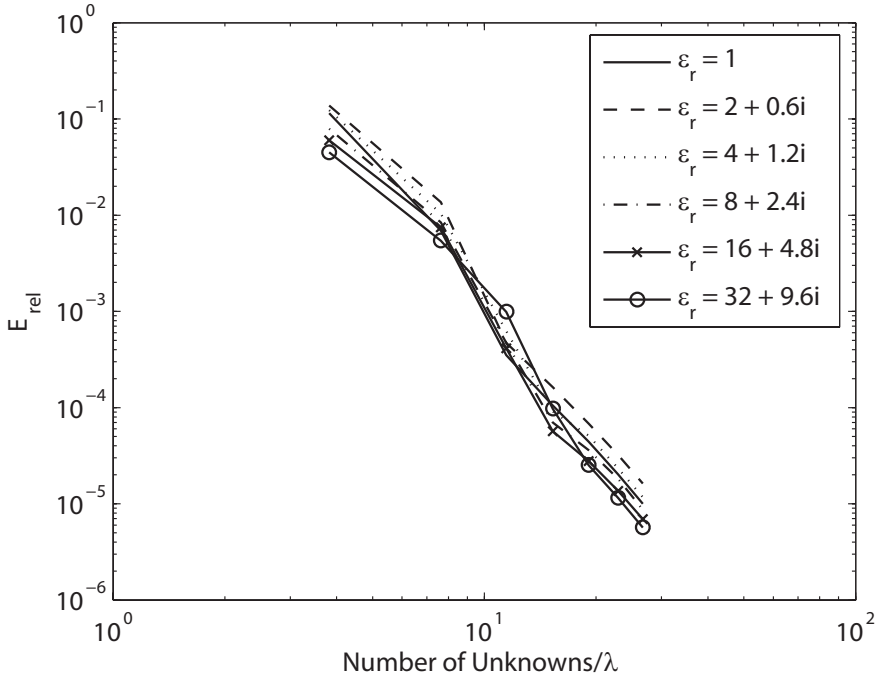

(b)

Figure B.11: TM, dielectric, PMCHWT, $N_q = 6$: (a) electric current; (b) magnetic current.

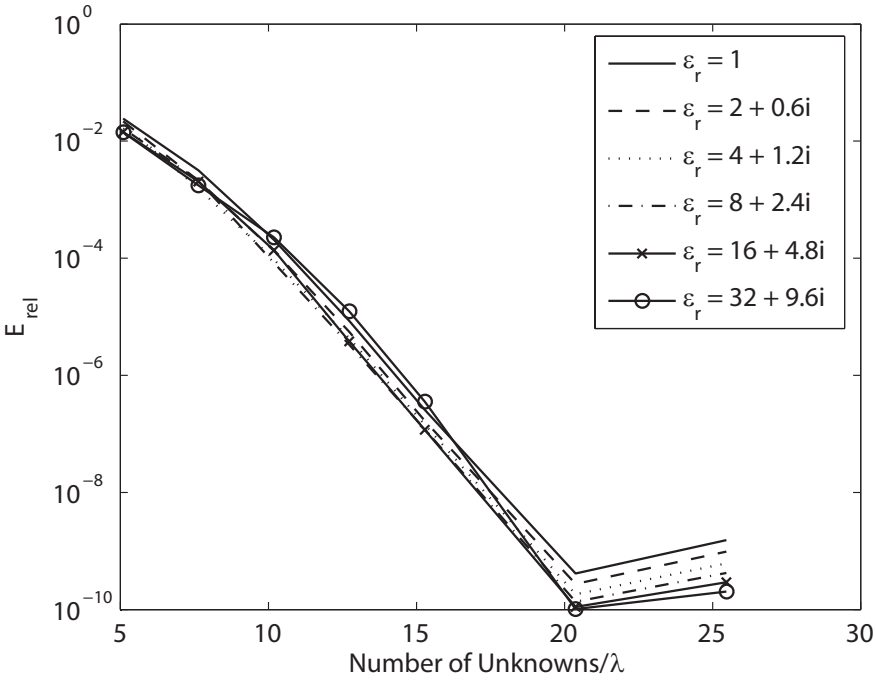

(a)

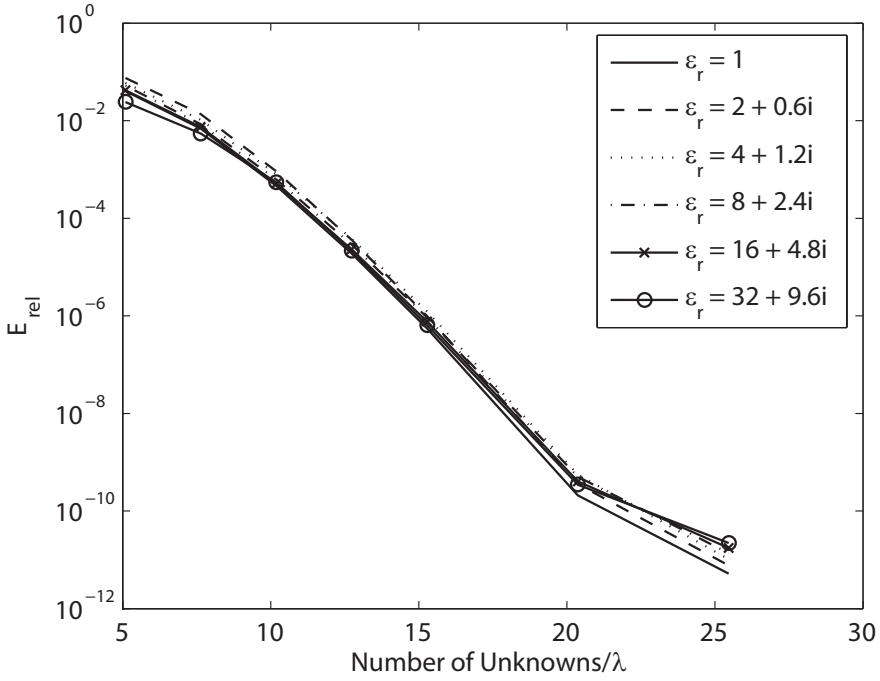

(b)

Figure B.12: TM, dielectric, PMCHWT, $N_s = 8$: (a) electric current; (b) magnetic current.

APPENDIX C

Second Order Asymptotic Green's Function for Half-Space—2D Case

The Sommerfeld integrals for calculating the electric fields radiating from an electric line source located above a dielectric half-space are given in [129]; analogous to the 3D problem investigated in Chapter II, saddle point integration can be applied in simplifying these integrals to their asymptotic forms; the resulting Green's function is given as follows:

$$\vec{E}^s(\vec{\rho}) = \overset{\approx}{G}_{2D}(\vec{\rho},\vec{\rho}') \cdot \vec{J}(\vec{\rho}'), \tag{C.1}$$

where

$$\overset{\approx}{G}_{2D}(\vec{\rho},\vec{\rho}') = \frac{\omega\mu_o e^{ik_o\rho}}{\sqrt{8\pi i k_o \rho}} \left[\overline{\overline{R}}(w_s) + \frac{1}{ik_o\rho}\left(\frac{1}{2}\overline{\overline{R}}''(w_s) + \frac{1}{8}\overline{\overline{R}}(w_s)\right)\right]; \tag{C.2}$$

$$\overline{\overline{R}}(w) = \begin{bmatrix} R_{TE}(w)\cos^2(w) & -R_{TE}(w)\sin(w)\cos(w) & 0 \\ R_{TE}(w)\sin(w)\cos(w) & -R_{TE}(w)\sin^2(w) & 0 \\ 0 & 0 & -R_{TM}(w) \end{bmatrix}; \tag{C.3}$$

$$\rho = \sqrt{(x-x')^2 + (y+y')^2}; \tag{C.4}$$

the saddle point is

$$w_s = \tan^{-1}\left(\frac{x'-x}{y'+y}\right); \tag{C.5}$$

and $''$ in (C.2) denotes the second derivative with $R_{TE}(w)$ and $R_{TM}(w)$ as the reflection coefficients in conventional forms.

APPENDIX D

Perturbation Solution for Scattering from Sinusoidal Surface

In the 2D case, assuming the excitation is $\vec{E}^{inc} = e^{i\left(k_x^i x - k_{0z}^i z\right)}\hat{y}$, i.e., TM polarized, the response of a sinusoidal dielectric surface of the form $\Delta f(x) = \Delta \sin(ax+\theta)$ can be summarized up to second order in the perturbation series as

$$\vec{E}^s = \left\{ E_i e^{i\vec{k}_i\cdot\vec{r}} + E_{i+a} e^{i\vec{k}_{i+a}\cdot\vec{r}} + E_{i-a} e^{i\vec{k}_{i-a}\cdot\vec{r}} + E_{i+2a} e^{i\vec{k}_{i+2a}\cdot\vec{r}} + E_{i-2a} e^{i\vec{k}_{i-2a}\cdot\vec{r}} \right\} \hat{y}, \quad \text{(D.1)}$$

where the Floquet mode coefficients can be derived from (6.7):

$$\begin{aligned} E_i \;=\; & \left\{ R_h^i e^{-ik_{0z}^i d} + \frac{\Delta^2}{4}\xi \left[ik_0^2 (\varepsilon_{r1}-1) \frac{g\left(k_{0z}^i\right)}{k_{0z}^i + k_{1z}^i} \right.\right. \\ & \cdot \left(\frac{k_{1z}^i}{k_{0z}^i} - 1 - k_0^2 (\varepsilon_{r1}-1) \frac{1}{k_{0z}^i} \left(\frac{1}{k_{0z}^{i+a} + k_{1z}^{i+a}} + \frac{1}{k_{0z}^{i-a} + k_{1z}^{i-a}} \right) \right) \\ & + \frac{k_{1z}^i}{k_{0z}^i} n\left(k_{0z}^i\right) - m\left(k_{0z}^i\right) - k_0^2 (\varepsilon_{r1}-1) \frac{n\left(k_{0z}^i\right)}{k_{0z}^i} \\ & \left.\left. \cdot \left(\frac{1}{k_{0z}^{i+a} + k_{1z}^{i+a}} + \frac{1}{k_{0z}^{i-a} + k_{1z}^{i-a}} \right) \right] \right\} e^{-ik_{0z}^i d}; \end{aligned} \quad \text{(D.2)}$$

$$E_{i+a} = \left\{ \frac{\Delta}{2}\xi \frac{1}{k_{0z}^{i+a}} \left[ik_0^2 (\varepsilon_{r1}-1) \frac{g\left(k_{0z}^{i+a}\right)}{e^{-ik_{1z}^{i+a} d}\left(k_{0z}^{i+a} + k_{1z}^{i+a}\right)} + n\left(k_{0z}^{i+a}\right) \right] \right\} e^{i\theta} e^{-ik_{0z}^i d}; \quad \text{(D.3)}$$

$$E_{i-a} = \left\{ \frac{\Delta}{2}\xi \frac{1}{k_{0z}^{i-a}} \left[ik_0^2 (\varepsilon_{r1}-1) \frac{-g\left(k_{0z}^{i-a}\right)}{e^{-ik_{1z}^{i-a} d}\left(k_{0z}^{i-a} + k_{1z}^{i-a}\right)} - n\left(k_{0z}^{i-a}\right) \right] \right\} e^{-i\theta} e^{-ik_{0z}^i d}; \quad \text{(D.4)}$$

$$
\begin{aligned}
E_{i+2a} \quad = \quad & \left\{ \frac{\Delta^2}{4} \xi \left[i k_0^2 \left(\varepsilon_{r1} - 1 \right) \frac{g\left(k_{0z}^{i+2a} \right)}{e^{-i k_{1z}^{i+2a} d} \left(k_{0z}^{i+2a} + k_{1z}^{i+2a} \right)} \right. \right. \\
& \cdot \left(\frac{-k_{1z}^{i}}{2 k_{0z}^{i+2a}} + \frac{1}{2} + k_0^2 \left(\varepsilon_{r1} - 1 \right) \frac{1}{k_{0z}^{i+2a} \left(k_{0z}^{i+a} + k_{1z}^{i+a} \right)} \right) \\
& - \frac{k_{1z}^{i}}{2 k_{0z}^{i+2a}} n\left(k_{0z}^{i+2a} \right) + \frac{m\left(k_{0z}^{i+2a} \right)}{2} + k_0^2 \left(\varepsilon_{r1} - 1 \right) \\
& \left. \left. \cdot \frac{n\left(k_{0z}^{i+2a} \right)}{k_{0z}^{i+2a} \left(k_{0z}^{i+a} + k_{1z}^{i+a} \right)} \right] \right\} e^{i 2\theta} e^{-i k_{0z}^{i} d}; \qquad \text{(D.5)}
\end{aligned}
$$

$$
\begin{aligned}
E_{i-2a} \quad = \quad & \left\{ \frac{\Delta^2}{4} \xi \left[i k_0^2 \left(\varepsilon_{r1} - 1 \right) \frac{g\left(k_{0z}^{i-2a} \right)}{e^{-i k_{1z}^{i-2a} d} \left(k_{0z}^{i-2a} + k_{1z}^{i-2a} \right)} \right. \right. \\
& \cdot \left(\frac{-k_{1z}^{i}}{2 k_{0z}^{i-2a}} + \frac{1}{2} + k_0^2 \left(\varepsilon_{r1} - 1 \right) \frac{1}{k_{0z}^{i-2a} \left(k_{0z}^{i-a} + k_{1z}^{i-a} \right)} \right) \\
& - \frac{k_{1z}^{i}}{2 k_{0z}^{i-2a}} n\left(k_{0z}^{i-2a} \right) + \frac{m\left(k_{0z}^{i-2a} \right)}{2} + k_0^2 \left(\varepsilon_{r1} - 1 \right) \\
& \left. \left. \cdot \frac{n\left(k_{0z}^{i-2a} \right)}{k_{0z}^{i-2a} \left(k_{0z}^{i-a} + k_{1z}^{i-a} \right)} \right] \right\} e^{-i 2\theta} e^{-i k_{0z}^{i} d}; \qquad \text{(D.6)}
\end{aligned}
$$

in which

$$
k_{mz}^{i+pa} = \sqrt{\left(k_m^2 - \left(k_x^{i+pa} \right)^2 \right)};\ m = 0, 1;\ p = 0, \pm 1, \pm 2; \qquad \text{(D.7)}
$$

$$
k_x^{i+pa} = k_x^{i} + pa; \qquad \text{(D.8)}
$$

$$
\vec{r} = x\hat{x} + z\hat{z}; \qquad \text{(D.9)}
$$

$$
\vec{k}_{i+pa} = k_x^{i+pa} \hat{x} + k_{0z}^{i+pa} \hat{z}; \qquad \text{(D.10)}
$$

$$
\begin{aligned}
g\left(k_{0z}^{i+pa} \right) \quad = \quad & \frac{i R_h^{i+pa}}{k_{1z}^{i+pa} - k_{0z}^{i+pa}} \left(e^{-i\left(k_{1z}^{i+pa} - k_{0z}^{i+pa} \right) d} - 1 \right) \\
& + \frac{i}{k_{1z}^{i+pa} + k_{0z}^{i+pa}} \left(e^{-i\left(k_{1z}^{i+pa} + k_{0z}^{i+pa} \right) d} - 1 \right); \qquad \text{(D.11)}
\end{aligned}
$$

$$
\xi = k_0^2 \left(\varepsilon_{r1} - 1 \right) \frac{k_{0z}^{i}}{k_{0z}^{i} + k_{1z}^{i}}; \qquad \text{(D.12)}
$$

$$R_h^{i+pa} = \frac{k_{0z}^{i+pa} - k_{1z}^{i+pa}}{k_{0z}^{i+pa} + k_{1z}^{i+pa}}; \tag{D.13}$$

$$n\left(k_{0z}^{i+pa}\right) = R_h^{i+pa} e^{ik_{0z}^{i+pa}d} + e^{-ik_{0z}^{i+pa}d}; \tag{D.14}$$

$$m\left(k_{0z}^{i+pa}\right) = R_h^{i+pa} e^{ik_{0z}^{i+pa}d} - e^{-ik_{0z}^{i+pa}d}. \tag{D.15}$$

The radiation from a TM line source located above the surface can be calculated using (6.30) and the formulations above; shown in Figures D.1 and D.2 are the results as compared to those obtained from full-wave simulations carried out with the numerical solver described in Chapter IV.

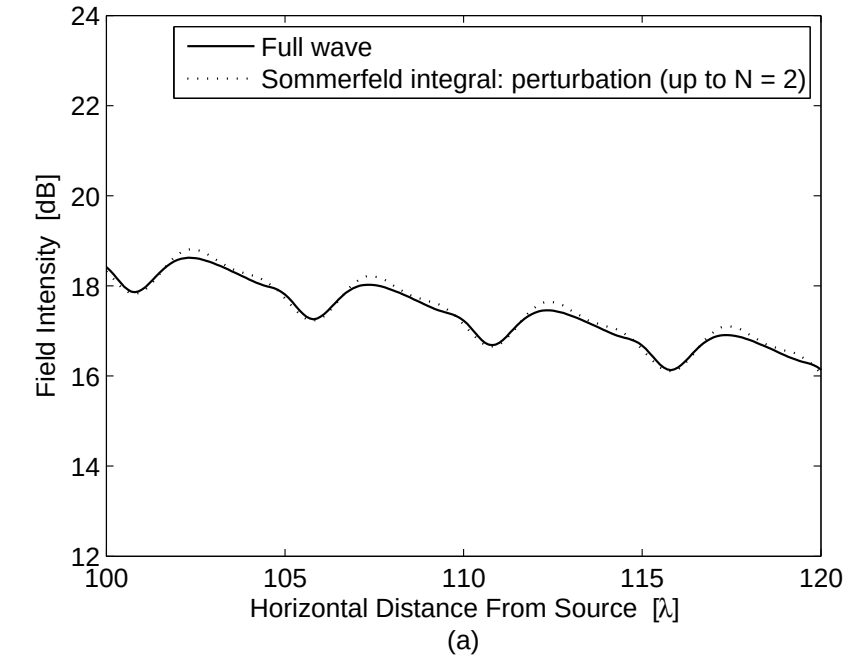

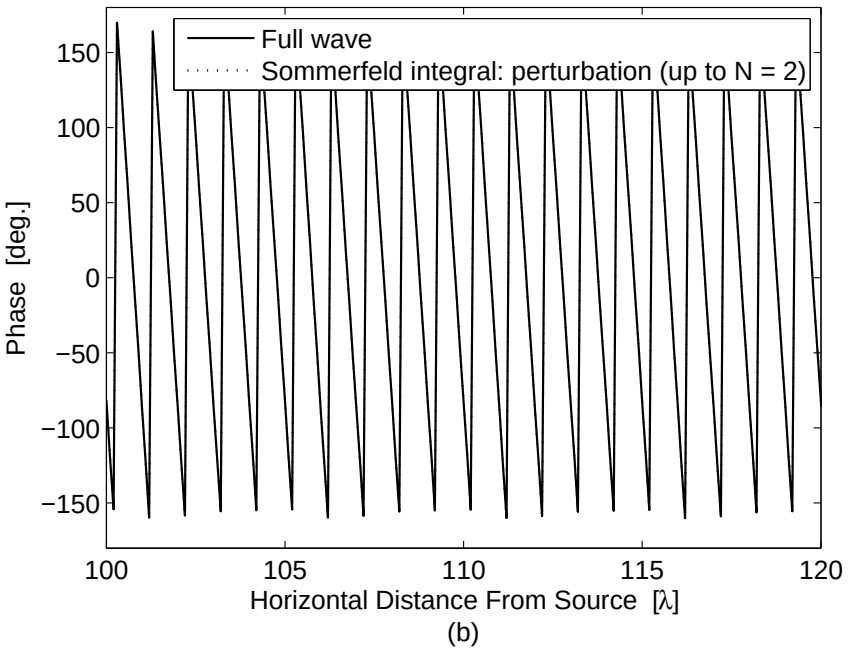

Figure D.1: Observed field (a) intensity and (b) phase from a TM line source located above a corrugated dielectric surface profile $\Delta f(x) = \Delta \sin\left(\frac{2\pi}{5}x\right)$ with $d = 2\lambda$, $\Delta = 0.25\lambda$; $\epsilon_{r1} = 2 + i$; $f = 300$ MHz; $z_{source} = 4.5\lambda$; $z_{observ.} = 3.5\lambda$.

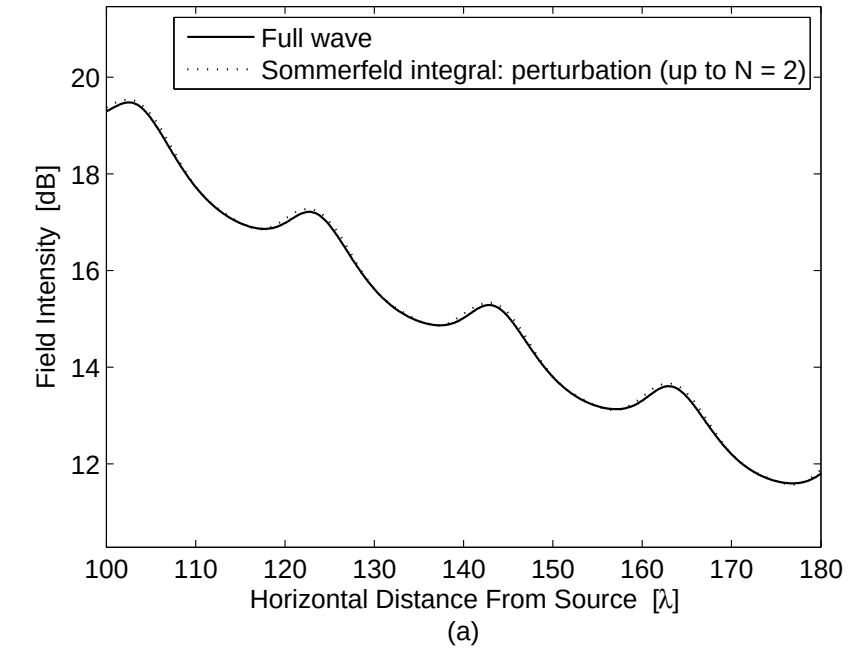

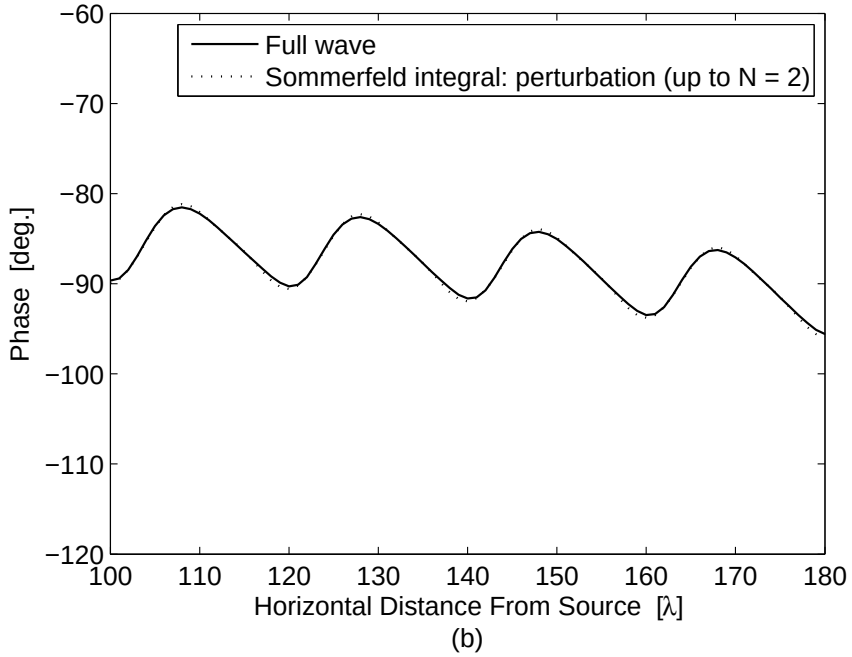

Figure D.2: Observed field (a) intensity and (b) phase from a TM line source located above a corrugated dielectric surface profile $\Delta f(x) = \Delta \sin\left(\frac{\pi}{10}x\right)$ with $d = 2\lambda$, $\Delta = 0.25\lambda$; $\epsilon_{r1} = 2 + i$; $f = 300$ MHz; $z_{source} = 4.5\lambda$; $z_{observ.} = 3.5\lambda$.

APPENDIX E

Supplement to Chapter VII

To reduce the singularity of the standard electric field integral equation, separate Green's functions can be defined to operate on the currents and charges. For a half-space problem, when the source and observation points are located in the upper medium, the following set of Sommerfeld integrals is needed to complete these Green's functions (detailed derivation is found in [105, 106]):

$$I_\Phi = \int_0^\infty -i\left[K - \frac{k_o^2(k_{oz}-k_{gz})}{k_\rho^2(k_{oz}+k_{gz})} - \frac{k_{oz}^2(\varepsilon_{rg}k_{oz}-k_{gz})}{k_\rho^2(\varepsilon_{rg}k_{oz}+k_{gz})}\right]\frac{k_\rho}{k_{oz}}e^{ik_{oz}(z+z')}J_o(k_\rho\rho)dk_\rho; \quad \text{(E.1)}$$

$$I_{xx} = \int_0^\infty i\left[\frac{k_{oz}-k_{gz}}{k_{oz}+k_{gz}}\right]\frac{k_\rho}{k_{oz}}e^{ik_{oz}(z+z')}J_o(k_\rho\rho)dk_\rho; \quad \text{(E.2)}$$

$$I_{xz} = K\cos\phi\int_0^\infty\left[\frac{2(1+\varepsilon_{rg})}{(k_{oz}+k_{gz})(\varepsilon_{rg}k_{oz}+k_{gz})} + \frac{1}{k_\rho^2}\right]e^{ik_{oz}(z+z')}J_1(k_\rho\rho)k_\rho^2dk_\rho; \quad \text{(E.3)}$$

$$I_{yz} = K\sin\phi\int_0^\infty\left[\frac{2(1+\varepsilon_{rg})}{(k_{oz}+k_{gz})(\varepsilon_{rg}k_{oz}+k_{gz})} + \frac{1}{k_\rho^2}\right]e^{ik_{oz}(z+z')}J_1(k_\rho\rho)k_\rho^2dk_\rho; \quad \text{(E.4)}$$

$$I_{zz} = \int_0^\infty i\left[\frac{k_{oz}-k_{gz}}{k_{oz}+k_{gz}} - 2K\frac{k_{oz}-k_{gz}}{\varepsilon_{rg}k_{oz}+k_{gz}}\right]\frac{k_\rho}{k_{oz}}e^{ik_{oz}(z+z')}J_o(k_\rho\rho)dk_\rho; \quad \text{(E.5)}$$

$$k_{oz,gz} = \sqrt{k_{o,g}^2 - k_\rho^2}; \quad \text{(E.6)}$$

$$\mathrm{Im}(k_{oz,gz}) > 0. \quad \text{(E.7)}$$

The MoM discretization here is based on the popular MPIE representation, although an alternate derivation—also compatible with RWG current expansion—has been proposed more recently by Chew *et al.* [130]; calculations of the interaction matrix elements in the new representation require only two Sommerfeld-type scalar Green's functions.

BIBLIOGRAPHY

BIBLIOGRAPHY

[1] T.K. Sarkar, R.J. Milloux, A.A. Oliner, M. Salazar-Palma, and D.L. Sengupta. *History of Wireless.* John Wiley and Sons, N.J., 2006.

[2] F.T. Ulaby and M.A. El-Rayes. Microwave dielectric spectrum of vegetation—Part II: Dual-dispersion model. *IEEE Trans. Geosci. Remote Sensing*, 25, Sep. 1987.

[3] M.C. Dobson, F.T. Ulaby, M.T. Hallikaiken, and M.A. El-Rayes. Microwave dielectric behavior of wet soil—Part II: Dielectric mixing models. *IEEE Trans. Geosci. Remote Sensing*, 23, Jan. 1985.

[4] J.E. Hipp. Soil electromagnetic parameters as functions of frequency, soil density, and soil moisture. *Proc. IEEE*, 62, Jan. 1974.

[5] G. Prado. Affordable unattended ground sensors: Technologies and challenges. *Unattended Ground Sensor Technologies and Applications VII, Proc. SPIE*, 5796, 2005.

[6] L.W. Barclay. Radiowave propagation - the basis of radiocommunication. *International Conference on 100 Years of Radio*, 1995.

[7] T. Bruns. Reconfigurable transceiver architecture for unattended ground sensors. *Unattended Ground, Sea, and Air Sensor Technologies and Applications VIII, Proc. SPIE*, 6231, 2006.

[8] G. G. Joshi, C. B. Dietrich Jr., C. R. Anderson, W. G. Newhall, W. A. Davis, J. Isaacs, and G. Barnett. Near-ground channel measurements over line-of-sight and forested paths. *IEE Proc.-Microw. Antennas Propagation*, 152, Dec. 2005.

[9] K. Sohrabi, B. Manriquez, and G.J. Pottie. Near-ground wideband channel measurement in 800-1000 MHz. *IEEE Vehicular Technology Conference*, 1, Jul. 1999.

[10] M. Casciato. *Radio Wave Diffraction and Scattering Models for Wireless Channel Simulation.* PhD thesis, The University of Michigan - Ann Arbor, 2001.

[11] I.-S. Koh. *Advanced Diffraction and Wave Propagation Models for Characterization of Wireless Communication Channels.* PhD thesis, The University of Michigan - Ann Arbor, 2002.

[12] A. Sommerfeld. Uber die ausbreitung der wellen in der drahtlosen telegraphie. *Ann. Physik*, 28, 1909.

[13] A. Sommerfeld. Uber die ausbreitung der wellen in der drahtlosen telegraphie. *Ann. Physik*, 81, 1926.

[14] A. Sommerfeld. *Partial Differential Equations in Physics.* Academic Press, New York, 1949.

[15] K. A. Norton. The propagation of radio waves over the surface of the earth and in the upper atmosphere: Part I. *Proc. IRE*, 24, Oct. 1936.

[16] K. A. Norton. The propagation of radio waves over the surface of the earth and in the upper atmosphere: Part II. *Proc. IRE*, 25, Sep. 1937.

[17] A. Banos. *Dipole Radiation in the Presence of a Conducting Half-Space*. Pergamon, Oxford, 1966.

[18] L.M. Brekhovskikh. *Waves in Layered Media*. Academic Press, N.Y., 1960.

[19] L.B. Felsen and N. Marcuvitz. *Radiation and Scattering of Waves*. Prentice-Hall, N.J., 1973.

[20] T. Tamir. On radio-wave propagation in forest environments. *IEEE Trans. Antennas and Propagation*, 15, Nov. 1967.

[21] T. Tamir. Radio wave propagation along mixed paths in forest environments. *IEEE Trans. Antennas and Propagation*, 25, Jul. 1977.

[22] L.W. Li, J.H. Koh, T.S. Yeo, M.S. Leong, and P.S. Kooi. Analysis of radiowave propagation in a four-layered anisotropic forest environment. *IEEE Trans. Geosci. Remote Sensing*, 37, Jul. 1999.

[23] G.P.S. Cavalcante and A.J. Giarola. Optimization of radio communication in media with three layers. *IEEE Trans. Antennas and Propagation*, 31, Jan. 1983.

[24] K. Sarabandi and I.-S. Koh. Effect of canopy-air interface roughness on HF–VHF wave propagation in forest. *IEEE Trans. Antennas and Propagation*, 50, Feb. 2002.

[25] J.C. Schelleng, C.R. Burrows, and E.B. Ferrell. Ultra-short wave propagation. *Bell Syst. Tech. J.*, Apr. 1933.

[26] K. Bullington. Radio propagation fundamentals. *Bell Syst. Tech. J.*, 1957.

[27] G. Millington, R. Hewitt, and F.S. Immirzi. Double knife-edge diffraction in field-strength prediction. *Inst. Elec. Eng. Monography 507 E.*, Mar. 1962.

[28] A.G. Longley and P.L. Rice. Prediction of tropospheric radio transmission loss over irregular terrain. *U.S. Department of Commerce, ESSA Rep. ERL-79-ITS-67*, 1968.

[29] R.J. Luebbers. Finite conductivity uniform GTD versus knife edge diffraction in prediction of propagation path loss. *IEEE Trans. Antennas and Propagation*, 32, Jan. 1984.

[30] R.J. Luebbers. Propagation prediction for hilly terrain using GTD wedge diffraction. *IEEE Trans. Antennas and Propagation*, 32, Sep. 1984.

[31] L.F. Canino, J.J. Ottusch, M.A. Stalzer, J.L. Visher, and S.M. Wandzura. Numerical solution of the Helmholtz equation in 2D and 3D using a high-order Nyström discretization. *J. Comput. Phys.*, 146, 1998.

[32] W.S. Ament. Toward a theory of reflection by a rough surface. *Proc. IRE*, 1953.

[33] R.M. Brown and A.R. Miller. Geometric-optics theory for coherent scattering of microwaves from the ocean surface. *NRL Rep. 7705*, 1974.

[34] A.R. Miller, R.M. Brown, and E. Vegh. New derivation for the rough-surface reflection coefficient for the distribution of sea wave elevations. *IEE Proc.-H*, 131, Apr. 1984.

[35] K. Sarabandi and T. Chiu. Electromagnetic scattering from slightly rough surfaces with inhomogeneous dielectric profiles. *IEEE Trans. Antennas and Propagation*, 45, Sep. 1997.

[36] W.C. Chew and J.A. Kong. Asymptotic approximation of waves due to a dipole on a two-layer medium. *Radio Sci.*, 17, May-Jun. 1982.

[37] M.A. Marin and P.H. Pathak. An asymptotic closed-form representation for the grounded double-layer surface green's function. *IEEE Trans. Antennas and Propagation*, 38, Nov. 1992.

[38] F.T. Ulaby, R.K. Moore, and A.K. Fung. *Microwave Remote Sensing.* Artech, Dedham, MA., 1986.

[39] M.E. Tiuri, A.H. Sihvola, E.G. Nyfors, and M.T. Hallikaiken. The complex dielectric constant of snow at microwave frequencies. *IEEE Journal of Oceanic Engineering*, 9, Dec. 1984.

[40] L. Tsang, J.A. Kong, and R.T. Shin. *Theory of Microwave Remote Sensing.* Wiley, N.Y., 1985.

[41] E.C. Jordan and K.G. Balmain. *Electromagnetic Waves and Radiating Systems.* Prentice-Hall, Englewood Cliffs, N.J., 1968.

[42] T. Tamir and A.A. Oliner. Guided complex waves. *IEE Proc.*, 110, 1963.

[43] T. Tamir. Inhomogeneous wave types at planar interfaces: II. Surface waves. *Optik*, 37, 1973.

[44] T. Tamir. Inhomogeneous wave types at planar interfaces: III. Leaky waves. *Optik*, 38, 1973.

[45] J.A Kong, L. Tsang, and G. Simmons. Geophysical surface probing with radio-frequency interferometry. *IEEE Trans. Antennas and Propagation*, 22, Nov. 1974.

[46] W.C. Chew. *Waves and Fields in Inhomogeneous Media.* Van Nostrand Reinhold, N.Y., 1990.

[47] R.J. Luebbers, J.W. Schuster, and K.C. Wu. Full wave propagation model based on moving window FDTD. *Military Communications Conference (MILCOM 2003)*, 2, 2003.

[48] J.W. Schuster, K.C. Wu, R.R. Ohs, and R.J. Luebbers. Application of moving window FDTD to predicting path loss over forest covered irregular terrain. *IEEE Antennas and Propagation Society International Symposium*, 2, 2004.

[49] S. Wang and F.L. Teixeira. A finite-difference time-domain algorithm optimized for arbitrary propagation angles. *IEEE Trans. Antennas and Propagation*, 51, Sep. 2003.

[50] F. Akleman and L. Sevgi. Realistic surface modeling for a finite difference time domain wave propagator. *IEEE Trans. Antennas and Propagation*, 51, Jul. 2003.

[51] R.F. Harrington. *Time-Harmonic Electromagnetic Fields.* McGraw-Hill, N.Y., 1961.

[52] K.-M. Chen. A mathematical formulation of the equivalence principle. *IEEE Trans. Microw. Theory and Techniques*, 37, Oct. 1989.

[53] M. Abramowitz and I.A. Stegun. *Handbook of Mathematical Functions with Formulas, Graphs, and Mathematical Tables.* U.S. Dept. of Commerce, National Bureau of Standards, Washington D.C., 1972.

[54] F. Aryanfar and K. Sarabandi. A millimeter-wave scaled measurement system for wireless channel characterization. *IEEE Trans. Microw. Theory and Techniques*, 52, Jun. 2004.

[55] F. Aryanfar and K. Sarabandi. Evaluation of a wave propagation simulator using a 95 GHz transceiver system. *IEEE Antennas and Propagation Society International Symposium*, 4, 2003.

[56] C. Brennan and P.J. Cullen. Application of the fast far-field approximation to the computation of UHF pathloss over irregular terrain. *IEEE Trans. Antennas and Propagation*, 46, Jun. 1998.

[57] C. Brennan and P.J. Cullen. Tabulated interactions method for UHF terrain propagation problems. *IEEE Trans. Antennas and Propagation*, 46, May 1998.

[58] C. Brennan and P.J. Cullen. Multilevel tabulated interactions method applied to UHF propagation over irregular terrain. *IEEE Trans. Antennas and Propagation*, 47, Oct. 1998.

[59] E. Bleszynski, M. Bleszynski, and T. Jaroszewicz. AIM: Adaptive integral method for solving large-scale electromagnetic scattering and radiation problems. *Radio Sci.*, 31, Sep. 1996.

[60] V. Rokhlin. Rapid solution of integral equation of scattering theory in two dimensions. *J. Comput. Phys.*, 86, Feb. 1990.

[61] W.C. Chew, J.M. Jin, E. Michielssen, and J.M. Song. *Fast and Efficient Algorithms in Computational Electromagnetics*. Artech House, Boston, MA., 2001.

[62] C.T.H. Baker. *The Numerical Treatment of Integral Equations*. Clarendon Press, Oxford, 1977.

[63] W. McLean. Asymptotic error expansions of numerical solutions of integral equations. *IAM J. Numer. Anal.*, 9, 1989.

[64] D.H. Liao, E. Michielssen, and K. Sarabandi. Simulation of terrain propagation and diffraction using a 2D high-order accurate FMM-accelerated Nyström's solver. *IEEE Antennas and Propagation Society International Symposium*, 4, 2007.

[65] R.J. Burkholder, P.H. Pathak, and C.J. Reddy. Asymptotic phasefront extraction applied to iterative physical optics for electrically large multi-bounce problems. *IEEE Antennas and Propagation Society International Symposium*, 4, 2004.

[66] K.R. Aberegg and A.F. Peterson. Application of the integral equation-asymptotic phase method to two-dimensional scattering. *IEEE Trans. Antennas and Propagation*, 43, May 1995.

[67] D.-H. Kwon, R.J. Burkholder, and P.H. Pathak. Efficient method of moments formulation for large PEC scattering problems using asymptotic phasefront extraction (APE). *IEEE Trans. Antennas and Propagation*, 49, Apr. 2001.

[68] I. Garcia-Tunon, J.M. Taboada, J.L. Rodriguez, F. Obelleiro, and L. Landesa. Efficient asymptotic-phase modeling of the induced currents in the fast multipole method. *Microwave Opt. Tech. Lett.*, 48, May 2006.

[69] O.P. Bruno and C.A. Geuzaine. An $\mathcal{O}(1)$ integration scheme for three-dimensional surface scattering problems. *J. Comput. Appl. Mathem.*, 204, 2007.

[70] F. Vico, G. Vecchi, and M. Ferrando. A new approach to asymptotic phasefront extraction in MoM. *IEEE Antennas and Propagation Society International Symposium*, 2007.

[71] A.J. Poggio and E.K. Miller. Integral equation solutions of three dimensional scattering problems. In R. Mittra, editor, *Computer Techniques for Electromagnetics*. Hemisphere, Washington D.C., 1987.

[72] Y. Chang and R.F. Harrington. A surface formulation for characteristic modes of material bodies. *IEEE Trans. Antennas and Propagation*, 25, Nov. 1977.

[73] T.K. Wu and L.L. Tsai. Scattering from arbitrarily-shaped lossy dielectric bodies of revolution. *Radio Sci.*, 12, Oct. 1977.

[74] T. Ida, T. Ishihara, and K. Goto. Frequency-domain and time-domain novel uniform asymptotic solutions for scattered fields by an impedance cylinder and a dielectric cylinder. *IEICE Trans. Electron.*, E88-C, Nov. 2005.

[75] E.I. Thorsos. The validity of the kirchhoff approximation for rough surface scattering using a gaussian roughness spectrum. *J. Acoust. Soc. Am.*, 83, Jan. 1988.

[76] J.J. Knab. Interpolation of band-limited functions using the approximate prolate series. *IEEE Trans. Info. Theory*, 25, Nov. 1979.

[77] S.D. Gedney. On deriving a locally corrected Nyström scheme from a quadrature sampled moment method. *IEEE Trans. Antennas and Propagation*, 51, Sep. 2003.

[78] S.O. Rice. Reflection of electromagnetic wave by slightly rough surfaces. *Commun. Pure Appl. Mathem.*, 4, 1951.

[79] M. Nieto-Vesperinas. Depolarization of electromagnetic waves scattered from slightly rough random surfaces: A study by means of the extinction theorem. *J. Opt. Soc. Am.*, 72, May 1982.

[80] D. Winebrenner and A. Ishimaru. Investigation of a surface field phase perturbation technique for scattering from rough surfaces. *Radio Sci.*, 20, Mar. 1985.

[81] E. Rodriguez and Y. Kim. A unified perturbation expansion for surface scattering. *Radio Sci.*, 27, Jan. 1992.

[82] P. Beckmann and A. Spizzichino. *The Scattering of Electromagnetic Waves from Rough Surfaces*. Pergamon, New York, 1963.

[83] V. Jandhyala, B. Shanker, E. Michielssen, and W. C. Chew. Fast algorithm for the analysis of scattering by dielectric rough surfaces. *J. Opt. Soc. Am. A*, 15, Jul. 1998.

[84] B.E. Barrowes, F.L. Teixeira, and J.A. Kong. Fast algorithm for matrix-vector multiply of asymmetric multilevel block-toeplitz matrices in 3-D scattering. *Microwave Opt. Tech. Lett.*, 31, Oct. 2001.

[85] A. Ishimaru. *Electromagnetic Wave Propagation, Radiation, and Scattering*. Prentice Hall, Englewood Cliffs, N.J., 1991.

[86] L. Boithias. *Radio Wave Propagation*. McGraw-Hill, New York, 1987.

[87] D.M. Milder. Surface shadowing at small grazing angle. *Waves in Random Media*, 13, 2003.

[88] C. Bourlier, N. Pinel, and V. Fabbro. Illuminated height PDF of a random rough surface and its impact on the forward propagation above oceans at grazing angles. Technical Report ESA SP626 SP, European Space Agency, 2006.

[89] F.G. Bass and I.M. Fuks. *Wave Scattering from Statistically Rough Surfaces*. Pergamon, New York, 1979.

[90] N. Bleistein. Uniform asymptotic expansion of integrals with stationary point near algebraic singularity. *Commun. Pure Appl. Mathem.*, 19, 1966.

[91] N. Bleistein and R.A. Handelsman. *Asymptotic Expansion of Integrals*. Holt, Rinehart, and Winston, New York, 1975.

[92] M.K. Hellen and I.J. Craddock. Calculation of the input impedance of dipoles in proximity to walls. *Proc.-Microw. Antennas Propagation*, 150, Oct. 2003.

[93] D. Poljak and V. Roje. Boundary-element approach to calculation of wire antenna parameters in the presence of dissipative halfspace. *IEE Proc.-Microw. Antennas Propagation*, 142, Dec. 1995.

[94] R.A. Kipp and C.H. Chan. A complex image method for the vertical component of the magnetic potential of a horizontal dipole in layered media. *IEEE Antennas and Propagation Society International Symposium*, 2, Jun. 1994.

[95] R.M. Shubair and Y.L. Chow. A closed-form solution of vertical dipole antennas above a dielectric half-space. *IEEE Trans. Antennas and Propagation*, 41, Dec. 1993.

[96] R.M. Shubair and Y.L. Chow. A simple and accurate complex image interpretation of vertical antennas present in contiguous dielectric half-spaces. *IEEE Trans. Antennas and Propagation*, 41, Jun. 1993.

[97] J.J. Yang, Y.L. Chow, and D.G. Fang. Discrete complex images of a three-dimensional dipole above and within a lossy ground. *IEE Proc.-H*, 138, Aug. 1991.

[98] J. Qian, K.L. Wu, and J. Litva. Impedance of a circular array of vertical dipoles above a lossy ground. *IEEE Antennas and Propagation Society International Symposium*, 2, May 1990.

[99] D.G. Fang, J.J. Yang, and G.Y. Delisle. Discrete image theory for horizontal electric dipoles in a multilayered medium. *IEE Proc.-H*, 135, Oct. 1988.

[100] E. Alanen and I.V. Lindell. Impedance of vertical electric and magnetic dipole above a dissipative ground. *Radio Sci.*, 19, Nov.-Dec. 1984.

[101] E.K. Miller, A.J. Poggio, G.J. Burke, and E.S. Selden. Analysis of wire antennas in the presence of a conducting half-space. Part I: The vertical antenna in free space. *Canadian Journal of Physics*, 50, 1972.

[102] E.K. Miller, A.J. Poggio, G.J. Burke, and E.S. Selden. Analysis of wire antennas in the presence of a conducting half-space. Part II: The horizontal antenna in free space. *Canadian Journal of Physics*, 50, 1972.

[103] R.G. Olsen and D.C. Chang. Input impedance change of a half-wave vertical antenna over a dissipative earth. *IEEE Trans. Antennas and Propagation*, 19, Sep. 1971.

[104] L.E. Vogler and J.L. Noble. Curves of input impedance change due to ground for dipole antennas. *U. S. National Bureau of Standards, Monograph 72*, 19, Jan. 1964.

[105] K.A. Michalski and D. Zheng. Electromagnetic scattering and radiation by surfaces of arbitrary shape in layered media, Part I: Theory. *IEEE Trans. Antennas and Propagation*, 38, Mar. 1990.

[106] K.A. Michalski and D. Zheng. Electromagnetic scattering and radiation by surfaces of arbitrary shape in layered media, Part II: Implementation and results for contiguous half-spaces. *IEEE Trans. Antennas and Propagation*, 38, Mar. 1990.

[107] K.A. Michalski. On the scalar potential of a point charge associated with a time-harmonic dipole in a layered medium. *IEEE Trans. Antennas and Propagation*, 35, Nov. 1987.

[108] S.M. Rao. *Electromagnetic Scattering and Radiation of Arbitrarily-Shaped Surfaces by Triangular Patch Modeling.* PhD thesis, The University of Mississippi, 1980.

[109] S.M. Rao, D.R. Wilton, and A.W. Glisson. Electromagnetic scattering by surfaces of arbitrary shape. *IEEE Trans. Antennas and Propagation*, 30, May 1982.

[110] J.D. Kraus. *Antennas.* McGraw-Hill, N.Y., 1988.

[111] T.F. Eibert and V. Hansen. On the calculation of potential integrals for linear source distributions on triangular domains. *IEEE Trans. Antennas and Propagation*, 43, Dec. 1995.

[112] R.D. Graglia. On the numerical integration of the linear shape functions times the 3-D green's function or its gradient on a plane triangle. *IEEE Trans. Antennas and Propagation*, 41, Oct. 1993.

[113] S.M. Rao, A.W. Glisson, D.R. Wilton, and B.S. Vidula. A simple numerical solution procedure for statics problems involving arbitrary-shaped surfaces. *IEEE Trans. Antennas and Propagation*, 27, Dec. 1979.

[114] Y. Hua and T.K. Sarkar. Generalized pencil-of-function method for extracting poles of an em system from its transient response. *IEEE Trans. Antennas and Propagation*, 37, Feb. 1989.

[115] T.K. Sarkar and O. Pereira. Using the matrix pencil method to estimate the parameters of a sum of complex exponentials. *IEEE Antennas and Propagation Magazine*, 37, Feb. 1995.

[116] N.V. Shuley, R.R. Boix, F. Medina, and M. Horno. On the fast approximation of green's functions in MPIE formulations for planar layered media. *IEEE Trans. Microw. Theory and Techniques*, 50, Sep. 2002.

[117] M.K. Hellen and I.J. Craddock. Improving the accuracy of the complex image technique. *Microwave Opt. Tech. Lett.*, 28, Mar. 2001.

[118] R. Fenwick and W. Weeks. Submerged antenna characteristics. *IEEE Trans. Antennas and Propagation*, 11, May 1963.

[119] R. Fenwick and W. Weeks. Submerged antenna performance. *IRE International Convention Record*, 10, Mar. 1962.

[120] P.E. Atlamazoglou and N.K. Uzunoglu. A galerkin moment method for the analysis of an insulated antenna in a dissipative dielectric medium. *IEEE Trans. Microw. Theory and Techniques*, 46, Jul. 1998.

[121] R.W.P. King, B.S. Trembly, and J.W. Strohbehn. The electromagnetic field of an insulated antenna in a conducting or dielectric medium. *IEEE Trans. Microw. Theory and Techniques*, 83, Jul. 1983.

[122] K.W. Leung. Efficient and accurate computation of an annular slot on a dielectric half-space. *IEEE Trans. Antennas and Propagation*, 48, Mar. 2000.

[123] C.Y.E. Tong and R. Blundell. An annular slot antenna on a dielectric half-space. *IEEE Trans. Antennas and Propagation*, 42, Jul. 1994.

[124] J.R. Mosig. Arbitrarily shaped microstrip structures and their analysis with a mixed potential integral equation. *IEEE Trans. Microw. Theory and Techniques*, 36, Feb. 1988.

[125] L. Barlatey, J. R. Mosig, and T. Sphicopoulos. Analysis of stacked microstrip patches with a mixed potential integral equation. *IEEE Trans. Antennas and Propagation*, 38, May 1990.

[126] I.P. Theron and J. H. Cloete. On the surface impedance used to model the conductor losses of microstrip structures. *IEE Proc.-Microw. Antennas Propagation*, 142, Feb. 1995.

[127] D.E. Barrick. Grazing behavior of scatter and propagation above any rough surface. *IEEE Trans. Antennas and Propagation*, 46, Jan. 1998.

[128] J. Ma, V. Rokhlin, and S. Wandzura. Generalized Gaussian quadrature rules for systems of arbitrary functions. *SIAM J. Numer. Anal.*, 33, Jun. 1996.

[129] K. Sarabandi. Scattering from dielectric structures above impedance surfaces and resistive sheets. *IEEE Trans. Antennas and Propagation*, 40, Jan. 1992.

[130] W.C. Chew, J.L. Xiong, and M.A. Saville. A matrix-friendly formulation of layered medium green's functions. *IEEE Antennas and Wireless Propagation Lett.*, 5, Dec. 2006.